# Numerical modeling of the links between earthquakes and landsliding during the seismic cycle : triggering processes, size distribution, and geological implications

Louise Jeandet

UNIVERSITE ECOLOGIE
BRETAGNE GEOSCIENCES
LOIRE AGRONOMIE ALIMENTATION

UNIVERSITÉ DE RENNES 1

# THESE DE DOCTORAT DE

L'UNIVERSITE DE RENNES 1
COMUE UNIVERSITE BRETAGNE LOIRE

ECOLE DOCTORALE N° 600
*Ecole doctorale Ecologie, Géosciences, Agronomie et Alimentation*
Spécialité : « *Sciences de la Terre et de l'environnement* »

Par
**Louise JEANDET**

# Modélisation numérique des liens entre séismes et glissements de terrain au cours du cycle sismique : processus déclencheurs, distributions de tailles et implications géologiques

**Thèse présentée et soutenue à Rennes, le 18/12/2018**
**Unité de recherche : Géosciences Rennes**

**Rapporteurs avant soutenance** :

Alexander Densmore, Professeur, Université de Durham
Rodolphe Cattin, Professeur, Géosciences Montpellier

**Composition du Jury :**

Philippe Yamato, Professeur, Géosciences Rennes / Président du jury

Alexander Densmore, Professeur, Université de Durham / Rapporteur

Rodolphe Cattin, Professeur, Géosciences Montpellier / Rapporteur

Mathilde Radiguet, Enseignant-chercheur, ISTerre, Université Grenoble-Alpes / Examinatrice

Oliver Korup, Professeur, Université de Potsdam / Examinateur

Dimitri Lague, Directeur de recherche, Géosciences Rennes / Directeur de thèse

Philippe Steer, Maitre de conférences, Géosciences Rennes / Directeur de thèse

## Résumé

Les interactions entre les processus tectoniques et l'érosion ont été peu étudiées à des échelles de temps courtes (< 1000 ans). Cependant, les séismes peuvent activement contribuer à l'érosion des chaînes de montagne en déclenchant de nombreux glissements de terrain. Des études récentes ont également montré que ces grands événements érosifs pourraient engendrer des changements de contraintes suffisants à proximité des failles actives pour modifier la sismicité régionale. Dans cette thèse, cette problématique a été abordée via une approche numérique. Dans un premier temps, le développement d'un modèle simple de glissements de terrain prenant en compte la topographie des versants a permis de démontrer le rôle des paramètres mécaniques (cohésion et friction), et de la forme des versants sur la distribution de taille des glissements de terrain. Ce modèle a été validé à l'aide de cas naturels de glissements de terrain co-sismiques Dans un deuxième temps, le rôle de la forme finie des versants sur la probabilité de grands glissements de terrain a été démontrée en se basant sur des données. Enfin, dans un troisième temps, le potentiel effet d'un grand évènement érosif sur la sismicité a été exploré à l'aide d'un modèle numérique de cycle sismique dans lequel ont été implémentées des variations temporelles de la contrainte normale sur la faille. Les résultats mettent en évidence le rôle du volume de sédiments, mais aussi de leur temps d'export. En particulier, les paysages caractérisés par une hauteur unstable des versants importante pourraient, en favorisant de grands glissements de terrain, induire une érosion assez importante et rapide pour modifier de façon significative la sismicité régionale.

## Abstract

Interactions between tectonic processes and erosion have been poorly investigated at short time-scales (<1000 years). However, earthquakes can largely contribute to the erosion of mountain belts by triggering widespread landsliding. Moreover, recent studies have shown that such large erosional events could induce stress changes in the fault environment efficient enough to influence regional seismicity. In this thesis, this problematic is tackled through a numerical approach. Firstly, the development of a simple mechanical model accounting for the complexity and variability of natural hillslopes allowed to demonstrate the role of mechanical parameters (cohesion and friction), and of hillslope shape in the probability density function of landslide sizes. This model has been validated using natural cases of co-seismic landsliding. Secondly, the role of unstable hillslope height on large landslide probability has been demonstrated based on natural data, and the exponential distribution of this unstable height has been shown. Finally, the potential effect of a large erosional event on seismicity has been explored with a numerical model of seismic cycle, in which has been implemented temporal normal stress variations. The results emphasize the role of eroded sediment volume, but also of the export time of sediments away from the mountain belt. In landscape with high unstable hillslopes, large landslides are favored and in turn, could induce fast an important enough erosion to modify regional seismicity.

# Résumé étendu

*Ce manuscrit de thèse est rédigé intégralement en anglais. Le résumé étendu ci-après est écrit dans le but de donner un aperçu du contenu de cette thèse à un lecteur non anglophone.*

## Chapitre 1 - Préambule

L'altitude et la forme actuelles des chaînes de montagnes résultent de l'action conjointe des processus qui les élèvent et des processus qui les nivellent. Une large gamme de processus de déformation et d'échelles de temps associées contribuent ainsi à l'évolution du paysage: d'une rupture sismique se propageant à plusieurs mètres par seconde en quelques secondes à la construction de chaînes de montagnes par l'accumulation de déformations tectoniques sur des millions d'années. Les processus d'érosion sont les processus de surface qui transportent les sédiments hors des chaînes de montagne via les rivières, l'ablation glaciaire, les glissements de terrains et autre processus gravitaires, l'altération chimique, etc. Ces processus contribuent à niveler les chaînes de montagnes et interagissent avec les phénomènes tectoniques à toutes les échelles de temps. Dans cette section, nous examinons brièvement les interactions entre la tectonique et l'érosion à des échelles de temps géologiques (1 Myrs - 100 Myrs) et intermédiaires (10 000 ans - 1 Myrs). Nous nous concentrons ensuite sur les interactions à des échelles de temps plus courtes ($<$ 1000 ans) et leurs principales implications pour la vie humaine ainsi que pour l'évolution des chaines de montagne.

Le fait que les processus d'érosion peuvent influencer la déformation des chaines de montagne à des échelles de temps géologiques est désormais largement accepté. A des échelles de temps plus courtes (10 000 ans - 1 Myrs), l'érosion pourrait également jouer un rôle sur la sismicité régionale via le rebond isostatique. A des échelles de temps plus courtes, ces interactions sont très mal contraintes. Cependant, elles ont de nombreuses implications sociétales et géologiques :

- Les grands séismes peuvent engendrer de nombreux glissements de terrain qui représentent un risque important pour les populations résidant dans des zones tectoniques à fort risque sismique;
- L'érosion co-sismique peut être aussi, voire plus importante, que le volume de roche élevé lors d'un séisme; ainsi, les grands séismes pourraient, dans certaines circonstances, avoir un budget topographique négatif;
- Enfin, les processus de surface peuvent significativement modifier la sismicité régionale. C'est le cas, par example, des processus cycliques tels que les processus hydrologiques. On peut alors s'attendre à ce que des épisodes érosifs ponctuels mais importants, comme l'érosion co-sismique, puissent également modifier le jeu des failles actives au moins dans les premiers kilomètres de la croûte.

# Chapitre 2 - Introduction

Ce chapitre vise à décrire les concepts à la base de mon travail. Il commence par décrire la mécanique des glissements de terrain et des séismes, en abordant les notions pertinentes pour comprendre leurs interactions à l'échelle de temps du cycle sismique. Je décris ensuite les interactions entre ces deux processus, en me basant principalement sur l'observation de cas naturels. Enfin, je me concentre sur les observations et les explications physiques de la taille des séismes et des glissements de terrain.

Cet état de l'art soulève des problèmes auxquels je m'efforcerai de répondre au cours de cette thèse. Ces questions en suspens sont résumées à la fin de chaque partie.

## Mécanique des séismes et des glissements de terrain

Les tremblements de terre et les glissements de terrain sont deux manifestations de la déformation fragile des roches lithosphériques. Les tremblements de terre se produisent lors du mouvement brusque de roches le long de failles de la croûte terrestre, qui rompent parfois jusqu'à la surface de la Terre. Les glissements de terrain sont caractérisés par la rupture catastrophique des versants, qui peuvent être déclenchées par un facteur externe tel que le mouvement co-sismique du sol. Dans un cas statique, une rupture de la roche peut survenir lorsque la contrainte motrice appliquée à une roche est supérieure à sa résistance à la rupture. Dans cette section, je présente d'abord la notion de résistance des roches et le problème macroscopique de rupture fragile. Je me concentre plus spécifiquement sur la mécanique des tremblements de terre dans une deuxième section, puis sur la mécanique des glissements de terrain dans une dernière partie.

Questions en suspens :

- Quelle est la résistance des roches, à l'échelle du paysage, impliquée à des échelles de temps pertinentes en géomorphologie ?

- Est-il possible de prédire la variabilité de la profondeur des glissements de terrain dans un modèle de glissement de terrain restant simple d'un point de vue mécanique ?

- La prise en compte explicite de l'accélération co-sismique est-elle nécessaire pour modéliser les glissements de terrain co-sismiques?

## Interactions entre séismes et glissements de terrain

Dans la première section, j'ai montré que les tremblements de terre et les glissements de terrain peuvent être déclenchés par des changements de contrainte dans leur environnement. En effet, les tremblements de terre peuvent être déclenchés par le changement de contrainte statique dû à un séisme important, et les glissements de terrain quant à eux peuvent être déclenchés par l'accélération due aux ondes sismiques. Certaines observations montrent que les processus de surface peuvent modifier le champ de contrainte autour des failles peu profondes, suffisamment pour déclencher des séismes. Cependant, les séismes ne provoquent pas systématiquement de nombreux glissements de terrain, et les processus de surface ne modifient pas systématiquement la sismicité régionale. Dans cette section, je décris les observations 1) de la réponse du paysage aux tremblements de terre et 2) des séismes déclenchés par les processus de surface, et je tente de montrer ce que ces observations nous disent des mécanismes de déclenchement au cours du cycle sismique.

***Questions en suspens :***

- Les failles actives sont-elles sensibles aux événements d'érosion, qui sont transitoires, mais non périodiques?

- Quelle est l'amplitude et la durée d'un événement d'érosion nécessaire pour augmenter significativement la sismicité régionale ?

- Un changement de contrainte transitoire est-il capable de changer la distribution des magnitudes des tremblements de terre?

## Taille des séismes et glissements de terrain

La distribution de taille des glissements de terrain et des séismes est un élément fondamental de l'évaluation des risques. En outre, la distribution de taille des glissements de terrain est essentielle pour quantifier l'érosion engendrée par un séisme de forte magnitude ou par des précipitations importantes. La taille des glissements de terrain et des tremblements de terre présentent une distribution en loi de puissance qui est observée dans de nombreux inventaires. Cependant, ces distributions varient dans le temps et dans l'espace. En particulier, la prévision d'événements importants est difficile, parce qu'ils sont si rares qu'ils ne sont pas toujours échantillonnés. Par exemple, le glissement de terrain du Langtang ou le tremblement de terre de Tohoku et le tsunami qui l'a suivi ont été particulièrement importants par rapport aux prévisions basées sur les inventaires historiques.

Dans cette section, je décris d'abord les distributions de tailles observées dans la nature pour les glissements de terrain et les séismes. Ensuite, je me concentre sur l'explication physique de leur distribution en loi de puissance et les variations potentielles de leurs exposants. Enfin, nous verrons que le modèle de loi de puissance ne décrit pas la distribution de taille des plus petits et des plus grands événements, et résumons les connaissances actuelles sur les facteurs qui contrôlent la taille des petits et des grands événements de rupture.

***Questions en suspens :***

- Qu'est-ce qui contrôle la distribution de taille des glissements de terrain? Est-ce la mécanique de la propagation de la rupture, ou bien l'hétérogénéité du système?

- Quelles sont les différences entre les mécanismes de rupture sismique et glissement de terrain qui pourraient expliquer l'absence de *rollover* pour les tremblements de terre?

- Qu'est-ce qui contrôle la probabilité des grands glissements de terrain ? La probabilité d'un tel événement destructeur est-elle prévisible?

# Chapitre 3 - Modélisation numérique de la distribution de taille des glissements de terrain

Dans la première section de ce chapitre, je présente le modèle développé au cours de cette thèse sous la forme d'un article soumis à *Geophysical Research Letter*. Dans ce papier, nous décrivons d'abord l'approche développée pour modéliser la distribution de profondeur et d'aire des glissements de terrain. Ensuite, nous validons ce modèle et calibrons les paramètres mécaniques (cohésion et friction) en utilisant six inventaires de glissements de terrains existant, induits par des séismes ou des typhons. Enfin, nous utilisons ce modèle pour mieux comprendre l'effet de la forme du paysage sur la distribution de taille des glissements de terrain, en utilisant des topographies synthétiques.

La seconde partie de cette section est dédiée à deux implications de ce modèle. Dans une première partie, j'utilise les résultats obtenus via mon modèle pour discuter de la résistance (cohésion et friction) effective des paysages aux échelles de temps géomorphologiques. Dans une seconde partie, je présente un cas d'étude à l'échelle d'un bassin versant qui met en évidence l'importance de la forme du paysage sur le volume total de sédiments mobilisés par les glissements de terrain.

Dans ce chapitre, nous montrons qu'un modèle simple prenant en compte la forme des versants et un critère de rupture statique de type Mohr-Coulomb peut tout à fait modéliser la distribution de taille des glissements de terrain. Nous mettons en avant le rôle de la cohésion dans l'émergence du *rollover* pour les petits glissements, et de la forme du paysage pour la distribution de taille des glissements les plus grands. Nous montrons également que la propagation de la rupture en 2D contribue à l'émergence d'une loi de puissance pour les glissements de terrain de taille moyenne.

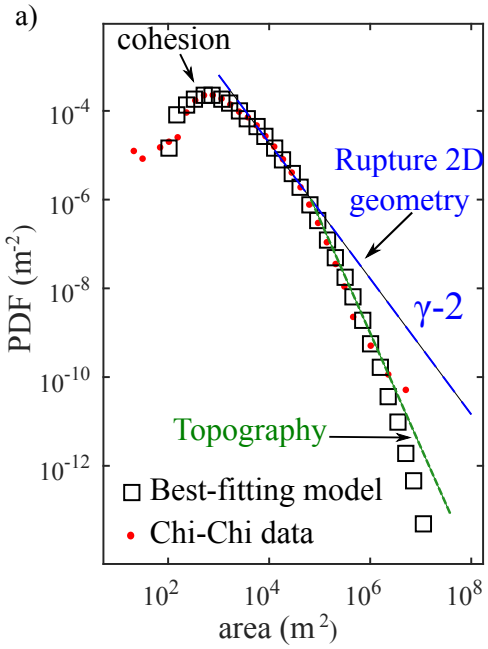


Figure 1 – PDF de l'aire des glissements de terrain observés (points rouges) et modélisés (carrés noirs) à partir du MNT de Taiwan (C = 18 kPa, $\Phi = 30^o$ et $\gamma = 0.47$). Les droites représentent la pente théorique de la PDF contrôlée par la géométrie de la rupture en 2D (droite bleue) et par la forme du paysage (droite verte).

## Chapitre 4 - Contrôle de la forme des versants sur la taille des glissements de terrain

Dans le chapitre précédent, j'ai défini un modèle mécanique simple prenant en compte la topographie et la résistance effective de la roche. A l'aide de ce modèle, j'ai clarifié la contribution respective de la friction, cohésion, propagation de la rupture et géométrie des pentes sur la distribution de taille des glissements de terrain. En particulier, j'ai démontré l'importance théorique de la longueur, de la hauteur et de la pente des versants finis sur la probabilité de grands glissements de terrain. Mais dans quelle mesure la forme du paysage contrôle-t-elle réellement la distribution de taille des glissements de terrain? Cette idée doit être comparée à des données. En utilisant le cas du bassin de la Dajia à Taiwan, j'ai souligné que la distribution de taille des glissements de terrain peut refléter la forme du paysage à l'échelle locale (au sein du même bassin versant). Dans ce chapitre, je profite de plusieurs inventaires de glissements de terrain existants pour explorer le rôle de la géométrie finie des pentes sur la distribution de la taille des glissements de terrain, en particulier pour la probabilité de grandes glissements de terrain. Ce chapitre est constitué d'un article en préparation dans lequel je compare la distribution de taille des glissements de terrain (pour plusieurs inventaires provenant de différents endroits du globe) à la géométrie du paysage, en passant par une métrique intégrant l'altitude maximale au-dessus de l'angle de friction. Je montre que cette métrique suit une distribution exponentielle, dans une région donnée, mais également à l'échelle mondiale. Cet article est suivi d'une discussion dans laquelle je propose d'approfondir mes recherches, via une approche analytique, sur le rôle de cette distribution sur la distribution de la taille des glissements de terrain.

## Chapitre 5 - Réponse d'une faille active à des événements érosifs extrêmes

Dans les deux chapitres précédents, j'ai étudié les contrôles potentiels sur la distribution de la taille des glissements de terrain et démontré le rôle fondamental de la géométrie du paysage. En particulier, les

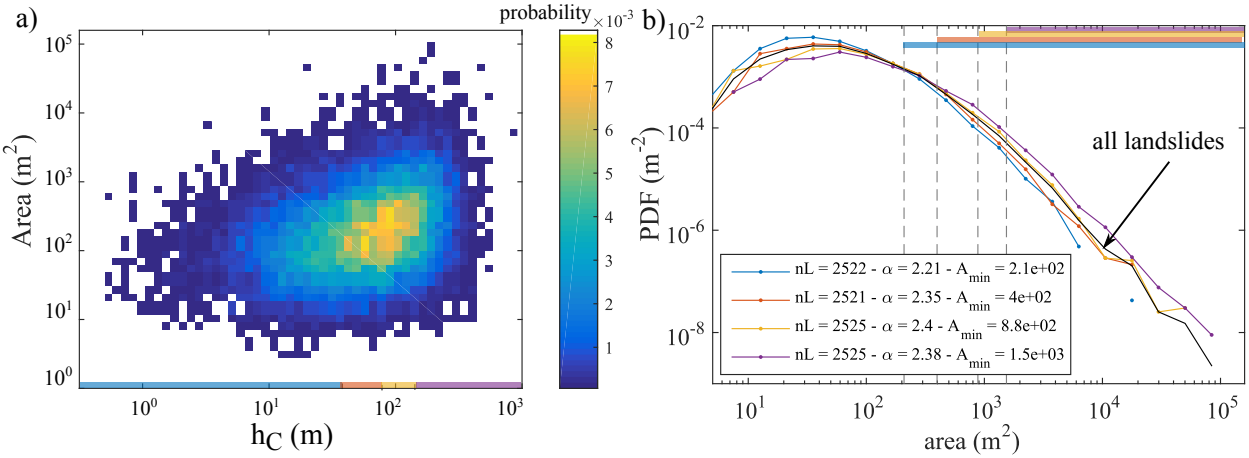


Figure 2 – a) Histogramme à deux variables représentant la probabilité des aires de glissement de terrain et de la valeur de $h_C$ correspondante. b) PDF des aires de glissement de terrains, pour quatre classes de $h_C$. La légende indique les paramètres de la loi de puissance modélisée ($\alpha$ et $A_{min}$) pour chaque PDF. Les quatre classes de $h_C$, shown in the bottom of a), are chosen to have a constant number of landslides nL.

paysages avec d'importante hauteurs instables sont capables de produire de grands glissements de terrain sous un forçage donné. Ces zones correspondent aux zones de collision à haut risque sismique, dans lesquelles des processus érosifs et tectoniques sont susceptibles d'être couplés. Par exemple, dans un travail en préparation (Annexe A), nous soupçonnons que les nombreux glissement de terrain déclenchés par le typhon Morakot a déclenché une sismicité superficielle et modifié la *b-value* des séismes pendant plusieurs années après le typhon.

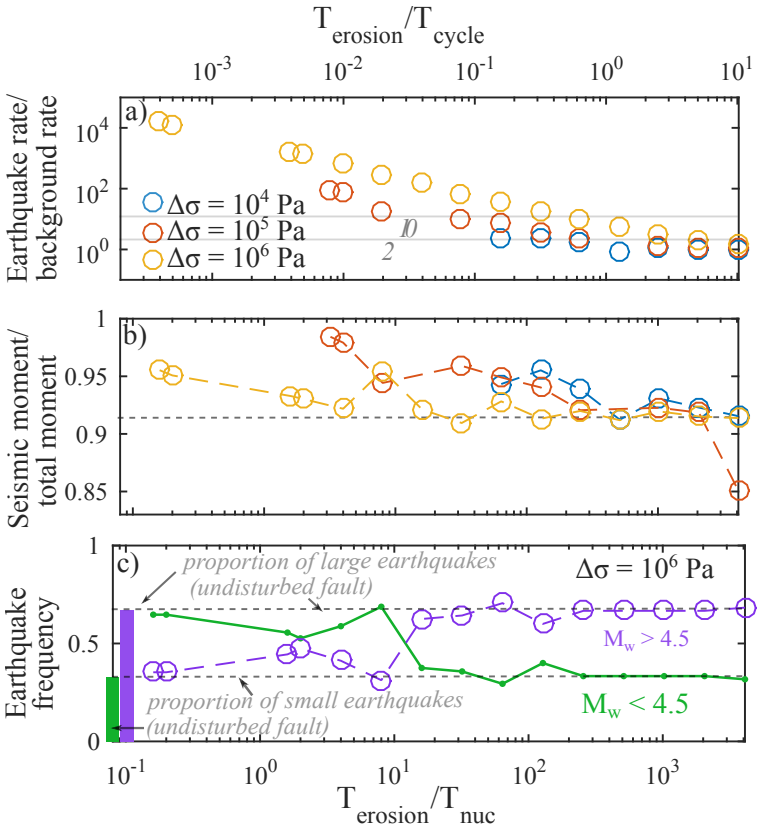


Figure 3 – a) Taux de sismicité pendant la période d'érosion, normalisé par le taux de sismicité dans le cas de la faille non perturbée. Chaque point représente un modèle dans lequel au moins un séisme se produit pendant la période d'érosion. b) Moment cumulé pendant la période d'érosion. c) Proportion de grands ($M_w$ > 4.5, violet) et petits ($M_w$ < 4.5, n vert) séismes pendant la période d'érosion pour chaque modèle avec $\Delta\sigma$ = $10^6$ MPa. Les pointillés représentent la proportion de petits et grands séismes dans le cas de la faille non perturbée.

Ces liens potentiels doivent être approfondis à travers une approche numérique. Par conséquent, dans ce chapitre, j'ai utilisé deux modèles numériques du cycle sismique pour étudier le rôle de grands événements d'érosion sur la sismicité. Je présente d'abord les méthodes numériques utilisés. Ensuite, je présente les principaux résultats obtenus sous la forme d'un article qui sera soumis à une revue scientifique après la soutenance. Dans cet article, j'ai modélisé les effets d'un événement d'érosion sur une seule faille avec des propriétés frictionnelles hétérogènes. Ensuite, je compare les principaux résultats de cette étude avec le comportement d'une faille homogène, et je présente enfin un travail en cours dans lequel je vise à étudier le rôle d'un événement érosif sur un réseau de failles.

Dans ce chapitre, je montre que la réponse d'une faille active à un grand événement érosif peut être significative, et dépend de la durée et de l'amplitude de cet événement. Je montre également que pour un changement de contrainte suffisamment important, la magnitude des séismes change également significativement, et la faille produit plus de petits séismes en proportion comparée à un cas où elle n'est pas perturbée. Je montre également que ces résultats se retrouvent pour une faille homogène, mais avec une réponse moins importante. Ces résultats devraient être étendus à une population de failles de différentes tailles, afin d'étudier le changement de *b-value* engendré par un changement de contrainte du à un grand événement érosif.

# Chapitre 6 - Conclusion

Ces travaux ont permis d'améliorer les connaissances actuelles sur les processus contribuant à façonner la surface de la Terre à court terme (10-1000 ans). Notre approche, basée sur des études numériques, a conduit aux résultats principaux suivants:

1) Un modèle mécanique très simple de glissements de terrain prenant en compte la géométrie des pentes est capable de reproduire la distribution de taille des glissements de terrain. Ce modèle a mis l'accent sur l'importance de la cohésion pour la distribution des petits glissements de terrain, sur la contribution de la propagation de la rupture en 2D à la loi de puissance, et sur l'influence de la forme du paysage sur la distribution de taille des grands glissements de terrain.

2) La géométrie des pentes a une importance fondamentale dans la distribution de taille des glissements de terrain. Un critère simple mesurant la hauteur des pentes instables, $h_C$, est reflété dans les inventaires de glissements de terrain. Cette métrique est distribuée de manière exponentielle dans de nombreuses régions du monde et contrôle la probabilité des grands glissement de terrain.

3) Les grands événements d'érosion peuvent potentiellement engendrer des séismes et modifier la distribution de taille des tremblements de terre lors de l'export des sédiments. La magnitude et la durée de l'érosion sont deux paramètres fondamentaux pour évaluer la réponse des failles. Notre étude, basée sur une seule faille, doit être étendue à une population de failles afin de quantifier le changement potentiel de *b-value* dû à de grands événements d'érosion.

# Contents

# Chapter 1

# Preamble

The present elevation and shape of worldwide mountain ranges result from the balance between the processes that build them and the processes that level them. A large range of deformation processes and associated time-scales contribute to landscape evolution: from an earthquake rupture propagating at meters per second over several seconds to the building of mountain ranges by accumulation of tectonic deformation over millions of years. Erosional processes are the surface processes that remove material away from mountain ranges by river sediment transport and erosion, glacial carving and ablation, landsliding and hillslope erosion, mechanical and chemical weathering, etc. These processes contribute to erode mountain ranges and interplay with tectonic uplift at all time scales. In this section, I briefly review the interactions between tectonics and erosion at geological (1 Myrs-100 Myrs) and intermediate (10 000 yrs - 1 Myrs) time scales. I then focus on those interactions at shorter time scales (< 1000 years) and their main implications for human life as well as for mountain building.

## 1.1 From geological time scales to the seismic cycle time scale

At the beginning of the XIX$^{th}$ century, scientists started recognizing that climate could dramatically change over geological time scales. Past continental glaciations had been recognized from their geomorphological evidence, such as the erratic blocks founded in the Alpine valleys. But how to explain such a major cooling that glaciers were extended enough to carry those blocks to the lowest parts of the valleys that are currently ice-free?

During the mid-XIX$^{th}$ century, the link with mountain building emerged as the most possible explanation. In his essay on Alpine glaciers, the German-Swiss geologist Jean de Charpentier observed the geometry of moraines and deduced that those deposits were likely to have been formed after the rise of the Alps (Charpentier, 1841). He proposed that orogenesis induced deep cracks and crevasses through which surface runoff water entered the warm depths of the Earth and vaporized, contributing to moisturize and cool the atmosphere (figure 1.1). Although the mechanism he proposed was incorrect, this was one of the first published attempts to draw a link between surface processes and the rise of mountain ranges. Then, during one century, several scientists (e.g., Dana, 1856, Lyell, 1875) took up and supported this novel idea, named the "relief hypothesis" by Ramsay (1924), that mountain ranges cool the atmosphere and cause a temperature decrease.

This theory was further investigated during the second half of the XX$^{th}$ century, together with the development of paleoclimatology. Extensive ocean coring programs such as the Deep Sea Drilling Project (begun in 1968) recovered a lot of Tertiary sediment cores well suited to investigate the Cenozoic evolution of global climate. The common outcome of numerous paleobotanic investigations (e.g., Wolfe, 1978) and oxygen isotopes measurements (e.g., Savin, 1977) was that the continental glaciations inferred by Charpentier and his contemporaries was the last step of a 50 Myr global cooling that temporally correlates with the late Cenozoic

rise of mountain belts such as the Himalayas or the Rocky Mountains. Further investigations have shown that mountain building can significantly change the climate at geological time-scales through several mechanisms. First, increasing mountain range elevation induces an increase of Earth's albedo, by leading to longer winters, increasing the area and duration of snow cover, and leading to the expansion of glaciers (Birchfield and Wertman, 1983). Moreover, weathering rates and river fluxes can increase with increasing uplift rates. This enhanced continental weathering would trap more $CO_2$ in the ocean and decrease greenhouse effect (Raymo et al., 1988). Mountain ranges can also dramatically change atmospheric flow, and favour cold climate (Kutzbach et al., 1989). An elevated topography enhances precipitations on the wind side of the mountain, and can induce strong monsoon in areas such as southern Asia. As mountain building enhances precipitation, it is likely to enhance erosional processes, which are strongly linked to climate (Wilson, 1973, Jansson, 1982). In climatological settings with efficient erosion, as in Taiwan (Suppe, 1981) or New Zealand (Adams, 1980), the uplift rate can be balanced by the rate of erosion, leading to a steady-state topography at geological time scales.

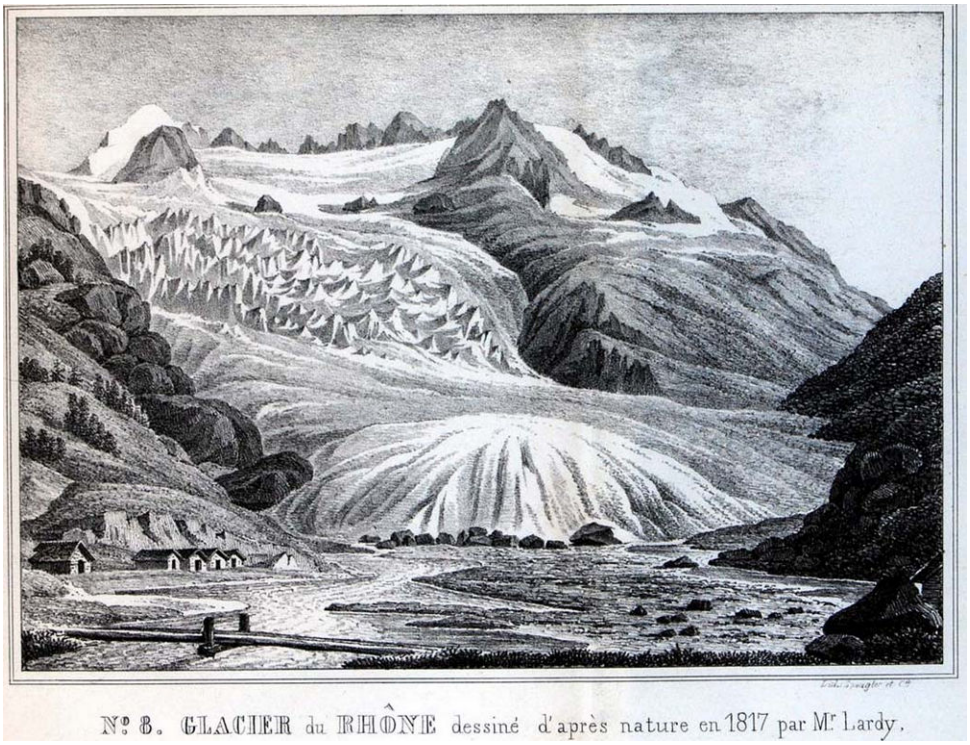


Figure 1.1 – *Glacier du Rhônes*, taken from "*Essai sur les glaciers*" by Jean de Charpentier. "Cette révolution (*l'orogenèse Alpine, N.D.A.*) a occasionné des fentes et des crevasses, [...] dont un grand nombre devait atteindre la profondeur où la température de la terre était assez élevée pour transformer l'eau (pluviale, lacustre ou marine) en vapeurs. [...] Ces vapeurs, en amenant beaucoup d'humidité dans l'atmosphère et en la refoidissant, durent occasionner une longue suite d'années pluvieuses et froides, qui, comme on le sait, favorisent singulièrement le développement des glaciers." *Jean de Charpentier, Essai sur les Glaciers, (1841), p. 315-318.*

However, since the end of the $XX^{th}$ century, geologists and geophysicists progressively changed their vision of climate and erosion as passive processes responding to mountain building. Since plate tectonics theory won general acceptance in 1967, and after the wartime boom in seismology research and the development of satellite imagery, geologists dramatically improved their knowledge of the surface and crustal structure of mountain belts. Over millions of years, mountains grow (at millimetres to centimetres per year) by thrusting and thickening of the upper crust under the compressional forces due to plate motions. Under this frame,

geologists and physicists start thinking of mountain as a wedge (similarly to the wedge developing in front of a bulldozer) that deforms until a critical slope is reached (Dahlen et al., 1984, Koons, 1990). In this model, surface processes cannot be ignored; if some material is removed from the top of the wedge, it changes the distribution of mass and stresses in the belt, and induces internal deformation that re-establishes the critical taper. During the 90s, the advances in numerical modelling have highlighted that erosion is expected to control the size, structure and pattern of deformation in several mountain belts (Koons, 1990, Willett, 1999, Willett et al., 1993, Beaumont et al., 1996). A striking example is the Southern Alps of New Zealand, where the asymmetry of rainfall, mainly coming from the west coast, is able to explain the asymmetric topographic profile and the pattern of uplift (Willett, 1999). Climate, erosion and uplift are now commonly considered as a series of feedbacks, and it is largely accepted that surface processes can strongly influence tectonic deformation over geological time scales (Whipple, 2009).

The increasing amount of geodetic data, the deployment of seismometer network, mainly in the Himalayas (e.g., Pandey et al., 1999), and then the development of the Global Positioning System (GPS) during the 90s (Bilham et al., 1997, Larson et al., 1999, Jouanne et al., 1999) allowed geologists to look at mountain deformation at shorter time scales. Long-term crustal thickening is mainly accommodated by slip along major faults, but if we look at shorter time scales, faults do not slip continuously. Over periods of 100-1000 years, they accumulate tectonic stress, and then release it during sudden, large ruptures (i.e., earthquakes). The succession of loading (aseismic) and relaxation (seismic) phases are commonly known as the seismic cycles. During the late $XX^{th}$ century, mountain building started being studied through seismotectonics (i.e., the study of earthquakes as a tectonic component). Because erosion removes crustal material, it partly drives continental rock uplift through isostatic rebound: the gravitational equilibrium between crust and mantle is restored by land's vertical motion. In a numerical model of long and short-term deformation of the Himalayas, Cattin and Avouac (2000) showed that erosion, through isostasy, is likely to interplay with tectonics during the interseismic period as well as during orogenic deformation. However, the role of erosion on fault slip is easier to decipher in some particular places, where long-term deformation is so low that it is hardly detected by GPS, and that yet experience seismic activity. It is the case in mountain ranges considered stable such as the Pyrenees or the Western Alps (Vernant et al., 2013) or for intraplate earthquakes such as in New Madrid (Missouri) (Calais et al., 2010). In those cases, fault slip is likely to be enhanced by the isostatic rebound of the lithosphere caused by erosion, which induces a normal stress decrease in the upper crust sufficient to unclamp pre-existing faults that are close to failure.

## 1.2 Why do we care about short-term interactions between tectonics and erosion ?

At geological time scales, rock uplift and river incision contribute to steepening hillslopes until their mechanical stability threshold is reached (Burbank et al., 1996, Mitchell and Montgomery, 2006), and the landscape responds by landsliding (Korup et al., 2007, Larsen and Montgomery, 2012). However, the landsliding rate in a mountain belt is not steady; the energy released during large earthquakes by seismic waves can cause strong ground motion that induces almost instantaneously a large amount of slope failures, especially in mountainous areas with steep topography. As recent examples of earthquakes that triggered tens of thousands of landslides, we can mention the 2015 Gorkha earthquake in Nepal (Roback et al., 2017), the 2016 Kaikoura earthquake in New-Zealand, or the recent 2018 Hokkaido earthquake (Japan). Those catastrophic landsliding events represent a major hazard for the populations living in seismically active settings. They also have strong geomorphological implications, because they instantaneously convert a large volume of rock to sediment that can be delivered to the rivers, and then mobilized (Yanites et al., 2010, Croissant et al., 2017). Those large erosional events could also modify the regional seismicity, because of the sudden stress

change they induce in the shallow crust (Steer et al., 2014). In the next sections, I will look at all of those three points.

### 1.2.1 Co-seismic landslides represent a major hazard for populations

Landslides triggered by earthquakes are a major hazard in seismically active regions. They can destroy villages and cause hundred of injuries and fatalities (Marano et al., 2010, Petley, 2012, Catlos et al., 2016). For example, between 20.000 and 100.000 fatalities due to the 2008 Wenchuan earthquake in China have been attributed directly to landsliding (Huang and Fan, 2013). Coseismic landslides can also block roads and railways, which is especially problematic in isolated, narrow and inhabitated valleys with limited accessibility. They also deliver large volumes of sediments to rivers, modifying their dynamics, causing hydro-sedimentary hazards such as river aggradation or landslide dams (Collins and Jibson (2015), figure 1.2 a). Landslides can be the primary source of co-seismic damage to infrastructure (figure 1.2 b) and can prevent the functioning of transportation. Therefore, they induce economic losses that can be even more important than those caused by direct ground shaking (Bird and Bommer, 2004).

Large landslides in particular can be very destructive, such as shown by the Langtang landslide triggered by the Gorkha earthquake, that destroyed an entire village and killed more than 200 people. In natural hazard management, the size of such large and therefore destructive events is critical for the overall hazard anticipation (Strauss et al., 1989, Sornette, 2006). Unfortunately, because large landslides are rare compared to smaller ones, their occurrence is also the most difficult to predict (Geist and Parsons, 2014).

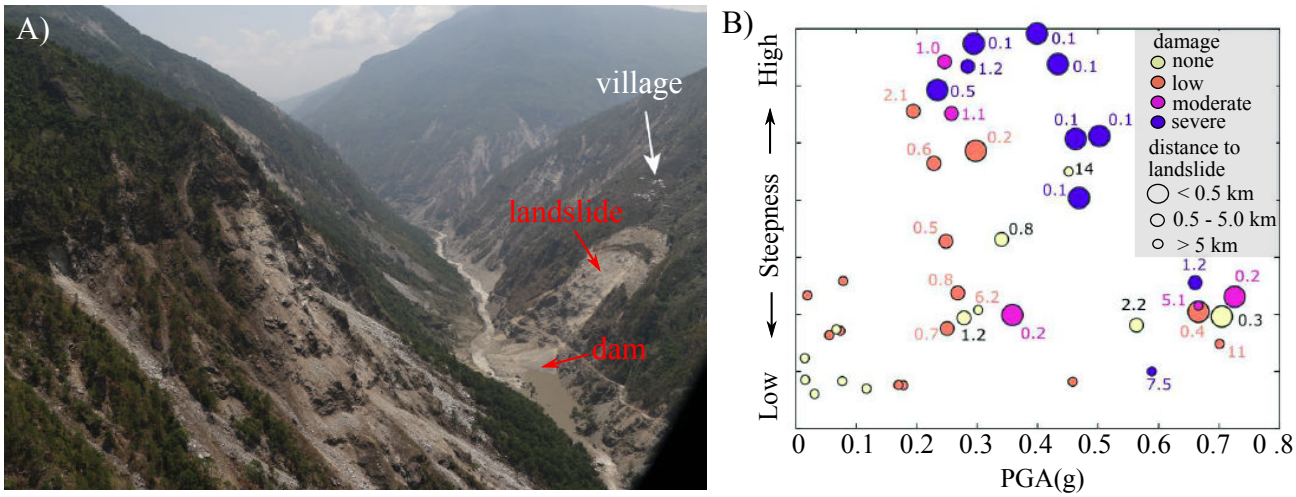


Figure 1.2 – a) Landslides triggered by the 2015 Gorkha earthquake and the subsequent landslide dam in the river. Top of scarp below village is approximately 400 m above river (after Collins and Jibson (2015)). b) Damage induced to hydropower projects in Nepal by the Gorkha earthquake. The size of the symbols shows the proximity to landslide. Data are plotted against peak ground acceleration (PGA) and river steepness (after Schwanghart et al. (2018)).

### 1.2.2 Earthquakes and coseismic erosion shape the landscape

The last decades have shown the fundamental importance of seismic rupture in mountain range building. Rocks move and uplift mainly during shallow earthquakes (Avouac, 2007), and the idea that seismic and interseismic deformation do not balance, but accumulate to create topography and form permanent structures (King et al., 1988), has been restored recently by observations (Le Béon et al., 2014) and numerical modelling (Simpson, 2015).

Moreover, earthquakes contribute significantly to the erosion of mountain belts. The total volume of coseismic landslides scales, at first order, with the earthquake magnitude (Keefer, 1994): during larger earthquakes, a larger volume of rock is converted to sediments that can be transported away the mountain

belt by rivers. Landslides therefore need to be considered in the mass balance of large earthquakes (i.e., the mass that is uplifted by seismic rupture minus the mass that is removed by erosion). More and more accurate estimates of the erosion induced by co-seismic landsliding have been possible during the last decades with the development of high-resolution satellite imagery accessible for the scientific community. This has led to many complete or nearly complete co-seismic landslide inventories (Tanyaş et al., 2017). Recent studies have shown that the mass balance of large earthquakes can be variable. For example, the Chi-Chi earthquake generated more uplift compared to landsliding volume (Hovius et al., 2011); however the topographic budget of the Wenchuan earthquake was nearly neutral (Parker et al., 2011, Li et al., 2014). Recent numerical modelling suggest that intermediate size earthquakes ($M_w$ 6-7.3) may cause more erosion than uplift (Marc et al., 2016a).

Moreover, the export time of landslide sediment is a debated question. If some studies suggest that rivers need more than several centuries to adjust to large landsliding events (Stolle et al., 2018), other studies propose an export time of several decades (Yanites et al., 2010, Howarth et al., 2012, Uchida et al., 2014, Wang et al., 2015, Xie et al., 2018). Other studies (Hovius et al., 2011, Croissant et al., 2017) propose an even shorter time scale (1-10 years) for the post-seismic export of landsliding sediments. These recent observations and numerical modelling are challenging the well accepted idea that large earthquakes always build topography.

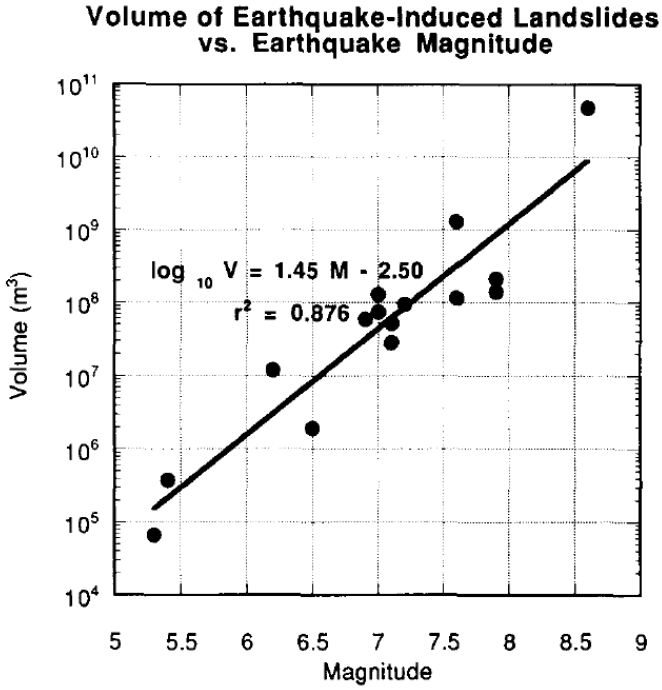


Figure 1.3 – a) Total volume of landslides triggered by earthquakes of different magnitudes (Keefer, 1994).

Therefore, understanding what controls the volume of sediments that is generated and then removed during and after an earthquake is fundamental to understand to what extent earthquakes build topography. This requires documentation of the number of landslides triggered by a specific earthquake and their size. Prediction of the total number of landslides remain challenging (Gorum et al., 2014) because landslide density depends on many parameters linked to seismic rupture, wave propagation, topography and rock strength (e.g., Massey et al., 2018). Moreover, the size distribution of landslides displays significant variations (Van Den Eeckhaut et al., 2007, Tanyaş et al., 2017) that remain poorly understood. Therefore, current estimations of the total volume of landslides remain challenging and predict total volume within a large error (Keefer, 1994, Marc et al., 2016b).

### 1.2.3 Surface processes can trigger seismicity at human-life time scales

Surface processes, including sedimentation and erosion, involve the transfer of material (sediments, water) at the Earth's surface. Sediment and water transfers induce stress changes at depth, with various periods (one day for tides, one year for the monsoon, to decades for co-seismic erosion). The amplitude of stress change decreases with depth, but appears in some cases to be sufficient enough to trigger shallow seismicity (e.g., Bollinger et al., 2007, Bettinelli et al., 2008).

For example, figure 1.4 shows the annual variations of seismicity in Japan (Heki, 2003). Insets a and b show that large earthquakes (magnitude $> 7$) are more frequent ($\sim$4 times) during summer than winter, with an annual periodicity. This is observed only in the area covered by snow during winter (fig. 1.4 c). The author of this study have explained this observation by the cycle of surface loading and unloading due to snow melt in spring and summer and snow cover in winter. Calculating the stress changes induced by this cycle on the crustal faults located below gives values of a few kPa. To give an order of idea, this is a hundred times smaller than the pressure of a bike tire.

Even though, the mechanisms of earthquake triggering by surface processes are not clearly understood yet, it appears that the rupture of shallow crustal faults can be activated by very small stress changes, as we also learned during the few last decades the triggered seismicity in the US (e.g., Chen and Talwani, 2001, Ellsworth, 2013). Therefore, at the time-scale of a seismic cycle, erosion is likely to influence the seismicity of active faults (Steer et al., 2014), and some feedbacks can be expected, for example between co-seismic erosion induced by landslides and shallow earthquakes. Nevertheless, those interactions have been poorly studied, and the conditions under which large erosional events can actually significantly interplay with seismicity remain unclear.

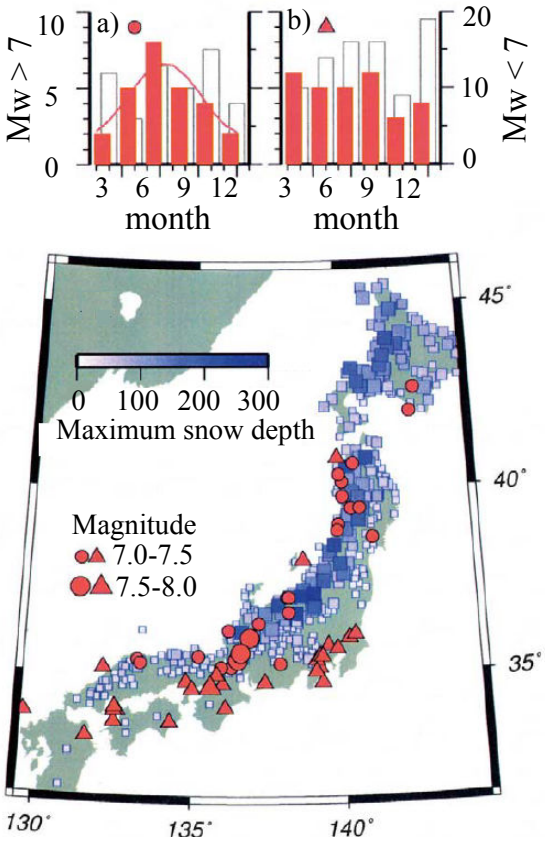


Figure 1.4 – Number of large (red) and small (white) earthquakes that occurred in 2-month intervals, within (a) and outside (b) the snowy region of Japan. The epicenters are shown in b) together with the maximum snow depth in winter. From Heki (2003).

# Chapter 2

# Introduction

This chapter is written to give an overview of the concepts at the basis of my work. It starts with the notions of landslide and earthquake mechanics that are relevant to understand their interactions at the time scale of a seismic cycle. I then describe those interactions, mainly based on the observation of natural cases. Last, I focus on the observations and physical explanations of earthquake and landslide sizes.

## 2.1 Earthquake and landslide mechanics

Earthquakes and landslides are two manifestations of the brittle deformation of Earth's upper lithosphere. Earthquakes occur by the sudden motion of rocks along crustal faults that sometimes ruptures up to the Earth's surface (figure 2.1a). Landslides are characterized by the gravity-driven catastrophic failure of hillslopes that can be triggered by an external factor such as co-seismic ground motion (figure 2.1b). In a static case, rock failure can occur when the driving stress applied to a rock or to a fracture is greater than its resisting stress, i.e. rock strength. In this section, I first introduce the notion of rock strength and the macroscopic problem of brittle failure. In the second and the third sections, I focus more specifically on earthquake and landslide mechanics, respectively.

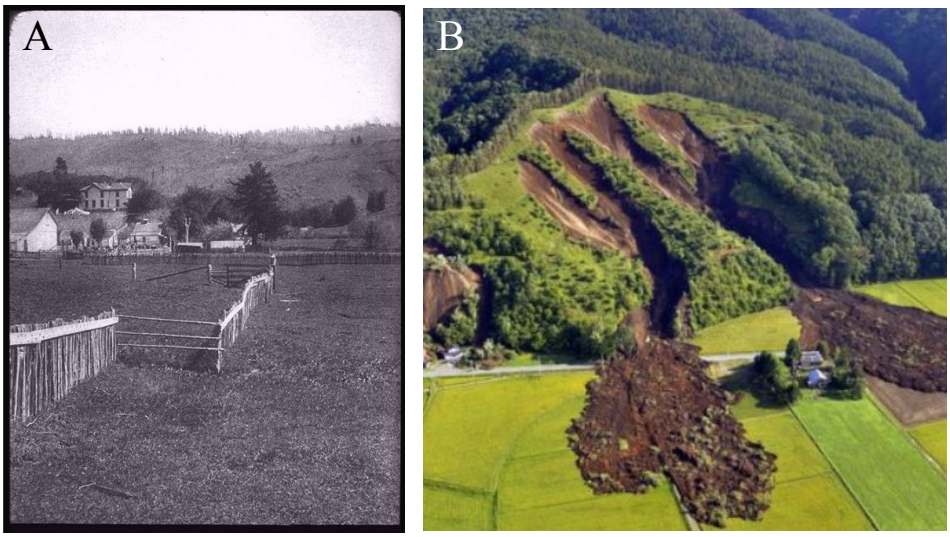


Figure 2.1 – Earthquakes and landslides, two manifestations of the brittle behavior of the Earth's crust. a) Picture taken by G.K. Gilbert near Bolinas, in Marin County, after the 1906 $M_w$ 7.9 San Francisco earthquake. The picture shows a fence that was offset about 8.5 feet along the trace of the fault (from UC Berkeley Earthquake Engineering Research Center). b) Landslides triggered by the 6 September 2018 Hokkaido earthquake (Japan) Photo: Jiji Press.

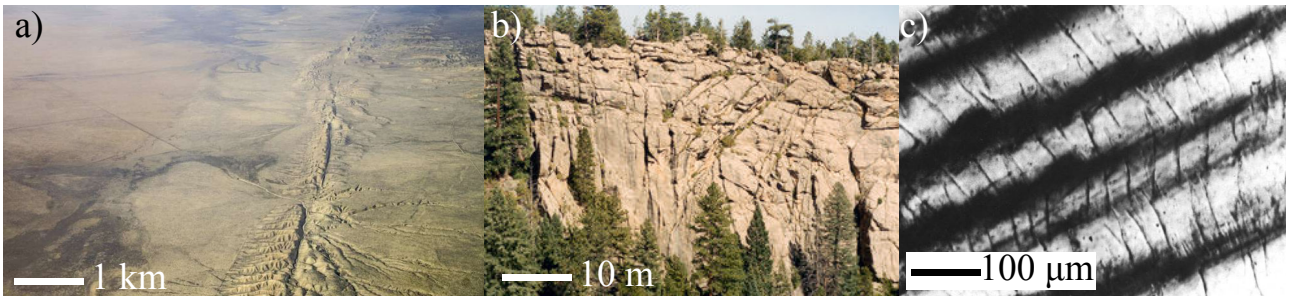


Figure 2.2 – Natural fractures at all scales. a) Southern portion of the San Andreas fault, across the Carrizo Plain in California. Credit : US Geological Survey. b) Cracks in a granitic cliff in western Jefferson County (US). Photo by J. Cain, USGS. c) Microcracks in a naturally deformed plagioclase, from Kranz (1983).

### 2.1.1 Rock strength and brittle failure

How much stress a material can hold and the critical stress that will induce failure is a very old problem. It is important for engineering, mining... The issue of interest to humans (for example landslide occurrence, or the failure of a bridge) implies macroscopic failure. However, macroscopic failure implies brittle failures at a wide range of scales, and involves two main modes of brittle deformation: crack propagation and sliding along pre-existing fractures. I hereinafter explain why rock strength and brittle failure is a scale-dependent problem; then I introduce rock friction, which is the macroscopic property controlling rock sliding; and finally I give the commonly used description of the macroscopic failure of rocks.

#### 2.1.1.1 A scale-dependent problem

The most common method of studying rock strength is the compression of a cylinder of rock with a press (uniaxial compression, or tri-axial compression if the rock is confined). Strength measurements consist of measuring the non-dimensional strain $\varepsilon$ under stress $\sigma$. The obtained stress-strain curve usually shows that the material first deforms elastically (equation 2.1) until a threshold is reached, inducing macroscopic failure of the material :

$$\sigma = E\varepsilon \tag{2.1}$$

where E is a constant called Young's modulus, or elastic modulus.

In those experiments, the maximum stress the rock can hold is referred to as compressive rock strength. Typical values of rock strength founded in the lab are about 10-100 MPa.

Our modern understanding of rock strength arises from the discrepancy between early empirical estimations of rock strength, and analytical solution brought by the theory of matter. Orowan (1949) calculated the theoretical stress $\sigma_t$ necessary to separate two atoms with an inter-atomic distance $a$, across a lattice plane :

$$\sigma_t = \left(\frac{E\gamma}{a}\right)^{1/2} \tag{2.2}$$

where $\gamma$ is the specific surface energy (the energy per unit area necessary to break the bonds) and E is Young's modulus. From this result, the typical stress necessary to break the atomic bonds in silicate rocks would be 1-10 GPa, which is several orders of magnitude greater than the actual rock strength, showing that the atomic scale is not appropriate to infer macroscopic rock strength.

So, what is a good scale to infer rock strength ? Experimental studies made on various rock types (e.g., Bieniawski, 1968, Jahns et al., 1966, Pratt et al., 1972, Hoek and Brown, 1997) have shown that rock sample strength decreases with increasing size. A theoretical explanation for this scale dependency was first

proposed by Griffith and Eng (1921), Griffith (1924). They calculated that rocks yield with increasing scale because they contain defects (cracks) which concentrate stress at their tips, allowing failure at stresses much lower than the theoretical stress. However, the problem of macro failure can not be addressed simply by the modelling of an expanding crack, because it involves several processes at all scales (Scholz, 2002). For example, a fault could be at first order modelled by a linearly expanding crack. However, if we zoom on a portion of this fault, we will notice a lot of complex features resulting from meter to decameter-scale fractures (figure 2.2b). Those cracks create lower strength surfaces along which rock mass can slide under tectonic stresses. At even smaller scale, rocks also contain micro-cracks (Kranz (1983), figure 2.2c) whose propagation is involved in the micromechanics of what can be seen as frictional sliding at larger scales (Scholz, 2002). Therefore, modelling macro failure events requires to use empirical or semi-empirical laws determined from laboratory experiments (Hoek and Brown, 1980b), that integrate the variety of processes occurring at smaller scales (Carpinteri, 1994, Senent et al., 2013). The two next sections focus on those macroscopic properties and how they contribute to rock failure at the macroscopic scale.

#### 2.1.1.2 Rock friction

Friction is the resistance to motion that occurs when a body slides tangentially to a surface on which it contacts another body. When a fracture already exists, sliding is controlled by the frictional resistance, which is a property of the interface more than a property of the material. Frictional strength acts in everyday life, and reducing friction is an important problem in engineering for machines with moving parts. Therefore, its first-order properties have been known since ancient times. The two main laws of friction were discovered by Leonardo da Vinci, and formulated 200 years later by Amonton (Amonton, 1699):

- Amonton's first law : the frictional force is independent of the size of the surfaces in contact
- Amonton's second law : the frictional force $F_f$ is proportional to the normal force $F_n$ with a friction coefficient $\mu_0$:

$$F_f = \mu_0 F_n \tag{2.3}$$

Byerlee (1978) compiled the shear stress necessary to slide a rock surface toward another from a variety of experiments, using either carbonate or silicate rocks (figure 2.3). He found that $\mu_0$ ($\sim 0.6$) was independent of lithology, and to first order, independent of velocity. Actually, at second order, friction slightly varies according to sliding velocity (Byerlee, 1970) and time (Rabinowicz, 1951). This is why, during frictional sliding, dynamic instability can occur (i.e, earthquakes). This arises from second-order frictional properties (section 2.1.2.1); the friction described by Byerlee (1978) is the *static* friction.

#### 2.1.1.3 Macroscopic failure of rock

The principal tools that are commonly used in engineering as well as Earth sciences to describe rock macro-failure are the Coulomb criterion and Mohr circle analysis. The underlying idea is to define an empirical failure criterion for a potential rupture plane, based on macroscopic strength of the material. This failure plane can be a tectonic fault, or a potential landsliding plane characterized by a fracture, for example.

First, one can derive the relationship between normal and shear stresses acting on a plane submitted to bidirectional principal stresses $\sigma_1$ and $\sigma_3$, and making an angle $\alpha$ with the direction normal to $\sigma_1$ (figure 2.4 a). The shear stress $\tau$ and normal stress $\sigma_n$ acting on this plane are (e.g., Jaeger et al., 2009):

$$\sigma_n = \sigma_{n,1} + \sigma_{n,3} = \sigma_1 cos^2(\alpha) + \sigma_3 sin^2(\alpha) - p \tag{2.4}$$

$$\tau = \tau_1 + \tau_3 = -\sigma_1 sin(\alpha)cos(\alpha) + \sigma_3 sin(\alpha)cos(\alpha) \tag{2.5}$$

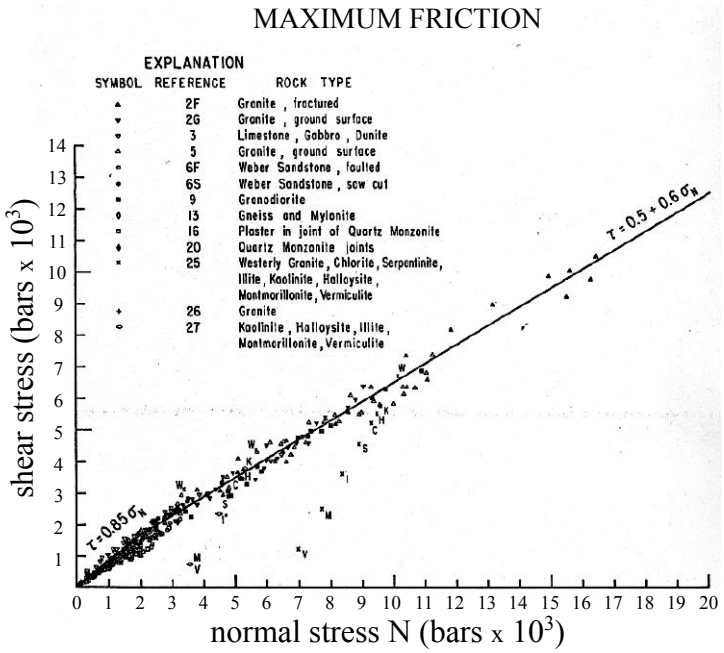


Figure 2.3 – Shear stress plotted as a function of normal stress at the maximum friction for a variety of rock types at normal stress to 20 kbar. (From Byerlee (1978)).

Using the trigonometric relationships :

$$sin(\alpha)cos(\alpha) = \frac{sin(2\alpha)}{2} \tag{2.6}$$

$$cos^2(\alpha) = \frac{1 + cos(2\alpha)}{2} \tag{2.7}$$

$$sin^2(\alpha) + cos^2(\alpha) = 1 \tag{2.8}$$

we obtain :

$$\tau = \frac{\sigma_1 - \sigma_3}{2} sin(-2\alpha) \tag{2.9}$$

$$\sigma_n = \frac{\bar{\sigma}_1 + \bar{\sigma}_3}{2} + \frac{\sigma_1 - \sigma_3}{2} cos(-2\alpha) \tag{2.10}$$

$\bar{\sigma}_1 = \sigma_1 - p$ and $\bar{\sigma}_3 = \sigma_3 - p$ are the effective stress, that is the stress applied minus pore pressure $p$.

Equation 2.10 and 2.9 represent the coordinates of a circle with center $(\bar{\sigma}_1 + \bar{\sigma}_3)/2$ and diameter $\sigma_1 - \sigma_3$ (Mohr circle). We note that moving an angle $\alpha$ in the physical space is equal to moving an angle $-2\alpha$ in the Mohr circle (figure 2.4b).

The Coulomb criterion assumes that failure occurs if the shear stress exceeds the shear strength of the material, which is induced by the frictional resistance (Heyman (1972), equation 2.5). Here it is important to note that the stress necessary to rupture a bulk rock is higher than the stress necessary to induce sliding on a pre-existing fracture. This supplementary strength (figure 2.4 b) is usually accounted for by adding a "cohesion" strength (Mercier et al., 1999, Labuz and Zang, 2012) that we can see as the contribution of the bonding between particles at molecular scale. We also note the contribution of pore pressure increase to failure or frictional sliding enhancement : for an increase $\Delta p$, the center of the circle will move toward the left by $\Delta p$. From the Mohr-circle criteria we can see that failure occur on two conjugate planes at angles $\theta$ :

$$\theta = \frac{\pi}{4} - \frac{\phi}{2} \tag{2.11}$$

This framework provides a basis to understand fault orientation under different tectonic conditions. In an extensional context, $\sigma_1$ is vertical, and failure is expected to occur at 60° with the horizontal considering a frictional angle of 30°. Under a compressional regime, $\sigma_1$ is horizontal, and failure is expected to occur at 30° with the horizontal. This corresponds to the global orientation of normal and reverse faults, respectively. Mohr-Coulomb analysis remains the principal tool that is used to understand long-term faulting, but also to assess slope failure hazard.

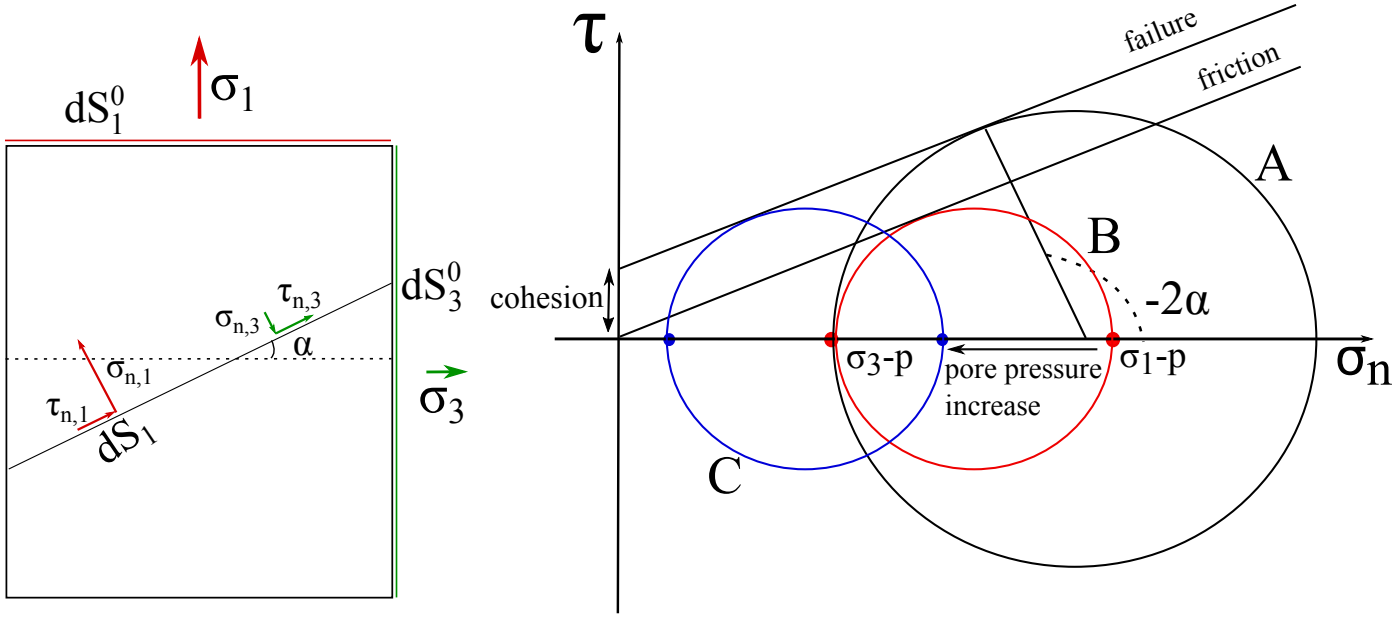


Figure 2.4 – a) Rock sample under bidirectional principal stresses, $\sigma_1$ and $\sigma_3$. A potential rupture plane is shown in black, with angle $\alpha$ with the normal direction $\sigma_1$. The normal and shear components of $\sigma_1$ and $\sigma_3$ are shown in red and green. b) Mohr circles under different stress conditions. A) shows the stress state of a rupture plane that can reach the failure envelope if it is suitably oriented. B) shows the stress state of a plane that could induce frictional sliding if it is suitably oriented. Under the same conditions, a pore pressure increase can induce fracture (circle C).

### 2.1.2 Earthquake mechanics

Most of the time, earthquakes do not cause surface rupture and can be felt far from their hypocenter. For those reasons, for millennia, human have experienced earthquakes without really understanding the origin of those destructive events. From the late $XIX^{th}$ century, the faulting origin of earthquakes appeared thanks to the advances in rock mechanics combined with observations of fresh scarps concomitant with earthquakes (Gilbert, 1884, Kotô, 1893). After the observation of the ground surface displacement which accompanied the 1906 San Francisco earthquake, the seismologist Henry Fielding Reid proposed in his "elastic rebound theory" (Reid, 1910) that earthquakes result from strain release caused by sudden rock fracture along a fault (figure 2.1 a).

Reid's theory laid the foundations of our modern understanding of the faulting origin of earthquakes. However, it was not able to explain the relatively low stress drop observed for large earthquakes, that are 10 to 100 times smaller than the stress drop induced in the lab by the fracturing of rocks (Chinnery, 1964). Brace and Byerlee (1966) proposed to explain this discrepancy by the fact that earthquakes do not involve the fracture of the crust, but the sliding on pre-existing faults. This idea seemed quite reasonable, especially in seismically active regions where the crust is likely to be already weakened by faults created by previous earthquakes.

Therefore, fault mechanics implies two time scales: over centuries to million of years, faults can be considered as quasi-static cracks with a frictional strength (this approach is explained in paragraph 2.1.1.3),

growing by the succession of seismic cycles. At short time scales, from years to seconds, rupture propagates dynamically along the fault, inducing sudden motion and generating seismic waves. Thanks to the development of continuous GPS during the last decade, observations have highlighted another fault slip mode, called 'slow slip', propagating from 0.5 km/h (Rogers and Dragert, 2003) to 1 km/day (SI et al., 2005).

In this section I focus on the mechanical properties implied in seismogenic behavior at short time scales, known as rate-and-state frictional properties (Dieterich, 1979, Rice and Ruina, 1983, Ruina, 1983). Then I will describe earthquake nucleation, and finally we will see how earthquakes interact with each other through their stress field.

#### 2.1.2.1 Static and dynamic friction

In their 1966 experiment, Brace and Byerlee (1966) introduced an artificial fracture in a rock sample and compressed it. They observed that the motion was not regular but that jerky sliding occurred along the saw-cut, each motion resulting in a low stress drop comparable to earthquake stress drop. They proposed that this motion, called "stick-slip", was the process by which earthquakes occurred and that this was controlled by the frictional properties of faults rather than by the bulk rock strength.

Frictional resistance arises from the fact that two surfaces in contact are never perfectly smooth but contain irregularities (Bowdon and Tabor, 1950, Bowden and Tabor, 1964) that make the actual surface of contact (asperities) smaller than the apparent contact area (figure 2.5 A and B). Following the work of Brace and Byerlee (1966), a great deal of attention was focused on fault frictional properties, leading to the two main following observations :

- the friction that needs to be overcome to initiate sliding (i.e, static friction) increases with the logarithm of the time of contact between two surfaces;

- the friction during sliding (i.e, dynamic friction) evolves as a function of sliding velocity. This evolution depends on temperature and material. When friction decreases with velocity, this dynamic weakening is able to induce dynamic instability (i.e, an earthquake).

After those fundamental observations, attempts have been made to propose constitutive laws to model the evolution of friction during stick-slip sliding experiments (e.g., Marone, 1998, Dieterich, 1994), the main issue being how to link static and dynamic friction evolution in a single model. For that purpose, a critical distance $D_c$ was introduced (Rabinowicz, 1958, Dieterich, 1979). This characteristic distance is often interpreted as the memory distance over which the population of contact area is renewed.

The modern form of the constitutive friction law which provides the best explanation for experimental data (Marone, 1998), is:

$$\tau = \bar{\sigma}_n \times \left[ \mu_0 + a \; log\left(\frac{V}{V_0}\right) + b \; log\left(\frac{\theta V_0}{D_c}\right) \right] \tag{2.12}$$

where $\bar{\sigma}_n$ is the effective normal stress, $V_0$ is steady-state velocity, and a and b are frictional parameters describing the velocity and state dependency, respectively.

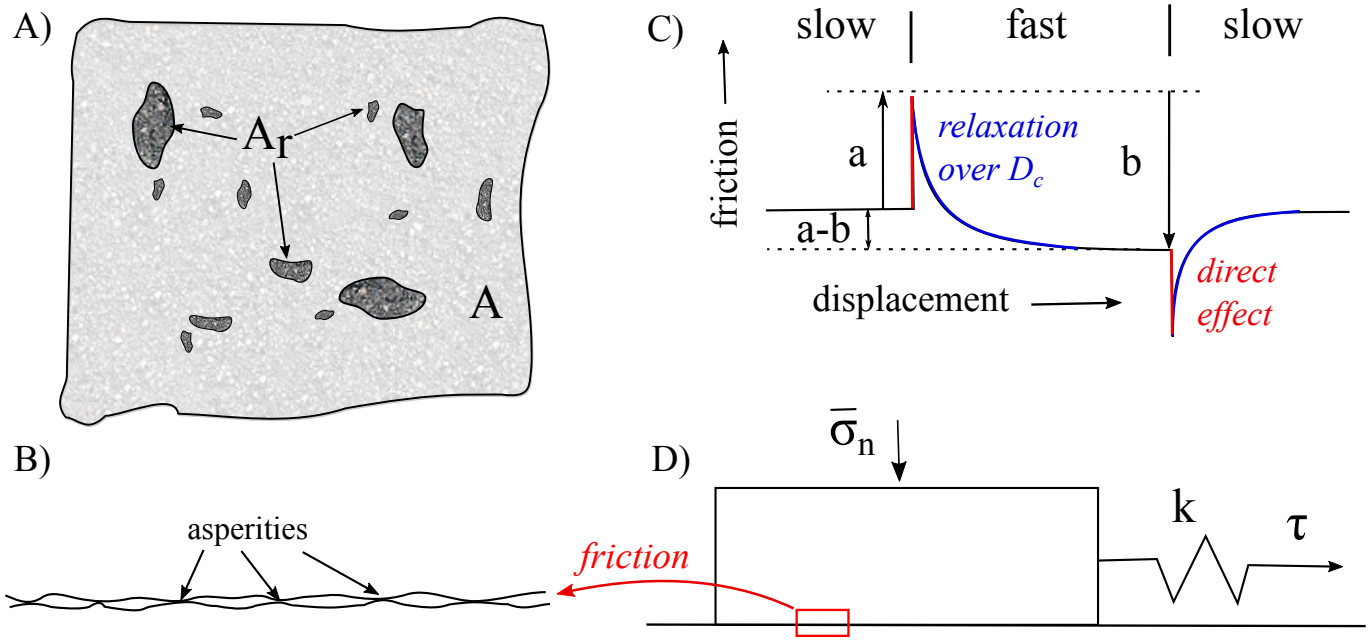


Figure 2.5 – Schematic diagram of contacting surface $A_r$ in plan view (a) and section (b) of an interface of area A. The dark regions in plan view represent the asperities. The total contact area is $A_r$. c) Typical displacement-friction curve resulting for velocity stepping experiment after Dieterich (1994). d) Setup of a spring-slider model. The slider is in contact with a frictional surface and loaded by a shear stress $\tau$ through a spring with stiffness k, under a normal load $\sigma_n$. Adapted from Scholz (2002).

The state variable $\theta$ (Ruina, 1983) is the life time of contact asperities. Its time-derivative $\dot{\theta}$ is usually described through an ageing law :

$$\dot{\theta} = 1 - \frac{V\theta}{D_c} \tag{2.13}$$

The base friction coefficient $\mu_0$ represents the rock frictional strength described by the second Amonton's law (equation 2.3). This first-order frictional property is not involved in seismogenic behavior. The coefficients a and b represent the rate-dependence and state-dependence of friction, respectively. Therefore these formulations are commonly called "rate-and-state friction laws". This rate and state dependency is commonly seen as responsible for the seismic behavior that I will focus on.

#### 2.1.2.2 Friction instability and seismogenesis

Stick-slip behavior is the result of nucleation (i.e, dynamic instability characterised by a phase of spontaneous accelerating slip), fast propagation of the shear rupture, and arrest. Understanding what controls those three steps of the seismic rupture, and in particular under what conditions dynamic instability can occur, is one of the most important questions in seismology.

At first order, the seismogenic potential of a fault is given by the rate-and-state parameters a and b. Indeed, from equations 2.12 and 2.13, we see that the friction at steady-state is :

$$\tau = \bar{\sigma}_n \times \left[\mu_0 + (a-b)\ log\left(\frac{V}{V_0}\right)\right] \tag{2.14}$$

Therefore, if a - b $> 0$, $\mu_{ss}$ increases with increasing velocity. This regime, called rate-strengthening, is stable: an earthquake cannot nucleate under this condition because any acceleration will be stopped by an increase in frictional resistance. If an earthquake propagates into a rate-strengthening region, it will stop rapidly. If a - b $< 0$, $\mu_{ss}$ decreases with increasing velocity. Under this regime, called rate-weakening, dynamic instabilities, such as fast earthquakes, can propagate.

Simple spring-slider models (figure 2.5 D) coupled with friction laws have been widely used to study what gives rise to dynamic instability (Ruina, 1983, Gu et al., 1984). The main outcome of those studies is the existence of a condition for instability under rate-weakening regime. This condition can be expressed either as a critical normal stress $\sigma_c$ (equation 2.15) or as a critical stiffness $k_c$ (equation 2.16).

$$\sigma_c = \frac{kD_c}{-(a-b)} \tag{2.15}$$

$$k_c = -\frac{\sigma_n(a-b)}{D_c} \tag{2.16}$$

Figure 2.6 a) shows the required velocity jump for instability as a function of the normal stress. If $\sigma_n > \sigma_c$ (or $k < k_c$), the system is unstable even if their is no velocity jump, i.e, steady loading. If $\sigma_n < \sigma_c$, or $k > k_c$, the system is said to be conditionally stable because it needs a certain velocity jump to accelerate dynamically. The implications for earthquake nucleation are the following: under steady loading (as tectonic loading), earthquakes can nucleate only in the unstable region. If they propagate into a conditionally stable region, inducing a high enough velocity jump, they can dynamically propagate.

Those simple considerations, derived only from spring-slider block models, allow definition of a first-order seismogenic zone that is in good agreement with data (figure 2.6 b). In theory, seismogenic areas should have rate-weakening rheology (a - b $< 0$) and be conditionally stable ($\sigma_n > \sigma_c$). The parameter (a - b) is a material property that depends primarily on temperature (e.g., Blanpied et al., 1991). For a granite, it is negative at low temperatures and become positive around 300°C, corresponding to the onset of crystal plasticity of quartz. Then, a general statement would be that earthquakes can nucleate only above this transition. Near the surface, faults favor stable slip because of the presence of gouge and other poorly consolidated materials that are likely to be rate-strengthening (Marone et al., 1990).

The development of numerical methods allowed the exploration of the behavior of a continuous fault embedded in an elastic medium, under tectonic loading and with rate-and-state friction laws (e.g., Rice, 1993, Lapusta et al., 2000). Numerous numerical experiments offered further insights into the nucleation process (e.g., Rubin and Ampuero, 2005, Kaneko and Lapusta, 2008). Nucleation starts at a localized zone of steady slip, and spontaneously evolves toward a state of accelerating sliding velocity, spreading out until the instability reaches the length scale $L_c$ (figure 2.6 c)). Currently relevant values of $L_c$ are (Rubin and Ampuero, 2005) :

$$\begin{cases} L_c = 2 * 1.13774 * L_b & for\ a/b\ > 0.3781 \\ L_c = 2 * \dfrac{L_b}{\pi(1-a/b)^2} & for\ a/b \to 1 \end{cases} \tag{2.17}$$

where $L_b$ (often called the cohesive zone) gives the spatial length scale over which the shear stress drops from its peak to residual values at the propagating rupture front (Palmer and Rice, 1973):

$$L_b = \frac{ED_c}{b\sigma_n} \tag{2.18}$$

Numerical models with rate-weakening patches smaller than $L_c$ only produce creep or slow-slip events (figure 2.6 c). However, the scaling of the key parameter $D_c$ is not understood, and could span several orders of magnitude, from $\mu$m in the lab to kilometres along natural faults (Dodge et al., 1996). The physical significance of $D_c$ and the size of nucleation zone for natural earthquakes are still open questions.

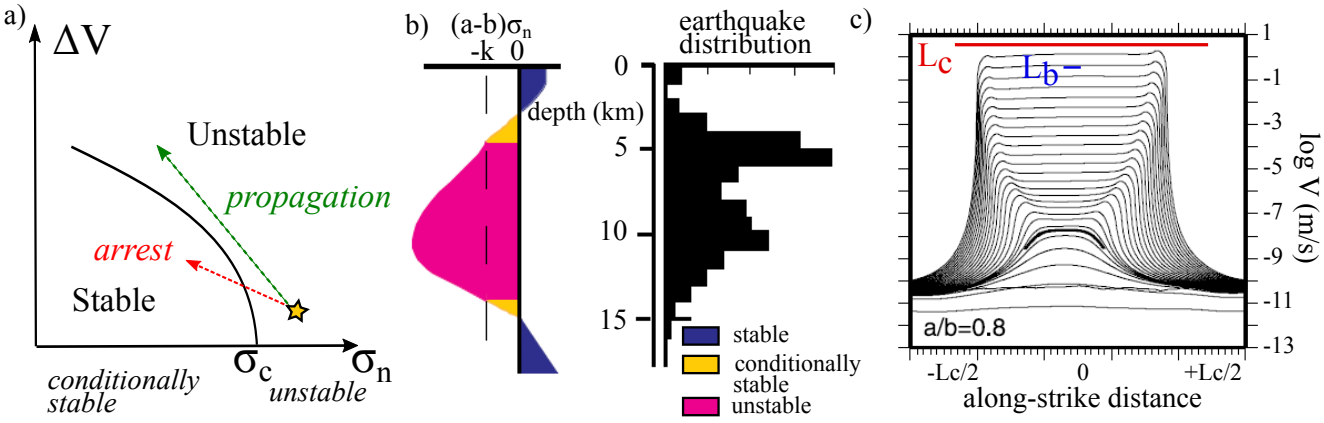


Figure 2.6 – a) Stable and unstable regimes as a function of normal stress $\sigma_n$ and velocity jump $\Delta V$. Nucleation (yellow star) is possible under unstable conditions, and can propagate in the conditionally stable zone if the acceleration is high enough (green arrow), or arrest in the stable zone if the consequent stress drop is too high (red arrow). b) Vertical profile of $(a-b)\sigma_n$ showing the distribution of stability regimes with depth (Scholz, 1988). For comparison the depth distribution of seismicity for a section of the San Andreas fault is shown (Marone and Scholz, 1988). c) Simulation of a nucleation with $L_c$ smaller than the rate-weakening patch. Characteristic lengths $L_c$ and $L_b$ are shown in red and blue, respectively. Each line represents the velocity at a time-step t, as a function of the distance along the fault. Adapted from Rubin and Ampuero (2005).

#### 2.1.2.3 Earthquake interactions

Observations show that many earthquakes do not occur as isolated events, but are part of a sequence (Gardner and Knopoff, 1974). Earthquake sequences are observed either before (Jones and Molnar, 1979, Ellsworth and Bulut, 2018) or after (Mendoza and Hartzell, 1988, Feng et al., 2017) a mainshock, i.e an earthquake of significantly larger size. They are called foreshocks and aftershocks, respectively. Earthquakes sequences are not always associated with a main shock (Klein et al., 1977, Toda et al., 2002); in this case, the sequence is called a swarm.

Aftershock sequences are well documented because they are observed to follow almost all earthquakes of significant size (figure 2.7a). The frequency decay of aftershocks was first described by the seismologist Fusakichi Omori in 1894 following the observation of the rate of aftershocks after the 1891 Nobi earthquake. He observed that the frequency of aftershocks roughly decreases with the inverse of time after the main shock. Utsu (1971) modified this expression to introduce an exponent p, which is near one, and a constant c:

$$n(t) = \frac{K}{(c+t)^p} \tag{2.19}$$

where n(t) is the number of aftershocks in a time interval at time t after the mainshock, and K is a constant.

Accurate understanding of earthquake triggering would need to constrain the actual fault slip velocity, but also all the mechanical parameters such as frictional parameters and pore pressure, acting on each fault in a certain environment. As this is impossible in practice, earthquake triggering is usually studied through the static stress changes in fault environment.

The most simple way to model this effect is to consider the Coulomb failure stress (CFS), which is the difference between the static shear stress in the potential slip direction $\tau_s$ and the frictional strength of the fault. In the case of a CFS change, potential for slip can be enhanced ($\Delta CFS > 0$) or delayed ($\Delta CFS < 0$).

The Coulomb stress change $\Delta CFS$, is simply defined by :

$$\Delta CFS = \Delta\tau_s - \mu\,(\Delta\sigma_n - \Delta p) \tag{2.20}$$

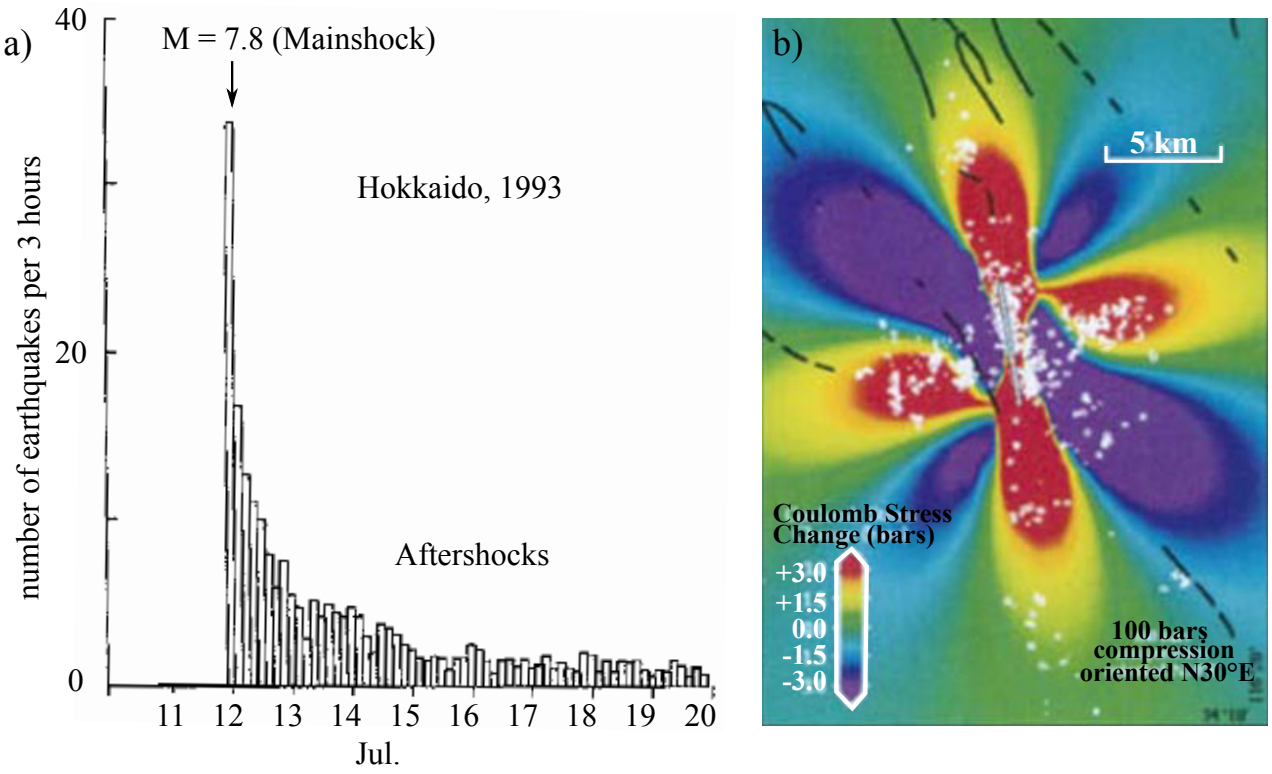


Figure 2.7 – a) Temporal variation in earthquake frequency after the 1993 Hokaido earthquake in Japan. After Utsu (2002). b) Modelled Coulomb stress change induced by the 1979 Homestead Valley earthquake in California. White line is the mainshock rupture and white symbols are aftershocks. From King and Cocco (2001).

where $\Delta\sigma_n$ is the change in normal stress on the fault, $\Delta\tau_s$ is the change in shear stress on the fault, and $\Delta p$ is the pore pressure change.

Spatial correlation between aftershock occurrence and $\Delta CFS$ show that static stress explains at first order the location of seismicity following large ruptures (King et al., 1994, Hardebeck et al., 1998) . For example, King and Cocco (2001) computed $\Delta CFS$ induced by the 1979 Homestead Valley earthquake and found a spatial correlation between the aftershocks and the areas of increased Coulomb stress. On the contrary, almost no earthquakes occurred in the stress shadow areas with a negative $\Delta CFS$ (figure 2.7b). It is interesting to note that those static stress changes are lower than the typical earthquake stress drop (10 -100 bars).

However, Coulomb stress changes cannot explain the time delay observed after the mainshocks, sometimes very short (days to months) compared to tectonic loading. The first explanation is the non linearity of earthquake nucleation (section 2.1.2.1). Moreover, Coulomb stress transfer is time-dependent and also involves a relaxation time. The main mechanisms responsible for this time dependency are the poroelastic effects (Peltzer et al., 1998, Cocco and Rice, 2002): in the case of an abrupt static stress change, the normal stress change induces an immediate pore pressure change of the same sign and of comparable magnitude. This is followed by pore pressure diffusion back to its previous value at a rate that is determined by the diffusivity of the system. This process introduces an additional time delay to the time delay set by frictional properties (Seeber et al., 1998).

Aftershock sequences are a natural laboratory to study fault response to a step-like stress change. This has been widely investigated (e.g., Gross and Kisslinger, 1997, Toda et al., 2012) mainly through the rate-and-state spring-slider model (Dieterich, 1994). However, since the last decade, advances in numerical modelling suggests that finite faults are more sensitive than spring-slider models to such static stress changes (Kaneko and Lapusta, 2008, Ader et al., 2014).

### 2.1.3 Landslide mechanics

We have seen in the previous section that crustal material moves along faults either by creeping, slow slip, or seismic ruptures, and that earthquakes represent the catastrophic part of this large slip spectra. In the same way, hillslopes move permanently. Material moves downward either by diffusive processes, or slow creep, but also through catastrophic ruptures that scar the landscape, called landslides. Therefore, similarly to faulting and earthquakes, static mechanics allow understanding of landslide phenomenology at first order, and its possible triggering. Landslide nucleation and rupture propagation must imply second-order mechanisms such as rate-weakening friction. However, landslide occurrence depends to first order on the occurrence and intensity of triggering events, such as earthquakes. Therefore, landslide dynamic properties are not commonly considered in understanding when and how much landslides are going to happen. Landslides include failure that involve only the regolith and occurs at the soil-rock transition (shallow landslides), and bedrock landslides that involve bedrock failure. The volume of bedrock-landslide inventories is dominated by fewer, but larger failures (Dussauge et al., 2003), more than inventories of shallow landslides. Based on this common observation, bedrock landsliding has been thought to be the only hillslope processes capable of keeping pace with the rapid uplift rate and river incision in active tectonic areas (Burbank, 2002).

In the following, I will focus on the simplest, static description of the problem of bedrock landsliding. I first define the hillslope strength; then I describe the force balance at rupture; and finally, I show the advantages and weaknesses of this force balance for understanding landslide potential triggering.

#### 2.1.3.1 Hillslope strength

The problem of rock strength scale described in section 2.1.1.1 also arises in geomorphology. The actual elevation of mountain ranges was conventionally attributed to the levelling operated by fluvial erosion (e.g., Whipple and Tucker, 1999). This conventional view was supported by simple hillslope stability analyses showing that the theoretical height of cliffs, derived from rock strength measured on laboratory samples, are much higher than the actual hillslope height (e.g., Schmidt, 1994).

Schmidt and Montgomery (1995) showed that landscape relief is well explained by landsliding, considering rock strength at the hillslope scale. Their hypothesis was the following : as a landscape grows, its height increases until the gravitational stress induced by rock material on a potential failure plane exceeds the shear strength of the material. They applied the Culmann criterion (Culmann, 1875) to the problem of hillslope height. In this approach, a failure block is modeled by a wedge. A simple force balance based on the Coulomb failure criterion gives a limit relationship between the wedge height and slope (in other words, the maximum height $H_c$ that can reach a given slope $\beta$ having a hillslope-scale friction $\Phi$ and a cohesion C) :

$$H_c = \frac{4C}{\rho g} \frac{sin(\beta)cos(\Phi)}{[1 - cos(\beta - \Phi)]} \tag{2.21}$$

Schmidt and Montgomery (1995) showed evidence for this relationship between hillslope height and slope for the Santa Cruz Mountains and the Cascade Range, and back-calculated cohesion values of 20-150 kPa, up to 1000 times smaller than values derived from lab experiments for the same type of rocks. This demonstrates that hillslope height is likely to be limited by landsliding, considering that hillslope strength decreases dramatically with increasing scale.

This notion of threshold hillslopes, that adjust rapidly to fluvial incision by widespread landsliding, have laid the foundations of the first physically-based landsliding numerical models (Densmore et al., 1998). It has been supported by the observation that in various tectonic settings, the histograms of slope angles are uniform (Burbank et al., 1996, Korup, 2008). This model is followed by the idea that cohesion plays a limited role in maintaining hillslope elevation at geological time scales (Montgomery and Brandon, 2002).

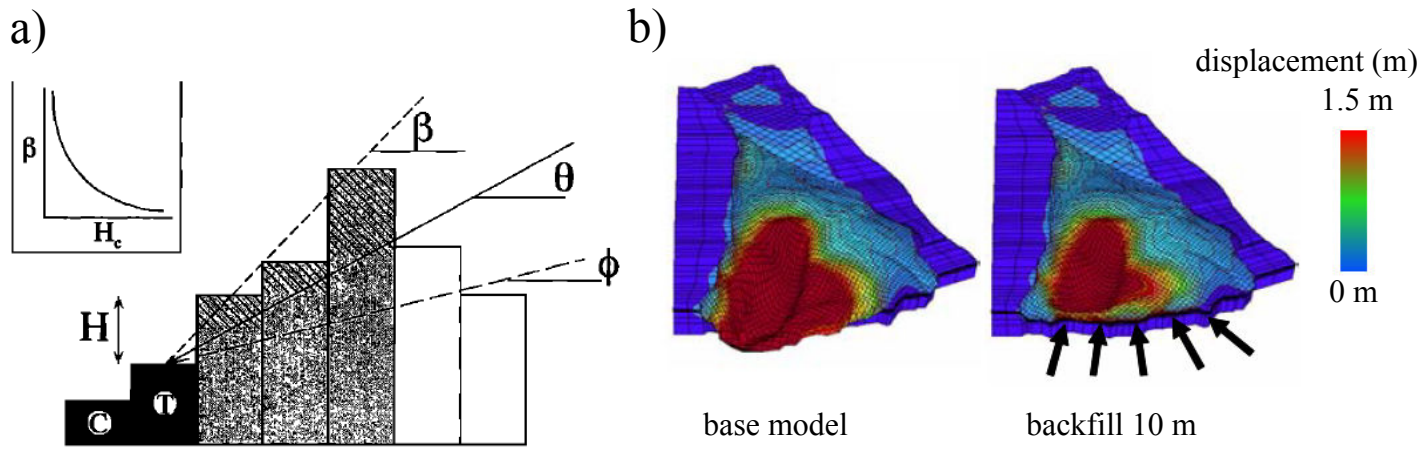


Figure 2.8 – a) Model of bedrock landsliding included in a landscape evolution model, from Densmore et al. (1998). The algorithm is based on the Culmann criterion applied to the hillslope scale. b) An elastoplastic 3D finite element hydromechanical model, applied to model the displacements of a slow landslide in Switzerland (Commend et al., 2004) over a certain period. The model is used to test the evolution of the landslide after several stabilization scenarios.

#### 2.1.3.2 Force balance at rupture

The problem of hillslope stability has been largely addressed by geotechnical studies (e.g., Terzaghi, 1962, Sidle et al., 1985). For engineering issues, and hazard assessment at the scale of one or a few hillslopes, approaches allowing the computation of the stress field and the corresponding deformation of the whole hillslope are preferred (figure 2.8 b). Those approaches generally consider 3D elasto-plastic rheologies, sometimes integrating dynamic-weakening processes (e.g., Brideau et al., 2006, Commend et al., 2004), and are therefore computationally expensive.

Geomorphological studies have a different goal. In order to understand landscape evolution, landslide modelling requires generation of thousands of landslides at the mountain range scale. For this purpose, static approaches based on a simple stability criterion are often preferred, for their short computation time and because they offer the simplest description of the problem (figure 2.8 a). In this section, for the purpose of simply approaching the underlying mechanics of landslides and their possible triggering, I show this simple description of hillslope stability.

Hillslope can be seen as a volume of material lying on a dipping plane with a slope $\alpha$ (figure 2.9). This plane can be the rock-soil interface (soil landslide, or shallow landslide) or a low strength plane, or joint plane in the bedrock (bedrock landslide). Failure occurs if the driving shear stress along this plane overcomes the resisting stress to sliding. This balance can be described by the factor of safety:

$$f^* = \frac{resisting\ forces}{driving\ forces} = \frac{resisting\ stress}{driving\ stress} \tag{2.22}$$

If f* $\geq 1$, the considered plane is probably stable, If f* $< 1$ the considered plane is probably unstable.

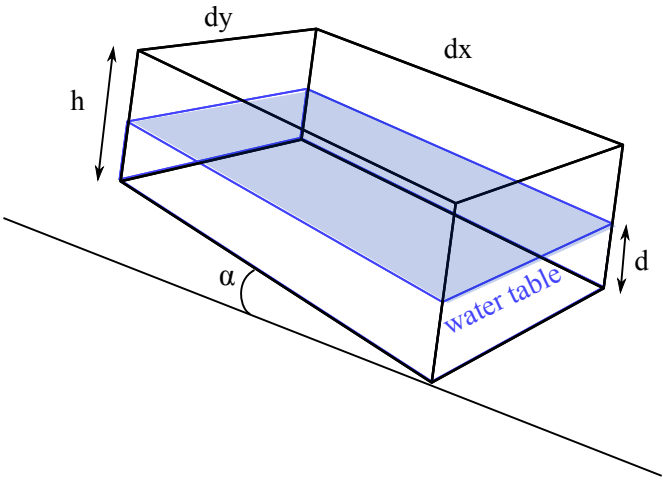


Figure 2.9 – A slab of regolith of area dx*dy and thickness h lying on a potential rupture plane dipping with an angle $\alpha$. Modified after Anderson and Anderson (2010).

The expected driving force is the weight of landslide material acting over the considered area. If the material behaves as a Coulomb material, the expected resisting force is a combination of cohesion (C) and frictional stress, which is proportional to the stress normal to the plane $\sigma_n$ :

$$S_r = \sigma_n * tan(\Phi) + C \tag{2.23}$$

Then we can express the factor of safety :

$$f^* = \frac{[\rho_b \ g \ h \ cos(\alpha) \ cos(\alpha) - \rho_w \ g \ d \ cos(\alpha)] \ tan(\Phi) + C}{\rho_b \ g \ h \ cos(\alpha) \ sin(\alpha)} \tag{2.24}$$

where $\rho_b$ is the bulk density of the material above the rupture plane, $\rho_w$ is the water density and g is gravitational acceleration, d is the water table height and $\Phi$ the internal friction angle. This expression shows that the factors that favours hillslope instability are high slopes $\alpha$, high water table, low cohesion and low friction.

#### 2.1.3.3 Landslide triggering

Several factors can destabilize hillslopes. Those factors either decrease the resisting stress to failure or increase the driving stress, and include earthquakes (e.g., Harp et al., 1981, Harp and Jibson, 1995, Liao and Lee, 2000), heavy rainfall (Chang et al., 2014), and also rapid snowmelt (Cardinali et al., 2000). In this section I focus on earthquake-triggered landslides, which are induced mainly by the transient effect of coseismic waves. Moreover, seismic waves could induce reversible damage to the rocks, decreasing its bulk strength (Brenguier et al., 2008).

Static approaches do not consider seismic acceleration. However, acceleration can be modelled, at first order, by adding a static force to equation 2.24 induced by the seismic acceleration (Schmidt, 1994). If we consider the horizontal component of seismic acceleration, which is proportional to the gravitational acceleration by a factor $K_h$ (for example, $K_h$g = 0.2g), the equation reformulates as:

$$f^* = \frac{[(cos(\alpha) - K_h \ sin(\alpha)) - (\rho_w \ g \ d)/\gamma_b] \ tan(\Phi) + C/\gamma_b}{(sin(\alpha) + K_h \ cos(\alpha))} \tag{2.25}$$

where $\gamma_b = \rho_b \ g \ h \ cos(\alpha)$.

Equation 2.25 shows that in this simple approach, the additional horizontal acceleration can decrease the resisting stress and increase the driving stress. However, this approach is too simplified, because periodic waves actually trigger either stabilization and destabilization cycles.

Because the case where $f^* < 1$ happens over a short period of time and does not systematically induce failure, static limit-equilibrium analysis are not well suited to predict co-seismic landsliding. A more accurate method is to compute the permanent displacement of rock caused by coseismic ground acceleration, and take this displacement as a limit for failure, as developed by Newmark (1976). Such a calculation requires a double integration of the acceleration time history which is in practise impossible because it implies a very good constraint of that history. Therefore, it is impossible to apply at regional time scale.

To overcome these difficulties, empirical relationships have been developed which describe the Newmark displacement as a function of the ratio between PGA and the yield acceleration $a_y$ necessary to displace the rock. $a_y$ comes from the expression of the safety factor :

$$a_y = (f^* - 1)gsin(\alpha) \tag{2.26}$$

with $\alpha$ the gradient of the hillslope.

Newmark displacements calculated from seismic records have been correlated to the landslide density for historical events (Jibson et al., 2000), showing the accuracy of the method for the regional scale study of coseismic landslides.

#### 2.1.3.4 Modelling landslides in landscape evolution

Many of the existing, physically-based landsliding models are rooted in the concept of threshold hilslopes and use the Culmann criterion to determine unstable points (Densmore et al., 1998, Egholm et al., 2013). In the approach developed in Densmore et al. (1998), the probability of failure is calculated from equation 2.21, and is the ratio between the local hillslope height H and the maximum stable hillslope height $H_c$ (figure 2.8 a). The considered target cell is the lowest point above the channel at which the local slope $\beta$ is greater than the frictional angle $\Phi$. The rupture plane angle, $\theta$, is calculated following the analysis of Culmann (1875) that predicts that failure occurs on a plane which is the bisector between slope angle and frictional angle :

$$\beta_c = \frac{\alpha + \Phi}{2} \tag{2.27}$$

The plane is projected outward and upward to the neighboring cells.

However, the concept of threshold hillslopes may apply only to deepseated landsliding, and the Culmann criterion might not integrate the strength of the soil and bedrock that characterizes many near-surface environments (Schmidt and Montgomery, 1995). Therefore, other approaches based on Newmark displacements have been proposed to model co-seismic landslides. Such an approach was used for example by Gallen et al. (2015), who performed an infinite-slope stability analysis based on Newmark displacements to model landslides triggered by the Wenchuan earthquake. They identified target cells that exceed a threshold surface displacement, and inferred the 3D shape by undercutting the slope with different geometries. They found that the best way to reproduce landslide area-frequency is to adapt a plane geometry for each individual landslide, resulting on either planar or concave-up failures depending on the shape of the considered hillslope.

Landslide modeling implies several assumptions on rupture plane geometry. At the hillslope scale, the Culmann criterion predicts that the rupture plane $\beta_c$ is the most unstable plane which is the bisector between friction angle and actual slope (equation 2.27). Geotechnical models that apply a limit-equilibrium analysis on a discretized hillslope predicts log-spiral failure shapes (e.g., Baker and Garber, 1978). Not enough observations of landsliding plane geometry are reported to derive general rules. For large bedrock landslides the rupture geometry varies from one landslide to another because many factors control it, in particular the geometry of pre-existing fractures (Lee et al., 2002, Sitar et al., 2005). Nevertheless, models of landsliding applied to landscape evolution generally use simple assumptions for rupture geometry, such as planar failure (e.g., Densmore et al., 1998) or sometimes concave-up rupture (Gallen et al., 2015); those geometries allow at first-order to compute landslide sizes in agreement with observations.

Another important assumption is made about the rupture depth. Calculation of a safety factor requires knowledge of the rupture depth to compute the lithostatic stress. The question of landslide depth can be bypassed by considering a cohesion-to-thickness ratio (Gallen et al., 2015), or by considering that rupture plane starts at the hillslope toe and propagates through a defined rupture plane (figure 2.8a; Densmore et al. (1998), Stark and Guzzetti (2009)). However, bedrock landslides have a wide range of rupture depths (Larsen et al., 2010). For instance, the probable variability of rupture depths and angle of bedrock landslides is not fully considered in landslide modelling.

***Outstanding issues***

- What is the landscape strength that is involved at the time scales that are relevant in geomorphology ?

- Is it possible to predict the variability of landslide depth in a simple model ?

- Is accounting explicitly for co-seismic acceleration necessary to reproduce co-seismic landslides ?

## 2.2 Interactions between surface processes and earthquakes at short time scale (< 1000 years)

In the previous section I have shown that earthquakes and landslides can be triggered by stress changes in their environment : earthquakes can be triggered by the static stress change due to large rupture, and landslides can be triggered by the acceleration due to seismic waves. But both processes can also be the cause of stress changes and not only a consequence; for example, observations show that surface processes can change the stress field around shallow faults enough to trigger seismicity. However, earthquakes do not systematically induce numerous landslides, and surface processes do not systematically change the regional seismicity. In this section I describe the observations of 1) landscape response to earthquakes and 2) earthquakes triggered by surface processes and what these observations tell us about the mechanism of triggering at seismic cycle time scales.

### 2.2.1 Landscape response to earthquakes

Keefer (1994) compiled the total surface area affected by landsliding for several historical earthquakes, and found that this area, and therefore the total volume of sediments, depends at first order on earthquake magnitude (fig 1.3). For example, the volume of landslides following a $M_w7$ earthquake is around 30 times greater than the volume produced by a $M_w6$ earthquake. This is pretty intuitive, as the surface rupture area increases with earthquake magnitude. However, the scatter around the landslide volume-earthquake magnitude relationship (figure 1.3) reaches one order of magnitude, as other second-order processes and parameters (landscape slope, intensity of ground shaking...) influence landslide density (Marc et al., 2016b). Landscape co-seismic and post-seismic evolution also depends on the evacuation of the sediments by the rivers, and therefore on river dynamics (Yanites et al., 2010, Croissant et al., 2017, Fan et al., 2018) .

Here I expose 1) the parameters that control the landslide density and 2) the time scales involved in the sediment evacuation.

#### 2.2.1.1 Landslide density

Which parameter makes a given landscape more or less prone to landsliding is still an open question.

Having studied three specific cases of earthquake-triggered landslides, Meunier et al. (2007) suggested that landslide density correlates with the pattern of seismic shaking (i.e the area of landslides per unit area):

$$P_{ls} = \alpha_A(PGA - PGA_{cr}) \tag{2.28}$$

where $\mathrm{PGA}_{cr}$ (critical peak ground acceleration) is the critical value below which no landslides are found, and $\alpha_A$ is an area sensitivity term that sets the hillslope likelihood to fail by landsliding for a given shaking. In most landslide inventories, landslides are found within an area having experienced PGA greater than 0.1-0.2 g (Roback et al., 2017, Tanyaş et al., 2017). The parameter $\alpha_A$ varies significantly and probably reflects the geomorphologic variability among landscapes, but also rock mechanics.

In some cases such as the 2015 Gorkha earthquake, landslide density correlates at first order with hillslope gradient (e.g., Roback et al., 2017). Spatial analysis after the 2016 Kaikoura earthquake revealed that the distance from the fault was the best parameter to explain landslide spatial distribution (Massey et al., 2018). Actually, the parameters correlated to landslide density are intrinsically linked; for example, when decreasing the distance to the fault rupture, high-frequency seismic waves are stronger, rock strength is likely to be smaller because of previous failures, and hillslopes can be steeper.

Therefore, landslide density is a function of all the local conditions that affect PGA (such as site effects and topographic amplification), but also of parameters such as slope, lithology and rock damage that controls the hillslope propensity to fail (Massey et al., 2018).

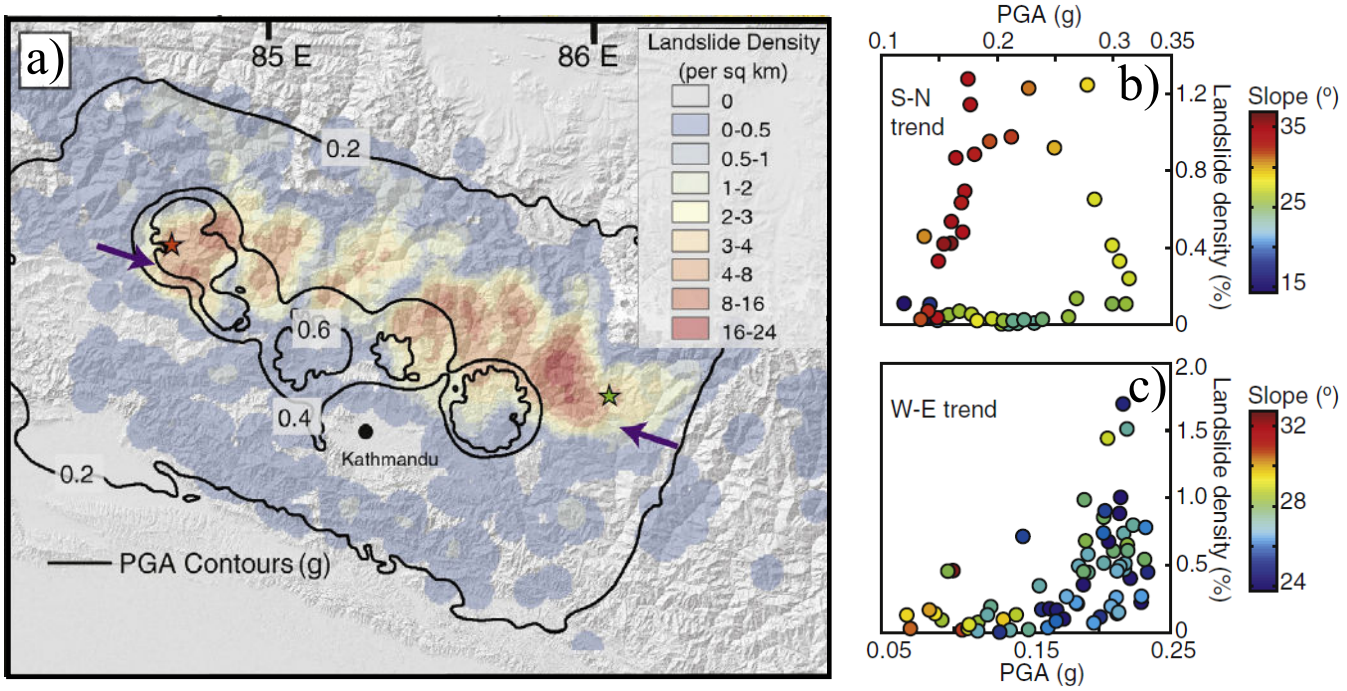


Figure 2.10 – a) Landslides density (number per square kilometer) triggered by the $M_w$ 7.8 Gorkha earthquake, compared to peak ground acceleration (PGA). b) and c) represent landslide area density as a function of PGA in a south-north (b) and west-est (c) profile. Modified from Roback et al. (2017).

#### 2.2.1.2 Sediment export

Earthquakes transform hillslope rocks into sediment that can be mobilized and evacuated from the epicentral area by rivers. Therefore, the implications of co-seismic landslides for the mass balance of large earthquakes, or for hazard assessment, depend on the timing of sediment evacuation away from the mountain belt. This process depends on landslide connectivity to the drainage network, which displays significant variation among catchments (Li et al., 2016). It is also controlled by river dynamics (Hovius et al., 2011, Yanites et al., 2010, Croissant et al., 2017), and the grain size distribution of landslide sediments (Sklar and Dietrich, 2006, Cowie et al., 2008, Egholm et al., 2013).

The evolution of the suspended load after a large earthquake can be monitored using stream gauges, and has been documented for a few large earthquakes (Hovius et al., 2011, Wang et al., 2015). Figure 2.11 shows that the suspended load in the rivers draining the epicentral area after Chi-Chi earthquake increased up to five times its background value, and relaxed over a characteristic period of 10 years.

Real-time monitoring of the bedload evolution following large earthquakes is more difficult to monitor at the catchment scale; however, the sedimentary record left by past earthquakes can give insights on the time scale needed for a landscape to recover from large landsliding events. A recent study conducted in the Himalayas (Stolle et al., 2018) suggests that even highly erosive rivers need more than several centuries to adjust to large landsliding events. Sedimentary records (Howarth et al., 2012) and landslide mapping (Uchida et al., 2014) in particular settings have shown that rivers can evacuate landslide sediments within several decades. Recent numerical modelling has found a post-seismic mean residence time of coarse sediments of several years to a few decades (Croissant et al., 2017), one order of magnitude lower than expected from previous theories (Yanites et al., 2010).

### 2.2.2 Seismic cycle response to surface processes

Surface processes (such as snow, erosion, tides) changes the stress field in the upper few kilometres of the Earth's crust. Those processes change the static stress around faults and can trigger or delay earthquakes

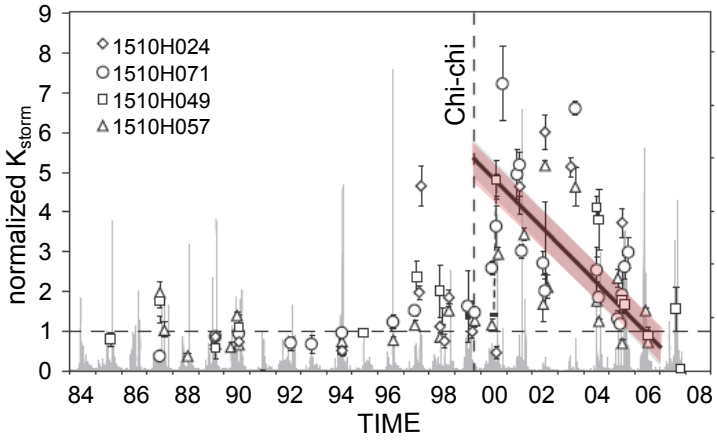


Figure 2.11 – Time evolution of the suspended sediment concentration measured at four stations in the Choshui River catchment (Taiwan) draining the epicentral area of the Chi-Chi earthquake. The red curve is the best fit to the post-earthquake data. After (Hovius et al., 2011).

depending on the local stress conditions. Spatial and temporal correlations exist between surface processes and seismicity changes, but the underlying mechanics is not well understood. During the last decade, triggered seismicity, especially in the US, has become an important subject of political and scientific discussion because of the development of hydraulic fracturing, or 'fracking'. But for decades, it has been recognized that earthquakes can be triggered by human activity, such as impoundment of reservoirs, mining, extraction of fluid and gas from the subsurface, and injection of fluid into underground formations (Scholz, 2002, Ellsworth, 2013). Human-induced seismicity affords further understanding of earthquake triggering not allowed in natural cases, especially when a seismic network has been deployed before the starting of the triggering period. From this natural lab, it has been observed that seismicity is commonly triggered by static stress changes as low as 0.1 bar (e.g Reasenberg and Simpson, 1992), which is very low compared to typical values of the earthquake stress drop. This low level of triggering stress suggests that many faults are very close to their critical point of rupture within continental plates or near plate boundaries (Townend and Zoback, 2000), even if there is no tectonic activity, and that small stress changes can induce earthquakes.

In this section I focus on the observations of seismicity triggered by surface processes that are not induced by human activities. In a second part, I address the implications of those observations for the potential effect of erosion on seismicity at the seismic cycle time scale.

#### 2.2.2.1 Observations

In various places, seismicity is potentially modulated with an annual periodicity (figure 2.12). This has been noted in many active tectonic settings such as Japan, (Heki, 2001, 2003), the western US (Christiansen et al., 2005, Gao et al., 2000), and the Himalayas (Bollinger et al., 2007, Christiansen et al., 2007, Ader and Avouac, 2013). A link between this periodicity and the hydrological cycle has been proposed in various settings. It has been correlated either with annual variations of snow cover in Japan and in western US volcanic areas (Heki, 2003, Christiansen et al., 2005), with seasonal variations of precipitation in the Himalayas (Bollinger et al., 2007), or with atmospheric pressure changes in California (Gao et al., 2000).

Earthquake triggering is usually discussed in terms of static Coulomb stress change (equation 2.20). Several mechanisms have been suggested to explain seasonal modulations : hydrological processes could modulate seismicity through changes in static stress by elastic loading/unloading linked to snow load variations (Heki, 2003, Bollinger et al., 2007) or ground water recharge/discharge (Christiansen et al., 2005), but also by pore pressure change through water infiltration to the fault surface (Bettinelli et al., 2008). Deciphering between those different mechanisms is difficult because of the complex interplays between all hydrological processes at

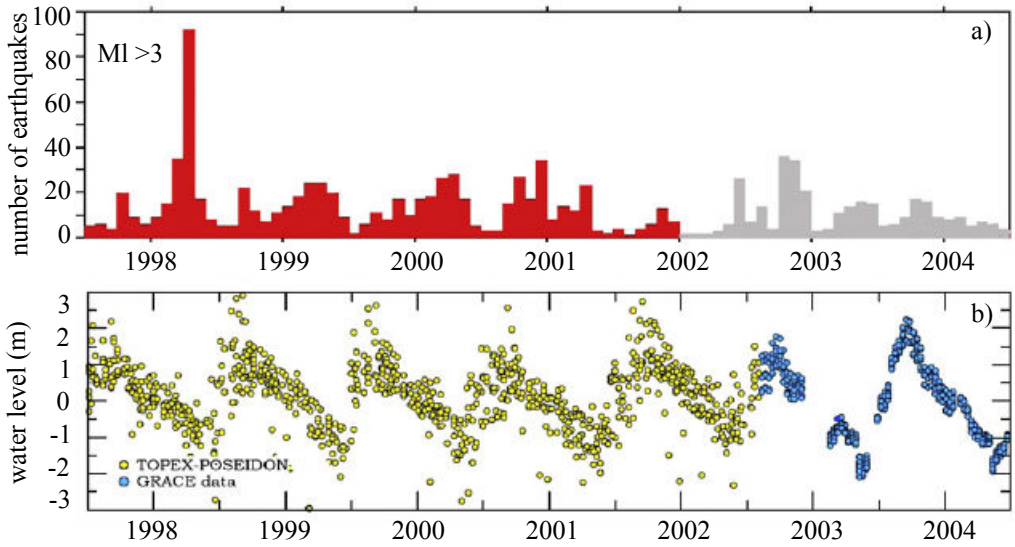


Figure 2.12 – a) Number of earthquakes in the Ganga Basin, India. The period over which the geometry of the seismic network has not changed is in red. b) Water level measured in the rivers in the Gange basin over the same period, modified from Bettinelli et al. (2008).

this time scale, but also because we do not fully understand the processes that control earthquake nucleation.

Despite that, those observations have led to two fundamental points about the mechanics of earthquake triggering. The first is that limited static stress changes can efficiently to trigger seismicity at the seasonal time scale. Indeed, the static stress changes induced by hydrological cycle are estimated to be about 1-5 kPa (e.g., Bettinelli et al., 2008, Christiansen et al., 2007).

The second point comes from the fact that seismicity does not seem to systematically vary at a tidal period (12 hours). Triggering of some shallow events by tides has been proposed in a few very specific places where local tidal stress acts in the same direction as the tectonic stress (Tanaka et al., 2004), or along axial ridges where there is a large ocean-loading component of tidal stress (Wilcock, 2001). However, no systematic response of seismicity at the tidal period has been found (Vidale et al., 1998, Cochran et al., 2004), although tides produce static stress changes (3-4 kPa) of the same order of magnitude as the hydrological cycle. This observation suggests a period dependency of seismicity to such small stress variations, and earthquake triggering implies a non-linear effect that cannot been simply described by static stress changes. Numerical modelling (Ader et al., 2014) and laboratory experiments (e.g., Beeler and Lockner, 2003, Savage and Marone, 2007) have shown such a period dependency, even though their results are difficult to extrapolate at the real seismic cycle time scale.

#### 2.2.2.2 Potential effects of erosion on seismic cycle

We have seen in Chapter 1 that models suggest that erosion could trigger seismicity at the time scale of 10000 yr - 1 Myr through isostasy (Vernant et al., 2013). At the time scale of a seismic cycle, recent mechanical modelling has shown that in active compressive orogens such as Taiwan, erosion rates that balance the rock uplift rate can raise the Coulomb stress in the upper few kilometres of the crust by 0.1-10 bars during the interseismic phase (Steer et al., 2014). Moreover, large erosional events, such as earthquake or rainfall-induced landslides, trigger a large amount of sediments that can be moved away from the nearby faults (section 2.2.1.2).

We have seen that faults respond to small stress change at certain periods; therefore, large erosional events could trigger seismicity, depending on the magnitude of erosion and the rate at which sediment is transported away by rivers. Few observations of seismicity triggered by a large landsliding event have been made yet. One example is the 2009 Typhoon Morakot in Taiwan, which triggered more than 10000 landslides,

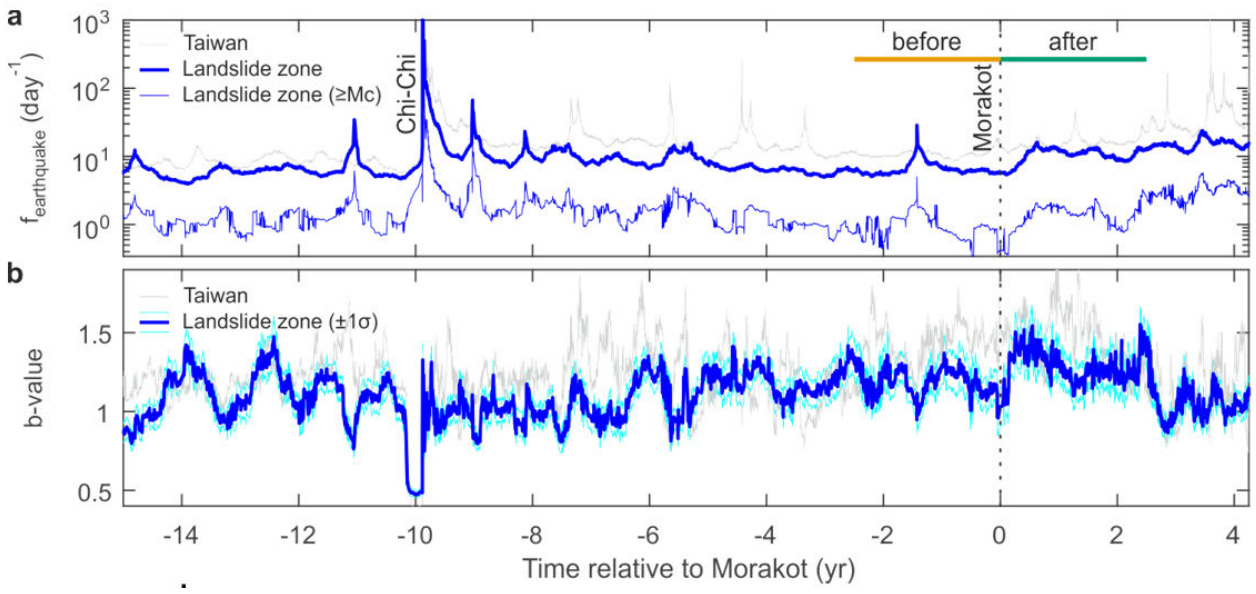


Figure 2.13 – a) Earthquake frequency and b-value (see section 2.3.1.2) as a function of time, in all Taiwan (grey line) and inside the landsliding zone (blue line), for all the catalogue (thick line) and above the magnitude of completeness (thin blue line). After Steer et al. (2018).

equivalent to 0.7 km$^3$ of sediment. Because those landslides were well connected to the rivers (West et al., 2011), the typhoon boosted sediment export that persisted over at least 2 years (Huang and Montgomery, 2013, Lee et al., 2015). In Steer et al. (2018) (Appendix A), we noticed an increase in both earthquake frequency and proportion of small earthquakes compared to large ones, after the typhoon, that last at least two years (figure 2.13). We suggest that the rapid unloading of the surface above active Taiwan faults have triggered this change in earthquake statistics. However, the link between erosion and seismicity is not clarified, and approaches such as developed by (Steer et al., 2014) are limited to a Coulomb analysis that do not take into account fault dynamics. The use of numerical models of the seismic cycle is essential for a better understanding of such links.

***Outstanding issues***

- Are active faults sensitive to erosional events, that are transient but non periodic ?

- What is the amplitude and duration of an erosional event that is necessary to trigger seismicity ?

- Is a transient stress change able to change the distribution of earthquake magnitudes ?

## 2.3 Earthquake and landslide sizes

The size distribution of landslides and earthquakes is a fundamental component of hazard assessment. Moreover, the size distribution of landslides is pivotal to infer erosion following a large earthquake or rainfall event. Both landslides and earthquakes display an incomplete power-law distribution that is observed in many inventories. However, those distributions vary in time and space. In particular, prediction of large events is difficult because they are so rare that they are not sampled in every inventory. For example, the destructive Langtang landslide (Collins and Jibson (2015), figure 2.14a) or the Tohoku earthquake and the consequent tsunami (Mori et al. (2011), figure 2.14b) were particularly large compared to predictions based on historical inventories.

In this section I first describe the observed sizes of landslides and earthquakes in nature. Then, I will focus on the physical explanation of their power-law distribution and the potential variations of their exponents. Finally, we will see that the power-law model does not hold for smallest and largest events, and summarize the current knowledge about the factors that control small and large rupture event size.

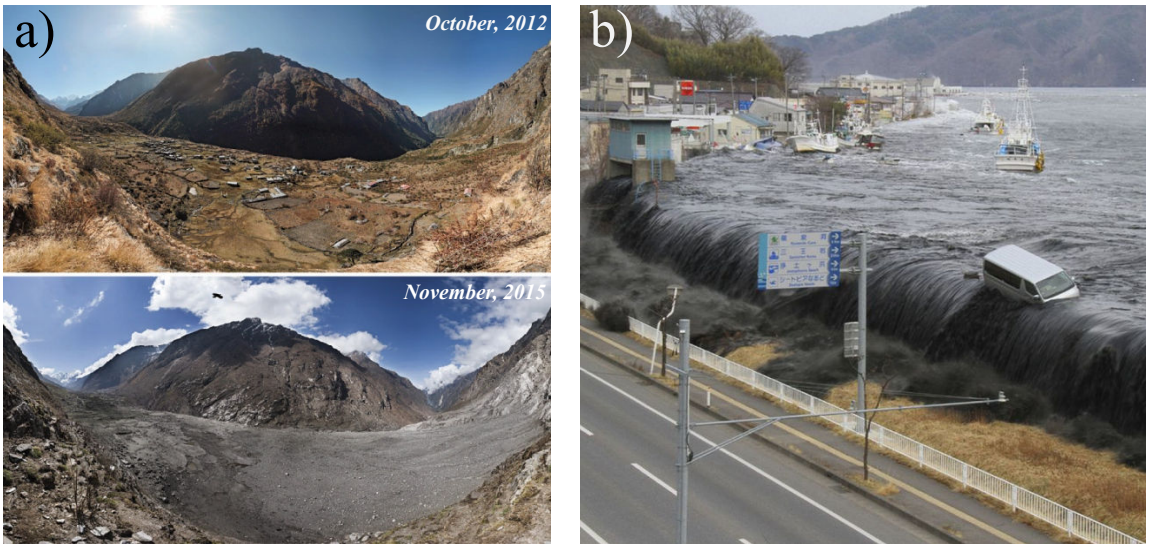


Figure 2.14 – a) Langtang village (Nepal) in October 2012 and in May 2015, one month after the $M_w$ 7.8 Gorkha earthquake. The village was destroyed by a large landslide with a volume of $2.10^6$ $m^3$ (Collins and Jibson, 2015)), resulting in more than 200 fatalities. Credit : David Breashears /Glacierworks. b) Tsunami induced by the $M_w$ 9.1 Tohoku-Oki earthquake of 11 March 2011 in Miyako City, Iwate Prefecture, north-eastern Japan.

### 2.3.1 Observations

#### 2.3.1.1 Magnitude-frequency distribution of rupture events

To characterize the distribution of rupture events (earthquakes or landslides) of different sizes in an inventory, it is required to know the empirical probability of events with size larger than A, where A is defined as landslide area. This function is called the cumulative distribution function (CDF) :

$$cdf(A) = P(X > A) \tag{2.29}$$

Size distribution can be also examined through the probability density function (PDF), which is the derivative of the CDF :

$$pdf(A) = \frac{dN(A)}{N_{TOT}} \frac{1}{dA} \tag{2.30}$$

where dN(A) is the number of events with a size between A and A+dA and $N_{TOT}$ is the total number of events.

The frequency-magnitude relationship of rupture events, such as landslides and earthquakes, is usually described by a power-law :

$$CDF(A) = CA^{-b+1} \tag{2.31}$$

$$PDF(A) = C'A^{-b} \tag{2.32}$$

where C, C' and b are constants. In seismology, the exponent of the frequency-magnitude distribution of earthquakes is called the b-value.

Power-law distributions are characterized by a slow decay for large events, which is also called a "heavy tail". This means that the decay is slower than for exponential or Gaussian distribution and that large events are more frequent than would be the case for such distributions. Power-laws are also free of characteristic scales, or scale-invariant. Indeed, from equation 2.32 we see that the number of events with size xA , where x is any positive number, will be the number of events of size A multiplied by a constant $x^{-b}$, regardless of the absolute size of the considered event:

$$PDF(xA) = C'x^{-b}A^{-b} = PDF(A)x^{-b} \tag{2.33}$$

This property is also called self-similarity.

Another important property of the rupture size distribution is that deviation from the power-law behavior, at small and large sizes, is usually observed. This can be modelled by a tapered Pareto distribution (Geist and Parsons, 2014), which is a model that includes exponential decay at sizes greater than a critical size $A_c$, (figure 2.15, red lines), or double-Pareto, which takes in account breaks in self-similarity at small and large sizes (Stark and Hovius, 2001).

#### 2.3.1.2 Earthquake sizes

The traditional measurement of earthquake size is the magnitude, which is a logarithmic scale based on the energy released by an earthquake. The first measured magnitudes were based on the measurement of the amplitude of certain seismic waves at specific periods, which offers a convenient way to measure earthquake size from a seismogram. Many types of magnitudes have been employed (surface wave magnitude $M_s$, body wave magnitude $m_b$, local magnitude $m_L$). However, those magnitudes are useful under different, specific conditions. Moreover, for large earthquakes, they underestimate the seismic moment (figure 2.16 a), which is a physical measure of seismic rupture :

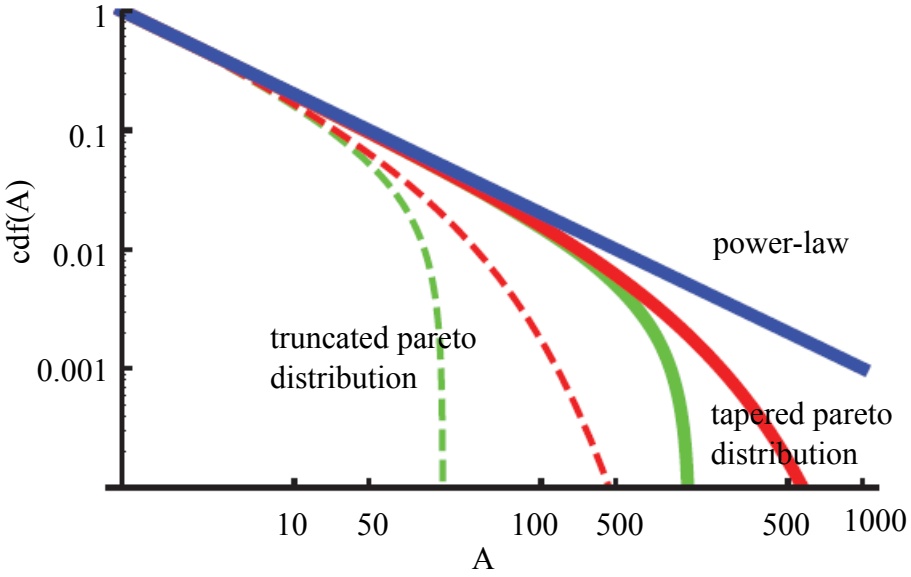


Figure 2.15 – Pure power-law distribution (blue), tapered (red) and truncated (green) Pareto distributions for a critical size of 20 (dashed line) and 200 (solid lines). After Geist and Parsons (2014).

$$M_0 = E\Delta u A \tag{2.34}$$

where $\Delta u$ is the mean slip averaged over the rupture area A and E is the shear modulus.

To overcome the discrepancies between different magnitude scales and the saturation problem, the magnitudes scales were unified under the concept of moment magnitude $M_w$ (Kanamori, 1977, Hanks and Kanamori, 1979). Considering the energy balance of a dynamically expanding shear crack, they derived analytical expression to link energy released by an earthquake and the seismic moment, providing an expression of earthquake magnitude based on static source parameters that can therefore be accurately determined from geodetic and/or fault length data. Moment converted to moment magnitude is:

$$M_w = \frac{2}{3} log(M_0) - 6.07 \tag{2.35}$$

The frequency-magnitude distribution of earthquakes is known as the Gutenberg-Richter law (Gutenberg and Richter (1955), figure 2.16 b). In any region, at a given period the number of earthquakes $N(M_0)$ with a magnitude $M \geq M_0$ tends to follow the relation (Gutenberg and Richter, 1944)

$$log_{10}(N) = a - bM_0 \tag{2.36}$$

where the parameter a varies in time and space and is representative of seismic activity. The b-value gives the relative scaling of large versus small earthquakes. Over long time periods and large regions, it is close to one, and displays significant spatial (Scholz, 2015) and temporal variations at smaller temporal and spatial scales. For example, a temporal b-value decrease within a few years has been observed in Japan (e.g., Imoto, 1991, Cao and Gao, 2002) and in Sumatra (Nuannin et al., 2005). These b-value decreases often precede large earthquakes and therefore are commonly seen as main shock precursors (e.g., Imoto, 1991, Smith, 1981, Nuannin et al., 2005).

Another important earthquake scaling relationship that has been noted for decades is that their stress drop seems at first order constant, and independent of rupture size (e.g Aki, 1972, Kanamori and Anderson, 1975). Seismic moment determined from long-period waves scales with fault area to the power 3/2 (figure 2.16 c)). This has been interpreted as a constant stress-drop of 10-100 bars (Chinnery, 1969, Aki, 1972),

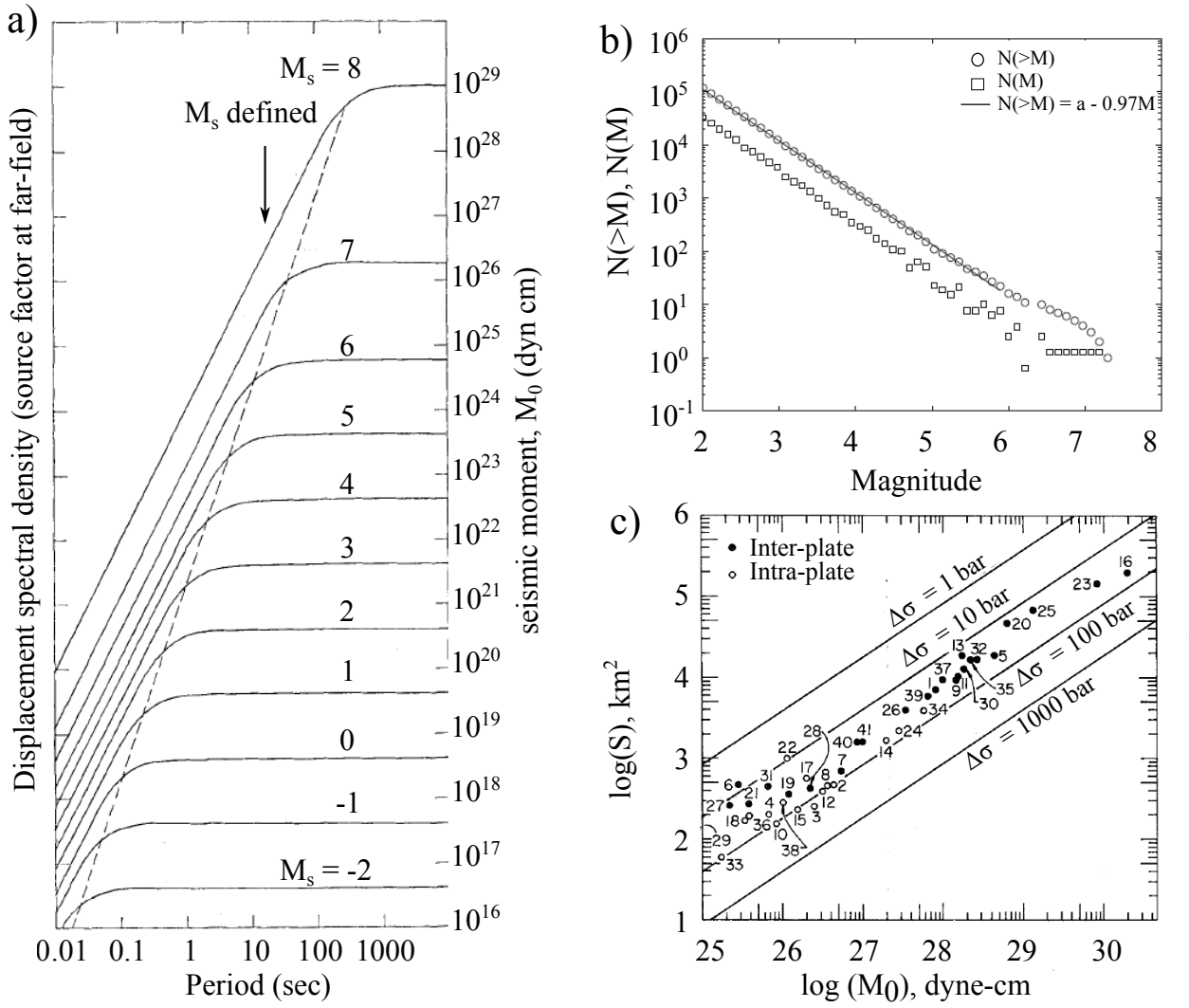


Figure 2.16 – a) Seismic spectra for surface waves, calculated from a theoretical model of earthquakes (Aki, 1967). The magnitude $M_S$ is usually measured at 20 s. The spectra are flat above a corner frequency. For small earthquakes enough, $M_s$ scales with the moment ($M_0 \sim Mw$), so the moment can be deduced directly from the wave amplitude. But for earthquakes so large that f0 is longer than 20 seconds, surface wave magnitudes underestimate the moment: the magnitude scale is said to saturate. b) Cumulative (N>M) and discrete N(M) distribution of earthquake magnitude in California from 1990 to 2010, from Amitrano (2012). c) Relation between fault surface area (S) and $M_0$ (seismic moment). The straight lines give the theoretical relation for constant stress drop ($\Delta\sigma$) for circular cracks (Kanamori and Anderson, 1975).

which is consistent with simple models of theoretical stress drop (Brune, 1970) showing that the moment of a circular crack with diameter a scales with $a^3$ :

$$M_0 = \frac{16}{7}\Delta\sigma a^3 \tag{2.37}$$

This constant stress drop actually displays significant variations, showing that equation 2.37 may not hold in every case. Actually, the moment of small earthquakes grows faster than the moment of large earthquakes. Those different regimes can be explained by the fact that a small patch can extend in every directions, whereas a patch reaching the seismogenic zone depth can only extend in one direction with a constant width (Shaw, 2013).

#### 2.3.1.3 Landslide size

Landslide inventories are currently the basis for statistical studies of landslide size (figure 2.17a). They provide precious information to study landslide mechanics but also to infer landslide hazard maps.

On the first landslide inventory maps (e.g Morimoto, 1951, Plafker et al., 1971), only the location of landslides were indicated. Then, aerial photography and manual mapping coupled with ground-based field work led to inventories with landslides depicted as polygons with a defined area (e.g., Harp et al., 1981, Harp and Jibson, 1996), allowing landslide size inventories. Such maps are now produced using high-resolution satellite imagery, sometimes coupled with ground-based field work. To overcome the problem of manual mapping, which is very time-consuming, some algorithms have been developed to automatically map landslides, but they face the problem of amalgamation: if two landslides are too close from each other and considered as one landslide, it can lead to overestimating the landslide area and volume (Marc and Hovius, 2014). Therefore, modern studies still prefer a manual method (e.g., Roback et al., 2017) or an automatic method coupled to manual check.

A common outcome of studies based on such inventories is that the PDF of landslide area follows a power-law scaling for intermediate to large landslides. Simple power-laws have been proposed (Hergarten, 2003), although double-Pareto (Stark and Hovius, 2001) or three parameter inverse-gamma (Malamud et al., 2004a)) distributions have also been suggested; nevertheless, all those studies consider that landslide size distribution is heavy-tailed. This power-law behavior holds whether it is the scar area (Hovius et al., 2000) or the total disturbed area including runout (Pelletier et al., 1997, Roback et al., 2017) that has been mapped, and for a long period of time or a single triggering event (Malamud et al., 2004a) (figure 2.17 b). According to recent reviews of 30-40 worldwide landslides inventories, (Van Den Eeckhaut et al., 2007, Tanyaş et al., 2017), the typical power-law exponent varies between 1.42 and 3.36, with a central tendency of 2.3-2.5.

Another important landslide scaling relationship is their volume-area relationship (figure 2.17c). Estimating the volume of landslides is a more difficult task than estimating their area because it requires a third dimension and cannot be directly derived from satellite imagery. Measurements of individual landslide volumes requires the comparison between pre and post-landslide digital elevation models, obtained by field mapping (e.g., Rice et al., 1969), and latterly by LiDAR data, satellite images or photogrammetry (Whitehouse, 1983, Martin et al., 2002, TAI, 2009), sometimes completed by field measurements.

A general observation is that the volume of landslides scales with area with an exponent $\gamma$ (Larsen et al., 2010):

$$V = \alpha_V A^\gamma \tag{2.38}$$

The exponent $\gamma$ is critical for volume assessment; small variations lead to strong variations in the total landslide volume (Larsen et al., 2010). Guzzetti et al. (2009) analyzed an inventory of 677 landslides worldwide, caused by different triggers in different environments, and found $\gamma = 1.45$. They concluded that volume-area scaling is not significantly influenced by the properties of failed rock. Larsen et al. (2010) analysed more than 4000 individual landslides and found $\gamma$ values significantly different for soil and bedrock

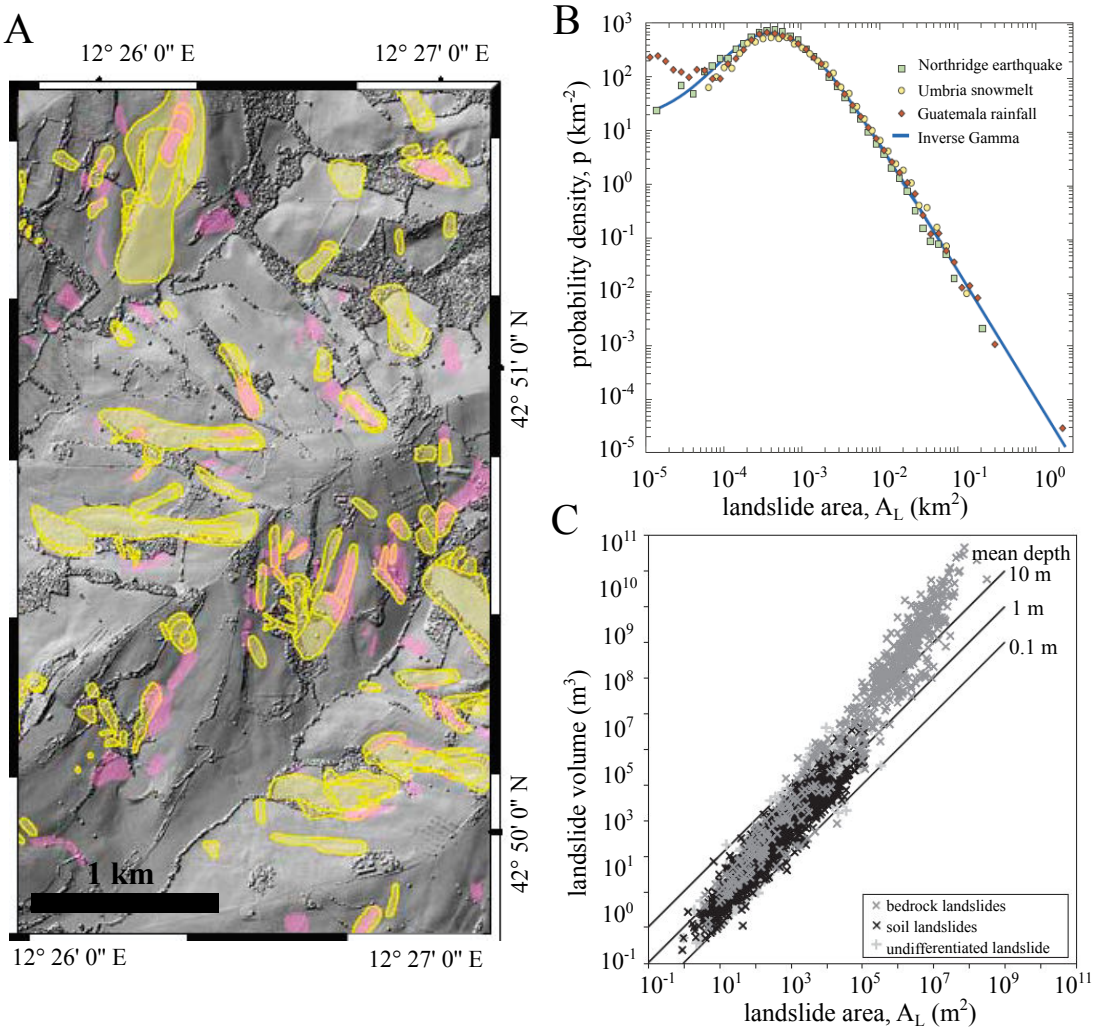


Figure 2.17 – a) Subset of two landslide inventories (Stark and Guzzetti, 2009) in Collazone, Umbria, central Italy. b) PDF of landslide areas triggered by three different events (Malamud et al., 2004a). c) Volume-Area scaling from a compilation of > 4000 soil and rock landslides (Larsen et al., 2010).

landslides. For soil landslides, $\gamma$ varies between 1.1 and 1.3 and for bedrock landslides, it varies between 1.3 (in the Himalayas) and 1.6 (in the Alps and Apennines). This difference between shallow and bedrock landslides can be explained by the soil-rock transition that confines shallow landslides to a certain depth, allowing them to extend only in their horizontal dimensions.

### 2.3.2 Physical meaning of power-law distribution and b-value variations

The theories explaining why rupture events follow power-laws and the spatial and temporal variations of the exponent are tightly linked. This problem has been addressed through several perspectives coming from the contributions of either mathematics or physics. I present three main explanations for power-law behavior of rupture events and b-value variations : the first one, which is not physically based, results from sandpile models and provide an interesting framework to think about system criticality. The two last are based on rupture physics and consider a geometric and dynamic origin of the power-law behaviour, respectively.

#### 2.3.2.1 Self-organised criticality

During the 90s, the sandpile model was largely compared to the behaviour of brittle rupture events such as landslides and earthquakes. This model is discretized into cells that initially contain a random number of grains. A constant input of grains drive the cells to instability when a threshold number of grains is reached; then the critical cell redistributes the grains to its neighbours, which can in turn become unstable and form avalanches of a certain size depending of the number of cells involved. In this very simple model, the size of avalanches follows a power-law distribution. The analogy between this result and the size distribution of rupture events have led to numerous attempts to model the behaviour of hillslopes using sandpile models (e.g., Noever, 1993, Densmore et al., 1997), or the behaviour of faults using a network of slider blocks connected by springs (e.g., Olami et al., 1992). A common outcome of those models, belonging to the family of cellular automata models, is the spontaneous emergence of a fractal distribution for the size of rupture events. The concept of self-organised criticality has been introduced (Bak et al., 1988) to characterize the behaviour of a sandpile model, and therefore of other rupture phenomena leading to similar behaviours.

This concept is well illustrated by the example of a nuclear chain reaction (Hergarten, 2003). Let us consider a fissioning nucleus releasing two neutrons, which in turn can cause other nucleii to fission with a certain probability q. The probability distribution of the chain reaction size (figure 2.18 a) strongly depends on q. When $q = 1/2$, meaning that there is the same density of fissionable and non-fissionable material in the considered space, the size distribution of avalanche is a power-law. This is called the critical point. If $q < 1/2$, the system is said to be sub-critical, and the probability of large avalanches decreases rapidly, leading to a higher apparent b-value. If $q > 1/2$, it is over-critical. Hergarten (2003) used this model to propose that landscapes are in a critical state which depends on a balance between hillslope steepening through erosion and uplift, and landslides that relaxes hillslope angles (figure 2.18b).

However, cellular automaton models only lead to a limited understanding of the size distribution of failure event, because they bypass the physical processes of the rupture. They also tend to overestimate the number of large events compared to the small ones. Nevertheless, they show that with only two ingredients, elastic interactions (modelled for example by the addition of sand grains) and initial heterogeneous media, the model evolves naturally toward a critical state characterized by a power-law distribution for the size of rupture events, independent of the initial conditions.

#### 2.3.2.2 Geometric origin of b-value

Landslide and earthquakes can be considered, in a static approach, as a rupture occurring when the shear stress acting over the rupture plane overcomes the shear resistance of the interface. Then, it is quite intuitive to suggest that the size of landslides and earthquakes is linked either to the size of low-strength areas (in the landscape or in the Earth's crust), or to the size of areas with rapidly increasing shear stress. Early experiments on brittle rocks suggested that the power-law behavior of earthquakes comes from fracture heterogeneities, with a low heterogeneity leading to a low b-value (Mogi, 1967). This idea is supported by measurements of fracture length in the Earth's crust at a wide range of scales, suggesting that fracture sizes are power-law distributed (Bonnet et al., 2001).

Moreover, factors that contribute to decrease hillslope stability include high pore pressure and high slope (section 2.1.3.2). Pelletier et al. (1997) observed a power law distribution of moisture patch sizes in the landscape, and Frattini and Crosta (2013) showed a fractal distribution of high slope patches in mountainous area. Both linked this low strength heterogeneity to the power-law behavior of landslides. Katz and Aharonov (2006) applied vibrations in a sandbox in different directions. Vertical accelerations led to fractures of different scales, and a power-law distribution of landslide sizes. Horizontal accelerations did not induce fractures and led to a characteristic size of landslides, linked to the sandbox size. They concluded that the formation of low strength heterogeneity was fundamental to induce rupture events with a power-law distribution.

Thus, observations and laboratory experiments support the link between material heterogeneity and the size distribution of rupture events at the landscape and at crustal scale. However, the observations that the

Gutenberg-Richter law is applicable on a single fault led to the suggestion that b-value is controlled by the dynamics of interacting rupture (Burridge and Knopoff, 1967). The purely geometric explanation seems to be actually a chicken-and-egg problem, because fractures grow with the propagation of rupture events.

#### 2.3.2.3 Dynamic origin of b-value

The b-value has been shown to be higher for normal faults than for reverse and strike-slip faults (Schorlemmer et al., 2005), and decreases with depth (Scholz, 2015). This suggests a link between b-value and differential stress, because stress is higher at depth (Scholz, 2015), and thrust faults tend to be under higher stress than normal faults (Schorlemmer et al., 2005). Such a b-value stress dependency have been investigated in the lab with acoustic emission experiments. Early work showed that for rocks samples compressed in the laboratory, the b-value decreases when the applied differential stress increases (Scholz, 1968). Lab experiments also showed that the b-value increases with fault roughness and decreasing stress localization (Goebel et al., 2017). Those experimental and natural observations have been reconciled in the general idea that there is a link between stress increase, strain localization, apparent or real b-value decrease, and the approach of a macro-failure event (Scholz, 1968, Locknet and Byerlee, 1995, Amitrano, 2012). This can explain the observation that b-value decreases in the years preceding a large earthquake (e.g., Imoto, 1991, Smith, 1981, Nuannin et al., 2005).

The fact that increase in differential stress leads to b-value decrease is now supported by numerous observations (Scholz, 2015) and laboratory experiments (Johnson et al., 2013, Goebel et al., 2017, Rivière et al., 2018). However, few numerical models have attempted to address this issue. Numerical solutions that simulate brittle failure at a large range of scales in elastic media (Amitrano, 2003, Girard et al., 2010) include very simple damage rules that do not capture earthquake mechanics. On the contrary, because of the current limitation of numerical methods, the use of existing models of the earthquake cycle to produce a wide range of magnitudes that allows statistically robust b-values in a reasonable amount of time is still challenging (Rice, 1993, Hillers et al., 2007, Aochi and Ide, 2004).

Same attempts have been made to link landslide size distribution to rupture mechanics. Stark and Guzzetti (2009) showed analytically that a power law distribution of landslide sizes arises from rupture propagation that behaves as a stochastic process: the probability of large rupture is the product of the probabilities of small ones coalescing to a large failure. Numerical modelling has also suggested that the b-value of landslide sizes increases with increasing rate of temporal weakening (Alvioli et al., 2014, Liucci et al., 2017), or with cohesive strength (Stark and Guzzetti, 2009). This could also suggest a link between increasing stress, decreasing strength, progressive clustering of the damage, and b-value decrease. But despite those observations and experiments, the origin of the power-law behavior of earthquake and landslide sizes and the reasons for temporal and spatial variations in the b-value are globally poorly understood.

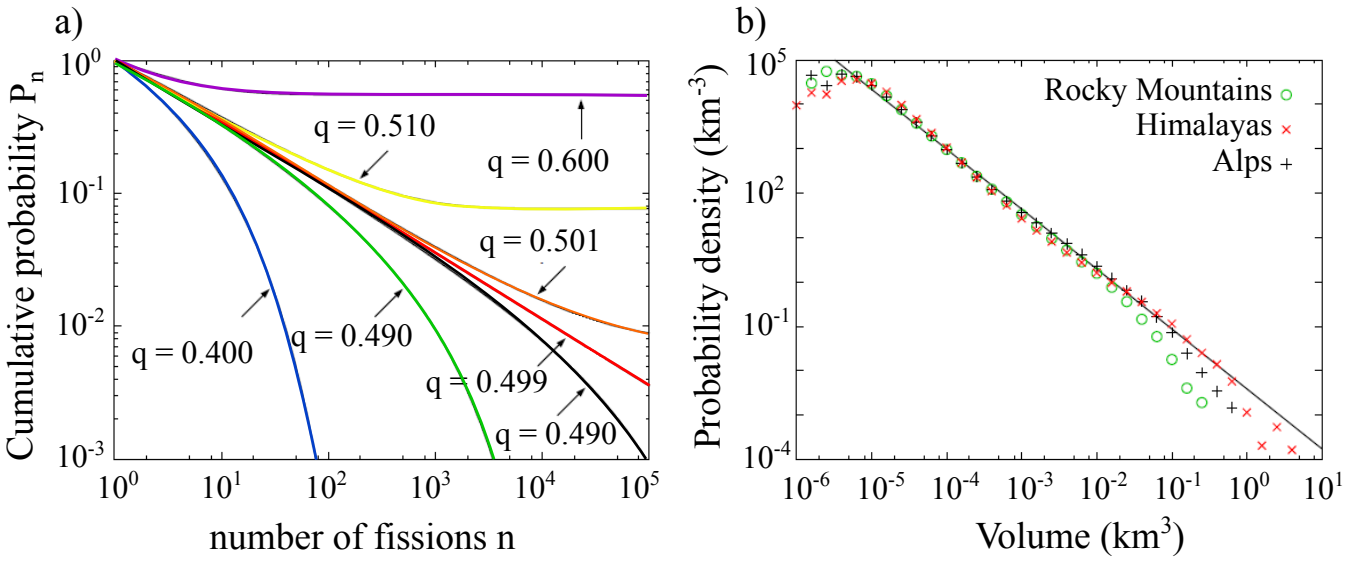


Figure 2.18 – Critical point theory applied to rockfall events. a) Cumulative size distribution of fission events in a nuclear chain reaction for different values of probability q. A power law occurs for the critical point q = 1/2. The colors are chosen to allow comparison with panel b). After (Hergarten, 2003). b) Probability density of rockfall volume predicted by a cellular automaton (Hergarten, 2012). For large events, the distribution diverges from the power-law, and this divergence can be seen as different states of criticality among the three landscapes.

### 2.3.3 Upper and lower limits to rupture size

Observations show that neither earthquake nor landslide catalogues have a power-law distribution over all event sizes. Frequency-magnitude plots display a rollover at small sizes (below a certain size, the probability decreases with decreasing size), and a deviation from power-law at large sizes (probability decreases faster than the power-law). I herein examine the possible explanations for both observations.

One of the possible reasons for rollover at small event sizes is the undersampling of small rupture events in the inventory. For example, the size of the smallest mapped landslide is set by the resolution of the original data sources (Stark and Hovius, 2001). Moreover, the life span of landslides in the landscape increases with their size; small landslides are removed quickly by erosional processes, or obscured by vegetation growth (Guzzetti et al., 2002). Earthquake catalogues also are complete above a completeness magnitude $M_c$, set by instrumental detection (Rydelek and Sacks, 1989). Several earthquake catalogues follow a power-law scaling for negative magnitudes (Reyes et al., 1975), and it is getting clearer that below $M_c$, a fraction of events is missed only due the limit of detection of the seismic network (Wiemer and Wyss, 2000, Woessner and Wiemer, 2005).

With the increasing resolution and quality of available landslide data sources, it is getting clearer that, contrary to earthquake catalogues, rollover is an intrinsic feature of landslide size distributions. We can rewrite the expression of the factor of safety (equation 2.24) in a way that isolates the cohesion-to-thickness ratio (we consider for simplification that shallow landslides do not involve the saturated zone of soil) :

$$f^* = \frac{\frac{C}{\rho_b \ g \ z \ cos(\alpha)} + tan(\Phi)cos(\alpha)}{sin(\alpha)} \tag{2.39}$$

From this expression we easily see that when landslide thickness decreases, cohesive force increases and controls hillslope stability at small depths. Thus, there must be a critical area and/or depth for landsliding, below which a landslide becomes too small to overcome the cohesive forces resisting sliding (Milledge et al.,

2014). A common outcome of several landslide numerical models is the emergence of the rollover due to the contribution of cohesion to hillslope instability (Stark and Guzzetti, 2009, Frattini and Crosta, 2013).

It is also often observed that the PDF of landslide or earthquake size displays a cut-off in power-law scaling which can be modelled by a Pareto distribution (figure 2.15). The more intuitive explanation for this is that each catalogue has an upper limit, which is the theoretical maximum rupture size. The idea that landslides cannot be larger than the hillslope seems intuitive; earthquake magnitude is limited by the size of the biggest fault. However, Geist and Parsons (2014) have shown that the size distribution of earthquakes has a lower limit than the one predicted from the system size, because the size of catalogues of rupture events is finite, and limited by the rate allowed by the triggering events. Therefore, the cut-off at large sizes can also result from the undersampling of the theoretical distribution.

***Outstanding issues***

- What controls the landslide size distribution ? Is it rupture propagation, system heterogeneity, or some other factors ?

- What are the differences between earthquake and landslide rupture mechanisms that could explain the absence of rollover for earthquakes ?

- What controls the probability of large landslides ? Is the probability of such destructive events predictable ?

This overview of earthquakes and landslide mechanics, interactions, and size distribution raises several outstanding issues that I will try to answer in the following chapters.

My thesis research is part of the ANR project EROQUAKE (2014-2019) that aims to investigate the relationships between tectonics and surface processes at short time scales. The project focuses particularly on the possible link between extreme climatological and landsliding events and earthquakes. My work was supervised by Philippe Steer (Géosciences Rennes), Dimitri Lague (Géosciences Rennes) and Nadaya Cubas (ISTEP, Paris VI). I also had the opportunity to work with Philippe Davy (Géosciences Rennes) and Harsha Bhat (ENS Paris). This manuscript is build around three publications resulting from this work. I also collaborated on two other publications, that are included in the appendix of this manuscript.

In **chapter 3**, I will present a simple, 1D numerical model that I have developed, taking into account the variability of landslide depth and rupture angle. I will use this model to understand the role of cohesion, friction, rupture propagation and landscape shape on landslide size distribution. The main outcome of this model is the role of cohesion in controlling the size distribution of small landslides, and the fundamental role of hillslope geometry in controlling the size distribution of large landslides.

This work resulted in a publication, **Jeandet et al. (2019)**, accepted to Geophysical Research Letters. The idea at the basis of this work emerged from discussion with the three co-authors. I have led the writing of this article, that have benefited from advice and rereading from Philippe Steer, Dimitri Lague and Philippe Davy.

In **chapter 4**, I look into the data to focus on the role of finite hillslope geometry in setting landslide size distribution. I take advantage of existing complete landslide inventories to show that the height of unstable hillslope controls the size distribution of landslides, and in particular the probability of large events. I show that this unstable height, which is exponentially distributed, leaves signatures in landslide inventories.

The manuscript ***Impact of finite hillslope geometry on large landslide probability*** by **Louise Jeandet**[1], Philippe Steer[1], Dimitri Lague[1] and Philippe Davy[1] will be submitted during 2019. I have led the writing of this article, that have benefited from advice, discussion and rereading from the other authors.

In **chapter 5**, I use a numerical model of the earthquake cycle to explore the response of a finite fault to normal stress perturbations due to one large erosional event. I show that the duration and magnitude of such erosional event controls the seismicity response, and that such events are able to increase earthquake rate and the proportion of small earthquakes if the sediments are evacuated in a short enough period time.

I have modified and run the codes and led the writing of the manuscript ***Response of a single fault to transient normal stress change, and implications of the effect of large erosional events on the seismic cycle*** by **Louise Jeandet**[1], Nadaya Cubas[2], Harsha Bhat[3] and Philippe Steer[1], that will be submitted to Journal of Geophysical Research. This article, based on an idea of Philippe Steer, have benefited from discussion with Nadaya Cubas and Harha Bhat who introduced me to the numerical codes used in this study.

Finally, in **chapter 6**, I sum up the main results of this thesis, and I step back to examine some common features of landslides and earthquakes, and discuss the implications of my results for landscape evolution.

At the end of the manuscript, I present as supplementary material two articles I have contributed to, that are currently in revision.

The article *Earthquake statistics changed by typhoon-driven erosion*, by Philippe Steer[1], **Louise Jeandet**[1], Nadaya Cubas[2], Odin Marc[4], Patrick Meunier[3], Martine Simoes[5], Rodolphe Cattin[6], J. Brue H. Shyu[7], Maxime Mouyen[1], Wen-Tzong Liang[8], Thomas Theunissen[9], Shou-Hao Chiang[10] and Niels Hovius[4,5], have been submitted to Nature Geosciences. I helped with the mechanical and statistical interpretation of the earthquake catalog and contributed to the writing of this manuscript.

The article *Modulation of post-seismic sediment evacuation by landslide dynamic connectivity*, by Thomas Croissant[1,11], Philippe Steer[1], Dimitri Lague[1], Philippe Davy[1], **Louise Jeandet**[1] and Robert G. Hilton[11], have been submitted to Geomorphology. I have contributed to the modeling of ground shaking induced by earthquakes, following the development of co-seismic landsliding models that I have calibrated during master's thesis (Jeandet et al., 2016).

[1] *Univ Rennes, CNRS, Géosciences Rennes - UMR 6118, F-35000 Rennes, France*

[2] *Sorbonne Université, CNRS-INSU, Institut des Sciences de la Terre Paris, ISTeP UMR 7193, F-75005 Paris, France.*

[3] *Laboratoire de Géologie, École Normale Supérieure, CNRS-UMR 8538, PSL Research University, Paris 75005, France*

[4] *Helmholtz Center Potsdam, German Research Center for Geosciences (GFZ), 144473 Potsdam*

[5] *Institut de Physique du Globe, Sorbonne Paris Cité, Univ. Paris Diderot, UMR 7154 CNRS, F-75005 Paris, France*

[6] *Géosciences Montpellier, Université Montpellier and CNRS UMR5243, 3490 Montpellier, France*

[7] *Department of Geosciences, National Taiwan University Taipei, Taiwan*

[8] *Institute of Earth Sciences, Academia Sinica, Taipei, Taiwan*

[9] *Institute of Earth Sciences, University of Bergen N-5007 Bergen, Norway*

[10] *Center for Space and Remote Sensing Research, National Central University, Taoyuan City 32001, Taiwan*

[11] *Department of Geography, Durham University, Durham, DH1 3LE, UK*

# Chapter 3

# Modelling landslide size distribution

## 3.1 Overview

The first section of this chapter presents the landsliding model developed during this PhD (Jeandet et al., 2019). I first describe the approach developed to model the distribution of landslide depths and area. Then I validate our model and calibrate the mechanical parameters by applying it to six landslide inventories triggered by typhoons or earthquakes. I finally use this model to investigate the effects of landscape shape on landslide size distribution, using synthetic, idealized topographies.

The second section of this chapter is dedicated to two outcomes of our model. In a first part, I use our modelling results to discuss the effective landscape strength at geomorphological time scales. In a second part, I present a case study at the catchment scale that emphasizes the fundamental importance of landscape shape on the total volume of sediments mobilized by landsliding.

## 3.2 Coulomb mechanics and relief constraints explains landslide size distribution

### 3.2.1 Introduction

In mountainous areas, the numerous landslides triggered by earthquakes or storms, represent a major hazard and contribute significantly to surface erosion (Malamud et al., 2004b, Keefer, 1994). Assessment of the total volume of such landslides is required to quantify the topographic changes in response to large earthquakes or rainfall events (Li et al., 2014, Hovius et al., 2011, Parker et al., 2011, Marc et al., 2016a). The frequency distribution of landslide area is a basic requirement for estimating large-scale landslide erosion using non-linear empirical relationships between landslide area and volume (Larsen et al., 2010). This distribution, generally characterized by a negative power-law for landslide areas larger than a given threshold, and a rollover for smaller landslides (Malamud and Turcotte, 1999, Stark and Hovius, 2001, Korup, 2005a, Guzzetti et al., 2002), is considered a universal property of natural systems regardless of the geological setting or triggering mechanism (Malamud et al., 2004a). However, the origin of the power-law behavior for large bedrock landslides and what controls variations in the inferred power-law exponent, ranging from -1.42 to -3.36 (Van Den Eeckhaut et al., 2007), remain unclear. Several studies suggested that mechanical heterogeneities, such as the size distribution of moisture patches (Pelletier et al., 1997) or fractures (Katz and Aharonov, 2006), control the frequency distribution of landslide size and its power-law exponent. However, previous numerical studies (Stark and Guzzetti, 2009)) reproduced the power law distribution of landslide sizes using homogeneous materials. (Stark and Guzzetti, 2009) shown that landslide size power-law scaling is an emerging feature of a simple mechanical model where landslide rupture and propagation behave as stochastic survival processes. However, in order to reproduce the observed Probability Density Function (PDF) of landslide areas, they needed to incorporate significant variations in both the initial rupture depth and area. Frattini and Crosta (2013) and Liucci et al. (2017) suggested that topography cannot be ignored when modelling landslide size distribution. The fractal distribution of areas of high slope is advocated to control the power-law scaling of landslide area (Frattini and Crosta, 2013). Cellular automaton models applying a stability criterion to natural topographies (Alvioli et al., 2014, Liucci et al., 2017) managed to reproduce realistic landslide size statistics, implying topography has an important role in controlling landslide size. However, as sliding only occurs at soil-rock transition in these cellular automaton models, they are only appropriate to simulate shallow landsliding and not for deep-seated landslides that require to account for the influence of the whole hillslope shape in the distribution of landslide size. Thus, it remains unclear how rock mechanics and landscape geometry influence the overall distribution of bedrock landslide sizes. In this paper, we focus on the distribution of the whole range of potential rupture depths for a given landscape. Our goals are to 1) define a simplistic yet robust 1D mechanical model of landslide rupture accounting for the influence of hillslope geometry and reproducing the size distribution of natural landslides and, 2) use this new model to determine the respective contributions of mechanical parameters and landscape geometry in controlling the landslide size distribution in various mountainous areas.

### 3.2.2 Methods

We developed a simple 1D probabilistic method to infer distributions of landslide depths in a given Digital Elevation Model (DEM), and then upscale the results to area distribution via a scaling argument. In the following, we assume rocks and soil behave as Mohr-Coulomb materials and consider that failure occurs only if the shear strength acting on potential rupture surfaces exceeds the resisting shear strength of the material, set by the frictional angle $\Phi$ and cohesion C. This static formalism is often used as its rapid computation time allows us to generate substantial landslide inventories (Stark and Guzzetti, 2009). The novelty in our approach results from combining a local stability mechanical criterion with topographic constraints. The underlying idea is that every plane is a potential landslide rupture plane regardless of the plane's depth and the corresponding dip angle, given the following conditions: 1) the plane is locally unstable under Mohr-Coulomb

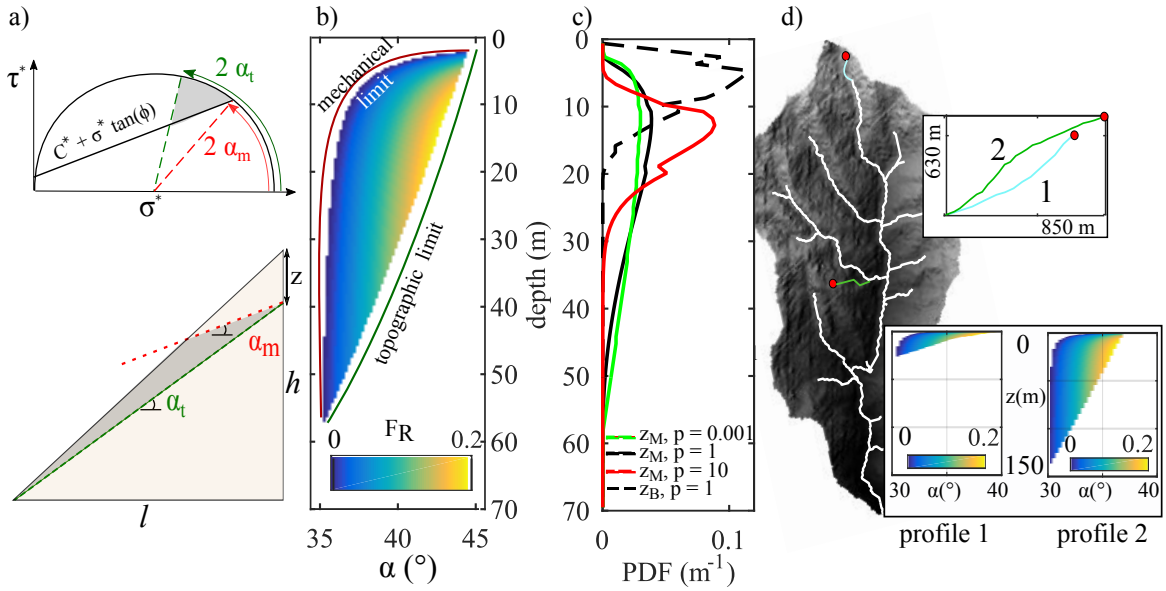


Figure 3.1 – Modelling approach used in this study. a) Mohr circle (top) and schematic hillslope of length l and height h (bottom) showing the range of potential rupture planes (in grey) at a certain depth z. $\tau^\star$ and $\sigma^\star$ are shear and normal stress, normalized by $\sigma_1$. $\alpha_m$ is the minimum rupture angle with $F_R > 0$ and $\alpha_t$ is the maximum rupture angle merging from the topography. b) Rupture factor as a function of rupture angle $\alpha$ and depth for an idealized $50^o$ slope of 500 m height (C = 5 kPa and $\phi = 30^o$). c) PDF of rupture depths computed from b). For p = 1, two ways of calculating z are represented: vertical maximum depth, and orthogonal to the surface mean depths ($\bar{z_B}$). d) Examples of sampling a DEM, showing two points (red dots) and the corresponding extracted profiles. The insets show the corresponding unstable zones.

laws (mechanical criterion) and, 2) the plane intersects the topographic surface in the downslope direction of the instability (topographic criterion) (figure 3.1). Previously developed models that integrated landsliding in landscape evolution models (Densmore et al., 1998) used a stability mechanical criterion based on finite slope mechanics and propagated the most unstable failure plane upslope, starting from the hillslope toe (figure 3.6). Because many landslide do not initiate at the hillslope toe, our model integrates all potential failure depths and angles in a landscape, which has not been attempted yet. Landslides triggered by earthquakes follow a complex spatial distribution that depend on many parameters such as Peak Ground Acceleration (PGA) (Meunier et al., 2007), slope pattern (Roback et al., 2017), or the distance from the fault (Massey et al., 2018). The objective of our paper is not to develop a predictive approach that would infer landslide spatial distribution, but to develop a simple and robust mechanical framework capable of deciphering the role of topography and mechanics on landslide size distribution. Then, the introduction of triggering parameters is beyond the scope of this study. We now describe the different methodological steps of our landsliding model.

**Mechanical criterion** - We propose that below a certain point (x,y) of the topography, a potential rupture plan $P_l$(x,y,z,$\alpha$), characterized by a local depth z and a dipping angle $\alpha$, is mechanically unstable if locally the driving stress $S_d$(z,$\alpha$) exceeds the failure resistance stress $S_r$(z,$\alpha$) (figure 3.1a). This is usually expressed as a factor of safety (e.g., Duncan and Christopher, 2004). Here we define a rupture factor:

$$F_R(\alpha, z) = \frac{S_d(\alpha, z)}{S_r(\alpha, z)} - 1 \tag{3.1}$$

We only consider the largest component of the stress tensor $\sigma_1$, that we assume to be vertical and to depend simply on rock mass $\sigma_1(z) = \rho_r\ g\ z$, with $\rho_r$ the rock density and g the gravitational acceleration. $\tau(\alpha, z)$ and $\sigma_n(\alpha, z)$ are the parallel and normal components of $\sigma_1(z)$ with respect to the failure plane, respectively. The resisting strength to failure is proportional to $\sigma_n$ : $S_r(\alpha, z) = C + tan(\Phi)\ \sigma_n(\alpha, z)$. Assuming that

$S_d(\alpha, z) = \tau(\alpha, z)$ we can write the rupture factor :

$$F_R(\alpha, z) = \frac{sin(\alpha)}{\frac{C}{\rho_r \ g \ z \ cos(\alpha)} + tan(\Phi)cos(\alpha)} - 1 \tag{3.2}$$

Equation 3.2.2 emphasizes the contribution of cohesion to shallow plane stability. At greater depths, the resistance to failure is almost frictional and $F_R$ approaches the rupture factor of a cohesionless material :

$$F_R(\alpha, z) = F_R(\alpha) = \frac{tan(\alpha)}{tan(\Phi)} - 1 \tag{3.3}$$

Previous stability analyses included a depth-dependent cohesion profile (Milledge et al., 2014, Frattini and Crosta, 2013) or fluid pressure (Stark and Guzzetti, 2009, Alvioli et al., 2014). Those alternate formulations imply a pre-existing soil/rock boundary or an unsaturated/saturated transition. We choose not to introduce depth-dependent complexity in the model to isolate the contribution of hillslope geometry, friction and cohesion in the distribution of potential rupture depths.

***Topographic criterion*** - For each sampled point (x,y), we extract the downslope hydrological profile to the river using a steepest slope algorithm (Schwanghart and Scherler, 2014) and we define a topographic rupture factor $T_R$(x, y, z, $\alpha$):

- $T_R$(x, y, z, $\alpha$) = 1 if the plane($\alpha$,z) intersects the topography
- $T_R$(x, y, z, $\alpha$) = 0 otherwise

The geometry of rupture is an open question in landscape-scale landslide modelling (Gallen et al., 2015) and observations show it depends on many factors such as the geometry of pre-existing fractures (Lee et al., 2002, Sitar et al., 2005). Here we take in account any unstable plane if its local tangent delights above the river. We assume planar failure to compute the geometric criteria, because it provides the simplest shape and so does not require additional parameters. As the probability of intersecting with the topography decreases with depth (figure 3.1a and 3.7), this criterion reduces the probability of deep rupture planes. Without this constraint, the planes that are deep enough so cohesion do not control their stability factor would have the same rupture probability (equation 3).

***Rupture probability*** - To test the model sensitivity to the distance to failure, we introduce a parameter p. Relative to $F_R$, the rupture probability can be independent (p = 0), linearly dependent (p = 1), or non-linearly dependent (p > 1). We thus define the chance of rupture $P_R$(x, y, z, $\alpha$) by

$$P_R(x,\ y,\ z,\ \alpha) = max(F_R, 0)^p \ \times T_R(x,\ y,\ z,\ \alpha) \tag{3.4}$$

We use the word 'chance' instead of 'probability' at this stage because their integral over the unstable domain does not necessarily equal one. The grouping of possible landsliding planes at one location (x,y) can be represented in a Mohr Circle using a range of potential rupture angles (figure 3.1a) for a given depth z. This defines an 'angle-depth' unstable domain (figure 3.1b) where the right and left boundary are set by the topographic slope angle and the mechanical parameters (frictional angle and cohesion), respectively.

***Landscape-scale PDF of unstable depths***

Local chances of rupture are computed for $n_{sample}$ = 10000 points randomly sampled in the same DEM. We integrate the chances of rupture to obtain the total chances of ruptures for the DEM:

$$P_{R,DEM}(\alpha, z) = \int_x \int_y P_R(x, y, z, \alpha)\ dxdy \tag{3.5}$$

We finally compute the PDF of unstable depths by integrating over all possible angles and normalizing :

$$PDF(z) = \frac{\int_0^{\pi/2} P_{R,DEM}(\alpha, z)\ d\alpha}{\int_{z_{min}}^{z_{max}} \int_0^{\pi/2} P_{R,DEM}(\alpha, z) d\alpha\ dz} \tag{3.6}$$

***Correction from oversampling*** - Equation 6 does not provide the number of landslides but the number of points potentially included in landslides. Since large landslides include several points in the same slope failure, we systematically overestimate the number of large landslides compared to smaller landslides. We demonstrate in the supplementary material (S1) that using the empirical relationship between landslide depth and area $z = \alpha A^{\gamma}$ (Larsen et al., 2010), with $\gamma$ an exponent varying between 0.3 and 0.6, we can deduce the PDF of landslides depth from the PDF of triggered points by dividing the latter by $z^{1/\gamma}$ . We also demonstrate that applied to a theoretical, straight hillslope, this normalization introduces a power-law scaling $PDF(z) \propto z^{-\gamma}$ in the landslide depth PDF.

***Landslide area PDF*** - Since measured natural landslide inventories are compiled as a distribution of landslide area and not depth, we use the scaling between depth and area to convert the modelled PDF of unstable depths to a PDF of landslide area, resulting in a scaling $PDF(A) \sim A^{\gamma-2}$ (supplementary material S2). Interestingly, this predicts that the power-law exponent on the PDF(A) without any geometric constraint and cohesion effect should vary between -1.7 to -1.4,. This is consistent with the most heavy tailed distribution of landslides observed in nature, but predicts a probability of large landslides compared to intermediate one much larger than typically observed pdf with exponents down to -3 (Van Den Eeckhaut et al., 2007).

***Model parameters*** - We moved this paragraph to the methods section for clarity. Among the model parameters ($\rho_r$, g, C, $\Phi$, p and $\gamma$), the last four are not well constrained. Cohesion is a scale-dependent parameter, spanning several orders of magnitude in natural geosystems (Sutcliffe et al., 2004, Sidle and Ochiai, 2006). Lab experiments define rock frictional angle that ranges from $20^o$ and $45^o$ (Hoek and Brown, 1997). The depth-area coefficient $\gamma$ varies regionally from 0.3 to 0.6 for bedrock landslides (Larsen et al., 2010). Finally, p is an ad-hoc parameter that we introduce to test the effect of the distance from rupture on the PDFs. Varying p from 0.001 to 10, we found the best fit to the data assuming a linear dependency between Fr and the rupture probability (figure 3.10). Consequently, we set p = 1 and run the model with $\Phi$ varying between 10 and $60^o$, C between 5 and 100 kPa, and $\gamma$ between 0.2 and 0.7 (figure 3.3). We ran the model on six DEMs (figure 3.4) corresponding to catalogues of landslides triggered by the 1999 $M_w$ 7.6 Chi-Chi earthquake (Liao and Lee, 2000), the 2004 $M_w$ 6.6 Niigata earthquake (GSI, 2005), the 2008 $M_w$ 7.9 Wenchuan earthquake (Xu et al., 2014), the 2015 $M_w$ 7.8 Gorkha earthquake (Roback et al., 2017), the 1994 $M_w$ 6.7 Northridge earthquake (Harp and Jibson, 1995) and the 2009 Morakot typhoon (Chang et al., 2014, Marc et al., 2018). To optimize the three unknown parameters values (C, $\Phi$ and $\gamma$), we compute the mean absolute distance between the logarithms of modelled and observed PDF of landslide areas, $d_{FIT}$.

### 3.2.3 Results

Figure 3.2a) shows the PDF of landslide area computed by applying the model to the digital elevation model (DEM) of Taiwan (SRTM 30 m), in the area affected by the $M_w$ 7.6 Chi-Chi earthquake (1999). We use C = 18 kPa, $\Phi = 30^o$ and $\gamma = 0.47$, corresponding to best-fitting parameters. To first order, the modelled PDFs reproduce the observed PDF with a rollover behavior for small landslides, a power-law decay for medium and large landslides and cut-off at large area. The correction from oversampling introduces a power-law scaling $PDF(A) \propto A^{\gamma-2}$ (supplementary material S2) that holds for medium landslides ($5.10^3$ - $10^5$ $m^2$). The distribution deviates from this scaling over several orders of magnitude ($10^5$-$10^7$ $m^2$). Figure 3.2b), c) and d) shows the impact of mechanical parameters on the modelled PDF. Cohesion is necessary for the emergence of a rollover (figure 3.7), as it increases shallow plane stability (equation 2). Increasing cohesion shifts the

location of the rollover toward larger area or depth values (Figure 3.2b). For a constant frictional angle of $30^o$, cohesion between 15-20 kPa is required to match the observed rollover positions ranging from 100 to 1000 $m^2$ (Malamud et al., 2004a). Increasing the frictional angle decreases the probability of large landslides (Figure 3.2c). Decreasing $\gamma$ produces larger landslides and shifts the rollover toward larger values (Figure 3.2d).

Having determined the role of mechanical parameters on the shape of the PDFs of landslide size for selected topographies, we now explore the influence of geometric, hillslope-scale parameters: the slope S, the length L and the concavity. We run the model on a series of uniform triangular prisms (figure 3.8), the simplest shape which allows us to explore the role relative importance of these three parameters. We set C = 10 kPa and $\Phi = 35^o$, corresponding to typical mechanical parameters. First, we set a constant slope of $45^o$ (Figure 3.2e) and vary L. The modelled distribution follows a classical PDF of landslide area. Increasing the hillslope size (length, and so height) extends the maximum depth of the modelled landslides and the tail of the modelled PDF has higher probability for larger landslide areas. Second, we set L to 960 meters and vary S (Figure 3.2f). An increase in the hillslope gradient (and so height) results in a shift of rollover values towards lower values and the tail of the modelled PDF implies higher probabilities for larger landslide areas. The range of modelled landslide areas reduces when reducing S. We also run the model with different slope geometry configurations (concave, convex, and straight in Figure 3.2g). The addition of concavity or convexity to the slope cause the rollover shifting towards lower landslide depth or area values. Convex and concave slope geometries respectively generate greater and smaller probabilities of large landslides. This shows the necessity of applying the model to real topographies in order to find accurate mechanical parameters.

Figure 3.3a) shows $d_{FIT}$ in the case of Chi-Chi earthquake as a function of cohesion and friction for $\gamma$ =

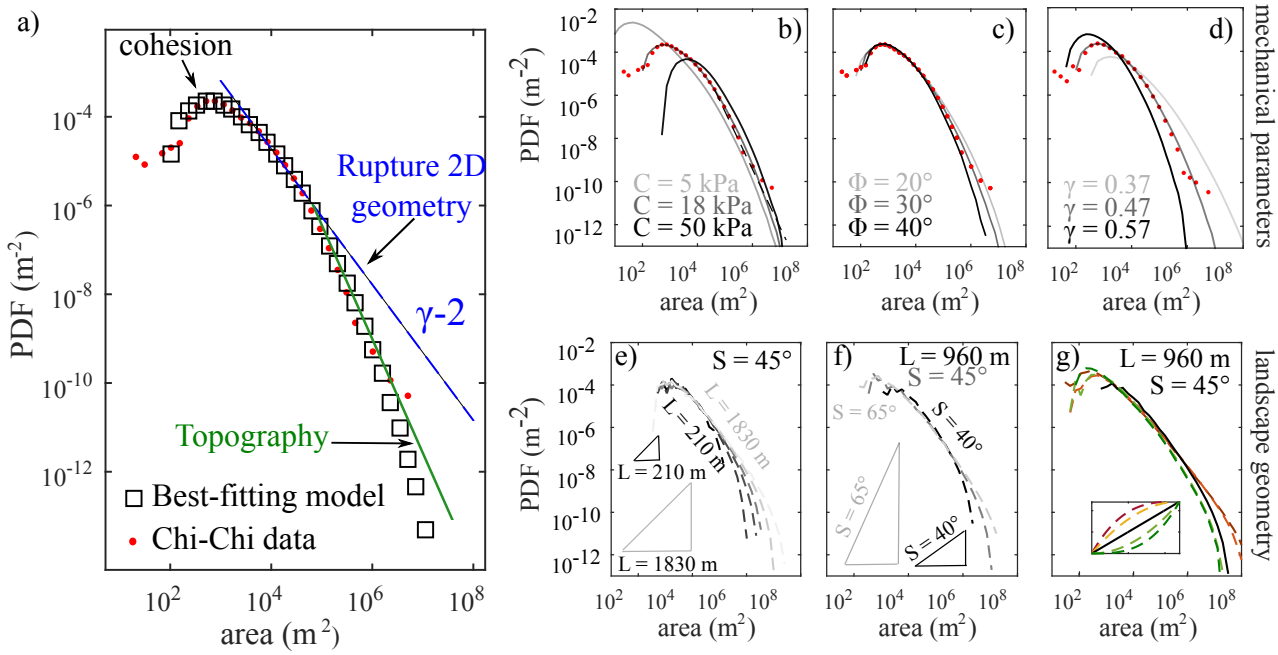


Figure 3.2 – a) Observed (red dots) and modelled (dark squares) PDF of landslide areas from Taiwan DEM with C = 18 kPa, $\Phi = 30^o$ and $\gamma = 0.47$. Blue line shows the theoretical slope of the PDF arising from 2D landslide geometry and green line shows the slope of the part of the PDF mostly controlled by landscape shape. Panels b), c) and d) show the influence of changing the cohesion, the friction angle or the landslide area-depth scaling exponent $\gamma$, respectively, with the values used in panel a) for the two constant parameters. e), f) and g) show the PDF of landslide area computed on synthetic triangular prisms with a slope of $45^o$ and various height (e), unique length of 960 meters and various slopes (f) or the same height and length but with different concavities (g). C = 10 kPa, $\Phi = 35^o$ and $\gamma = 0.42$.

0.47 (the best-fitting $\gamma$ value). Setting $d_{FIT} \leq 0.2$ as the range of acceptable models, we found the cohesion and the frictional angle to range between 15-21 kPa and $22^o$-$34^o$, respectively. Figure 3.3b) shows a synthesis of the misfits for the six studied cases. We calculate the range of admissible parameters with $d_{FIT} \leq 0.2$. The narrow range of best fit values for $\gamma$ is striking (between 0.47 for Chi-Chi and 0.56 for Wenchuan). The cohesion range are 3 kPa (Niigata), 7-15 kPa (Northridge), 8-18 kPa (Gorkha), 12-20 kPa (Wenchuan), 15-21 kPa (Chi-Chi), and 22-35 kPa (Morakot). The ranges for the frictional angles for the tested scenarios were sometimes broad: $10^o$ (Niigata), 17-$35^o$ (Northridge), 35-$52^o$ (Gorkha), 29-$41^o$ (Wenchuan), 22-$34^o$ (Chi-Chi), and 10-$25^o$ (Morakot).

### 3.2.4 Discussion and concluding remarks

Our proposed 1D model is capable of generating realistic PDFs of landslide depth and area. We reproduced the rollover for small landslides, the power-law decay for medium and large landslides and an upper bound in power-law scaling for large areas. It is possible to isolate the contribution of the model assumptions to the generated PDF (Figure 3.2a). The rollover at small depth and area arises from the contribution of cohesion to hillslope stability (equation 2). The correction from oversampling we apply to the raw PDF of landslide depths introduces a powerlaw trend that dominates the scaling relationship for medium landslides. This correction, based on the scaling relationship between landslide depth and area (Larsen et al., 2010), is necessary to take in account the fact that a deep landslide is statistically larger than a shallow landslide and has in turn more chances to be sampled because of its 2D extension. The scaling argument, $\gamma$, integrates how rupture propagates in two dimensions. This correction thus captures the physics of lateral rupture propagation that our model does not directly compute. It shows that rupture propagation itself produces the emergence of a power-law behavior, as already suggested (Stark and Guzzetti, 2009). Nevertheless, this effect holds only for a limited range of magnitudes when the model is applied to a real landscape as the shape of sampled hillslopes plays a larger role by controlling the tail of the distribution for medium to large landslides. For larger landslides, the distribution deviates from this power-law scaling toward a distribution that reflects the sampled landscapes geometry. The use of the geometric criterion in our model and the finite size of hillslopes induces a cut-off in the landslide size distribution (figure 3.7). We sum up the contribution of cohesion, scaling argument, and hillslope geometry to the modelled PDF in figure 3.2a.

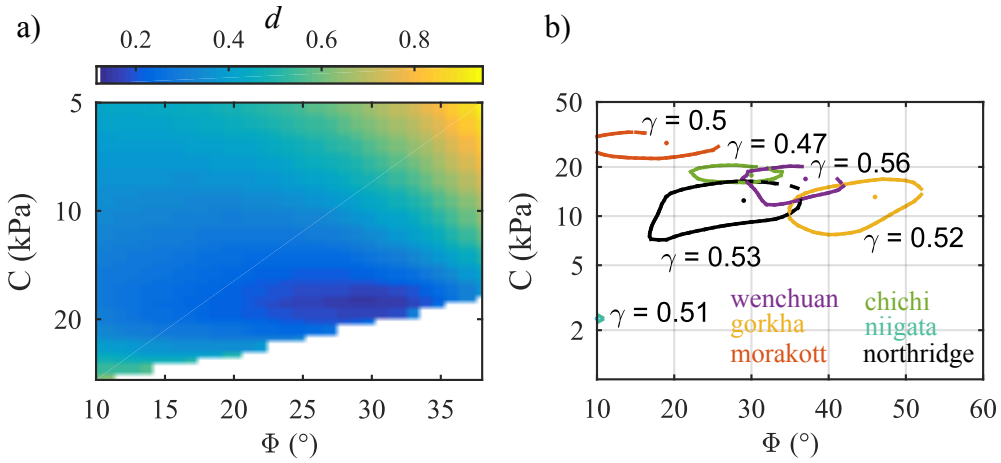


Figure 3.3 – a) Distribution of $d_{FIT}$ for Chi-Chi landslide, as a function of friction and cohesion, ($\gamma = 0.47$). The best fit values are : $\gamma = 0.47$, $\Phi = 30^o$ and C = 18 kPa. b) Best-fit values of cohesion and friction for the six studied cases, for the best-fit $\gamma$ value ($d_{FIT} = 0.2$ contour).

Our model reproduces the first-order sensitivity of rollover location to cohesion (Stark and Guzzetti, 2009, Frattini and Crosta, 2013)). There are other potential explanations for this rollover such as the likely under-sampling of small landslides (Hovius et al., 1997, 2000, Stark and Hovius, 2001) or the existence of potential

cohesion gradients with depth, in particular at the transition between soil and rock (Frattini and Crosta, 2013, Milledge et al., 2014). However, we also reproduce both the rollover and the power-law behavior of the observed PDF of landslide area without using a depth-dependent change in cohesion or friction assumption.

The range of best-fit values of the depth-area scaling exponent $\gamma$, is narrow ($0.47< \gamma <0.56$) compared to the initial specified range (0.2-0.7) and consistent with natural data, (Larsen et al., 2010). Friction and cohesion show strong dependence on $\gamma$, as shown in figure 3.12. Indeed, increasing $\gamma$ has similar effects on the PDF as decreasing cohesion or increasing friction (figure 3.2). This explains why best-fit friction and $\gamma$ are negatively correlated while cohesion and $\gamma$ are positively correlated. For example, changing the $\gamma$ value by 10% would lead to a change of $10^o$ in the inferred friction angle. This trade-off demonstrates the need for a better calibration of $\gamma$ in different regions in order to reproduce the observed distributions.

The range of inferred cohesion, 10 to 35 kPa, is roughly comparable with those previously inferred using other landsliding models applied to landslide inventories (Frattini and Crosta, 2013, Gallen et al., 2015). However, the cohesion values obtained are low and are more consistent with typical values obtained for soils with resisting roots 10-30 kPa (Sidle and Ochiai, 2006), rather than for fractured or weathered bedrock $\sim$ 100 kPa to 1 MPa (Sutcliffe et al., 2004). In contrast, the best-fit frictional angles, 20-45$^o$ (except for Niigata), are in agreement with experimental measurements (Hoek and Brown, 1997). Overall, the cohesion and friction angles we found reflect the fact that we did not explicitly incorporate some static and dynamic processes, such as static fluid pressure, dynamic reduction of friction (Viesca and Rice, 2012), and also pore pressure change or passing seismic waves in the case of landslides triggered by storms or large earthquakes, respectively. Thus, we can interpret the inferred parameters only in terms of effective friction and cohesion related to one triggering event. Nevertheless, using median values found in this study (10-35 kPa for the cohesion and 20-45$^o$ for friction), one could assess first-order prediction of landslide area distribution in a given landscape following an earthquake or storm event with more reliability than using higher, classical cohesion values. Interestingly, different triggering events in the same region can produce landslides with very different rollover position, as the landslides induced by the Chi-Chi earthquake and Toraji typhoon in the Dajia river basin (Huang and Montgomery, 2014). In that case, typhoon-triggered landslides display a rollover shifted toward largest areas, meaning, according to our model, a greater cohesion. Possible explanation would be that pore pressure increase following a typhoon is mechanically equivalent to a reduction in frictional strength, whereas co-seismic peak ground acceleration would be equivalent to a reduction in effective cohesion (Marc et al., 2015). Modelling of more typhoon-induced triggered landslides is required to validate this hypothesis, which is in agreement with the low friction values inverted in this paper from Morakot dataset (figure 3.3).

Our results also illustrate the two major influences (figure 3.2e, f and g) of landscape shape on the PDFs of landslide depth or area. First, the available volume above the friction angle must increase to increase the probability of deeper landslides. This can be achieved in three ways: 1) increasing the hillslope length while keeping a constant slope; 2) increasing the slope while keeping a constant length; and 3) increasing convexity. Second, since cohesion controls the shear strength at shallow depths, mechanical instabilities can only occur for steep planes associated with higher shear stress (figure 3.1). As only the planes less steep than the topographic surface can meet the topographic criterion, steep slopes within the model favors the occurrence of shallow and small landslides. Our results are consistent with the idea that the PDF of landslide area is strongly influenced by the availability of high slope patches and that rheological mechanical properties modulates the power-law exponent (Frattini and Crosta, 2013). We extend this idea by showing that not only the local slopes, but also the entire hillslope slope, height, length and concavity control landslide size distribution, especially for large landslides.

Then, our 1D model, which integrates mechanics and landscape geometry, explains the observed PDFs of landslide areas. It is fully capable of isolating the relative contributions of mechanical processes and landscape geometry to landslide size distribution: at first order, cohesion is fundamental for the emergence of the rollover, 2D rupture propagation leads to a power-law scaling for intermediate landslides, and landscape geometry controls the size distribution of large landslides. To further understand how mechanical processes, especially 2D landslide geometry, controls landslide size distribution, three-dimensional numerical modelling

(e.g., Moon et al., 2017), would be a natural development of this work.

Our results have important geomorphological implications for landslides triggered in landscapes with different geomorphological properties. Interestingly, the PDFs of all landslide areas triggered by Chi-Chi and Morakot are very similar despite different triggering mechanisms (figure 3.5). Both inventories cover a surface area of 10000-20000 $km^2$, without marked differences in terms of topography. However, at the catchment scale, the PDF of landslides triggered by Toraji typhoon and Chi-Chi earthquake displays different tail, with the probability of landslides $> 10^5$ $m^2$ much larger for the typhoon-triggered landslides (Huang and Montgomery, 2014). This could be explained by differences in hillslope geometry, between the lowest part of the basin impacted by the earthquake and the highest and steepest part impacted by the typhoon. Both observations supports the idea that landscape geometry exerts a first-order control on the landslide size distribution. Therefore, the same mechanical triggering acting in different geomorphological settings should induce landslides with different size distribution. In turn, landscape geometry properties is likely to exert a first order control on the volume of material produced by landslides. This could explain the large variability of total landslide volume observed for earthquakes of similar magnitudes (Keefer, 1994, Marc et al., 2016a), and the presence of extremely large paleo-landslides ($> 0.1$ $km^3$) in regions characterized by high relief with long and steep slopes (Korup et al., 2007). Consequently, accounting for landscape shape is essential to improve hazard assessment, particularly in regions characterized by high relief and slope where large landslides may occur with high probability.

## 3.3 Supplementary material

In this section, I first present the six studied datasets. Then I provide supplementary information regarding the method employed and the role of model parameters and assumptions on the final modelled PDF of landslide depth and area. I finally present best-fitting results for each studied case.

### Datasets

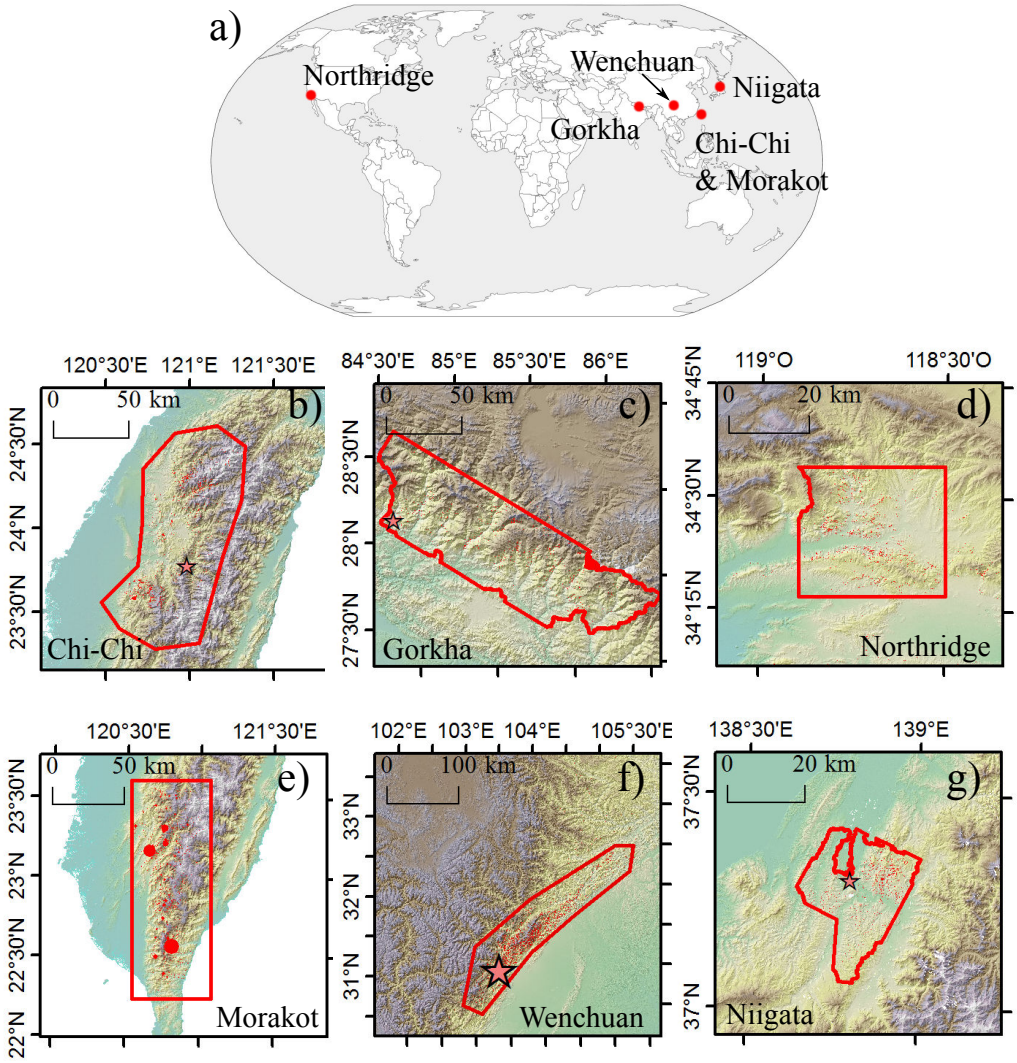


Figure 3.4 – Shaded DEM (SRTM 30) used to model the distribution of landslide areas. Landslides are represented as red polygons, except for Morakot, where the size of the round is proportional to landslide area. The red line shows the area used to sample the hillslope profiles. The red stars show the location of the epicenter of the triggering earthquake.

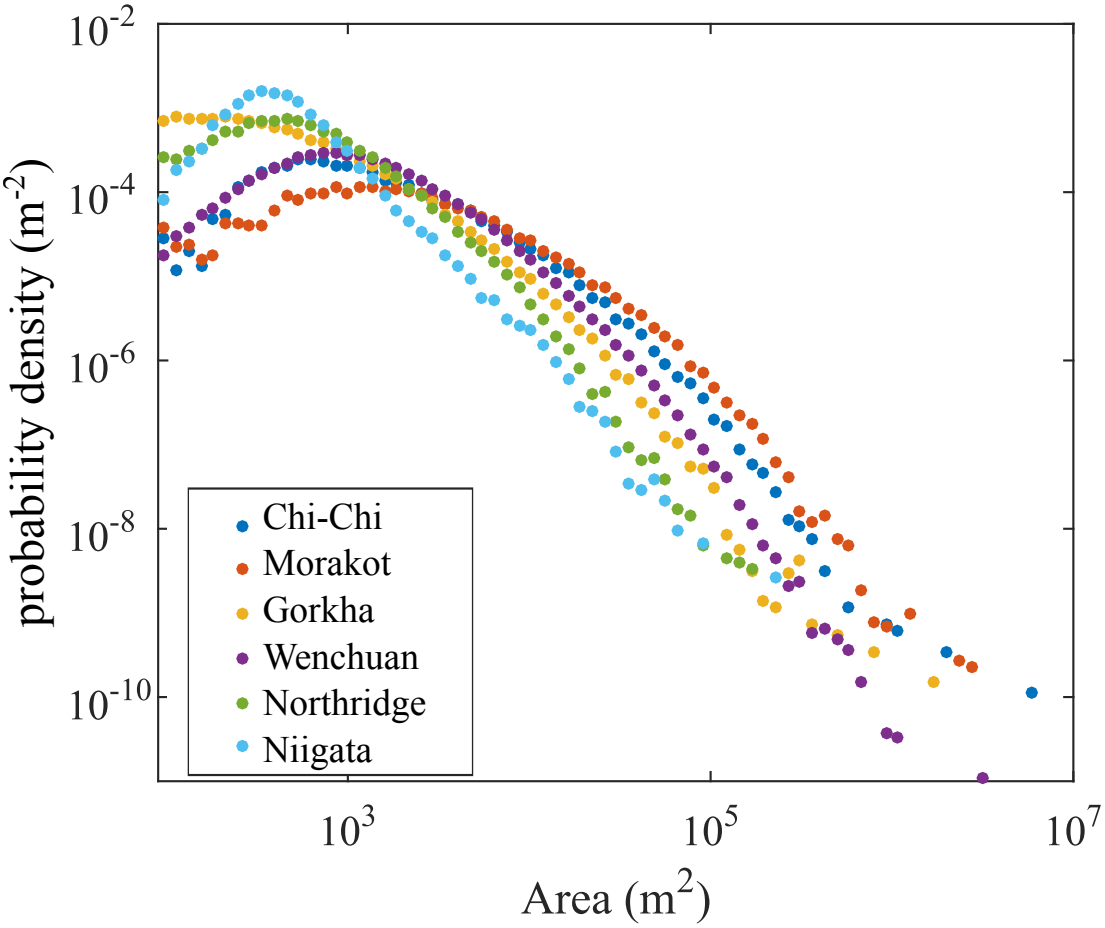


Figure 3.5 – PDFs of the landslide area data used in this study, considered above 90 $m^2$.

### More details on the methods

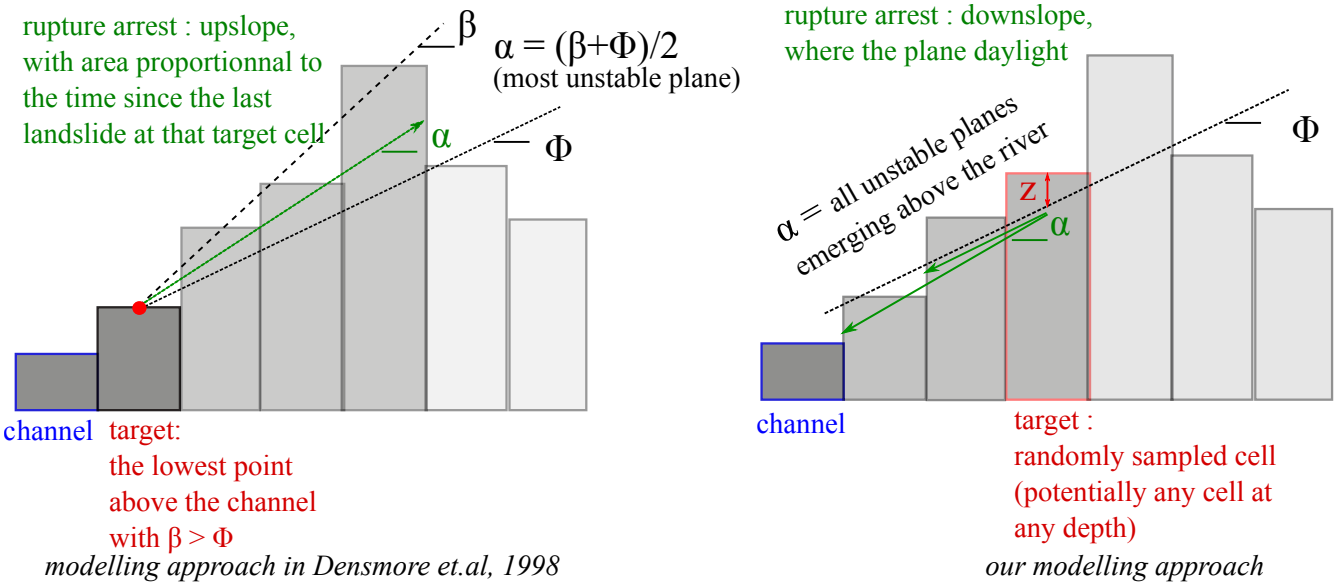


Figure 3.6 – Landslide modelling approach in Densmore et al. (1998) (left panel) and in this study (right panel). We show the target cell and depth (in red), the potential rupture plane (green arrows), the local slope $\beta$ and the friction angle $\Phi$.

We describe here the method used to correct the PDF from oversampling and compute the landslide area PDF

We call $\mathrm{PDF}_P$(z) the PDF given by equation 6 in the main text, i.e the number of points x,y that belong to a landslide of depth z. We are looking for the PDF of landslides having a depth z, $\mathrm{PDF}_G$(z). Because we sample the landscape randomly, the chances to select each point of the DEM are equal. Then, the number of points included in landslides of a certain size is higher than the number of landslides of this size, and increases with the landslide area. Then $\mathrm{PDF}_G$(z) is proportional to $\mathrm{PDF}_P$(z) divided by the area of landslides of thickness z :

$$PDF_G(z) \propto \frac{PDF_P(z)}{A(z)} \tag{3.7}$$

We assume a power-law scaling between depth and area $A(z) = \alpha\ z^{1/\gamma}$ , with $\gamma$ between 0.3 and 0.6 (Larsen et al., 2010). Then we have :

$$PDF_G(z) = C * \frac{PDF_P(z)}{z^{1/\gamma}} \tag{3.8}$$

where C is a rescaling constant used to insure that the integral of $\mathrm{PDF}_G$ is equal to one. Then, in a case of cohesionless material without topographic criteria, (equally probable depths, as shown in figure 3.7), the scaling of the corrected PDF of landslide depths would be $PDF(z) \propto z^{-1/\gamma}$.

We compute the PDF of landslide areas from the relationship :

$$PDF(A)\ dA = PDF(z)\ dz \tag{3.9}$$

From the empirical scaling between A and z (Larsen et al., 2010) we have :

$$PDF(A) \sim PDF(A^\gamma)\ \frac{d(A^\gamma)}{dA} \tag{3.10}$$

If the scaling of the previously computed PDF(z) is $PDF(z) \sim z^{-1/\gamma}$ (S1), we have

$$PDF(A) \sim (A^\gamma)^{-1/\gamma}\ A^{\gamma-1} \tag{3.11}$$

The theoretical scaling of the PDF of landslide areas, if all the depths at all points were equiprobable, would be $PDF(A) \sim A^{\gamma-2}$ (see figure 3.7e).

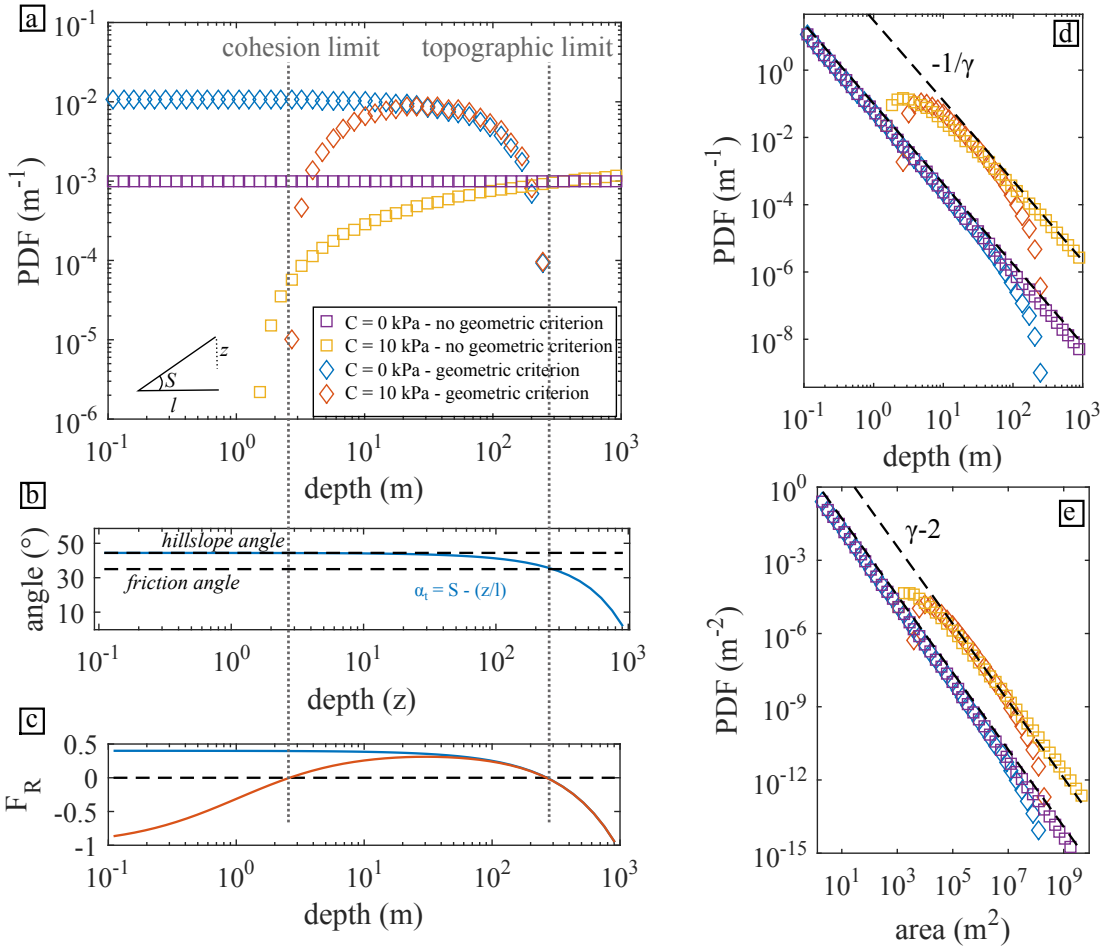


Figure 3.7 – Effect of the basic assumptions of the model on the PDF of landslide depth and area. We use a single hillslope with a downslope profile of length L = 500 meters and a slope S = 45$^o$, $\gamma$ = 0.42 and $\Phi$ = 35$^o$, with either cohesive or cohesionless material and with or without topographic criterion. a) Raw PDF of the maximum unstable depths. b) Maximum rupture angle (topographic limit) as a function of depth (blue line). The dashed lines show the hillslope slope and the friction angle. c) Rupture factor considering the rupture angle shown in panel b) as a function of depth, for either a cohesive (red line) or cohesionless (blue line) material. d) Same as a) but showing the PDF of depths after correction for oversampling. The dotted lines show the expected slope after correcting the PDF from oversampling. e) Same as b) after converting the depth PDF into area PDF. The dotted lines show the expected slope.

**Design of the synthetic landscapes used to infer hillslope length, slope and concavity on landslide size distribution**

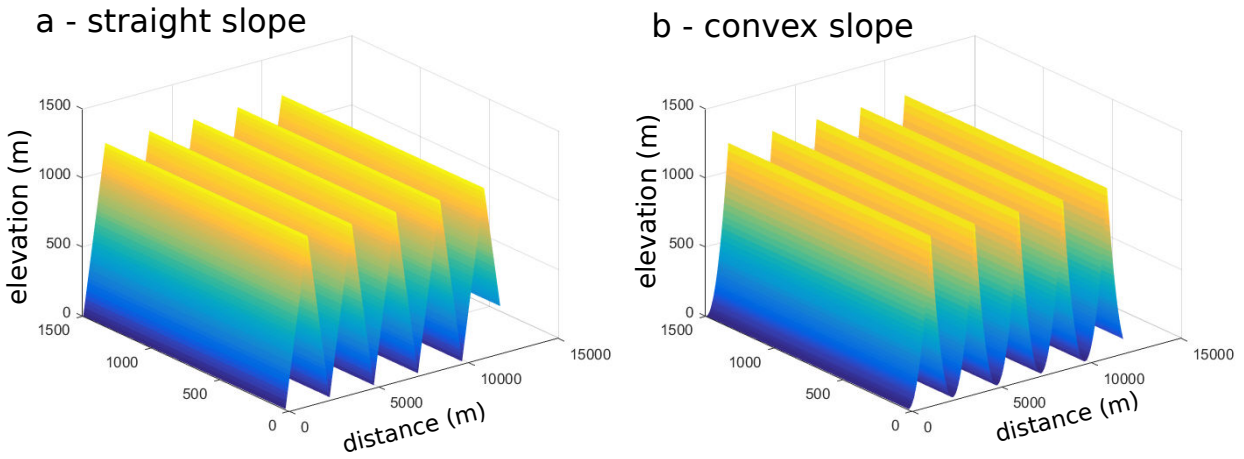


Figure 3.8 – Two synthetic landscapes of L = 1200 m and S = 45$^o$, with a linear shape (a) or concave shape (b).

**Influence of model parameters on the PDFs**

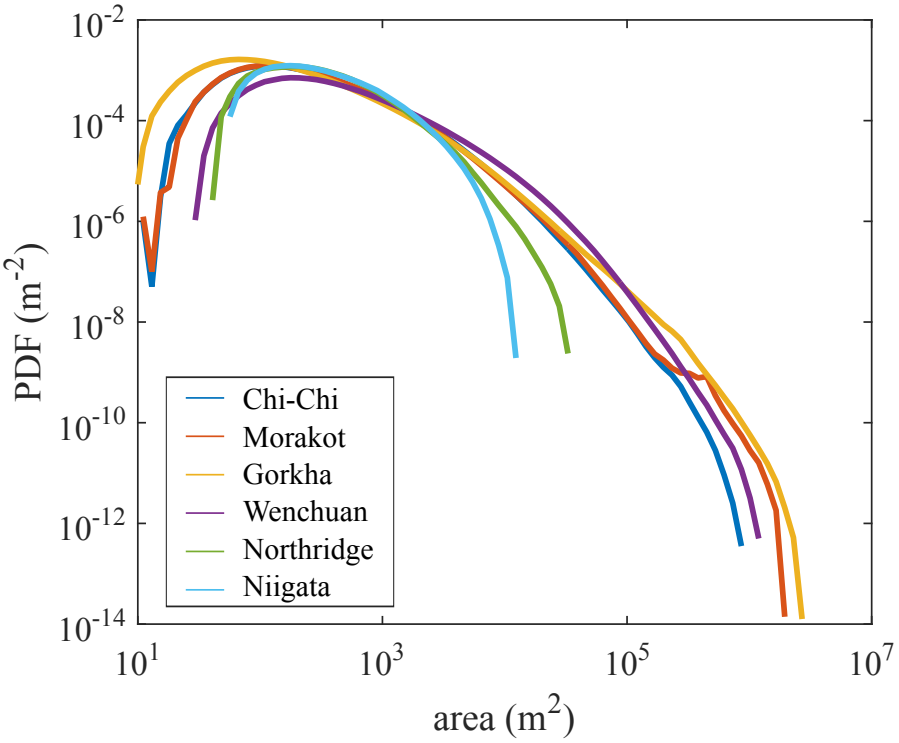


Figure 3.9 – Influence of real landscape shape on landslide size distribution. We show here the PDF modelled on the six DEMs, with constant mechanical parameters (C = 10 kPa, $\Phi = 30^o$, $\gamma = 0.5$).

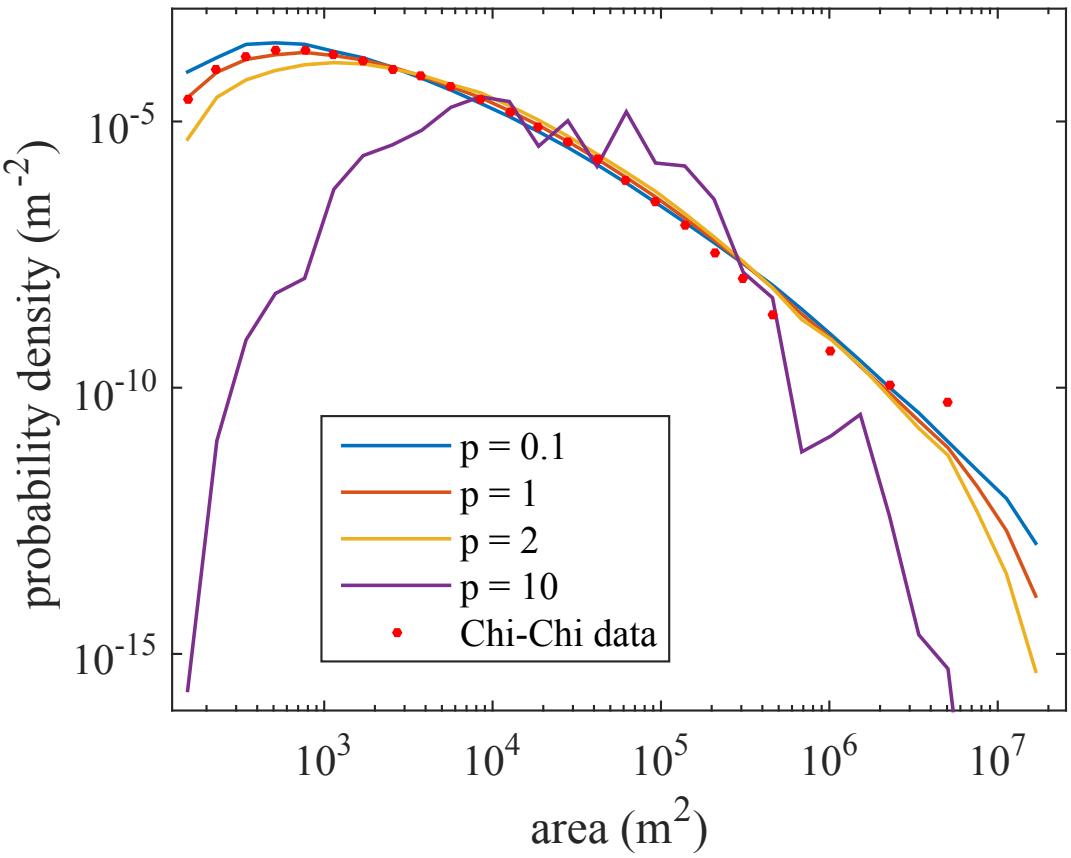


Figure 3.10 – Influence of p on the modelled PDFs from the Taiwan DEM for C = 18 kPa, $\Phi = 30^o$ and $\gamma$ = 0.47. When p increases, the probability of a rupture plane different from the most unstable one tends to zero, and the distribution tends to a characteristic size rather than a power-law.

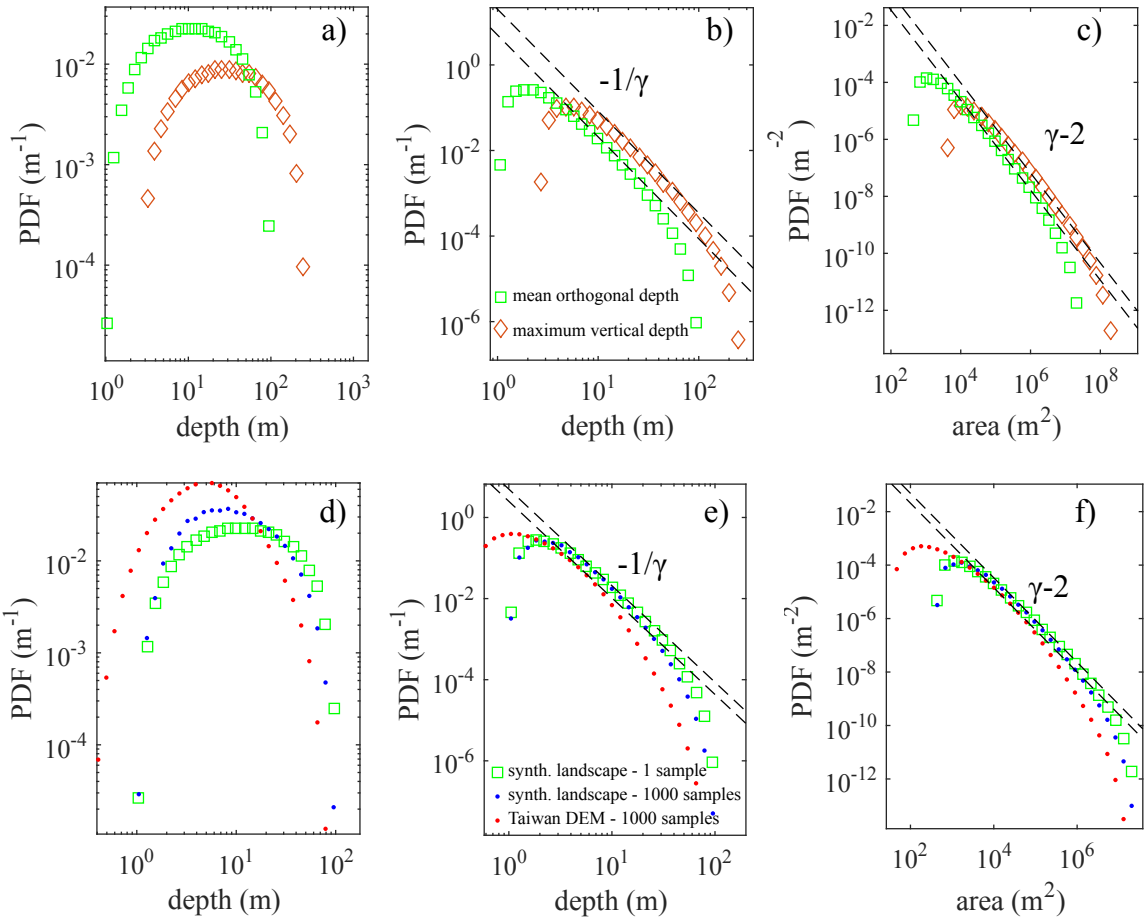


Figure 3.11 – Modelled PDFs of raw landslide depth (a,d), landslide depth corrected from oversampling (b,e) and area (c,f). We either compute landslide depth with one single point on a synthetic, idealised slope such as in figure 3.7 (green squares), 1000 samples within same synthetic landscape (blue dots) and Taiwan DEM (red dots). a, b and c show the influence of the way we calculate the depth. We consider either the vertical depth below the sampled point (brown diamonds) or the mean depth orthogonal to the rupture plane, from the failure point to the point where the rupture plane daylight (green squares). d, e and f show the influence of sampling. Dotted black lines show the theoretical slope of the distribution considering the simplest case in figure 3.7. The number of samples do not strongly change the results, but the sampling of a real landscape introduces a deviation for the theoretical slope at medium depths and areas.

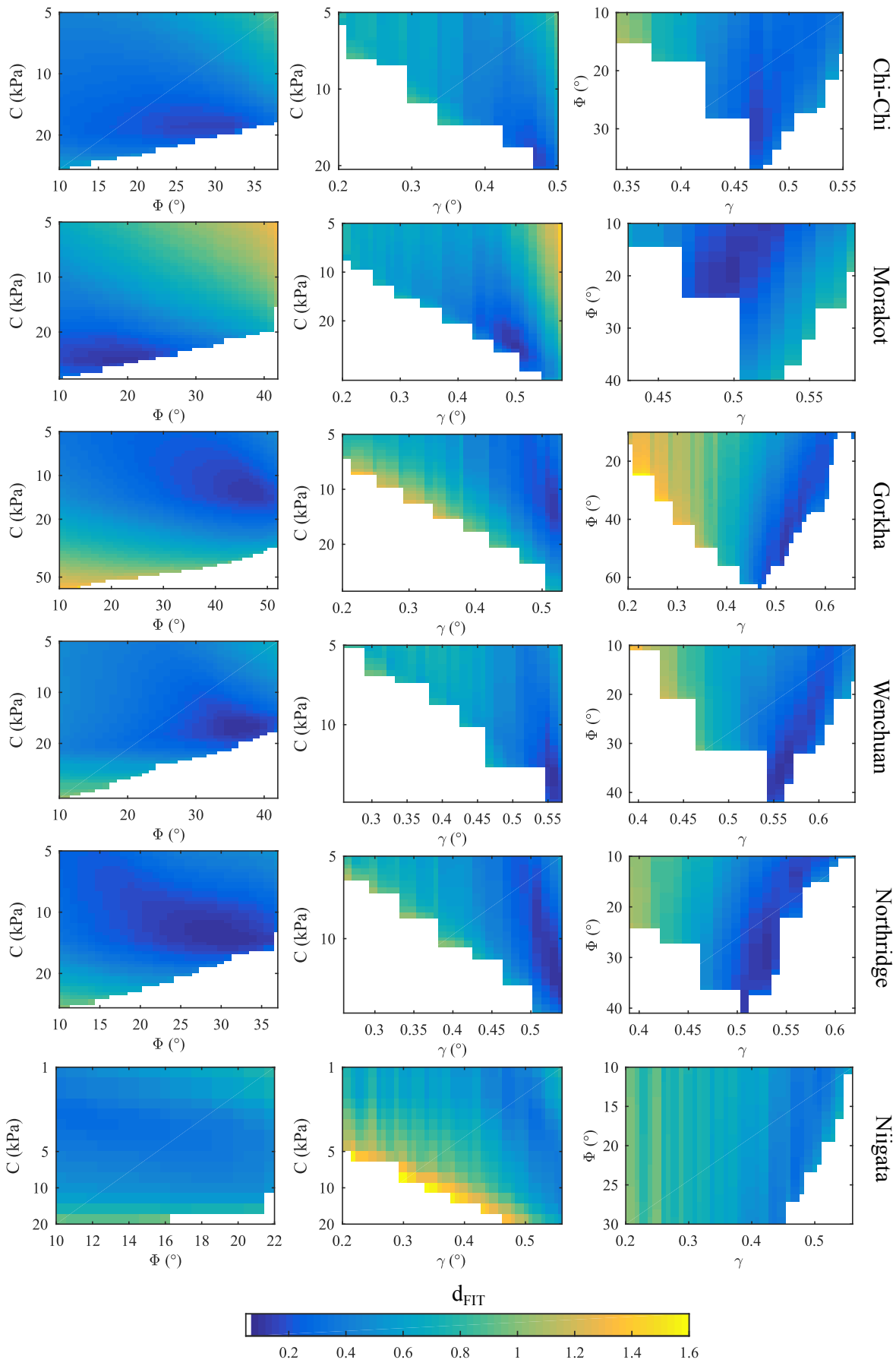


Figure 3.12 – Mean absolute distance distance between the logarithm of modelled and observed PDFs of landslide areas for the best-fitting $\gamma$ (left panels), the best-fitting $\Phi$ (center panels), and the best-fitting cohesion (right panels). We keep only the models covering the whole range of observed landsliding areas.

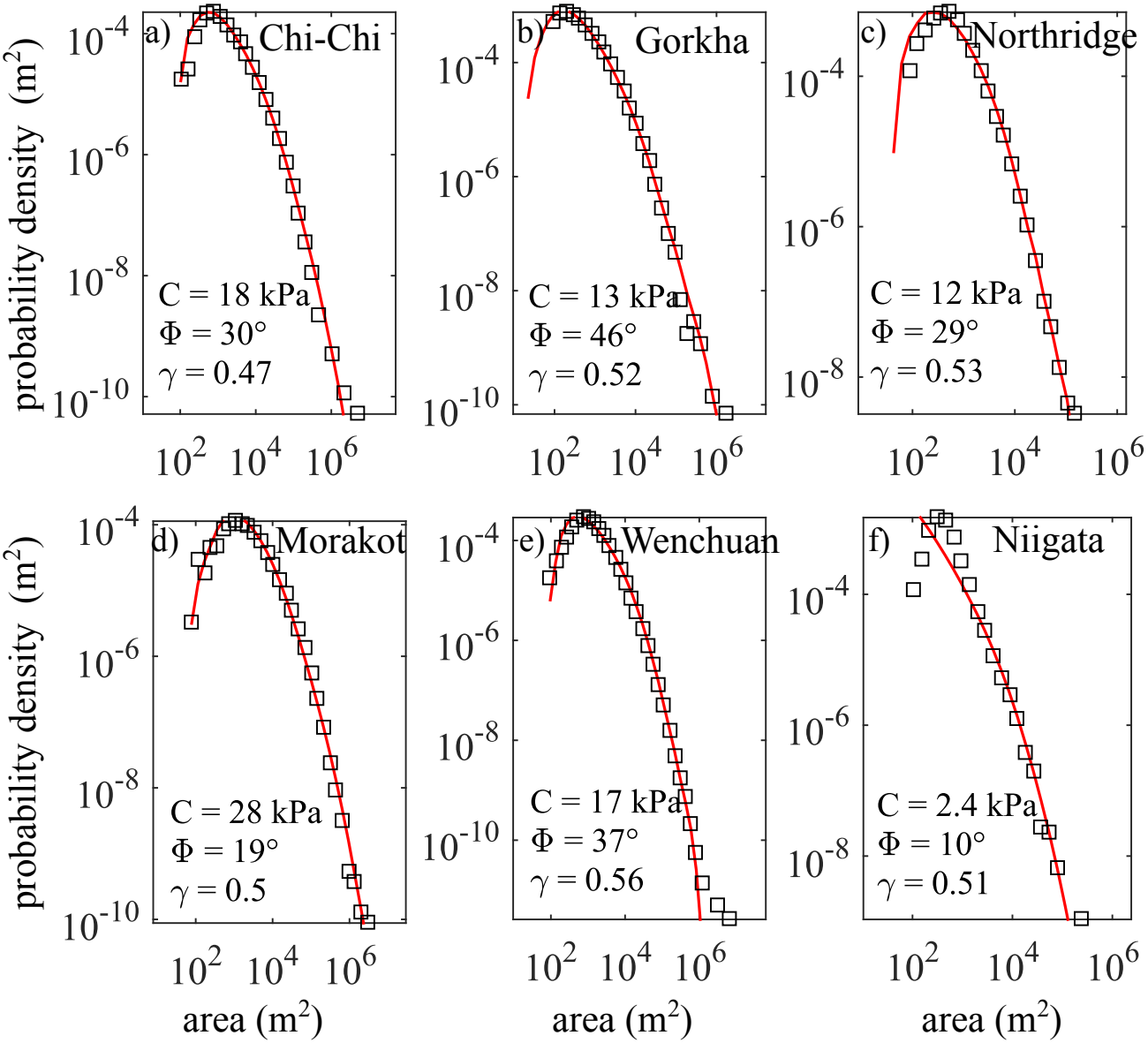


Figure 3.13 – PDF of landslide areas for the best fit model (red line) compared to the PDF of landslide area data (black squares), for the six studied cases.

## 3.4 General discussion

### 3.4.1 What is landscape strength ?

Quantifying near-surface rock strength at a time and spatial scale that is meaningful for landscape evolution remains difficult (Hoek and Brown, 1980a, 1997), and cannot be derived from laboratory sample strength (Gallen et al., 2015). The idea that hillslopes steepen until their mechanical threshold is reached and adjust to tectonic uplift and fluvial erosion through pervasive landsliding is a starting point for numerous landslide modelling studies (Schmidt and Montgomery, 1995, Gallen et al., 2015). This implies the long-term contribution of friction and cohesion to hillslope stability, modulated by time-temporal weakening (Densmore et al., 1998). The role of cohesion in hillslope stability is still debated; the observation that the slope distribution is modal and roughly identical within similar geological settings has mainly supported the concept of hillslopes as defining a repose angle that should reflect the landscape-scale frictional strength (e.g., Burbank et al., 1996, Korup, 2008). However, considering the modal value of slope distribution as an indicator of rock mass strength has been questioned by Anderson et al. (1980).

In this section, we examine what can be learned about landscape strength and its role in landscape shape from our modelling approach, which is based on the idea that every plane in the landscape is a priori unstable.

We compare the best-fitting effective friction angles found from our approach with the landscape slope distribution in the six studied cases (figure 3.14). We compute the DEM slopes using a steepest downward gradient algorithm. The slopes of landsliding hillslopes are taken as the local slope of the sampled unstable points (i.e., the points where at least one rupture plane is unstable).

The range of effective friction is equal to or greater than the modal slope for the Wenchuan, Northridge and Gorkha earthquakes, and is equal to the modal slope for the Chi-Chi earthquake. Because of the geometric assumptions of our model, landslides occur only on hillslopesthat are stepper than the effective friction angle. The fact that landslides are located on slopes higher than the modal slope is a common feature of earthquake-triggered landslide inventories, such as those from the Gorkha (Roback et al. (2017), figure 3.16), Finisterre Mountains, (Meunier et al., 2008), Northridge (Parise and Jibson, 2000), and Wenchuan (Dai et al., 2011)

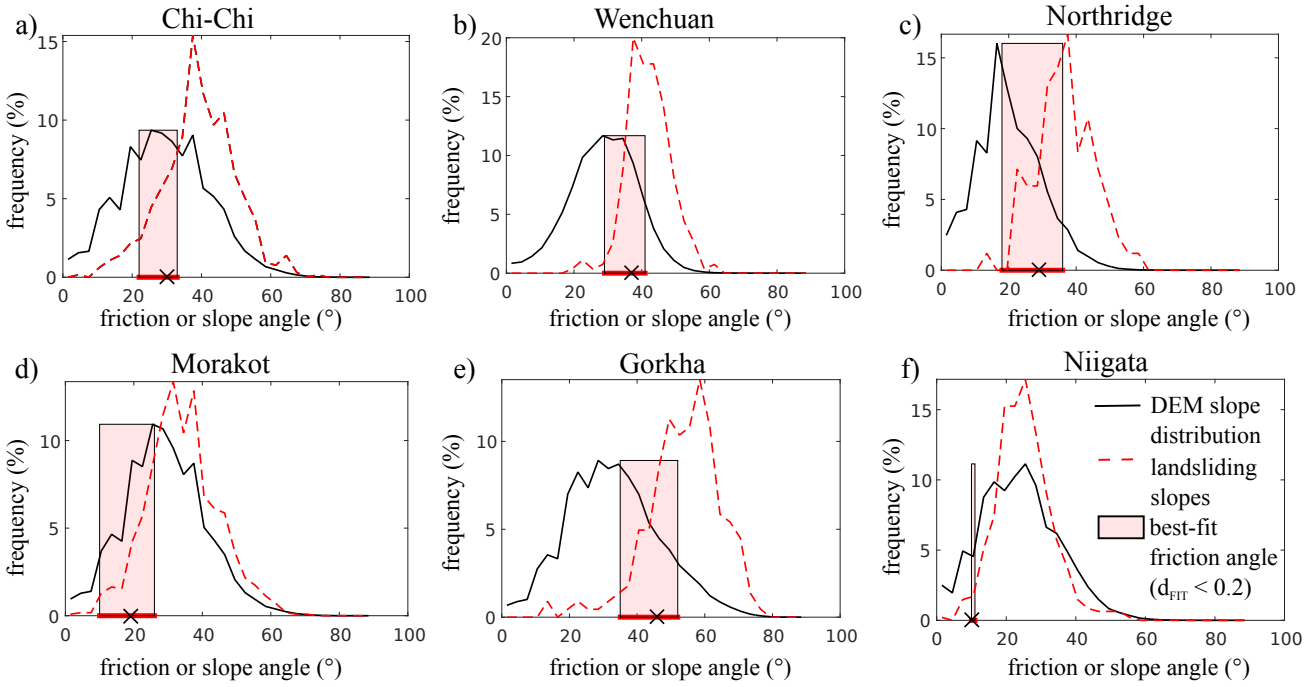


Figure 3.14 – Slope distribution for the six studied DEMs, plotted with the range of inverted best-fit friction angles.

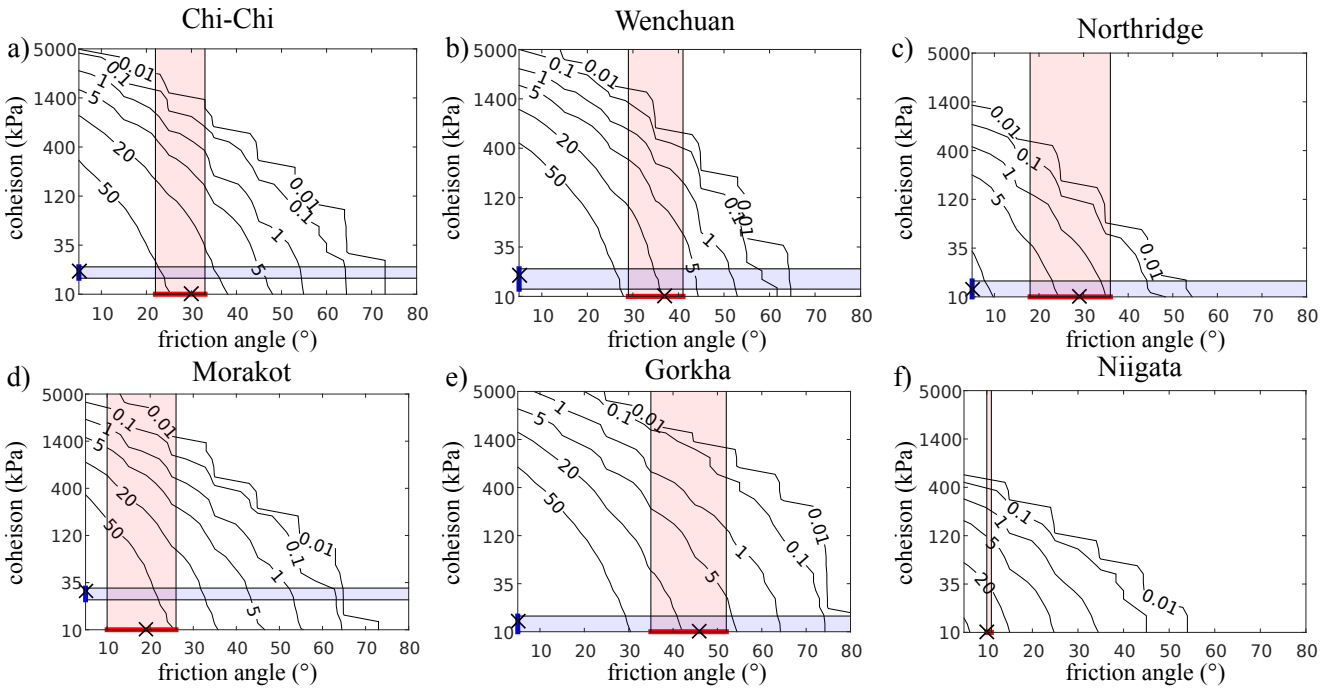


Figure 3.15 – Percentage of unstable points as a function of friction angle and cohesion for the six studied cases, plotted with the range of inverted best-fit friction angles and cohesion.

earthquakes. On the contrary, the inferred friction angles are higher, equal (Chi-Chi), or lower (Morakot and Niigata) than the landscape modal slope for the different inventories. This shows that the potential link between rock strength and modal slope (Burbank et al., 1996, Korup, 2008) is not straightforward.

Interestingly, the same slope distribution for Chi-Chi and Morakot is observed but a lower friction angle is required to reproduce the typhoon-induced landslides, resulting in landsliding on lower slopes, than for the earthquake-induced landslides (figure 3.14). We suggest a mechanical cause to this difference. Indeed, the frictional strength $\tau_f$ depends on pore pressure p, normal stress $\sigma_n$ and the friction coefficient $\Phi$:

$$\tau_f = tan(\Phi)(\sigma_n - p) \tag{3.12}$$

An increase in pore pressure due to rainfall results in a decrease in the apparent frictional strength. Because we did not include pore pressure in our model, we need a lower effective friction angle $\Phi$ to account for this process. From equation 2.24, we can calculate the ratio between apparent friction (that integrates pore pressure) and expected friction without pore pressure. This ratio depends on the angle of rupture, $\alpha$. If we consider that the medium is saturated, taking a rock density of 2.7, and $\alpha$ between 20 and 40 °, we find that we underestimate tan($\Phi$) by 30-50%. Typically, with rupture angle $\alpha = 30°$, the apparent frictional angle is 16°. This could explain why we find low friction values for the Morakot inventory.

We would need to apply our model to more typhoon-triggered landslide inventories to validate this hypothesis. Nevertheless, our results imply that effective rock strength in a given setting evolves through time, as a function of the transient and static stress changes induced by the hillslopes. For example, Lin et al. (2004) have shown that before the Chi-Chi earthquake, landsliding occurred mainly on slopes of 20-30 °, and 40-60° in the years following the earthquake. They interpreted this as the result of numerous extension cracks generated on hillslopes during ground shaking.

We have emphasized that the inferred cohesion and friction angles do not necessarily reflect landscape strength. Here, we try to infer landscape strength, i.e., the strength for which no landslide occurs. We run our model for a large range of cohesion (10 kPa to 5000 kPa) and friction angles (5 to 80°) and count the number of unstable points (i.e., the number of points for which one or more unstable plane exists).

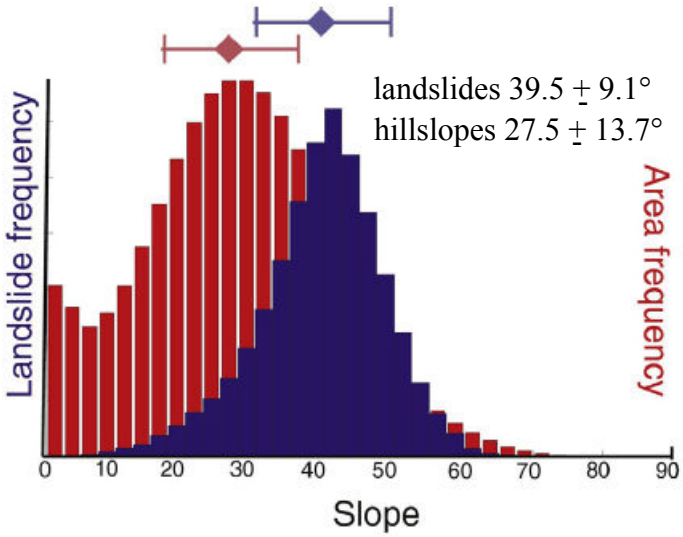


Figure 3.16 – Histogram of mean slope of Gorkha landslides (blue) compared to the entire landscape (red). Symbols indicate the mean values ± the standard deviation. After Roback et al. (2017).

Figure 3.15 shows the percentage of unstable points for each DEM. As expected, it decreases with both increasing friction angle and cohesion. As a landsliding of zero never happens in nature, we have to define a minimum threshold in terms of the fraction of landslides for which cohesion and friction angle can be considered as representative of the rock strength, without any external forcing. This percentage represents the proportion of the surface included in a potential landslide and then can be directly compared to the landslide density as computed for example in Meunier et al. (2007), who defined the landslide density as the landslide surface area divided by the whole surface area. They found landslide density between 1 and 5% for landslides triggered by the Chi-Chi and Northridge earthquakes, and up to 10% for the Finisterre earthquake; Roback et al. (2017) found landslide density between 0 and 2% for the Gorkha earthquake. We arbitrarily set that a density of unstable points 10-100 times smaller than those values (i.e., between 0.01 and 1%) is representative of the "background" landslide fraction. Considering a standard friction angle of 30°, we find cohesion values between 500 and 1500 kPa for Chi-Chi, Morakot and Wenchuan, 1500-2500 kPa for Gorkha, 100-500 kPa for Northridge and 50-200 kPa for Niigata. Those values are one to two orders of magnitude above the effective values inferred by our model for triggering events. We also find similar results using a different friction angle between 20 and 40°. Those values are close from the ones derived from laboratory experiments for sedimentary rock strength (1000 to 20000 kPa after Hoek and Bray (1981)). This implies the fundamental role of cohesion in long-term hillslope stability. On the other hand, we show that the effective cohesion at the onset of landsliding is orders of magnitude lower than landscape strength, suggesting again that rock strength evolves through time. My assumption is that hillslopes behave as cohesive over geological time-scales, maintaining a "stock" of potential landsliding planes that fall catastrophically under an effective cohesion decrease induced by rapid and intense events, such as earthquakes or rainfall events.

Interestingly, the landslide density expected for the inverted effective parameters in the case of the Chi-Chi and Niigata earthquakes (> 20 %) and Morakot (> 50 %) are far too high compared to observations (Meunier et al., 2007). This can be explained by several reasons. Firstly, it is observed that within the years following large earthquake, the landsliding rate is maintained at higher than its background value, suggesting that damaged hillslope gradually fails. Therefore, it is possible that all possible failures do not occur at the same time (Marc et al., 2015). This temporal dimension, that we do not include in our model, may cause this bias. Moreover, in our model, we consider that a rupture plane is unstable if the shear stress exceeds the shear strength, i.e, if the rupture factor $F_R$ is positive. However this criterion is empirical, and the choice of a threshold for the factor of safety involves a lot of uncertainty (Duncan, 2000). In our case, we defined

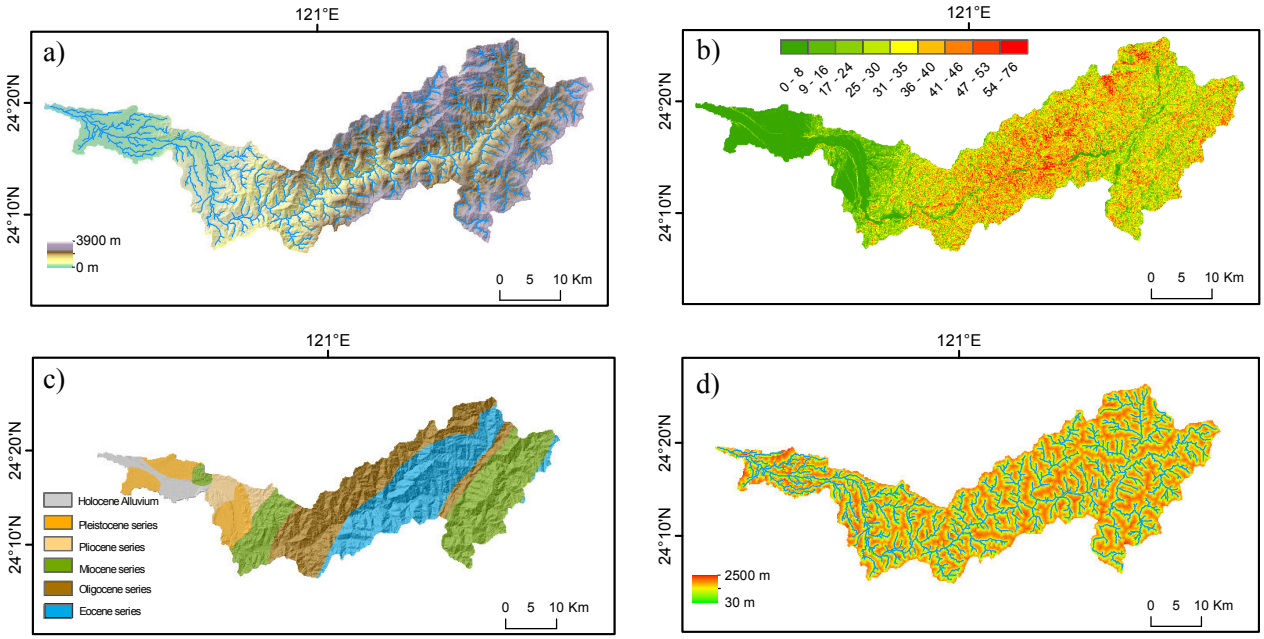


Figure 3.17 – a) Shaded DEM of the Dajia river basin, Taiwan, from SRTM 30 m. The drainage network for drainage areas $> 0.5$ km$^2$ is shown in blue. b) Slope map computed with a eight-neighbors algorithm. c) Simplified geological map, from the National Central University (http://gis.geo.ncu.edu.tw). d) Horizontal distance to the drainage network shown in panel a), computed from a steepest descent algorithm.

as unstable all the points for which at least one plane has a rupture factor $> 1$. This include the points for which only one unstable plane at depth z and angle $\alpha$ can emerge from the topography. Therefore, in our case, the use of a higher rupture factor (1.5, or 2) in order to prevent those limit cases would give more realistic results in term of the number of unstable points.

### 3.4.2 Consequences for landsliding volumes

This section provides an illustration of the effect of hillslope height and slope on the PDFs of landslide areas and the resulting landsliding volume. It is based on the observations published in Huang and Montgomery (2014) and mentioned in section 3.2. Two landslide inventories within the Dajia river catchment in Taiwan have been studied: one triggered by the Chi-Chi earthquake, and the other by the 2001 Typhoon Toraji. Earthquake-induced landslides were smaller than rainfall-induced landslides : the authors noted that 90% of the earthquake-induced landslides were smaller than 4000 m$^2$, whereas this was true of only 20% of the landslides triggered by the typhoon. This difference is also expressed through marked differences between respective the respective PDFs of landslide area (figure 3.18a) : for the typhoon-triggered landslides, the rollover is shifted toward larger sizes and the tail extends to larger landslides ($1.10^6$ m$^2$, against $2.10^4$ m$^2$ for earthquake-triggered landslides).

The fact that typhoon-triggered landslides are significantly larger than earthquake-triggered landslides was attributed in Huang and Montgomery (2014) to the amalgamation of several landslides in the original mapping of the former. In addition, they proposed that the long runout distances of some rainfall-triggered landslides may contribute to the greater mapped size of the landslides induced by Toraji.

Here we explore the potential effect of landscape shape within the catchment on the probability of large landslides. This is encouraged by the observation that earthquake-triggered and typhoon-triggered landslides are located in different parts of the Dajia catchment (figure 3.18a). Most earthquake-triggered landslides occurred in the lower part of the catchment, characterized by lower and flatter topography than the upper part of the catchment (figure 3.17 a and b). On the contrary, landslides triggered by the typhoon occurred in the middle part of the catchment, displaying significantly higher slopes (figure 3.17b). Hillslope length

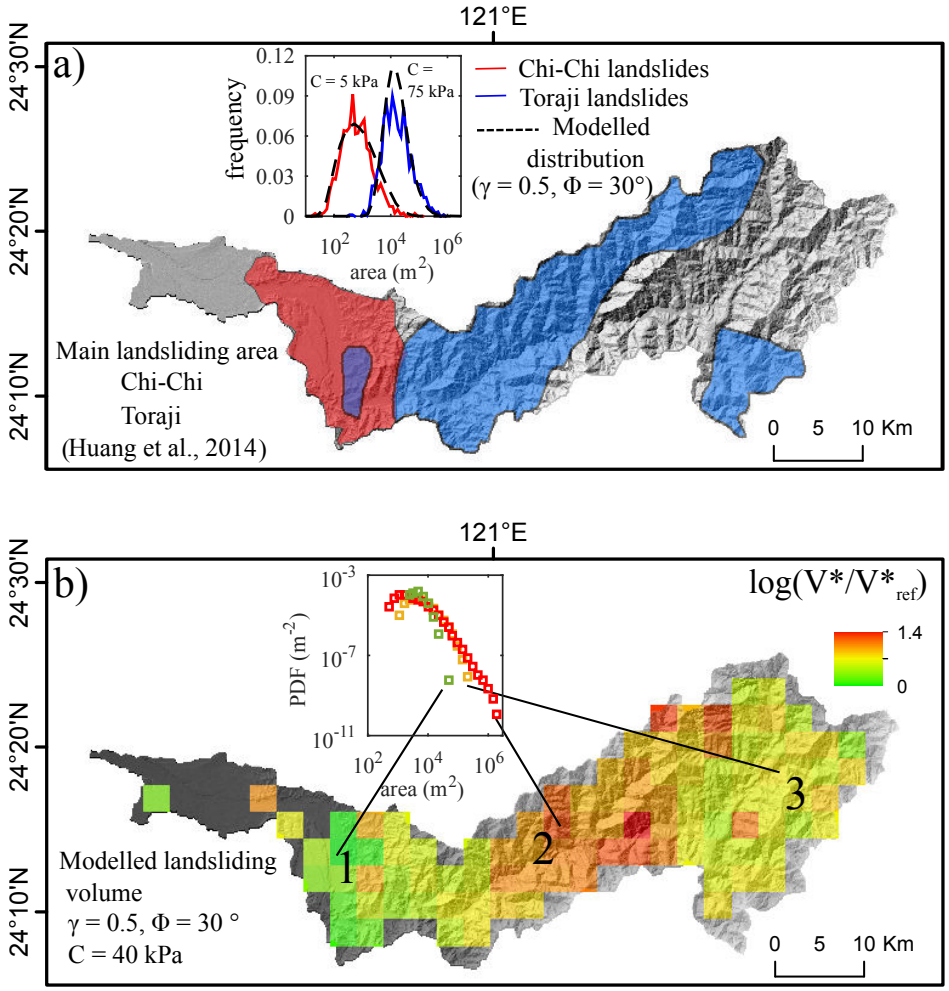


Figure 3.18 – a) Shaded DEM of the Dajia river basin (Taiwan), with the area where landslides were triggered by Typhoon Toraji (blue) and the Chi-Chi earthquake (red). The inset shows the frequency of landslide areas for both events, after (Huang and Montgomery, 2014). The dotted black lines show the best-fitting solutions with $\Phi = 30°$ and $\gamma = 0.5$ and cohesion as a free parameter. b) Normalized volume of landslides computed on a smoothing window. Volume of landslides computed for a fixed number of landslides on a sliding window, divided by the volume of landslides in the in pixel 1. The inset shows the PDFs of landslide area at tree selected pixels 1, 2 and 3, pointed by the dark lines. We used for all the simulations C = 40, $\Phi = 30°$ and $\gamma = 0.5$.

(figure 3.17d) is quite homogeneous within the whole catchment. This results in high relief in the middle part of the basin, where hilltops are located up to 1500 meters above the river (figure 3.17a).

First, to infer potential differences in effective parameters, we apply our model to the areas affected by the typhoon and the earthquake, respectively, and find the cohesion that allows a best fit to the area frequency data published by Huang and Montgomery (2014). We set the friction angle to 30° and $\gamma$ to 0.5, corresponding to classical values. We only vary cohesion here to run this first-order test, because it is the parameter that most likely explains the two orders of magnitude difference in rollover position between both inventories. We find C = 5 kPa for Chi-Chi and C = 75 kPa for Toraji, which reflects differences in effective cohesion potentially linked to the different triggering events. Nevertheless, such a cohesion difference does not explain the one order of magnitude difference in the size of the largest landslides of both inventories. In our model, higher cohesion shifts the rollover position toward larger sizes but does not change the maximum size in the inventory, because it does not control the probability of large landslides. One could argue that the difference between the two PDFs can be explained by lithological differences. The Dajia river flows through Tertiary

sediments; in the lowest part of the basin, rocks are younger and less consolidated than the Oligocene and Eocene series constituting the upper part of the basin (figure 3.17c). However, pristine rock strength is not likely to be reflected in the PDFs of landslides areas, as shown in section 3.2. If effective cohesion can explain the difference in the observed rollover position, we propose that the differences observed for large landslide probability can be explained by the differences in landscape shape between the two areas impacted by both triggering events.

To investigate the role of landscape shape within the catchment, we sample the DEM using a 3 kM square moving window and we apply our model on each sampled inventory (2000 sampled points) with fixed mechanical parameters: C = 40 kPa (which is a mean of the best-fitting cohesion for both events), $\Phi = 30°$ and $\gamma = 0.5$. We compute the PDF of landslide volumes using the scaling relationship between volume and area (Larsen et al., 2010) and compute a unitary volume. This represents the total volume of landslides following such a PDF, divided by the number of landslides in the inventory :

$$V^\star = \int_V PDF(V) * dV * V \tag{3.13}$$

Figure 3.18b) shows the landsliding volume $V^\star$ divided by $V^\star$ computed for the pixel 1 in figure 3.18. $V^\star$ displays significant variations across the basin, up to 1.4 order of magnitude. It is higher in the central, steepest part of the catchment and lower in the upper part and lower part. This results shows that under similar mechanical parameters, and for the same number of landslides, landsliding volume produced in the steepest part of the basin is up to 25 times higher than in other parts. This comes from the higher probability of large landslides due to higher and steeper landscape. Because the number of landslides is usually higher in steepest slopes (Parise and Jibson, 2000, Dai et al., 2011), this effect would be even more significant considering a variable number of landslides. This suggests the first-order role of landscape shape on landslide volume and may have strong implications for hazard assessment or topographic budget of large earthquakes in different geomorphological contexts.

# Chapter 4

# How hillslope shape controls landslide size

## 4.1 Overview

In the previous chapter, I have defined a simple mechanical model that takes into account topography and effective rock strength. I have clarified with this modelling approach the respective contribution of effective friction angle, cohesion, rupture propagation and hillslope geometry on landslide size distribution. In particular, I have demonstrated the theoretical importance of finite hillslope length, height and slope for the probability of large landslides. But to what extent does landscape shape actually control landslide size distribution? This idea needs to be compared to landslide data. Using the case study of the Dajia river basin in Taiwan, I have pointed out that landslide size distribution may reflect landscape shape at a local scale (within the same catchment). In this chapter, I take advantage of several existing landslide inventories to explore the role of the finite geometry of hillslopes on landslide size distribution, especially for the occurrence of large landslides. This chapter consists of an article in preparation, in which I compare landslide size distribution from worldwide inventories to landscape geometry, through a metric that integrates the maximum elevation above the friction angle. I show that this metric follows an exponential distribution, within a given region but also at the worldwide scale. This article is followed by a discussion in which I propose to investigate further, thought analytic calculation, the control of this distribution on the landslide size distribution.

## 4.2 Impact of finite hillslope geometry on large landslide probability

### 4.2.1 Introduction

In mountainous areas, landslides triggered by earthquakes or storms are important actors of surface erosion (Keefer, 1994, Marc et al., 2016a), and represent a major hazard to human societies (Bird and Bommer, 2004). In particular, large landslides ($> 10^8$ m$^3$) contribute significantly to the denudation of mountain belts (Korup et al., 2007, Korup, 2005b), represent the largest source of sediments for the fluvial networks (Croissant et al., 2017) and are especially devastating (Kargel et al., 2016). Assessing the size of the largest landslides triggered during a large earthquake or rainfall event is therefore critical in natural hazard management (Sornette, 2006, Strauss et al., 1989).

Large landslide hazard assessment relies on landslide size distributions obtained from previous events and catalogues. A landslide area distribution is commonly described by heavy tails distribution, sch as a double Pareto distribution with a power-law scaling for intermediate to large landslides and cutoffs at large and small areas (Guzzetti et al., 2002, Stark and Hovius, 2001, Malamud and Turcotte, 1999). This distribution holds for different triggering mechanism and geological settings (Malamud et al., 2004a), while displaying a strong variability of the power-law exponent (Van Den Eeckhaut et al., 2007, Tanyaş et al., 2017), ranging at least from 1.7 to 3.3. While numerous studies have focused on explaining the exponent of the power-law (Frattini and Crosta, 2013, Alvioli et al., 2014, Stark and Guzzetti, 2009), very few have investigated what controls the upper limit of landslide size distribution. Theoretically, each catalogue has an upper limit which is set by the maximum size of the system (Geist and Parsons, 2014), although in practice this limit could be much lower because the size of the catalogues of rupture events is finite and limited by the rate allowed by the triggering mecanism. Based on the study of natural event catalogues, including earthquakes, floods and tsunamis, Geist and Parsons (2014) proposed that the upper limit, and therefore the large event probability, is impossible to predict based on historical precedent.

Over the last decade, observations have shown that giant landslides are concentrated in a small portion of mountain belts, where mean local relief (i.e, elevation difference between river and hilltop) and slope are highest (Korup et al., 2007). Some mountain ranges, such as the Karakoram Mountains, have experienced numerous giant landslides compared to other mountain belts (Hewitt, 2009, Korup et al., 2010). In these regions, Blöthe et al. (2015) proposed that the occurence of large landslides correlates spatially with high excess topography, i.e., the height of material between the topographic surface and an idealized, threshold hillslope.

Those spatial correlations suggest a potential causal relationship between the first-order geometrical properties of landscapes and the probability of large landslides. Frattini and Crosta (2013) proposed that the power-law scaling of landslide area is controlled by the availability of high slope patches at all scales. Jeandet et al. (2019) showed through a simple stability model applied to synthetic hillslopes that their finite dimensions should strongly control the distribution of landslide size, especially at large areas. However, how such hillslope finite geometry affects large landslide probability is still poorly understood.

Here, we define $h_C$, a simple geometrical and mechanical criterion that quantifies the maximum height of hillslopes above a frictional stability plane. Compared to Blöthe et al. (2015), the originality of our approach is to consider the finite geometry of hillslopes, by considering only the horizontal and vertical distance in between the lowest (i.e., rivers) and highest (i.e., hilltops) boundaries of hillslopes. This metric is easy to extract from a Digital Elevation Model (DEM). We therefore compare its spatial distribution to large landslide occurrence in several landslide inventories, and find that the probability of large landslides spatially correlates with high $h_C$ hillslopes. We find that the $h_C$ values are exponentially distributed, and that the mean $h_C$ in several landscapes is likely to control the size distribution of landslide depth, in particular for deep landslides, and therefore the probability of large landslides.

### 4.2.2 Methods

We introduce h, a metric that characterizes the height of material above a frictional stability plane (figure 4.1 a). For a simplified, straight hillslope of length L and slope S, the maximum value of h, that we call $h_C$, is located above the crest and is simply :

$$h_C = L(tan(S) - tan(\Phi)) \tag{4.1}$$

where $\Phi$ is the friction angle.

In order to test to what extent $h_C$ controls the occurrence of large landslides, we extract $h_C$ values of a landscape for which we have a complete landslide inventory. We choose to focus on the Gorkha earthquake for which a complete landslide inventory is available (Roback et al., 2017). Moreover, landslide scars and runout have been mapped separately, avoiding potential bias in landslide location and area induced by long landslide runout.

We use the Matlab Topotoolbox (Schwanghart and Scherler, 2014) to map the hilltops and to compute $h_C$ from elevation data (SRTM 30 m). We extract the river network using a critical drainage area of 0.5 $km^2$ and we define hilltops, or crest points, as the intersecting edges of drainage basins at all stream orders, following Hurst et al. (2012) and Grieve et al. (2016) (figure 4.1b). At each point of the DEM, we compute

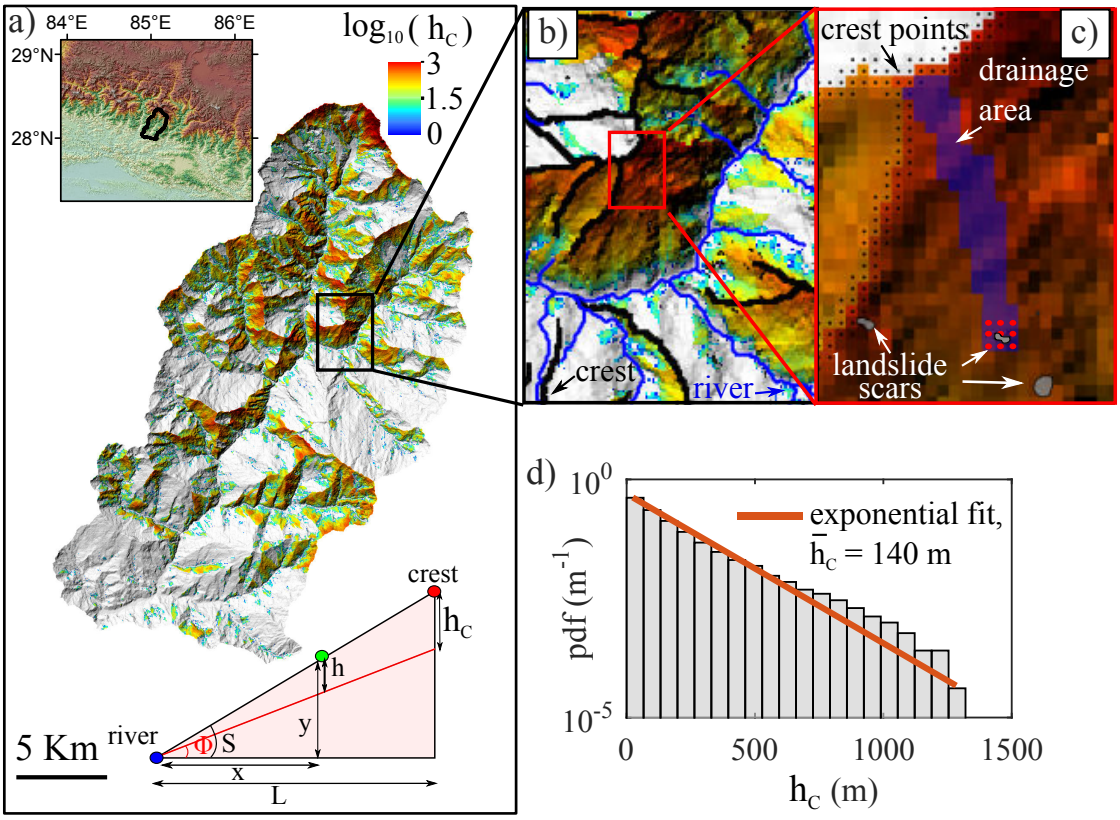


Figure 4.1 – a) Shaded relief DEM of the catchment of one tributary of the Trishuli River, Nepal. The inset shows a schematic representation of a hillslope with length L, slope S and friction angle $\Phi$. At each point (green dot), we extract the horizontal distance to drainage network (x) and the vertical distance to drainage network (y). h is the height above the friction angle. Its maximum value, $h_C$, is located at the crest. Only positive values of $h_C$ are shown. b) Zoom showing the drainage network (blue lines) and the crests (dark lines). c) Zoom on a portion of the hillslope shown in b). Grey polygons represent landslide scars. Red dots show the pixels used in the calculation of the landslide drainage area (purple area). The crest points are shown in black. d) Distribution of $h_C$ of that crest points in the area struck by Gorkha earthquake. The red line is an exponential fit.

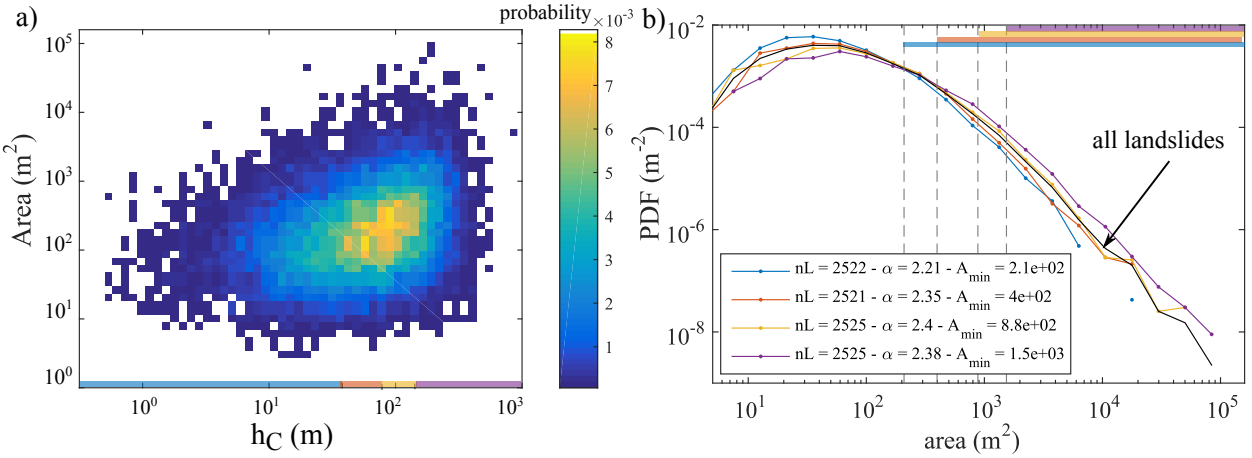


Figure 4.2 – a) Joint probability distribution for landslide area and $h_C$ values of the corresponding crest. b) Probability density function of landslide areas, in four classes of $h_C$. The parameters of the fitted power-law ($\alpha$ and $A_{min}$) are shown for each PDF. The four $h_C$ classes, shown in the bottom of a), are chosen to have a constant number of landslides nL.

the vertical (y) and horizontal distance (x) along the flowpath to the nearest river, and an idealized slope S, which is simply tan(S) = y/x. The local h value is x(tan(S) - tan($\Phi$)), with $\Phi = 30°$; in the following analysis, we will consider only the values of h located on crest points, $h_C$.

We then attribute to each landslide the corresponding crest points. We consider that the upslope portion of the hillslope including a landslide is the area draining toward the landsliding scar (figure4.1c). To avoid potential bias due to the landslide area, we define landslide scar area as the 8-neighboring pixels of landslide scar center. In doing so, we avoid the discrimination of small landslides, for which drainage area would have less chance to reach a crest point. For each landslide, we extract all the crest points included in this drainage area and compute the $h_C$ mean value of those crest points. We call $h_{C,ls}$ the $h_C$ values corresponding to landslides. We then bin the landslide inventory as a function of their $h_C$ values, and compute the PDF of landslide areas in each bin. We fit a power-law to each sub-inventory for areas greater than an area $A_{min}$, following Clauset et al. (2009). The fitting procedure works as follows: 1) for each possible choice of $A_{min}$, we estimate the power-law exponent $\alpha$ via the method of maximum likelihood; 2) we compute the corresponding Kolmogorov-Smirnov goodness-of-fit statistic D; and 3) we then select as our estimate of $A_{min}$, the value that gives the minimum value D over all values of $A_{min}$.

### 4.2.3 Results

Figure 4.1 a) illustrates the spatial pattern of h in the catchment of one tributary of the Trishuli River, in Nepal. We only show the positive h values, i.e., where S is higher than the assumed frictional angle. 87% of the landslides occurred on hillslopes with positive h (figure 4.6). Values of $h_C$ (h extracted along the crest points) of the Trishuli catchment follow a negative exponential distribution, characterized by a mean value of 140 m (figure 4.1d). The $h_C$ values corresponding to landslides follow similar distribution, with a mean of 106 meters (figure 4.6).

Figure 4.2b) shows the PDF of landslide areas in the four bins of the inventory that we separated as a function of their $h_C$ values. The four PDFs display significant differences despite having the same number of samples included in each class. The fitted power-law exponent $\alpha$ varies from 2.21 for the smallest $h_{C,ls}$ bin to 2.4 for the third bin. The $A_{min}$ value increases with the $h_{C,ls}$ class, from $A_{min} = 2.2\text{x}10^2$ m$^2$ to $A_{min} = 1.5\text{x}10^3$ m$^2$. The probability of large landslides is significantly higher for the bin with the largest $h_{C,ls}$. The joint probability distribution for landslide area and $h_{C,ls}$ values (figure 4.2a) is characterized by an upper limit showing a positive relationship between the largest landslide area and $h_{C,ls}$ value. The size of the smallest landslides, on the contrary, is not related to $h_{C,ls}$, except for large $h_{C,ls}$ for which the absence of

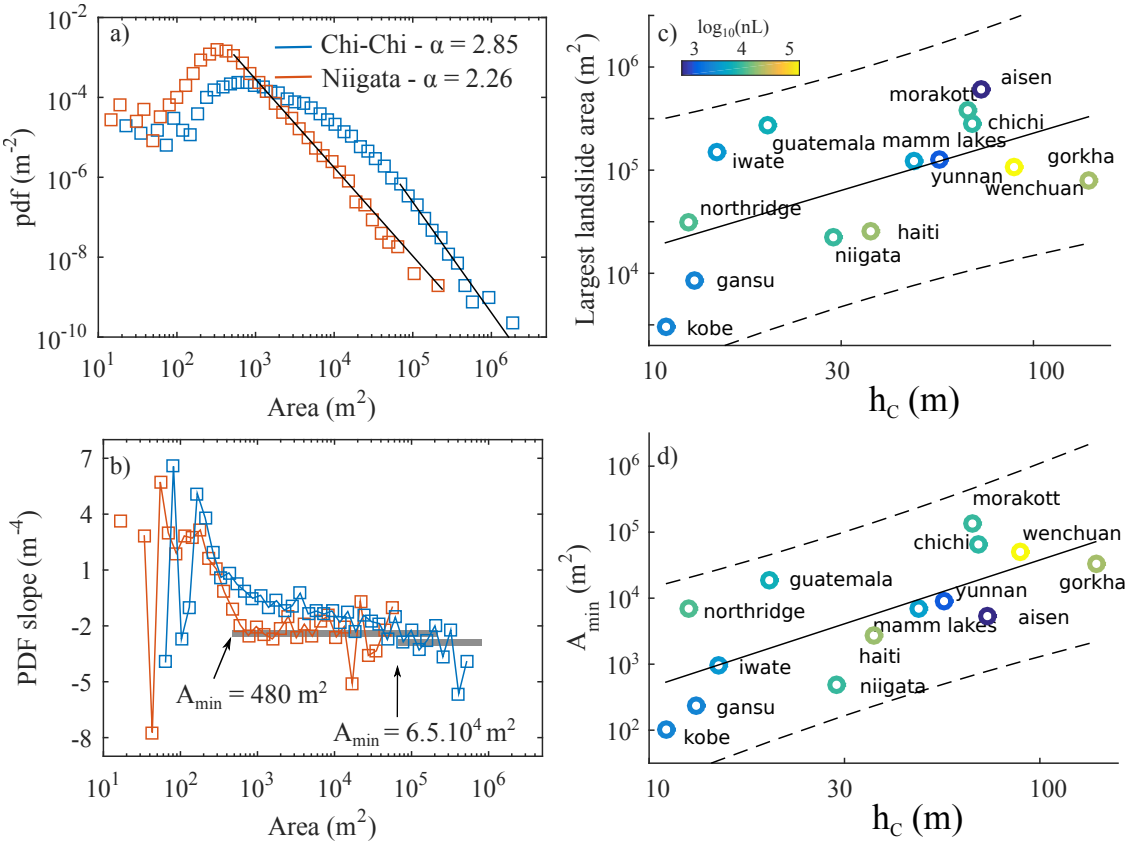


Figure 4.3 – a) PDFs of landslide areas triggered by Chi-Chi (nL = 9509) and Niigata (nL= 10526) earthquakes. The dark line shows the best-fitting power-law for area greater than $A_{min}$. b) d(PDF)/d(Area) for the same inventories. The grey line shows the exponent $\alpha$ of the best-fitting power-law for area greater than $A_{min}$. c) Mean area of the 1% largest landslides of the catalogues as a function of the mean $h_C$. Black line shows the best-fit (least square) linear regression on the logarithmic values, and dotted lines show the 95% confidence interval. d) $A_{min}$ as a function of the mean crest $h_C$.

smallest landslides is likely due to undersampling. Based on the analysis of the Gorkha earthquake landslide inventory, we find that large landslides are preferentially located on high $h_C$ hillslopes. This suggests that the distribution of $h_C$ within a landscape strongly controls the overall distribution of landslide sizes.

To test this idea, we fit a power law following the same method on several landslide inventories triggered by earthquakes or storms. The 14 inventories display strong variations in there $A_{min}$ and $\alpha$ value.

For example, figure 4.3 a and b show the PDF of landslide areas for the landslides triggerred by the Chi-Chi and Niigata earthquakes. For the Niigata earthquake, the minimum area for the best-fitting power-law (480 $m^2$) is just above the area corresponding to the rollover position. $A_{min}$ for the Chi-Chi earthquake is located at least one order of magnitude greater than the rollover position, at $6.5.10^4$ $m^2$, and the power-law holds for only one order of magnitude. The resulting values of $\alpha$ are significantly different. For each inventory, we extract the mean $h_C$ value on the area impacted by the triggering event and we compute the mean area of the 1% largest landslides in the inventory. Figure 4.3 c and d shows that both the mean area of largest landslides and the $A_{min}$ value tend to increase with increasing $h_C$, albeit with a large variability around the mean trend. This relationship is independent of the number of landslides in the inventory, which varies from 517 (Aisen) to 184106 (Wenchuan).

Therefore, $h_C$ is likely to indicate at first order the landscape potential to host large landslides. We have thus extracted $h_C$ on each available SRTM tile (at 90 m resolution) and map the worldwide mean $h_C$ (figure 4.4). Interestingly both the global distribution of worldwide $h_C$ and the distribution for selected orogens (Taiwan, New Zealand Southern Alps, European Alps, and Patagonian Andes) follow an exponential

distribution (figure 4.4a). Some areas display high values of $h_C$ compared to the rest of the world, and correspond, not surprisingly, to orogens where high relief is found: the Himalayas, the European Alps, the New Zealand Southern Alps, the Andean Belt (the Patagonian Andes and Cordillera Blanca), and the Alaska Ranges. This exponential distribution does not change according to the threshold area defining the rivers (figure 4.8 b). However, it is influenced by the chosen frictional angle (figure 4.8 a). This is expected from the $h_C$ calculation method, lower values of $\Phi$ leading to higher values of $h_C$ (equation 4.1).

### 4.2.4 Discussion and concluding remarks

We have defined a metric, $h_C$, characterizing the maximum height above the friction angle. Spatial analysis of landslides triggered by the Gorkha earthquake suggests that $h_C$ actually controls the size distribution of landslides, with a higher probability of large landslides on large $h_C$ hillslopes. In the Gorkha landslide inventory, the area threshold above which landslide area follows a power-law increases with increasing $h_C$. $h_C$ integrates hillslope length and slope, and therefore, we could suspect that both metrics controls the potential for large landslides. However, interestingly, this dependency is found for hillslope slope (figure 4.5b), but not for hillslope length (figure 4.5b).

Those observations seem to hold for several worldwide landslide inventories, for which both the area of the largest landslides and the threshold $A_{min}$ increase with increasing $h_C$. This observation displays a large variability. The first cause of such variability could be the number of samples in the inventory, a higher number of samples leading to an increasing chance of sampling large events. However, the number of samples here does not correlate to the $h_C$ value (figure 4.4c and d). Our $h_C$ metric criteria does not include the full hillslope shape, and masks differences in concavity and convexity, which can influence large landslide probability (Jeandet et al., 2019). It does not include local slope variations either, which have been suggested to control the landslide size distribution (Frattini and Crosta, 2013). We have assumed a constant friction angle, but it is expected that the shape of the PDF and large landslide probability will depend on this mechanical parameter (Stark and Hovius, 2001, Jeandet et al., 2019). Further work using the effective friction angle inverted from landslide size distributions (Jeandet et al., 2019) may help in refining our approach.

Those results question the validity of the power-law model for landslides with area greater than the rollover. In certain cases (for example Chi-Chi, Gorkha, Morakot), the threshold area $A_{min}$ is several orders of magnitudes larger than the rollover and the power-law holds for a reduced range of areas. This observation, which holds for landscapes characterized by high $h_C$, confirms the results of (Jeandet et al., 2019), who proposed that the landscape shape sets the power-law distribution for landslides larger than a certain threshold, and below which smaller landslides result from the contribution of cohesion to plane stability, and from the physics of 2D rupture propagation. Our results confirm that such a threshold area and the power-law tail for large landslides above it is related to the landscape geometry. The $h_C$ exponential distribution seems universal, as we show with the worldwide distribution (figure 4.4). Interestingly, even if $h_C$ directly depends on the hillslope slope and length, none of the above metrics display clear exponential distributions (figure 4.7). However, a full understanding of how the $h_C$ distribution controls the shape of the landslide size distribution requires further investigations.

Our results suggest that the distribution of $h_C$ in a landscape influences the whole PDF of landslide size and is setting the lower and upper limits for power-law scaling. This extends the idea that increasing the height of material above a friction angle favors the occurrence of large landslides, as already suggested (Korup et al., 2007, Blöthe et al., 2015). Despite the fact that the upper bound for natural hazard must be difficult to predict (Geist and Parsons, 2014), we show that the first-order geometric properties of landscapes leave signatures in landslide inventories. This encourage further examination of the links between landscape shape and landslide size inventories, in order to better assess giant landslide probability in regions characterized by high $h_C$ and high seismic hazard.

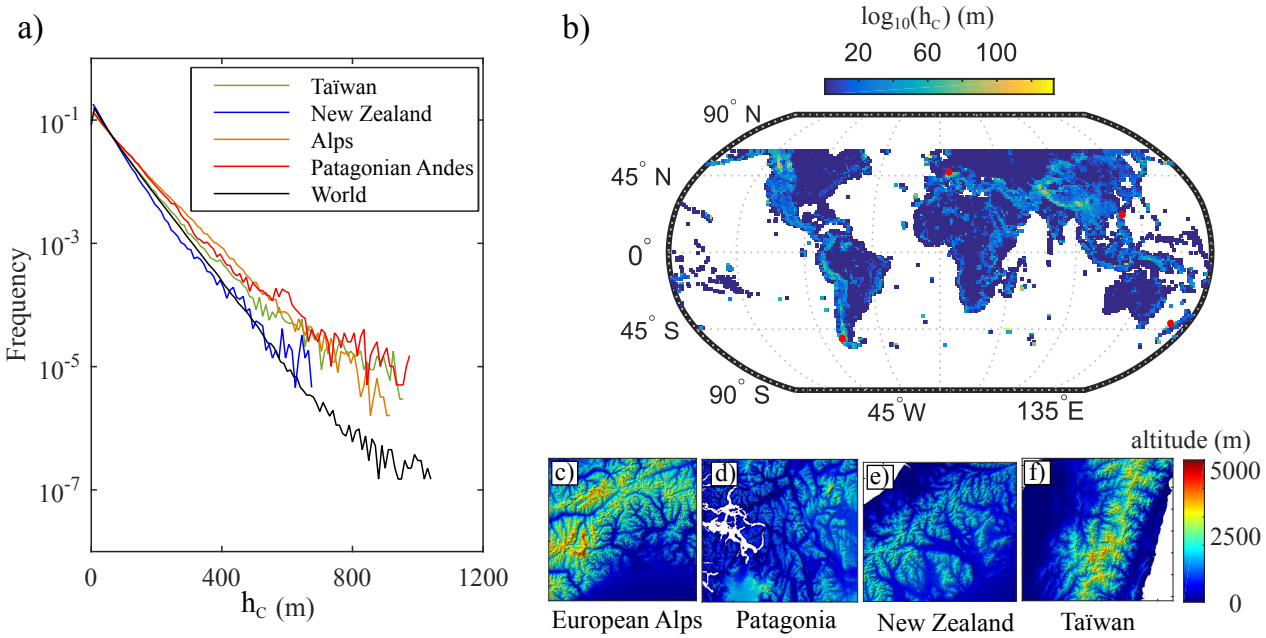


Figure 4.4 – a) Non cumulative frequency of $h_C$ values for the world, and for four DEM (insets c-f). b) World Map of mean $h_C$ computed on each SRTM 90 m tile.

## 4.3 Supplementary material

Figure 4.5 shows the same results as figure 4.2, but binning the landslides as a function of hillslope length (a-b), hillslope slope (c-d) and hillslope height (e-f). Our classes are chosen to contain the same number of landslides. Hillslope length does not influence significantly the PDF of landslide areas. In contrast, for higher slope and height, the probability of larger landslides is higher.

Figure 4.6 shows the area distribution of the studied landslides compared to the whole landslide inventory. For 87% of the landslides, positive values of $h_C$ are found in their corresponding drainage area. For 56% of the landslides, crest points are located in their drainage area. Therefore, we can extract a $h_C$ value for 43% of the landslides. All PDF are very similar, we thus consider that using a reduced set of landslides does not bias our main results.

Figure 4.7 shows the distribution of slope gradient S, length L and $h_C$ for the Taiwan DEM. Among those four metrics, only $h_C$ follows an exponential distribution. Slope distribution is also exponential above a threshold that is close to the frictional angle I used, which is likely to exert an important control on $h_C$ distribution.

Figure 4.8 shows the distribution of slope gradient S, length L and $h_C$ for the Taiwan DEM, with different values of friction angle (a) and critical drainage area (b).

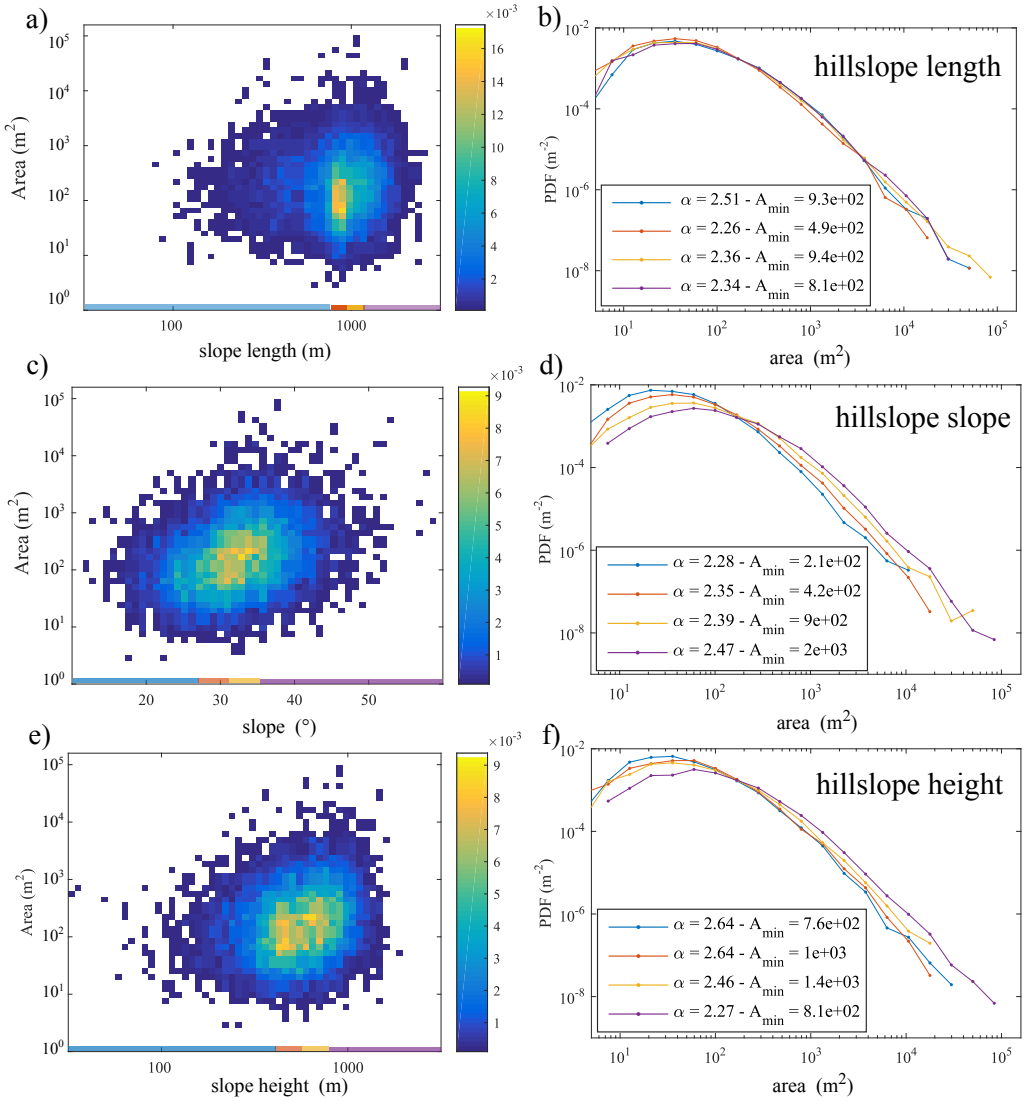


Figure 4.5 – Same as figure 4.2, but with the hillslope length L (a-b), gradient S (c-d), and height H (e-f).

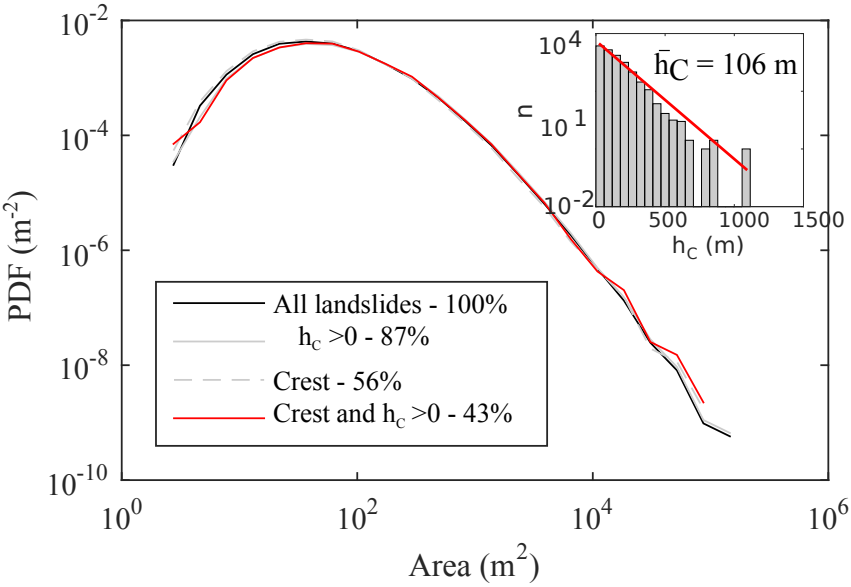


Figure 4.6 – PDF of landslide areas in the inventory (dark line), with positive $h_C$ values in there drainage area (grey line), with crest points in there drainage area (dotted grey line) and with crest points with positive values in there drainage area (red line). The inset shows the $h_C$ distribution for landslides.

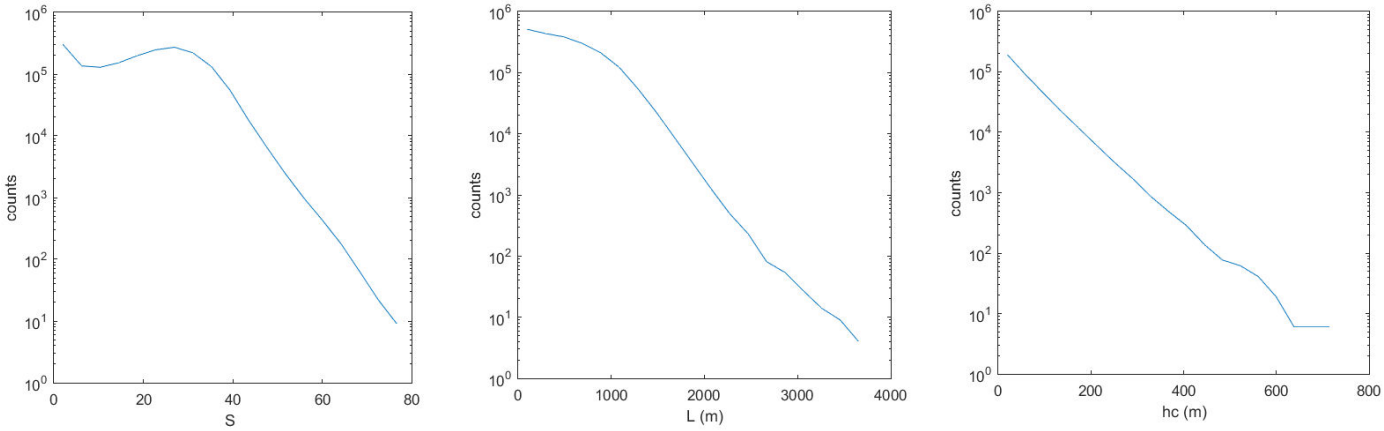


Figure 4.7 – Histogram of slope gradient S, length L (m) and $h_C$ (d) for the Taiwan DEM.

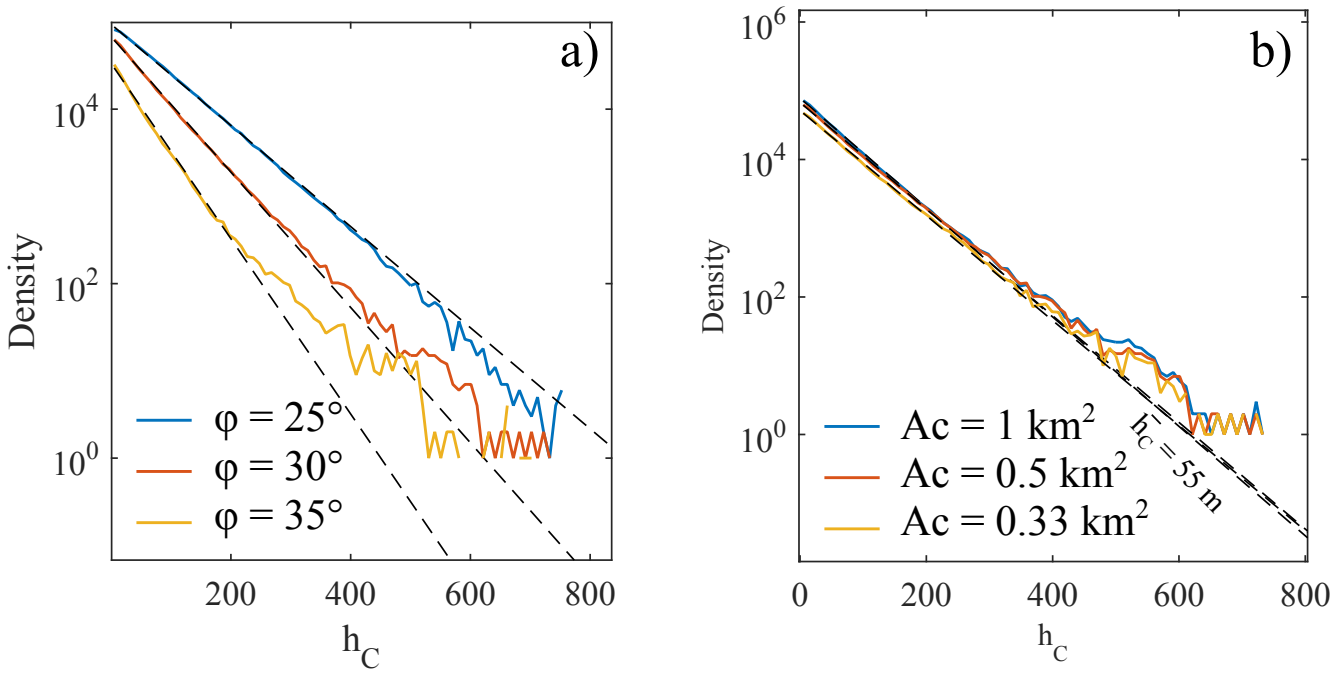


Figure 4.8 – Distribution of $h_C$ values in Taiwan, as a function of friction angle Φ (a) and critical drainage area $A_c$ (b).

## 4.4 General discussion

In this section, I calculated an analytic solution for the distribution of unstable depths in a simplified hillslope model. I show that this solution depends only on $h_C$. Further work is planned to link this model to landslide data presented in 4.2, and to demonstrate the control of landscape $h_C$ distribution on landslide size distribution. In a second part, I present implications of the worldwide distribution of $h_C$ for landslide hazard assessment and erosion in seismically active regions.

### 4.4.1 Linking model and landslide data

We consider a simplified and straight hillslope (figure 4.9 a) of length L and slope angle S. We aim at assessing the probability of unstable depth in this wedge, given simple geometric assumptions. At a coordinate x located in this wedge, we assume that any plane, defined by its local depth z and dipping angle $\alpha$, is a potential rupture plane if 1) $\alpha$ is greater than the internal frictional angle $\Phi$ and 2) it intersects the surface topography upstream of the base of the hillslope. All planes meeting the two conditions in this wedge have the same rupture probability, i.e., we do not consider that rupture probability increases with increasing shear stress/shear strength ratio. Compared to Jeandet et al. (2019) who used a Mohr-Coulomb criterion, we neglect cohesion because that was found to mostly influence the stability of shallow and small landslides.

Therefore, the rupture factor at a depth z and rupture angle $\alpha$ is purely frictional:

$$F_R(z, \alpha) = \frac{\alpha}{\Phi} \tag{4.2}$$

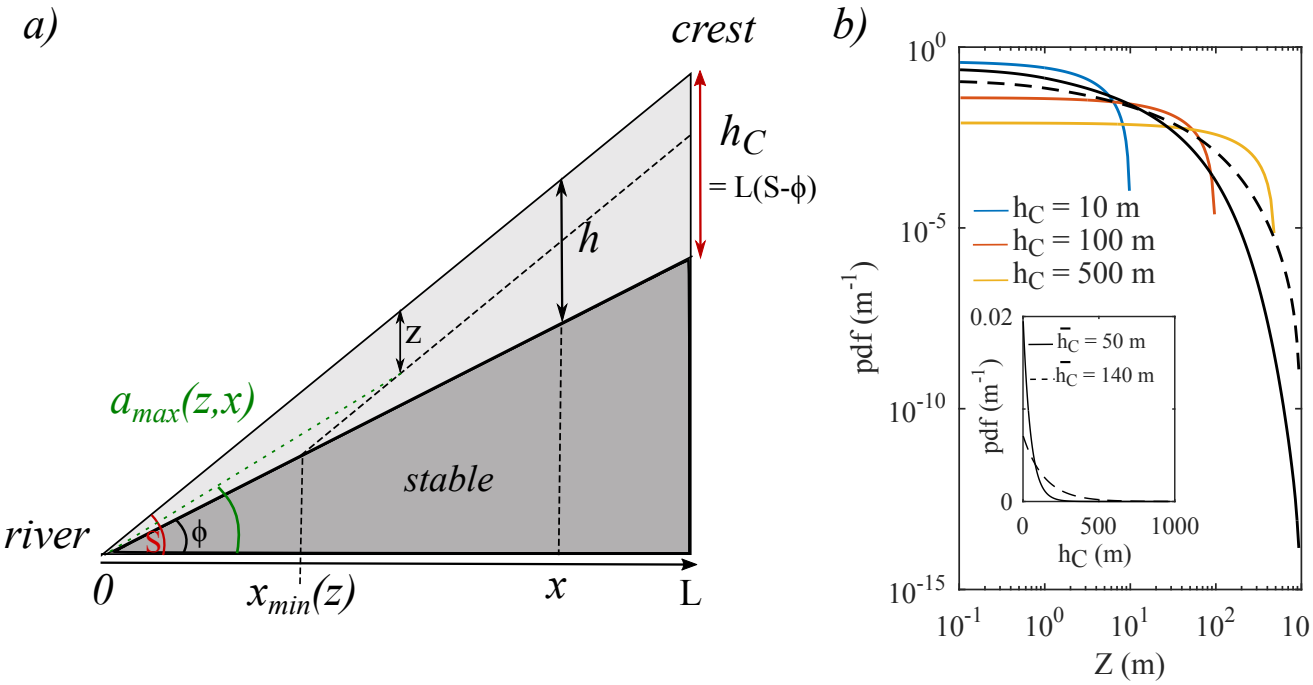


Figure 4.9 – Schematic wedge of length L, slope S and frictional angle $\Phi$. At coordinate x, the maximum material height above the frictional angle is h(x). A depth z can be considered as a rupture depth for positions greater than $x_{min}$(z). The maximum h value in this wedge is located below the crest point and called $h_C$. b) PDF of unstable depths in a wedge characterized by a $h_C$ = 10 m (blue line), 100 m (red line) and 500 m (yellow line). The dark lines show the PDF of unstable depths given exponential distributions of $h_C$ with means of 50 m (solid) and 140 m (dashed).

For simplicity, I assume that the rupture probability at depth z and rupture angle $\alpha$ is:
$P_R = 1 \; if \; F_R(z, \alpha) > 1$
$P_R = 0 \; if \; F_R(z, \alpha) \leq 1$

I further add a topographic constraint, assuming that a rupture plane should emerge above the hillslope toe. The maximum rupture angle at depth z and coordinate x is then $\alpha_{max}(z, x) = \mathrm{S} - (\mathrm{z/x})$. Therefore, the rupture probability at depth z and coordinate x is:

$$p_R(x, z) = \int_{\Phi}^{\alpha_{max}} P_R(z, \alpha) d\alpha = S - \Phi - \frac{z}{x} \tag{4.3}$$

A rupture plane of depth z can exist only at $\mathrm{x} > x_{min}(z)$, and at each point x there is a maximum local depth h, that can be expressed as : $\mathrm{x}_{min}(\mathrm{z}) = \mathrm{z}/(\mathrm{S}\text{-}\Phi)$ and $\mathrm{h(x)} = \mathrm{x(S}\text{-}\Phi)$. Integrating $p_R$(x,z) over the wedge gives:

$$p(z) = \frac{\int_{z/(S-\Phi)}^{L} p_R(z, x) dx}{\int_0^L \int_0^{x(S-\Phi)} p_R(z, x) dz dx} \tag{4.4}$$

The numerator of equation 4.3 is :

$$\int_{z/(S-\Phi)}^{L} (S - \Phi)(L - \frac{z}{S - \Phi}) - z(ln(S - \Phi) - ln(z)) \tag{4.5}$$

The denominator is :

$$\int_0^L \int_0^{x(S-\Phi)} (S - \Phi) - \frac{z}{x} dz dx = \int_0^L \frac{x(S - \Phi)^2}{2} = \frac{L^2 (S - \Phi)^2}{4} \tag{4.6}$$

We call $h_C$ the maximum depth above friction angle, giving:

$$PDF(z) = 4 \left[ \frac{h_C - z - z(ln(z))}{{h_C}^2} \right] \tag{4.7}$$

Under such simple mechanical and geometrical assumptions, the PDF of rupture depth is constant at small depths, due to the lack of cohesion stabilizing shallow planes in my simplified model, and decreases at large depths toward a cut-off at $h_C$ (figure 4.9 b). In turn, the length and slope of a hillslope set the maximum depth and size of potential landslide ruptures occurring on it.

Figure 4.9b) also shows the theoretical probability density function of depth z for a given exponential distribution of $\mathrm{h}_C$ :

$$\int pdf_{h_C}(z) * pdf(h_C) dh_C \tag{4.8}$$

where $pdf_{h_C}(z)$ is the probability density function of z at a given $h_C$ given by equation 4.7 and $pdf(h_C)$ is the probability density function of an exponential distribution.

This work in progress will allow further investigation of how the mean $\mathrm{h}_C$ value strongly controls the probability of deep, and therefore large (Larsen et al., 2010), landslides, but also the overall PDF of landslide areas.

### 4.4.2 Implications for large landslide hazard in seismically active regions

The probability of large landslides is likely to be explained by 1) landscape morphometry (Blöthe et al. (2015), Korup et al. (2007), and this study) and 2) the frequency of triggering, which increases the chance to sample the tail of the landslide size distribution (Geist and Parsons, 2014). Therefore, I examine here in which parts of the Earth's surface those two conditions most likely be.

I have shown that $h_C$ is likely to indicate the potential of a given landscape to experience large landslides. The highest $h_C$ values are located, not surprisingly, along the collision zones, in mountain belts with high relief. Here, I compare the $h_C$ world map with the Global Seismic Hazard Map (Giardini et al., 1999). This

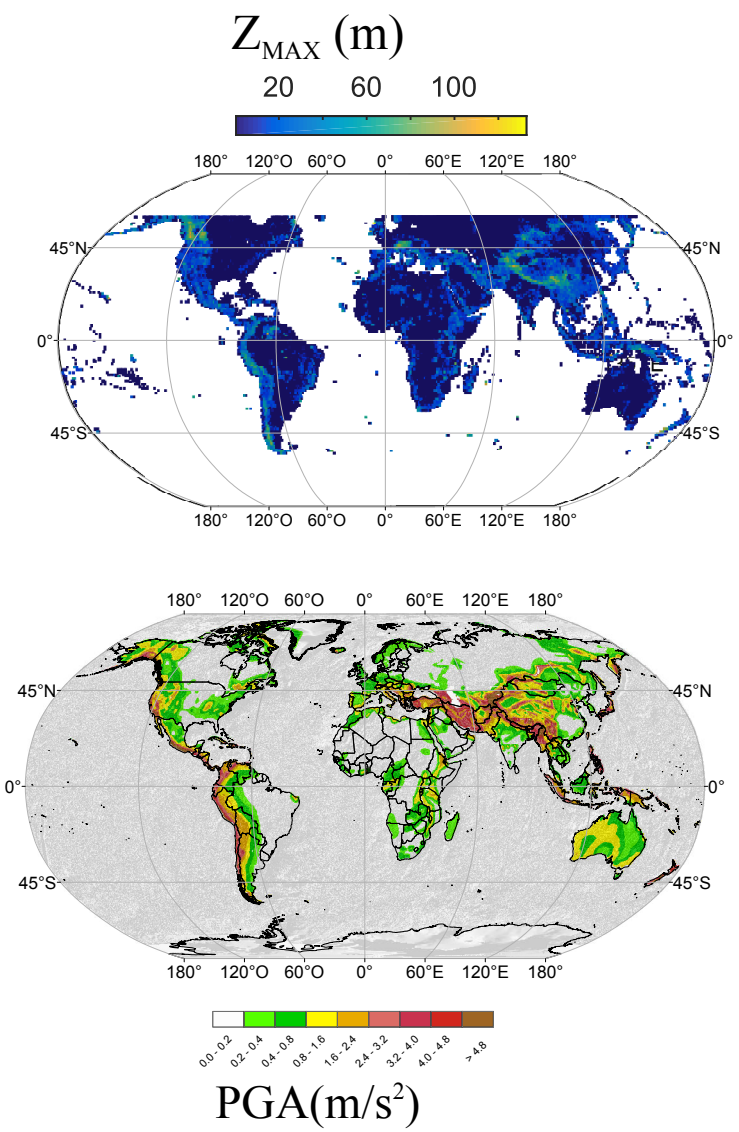


Figure 4.10 – $h_C$ map from our study (top) and Global Seismic Hazard Map (bottom). The hazard is depicted as peak ground acceleration(PGA) with 10% probability of exceedence in 50 years, corresponding to a return period of 475 years (Giardini et al., 1999).

map shows the seismic hazard as peak ground acceleration(PGA) with 10% probability of exceedence in 50 years, corresponding to a return period of 475 years.

If we consider that a PGA of 2 $ms^{-2}$ is required to trigger landsliding (Meunier et al., 2007), we see that some areas with high $h_C$ are prone to high enough ground motion to trigger landslides, such as the Andean chain, the Southern Alps of New Zealand or the Himalayas. In other places such as the Northern Island of New Zealand, even if the seismic hazard is high, mean $h_C$ values are below 40 m. Other areas are not subjected to high enough seismic hazard, such as the Northern European Alps or Alaska range. However, numerous giant landslides are found in the European Alps (Korup et al., 2007). This illustrates that going further in large landslide hazard assessment at the global scale, would require considering all the potential triggering, such as typhoon or snowmelt.

The comparison of those two maps shows that landscapes that favors large landslides are also prone to high seismic hazard in many parts of the world. Therefore, in those areas, the probability of large landslides is increased by frequent seismic triggering. In the next chapter, I examine to what extent such large erosional events could, in turn, influence regional seismicity.

# Chapter 5

# Modelling the response of active faults to large erosional events

## 5.1 Overview

In the two previous chapters, I have investigated the potential controls on landslide size distribution and I have demonstrated the fundamental role of landscape geometry. In particular, landscapes with high values of unstable height are able to produce large landslides under a given forcing. Those areas correspond to collision zones with high seismic hazard, in which erosional and tectonic processes are likely to be coupled. For example, in a work in preparation (Appendix A), we suspect that the large landsliding event triggered by the typhoon Morakot have triggered shallow seismicity, and changed the earthquake b-value during several years after the typhoon. Those potential links need to be investigated further through a numerical modelling approach. Therefore, in this chapter, I used two numerical models of the seismic cycle to investigate the role of large erosional events on seismicity. I first introduce the numerical methods. Then, I present my results of numerical modelling of the effects of one erosional event on a single fault with heterogeneous frictional properties. Then, I compare the main results of this study with the behaviour of one homogeneous fault, and I finally present a work in progress in which I aim to study the role of one erosional event on a fault network.

## 5.2 General presentation of the methods

To study fault response (in terms of both seismicity rate and b-value) to time-dependent normal stress, there are several hindrances to overcome. The major challenge is to simulate earthquake cycles with sufficient variability in earthquake magnitudes to infer meaningful b-value. Such a variability implies an increasing number of cells in the modelled fault (see section 5.2.2), leading to an increase in the computational time. The second challenge was to find a compromise between the range of modelled earthquake magnitudes and the computation time. Finally, in the existing models of earthquake cycles (e.g., Lapusta and Liu, 2009, Luo et al., 2017), the normal stress is implemented as a constant parameter in time and space; the last technical issue is to change the implementation of normal stress as a time-variable parameter. During this work, I have explored the potential of several existing numerical codes to address those issues.

This part of my PhD work began with the use of BiCycle, a numerical code developed by Lapusta et al. (2000) and Lapusta and Liu (2009) that models the seismic cycle on a single fault embedded in an elastodynamic medium under tectonic loading. Such full dynamic simulations compute the wave-mediated stress transfer. Because this effect is inertial, it implies a convolution integral in time that takes into account slip rate and its history (Perrin et al., 1995, Lapusta et al., 2000, Thomas et al., 2014) and is computationally expensive. Other quasi-dynamic approaches (Rice, 1993, Hillers et al., 2006, Ziv and Cochard, 2006) ignore this term and account for inertial effects through a static radiation damping term, saving significant amounts

of simulation time.

Wave-mediated stress transfer is important to study the dynamics of rupture propagation, because it concentrates stress at the tips of the rupture (Lapusta et al., 2000, Lapusta and Liu, 2009) and allows supershear ruptures (e.g., Xia et al., 2004, Dunham, 2007). However, numerical simulations based on the quasi-dynamic and dynamic approaches results in the same qualitative slip pattern (Thomas et al., 2014). The differences lie in the slip velocity and rupture arrest during earthquakes, which are not critical for the purpose of studying the fault response at the seismic cycle time scale. Therefore, I switched to a quasi-dynamic approach. The next section describes the two quasi-dynamic codes I used during this work.

### 5.2.1 Presentation of the two numerical models

The first model I used, QDYN v1.1, (Luo et al., 2017) has been developed by Yingdi Luo et al. at the California Institute of Technology and released in 2017. The second model I used, FastCycle, is the outcome of the PhD work of Pierre Romanet (Romanet et al., 2018) at the Institut de Physique du Globe (Paris). Both models are based on the same physical approach. Their major difference lie in the acceleration algorithms implemented in FastCycle, which allow modelling of to model a population of faults with potentially complex geometries, instead of one planar fault.

#### 5.2.1.1 Physical ingredients

Both QDYN and FastCycle are based on the same physical recipes : they model a 1D fault under tectonic loading, embedded in a 2D elastic medium, which is storing energy before it is released during an earthquake. The resistance of the interface to sliding is characterized by a rate-and-state friction law.

- **The loading**

  The loading is done either by a global stress rate field (in FastCycle) or by a loading velocity (in QDYN).

  In QDYN, the loading velocity is used to compute the elastic stress changes (second term in the equation 5.6). The fault is slipping in mode II (in plane), i.e the direction of rupture is parallel to the slip direction. In FastCycle, the loading rate is used to compute the background shear traction on the fault (first term of equation 5.6). The studied faults are slipping in mode III (out of plane), i.e the rupture is perpendicular to the slip direction.

- **The elastic medium**

  The stress change along the fault due to sliding comprises 1) the stress redistribution after a certain amount of slip (i.e, the static stress transfer) and 2) the wave mediated stress redistribution (elastodynamic stress transfer). The dynamic radiation away from the fault is accounted for using a radiation damping term (i.e the instantaneous shear stress drop in the medium due to sliding) :

  $$\tau_{rad} = -\frac{G}{2c_s}V \tag{5.1}$$

  where G is the shear modulus of the medium, V the slip velocity and $c_s$ the shear wave speed of the medium.

- **The friction law**

  Frictional strength of the fault $\tau_{fr}$ is proportional to the normal stress $\sigma_n$ with a friction coefficient, $\mu(t)$ :

  $$\tau_{fr} = \sigma_n \times \mu(t) \tag{5.2}$$

The friction evolution through time is modelled by the rate-and-state friction law in its modern form proposed by (Marone, 1998).

$$\tau_{fr} = \sigma_n \times \left[\mu_0 + a\ log\left(\frac{V}{V_0}\right) + b\ log\left(\frac{\theta V_0}{D_c}\right)\right] \tag{5.3}$$

We use an ageing law to describe the evolution of the state variable :

$$\dot{\theta} = 1 - \frac{V\theta}{D_c} \tag{5.4}$$

#### 5.2.1.2 Governing equations

The stress acting on the fault $\tau_f$ is the sum of the far-field loading stress $\tau_{load}$, the elastic stress $\tau_{el}$ and the radiation damping term $\tau_{rad}$.

$$\tau_f = \tau_{load} + \tau_{el} + \tau_{rad} \tag{5.5}$$

In this formulation, the most computationally expensive part is the second term, i.e the shear stress resulting from elastic interactions.

Assuming that the shear stress acting on the fault is equal to the frictional resistance and differentiating with respect to time leads to the equation that is used to solve for velocity at each time step and at each point of the fault :

$$\dot{V} = \frac{\overbrace{\dot{\tau}_{load}}^{far\ field\ loading} + \overbrace{\dot{\tau}_{el}}^{static\ stress\ change\ due\ to\ slip} + \overbrace{\dot{\sigma_n}\mu(t)}^{normal\ stress\ variations} - \overbrace{\sigma_n \frac{b}{\theta}\dot{\theta}}^{static\ friction\ changes}}{\underbrace{\frac{G}{2c_s}}_{radiation\ damping} + \underbrace{\frac{a\sigma_n}{V}}_{direct\ effect}} \tag{5.6}$$

The two codes consider constant normal stress through time, so the third term is not implemented in QDYN and FastCycle. I implemented the temporal normal stress change due to erosion in this equation, by changing $\sigma_n$ at each time step and adding the normal traction rate term.

#### 5.2.1.3 Numerical methods

The elasticity response (second term of equation 5.6) is solved using the boundary elements method (Tada, 1996, Tada and Madariaga, 2001) : contrary to finite element methods, the elasticity problem is solved in the form of an integral only along the fault, where displacement and stress are known at each cell. This method has the advantage that only the fault has to be discretized. However, it is computationally expensive as the computation time grows as the square of the number of cells on the fault N. To overcome this issue, acceleration algorithms have been implemented in FastCycle, reducing the computation time from the order of $N^2$ to N log(N), while keeping excellent precision. This allows the resolution of the problem for several faults, potentially with different geometries (Romanet, 2017).

An usual issue in earthquake cycle modelling is to cover the multiple time scales involved in the seismic cycle. A time step that is too large would not capture seismic ruptures, but a time step too small would lead to a huge number of useless data computed during interseismic phases. This problem is solved using an adaptive time-step solver algorithm following (Bulirsch and Stoer, 1966). It allows efficient computation through the inter-seismic periods (using long time steps) while keeping a good accuracy during earthquakes (using short time steps).

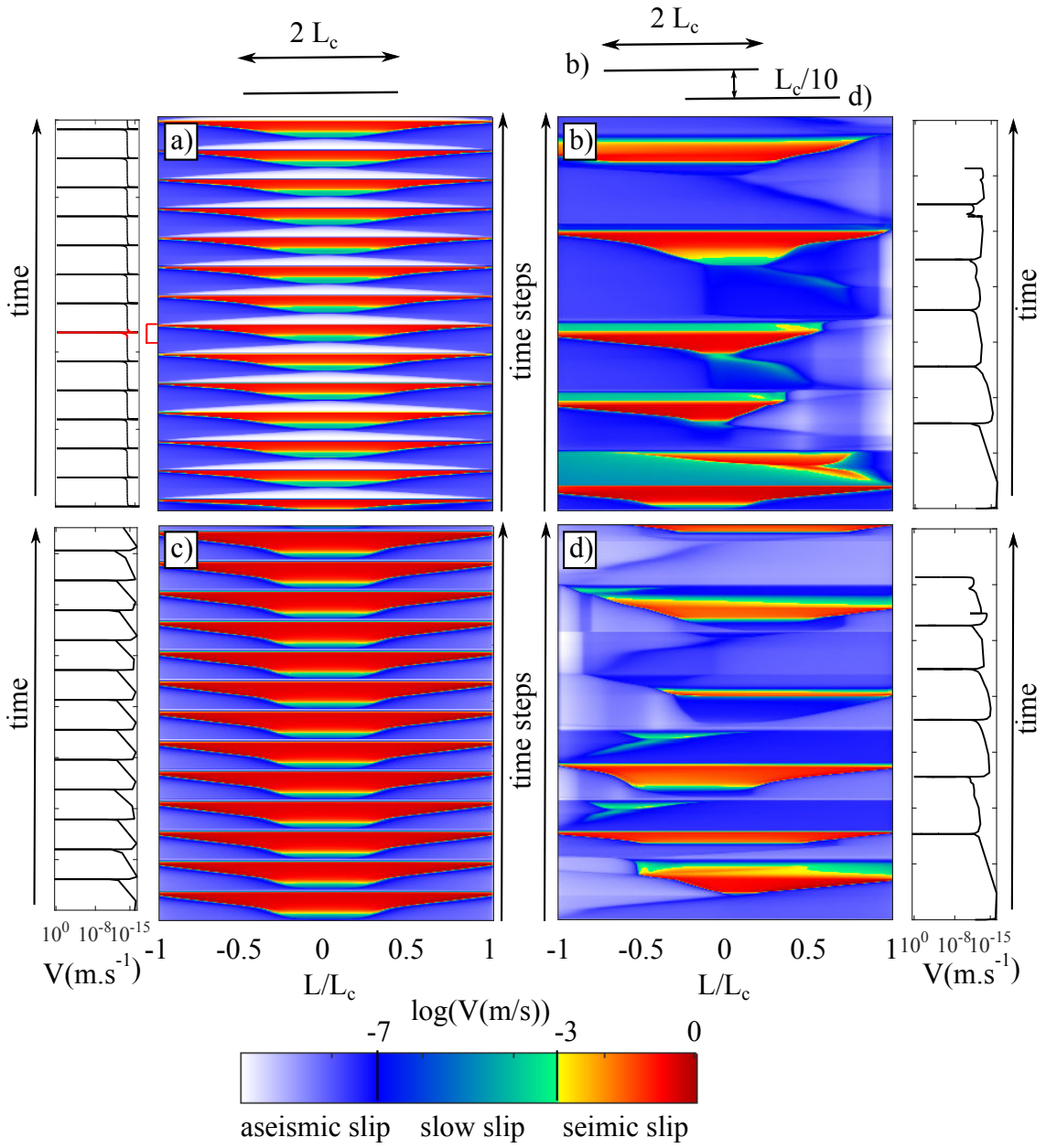


Figure 5.1 – Seismic cycle modelled with QDYN (a) and with Fastcycle (b, c and d), on one single fault (a and c) and on two faults separated by the tenth of their nucleation size (b and d). The horizontal axis shows the fault length normalized by the nucleation size. Velocity is plotted at each time-step and color-coded as a function of dynamic ($> 10^{-3}$ ms$^{-1}$), quasi-dynamic ($> 10^{-6}$ ms$^{-1}$) or aseismic ($< 10^{-7}$ ms$^{-1}$) values.

### 5.2.2 How to model earthquakes of different sizes ?

The first quasi-dynamic model I used, QDYN, inherently produces a regular seismic cycle with periodic earthquakes of similar magnitudes. To overcome this difficulty, several methods exist, which are described in section 5.2.2.1. However, this lead to an increase in computational time which can become problematic when it comes to model earthquakes with several orders of magnitude (section 5.2.2.2 ).

#### 5.2.2.1 Spatio-temporal complexity in earthquake cycle

In quasi-dynamic simulations, well discretised faults with constant friction parameters do not lead to any complexity (Rice, 1993). As an example, figure 5.1a shows a typical earthquake cycle modelled with QDYN,

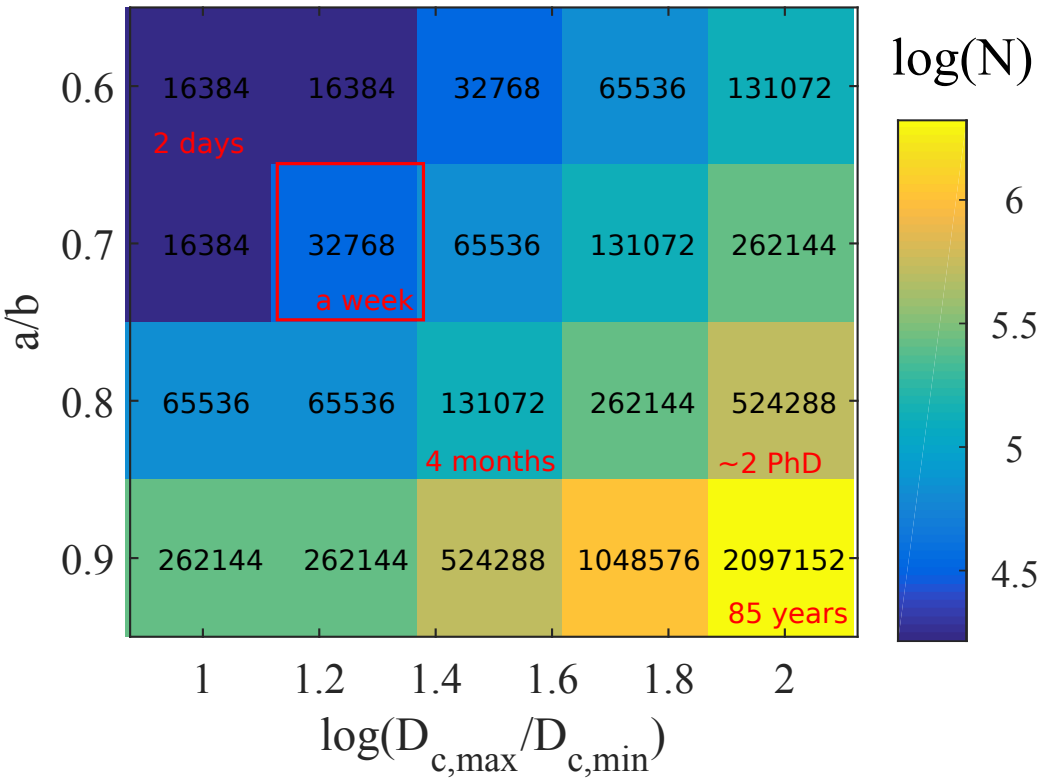


Figure 5.2 – Number of cells N needed in simulations with heterogeneous $D_c$ as a function of the ratio (a/b) and the ratio between maximum and minimum values of $D_c$. Approximative computation times are indicated in red. Red box shows the simulation parameters (a/b = 0.7, $\frac{D_{c,max}}{D_{c,max}} = 17$) chosen for QDYN simulations detailed in section 5.3.

on a fault with standards and homogeneous friction parameters. In the figure, velocity is plotted as a function of the position along the fault (x axis) and the time-step (y axis). In this type of plot, we use the time-step number to plot velocity instead of time, which is non-linear because of the adaptive time-stepping procedure. Therefore, the seismic events are stretched and the interseismic periods are compacted. In figure 5.1a, the fault ruptures periodically, producing the same event that ruptures the whole fault.

In order to introduce some variability in the earthquake sequence, two types of methods have been previously used in quasi-dynamic simulations. The first uses a multiscale heterogeneous distribution of frictional properties (Hillers et al., 2006, 2007, Ide and Aochi, 2005). This can generate earthquake frequency-size statistics spanning several orders of magnitude. The other type of method is to use a spatially discrete model, i.e., a model where the computational cell is oversized compared to the nucleation size predicted by the rate-and-state parameters (Ziv and Cochard, 2006). This method has been criticized because of the problem of reproducibility, as the results are very sensitive to numerical errors in this approach (Rice, 1993). Therefore, I choose to implement a self-similar spatial variation of $D_c$ following Aochi and Ide (2004), Ide and Aochi (2005) to model several earthquake magnitudes.

#### 5.2.2.2 The issue of computational time

To produce earthquakes, the fault must be long enough so the rupture can reach seismic velocities. This length is determined by the nucleation length $L_c$ (I recall here equation 2.17 for a/b > 0.38) :

$$L_c = 2 * \frac{L_b}{\pi(1 - a/b)^2} \tag{5.7}$$

In practice, a ratio of $\sim 10$ between fault length and nucleation size is enough to model seismic ruptures. Moreover, to correctly solve earthquake nucleation, the cell size must be smaller (7-10 times) than the cohesive zone $L_b$ (equation 2.18) :

$$L_b = \frac{ED_c}{b\sigma_n} \tag{5.8}$$

For computational reasons, the number of cells must be a power of 2. Therefore, the number of cells N in a fault is the next power of 2 of $n = R * L/L_b$ (with L the fault length and R the resolution, i.e. the number of $L_b$ units in one cell). The size of the minimum cohesive zone is dependent of the minimum $D_c$ value, and the maximum nucleation size depends on the maximum $D_c$ value. Then, n is expressed as :

$$n = R * L^\star * \frac{2}{\pi} * \frac{1}{(1-\frac{a}{b})^2} * \frac{D_{c,max}}{D_{c,min}} \tag{5.9}$$

Obviously, n increases with $L^\star$ (the ratio between fault length and the maximum nucleation size), and model resolution. Equation 5.9 also shows that the number of cells increases with increasing (a/b) ratio and with the ratio between smallest and largest critical distance $D_c$. Because getting several orders of magnitudes requires several orders of $D_c$, and because the computation time increases as the square of n, we can see difficulty in simulating a significant range of magnitudes (figure 5.2). In the simulations conducted with QDYN and presented in the next section, we set a ratio $D_{c,max}/D_{c,min}$ of 17, which is a good compromise between computation time (approximately one week of simulation for 45 earthquakes) and the ratio between smallest and largest earthquake moment ($\sim$20). Therefore, those simulations do not allow to make statistically robust b-values. However, they provide qualitative insights on the changes in earthquake size distribution under normal stress variations (section 5.3).

## 5.3 Response of a single fault to transient normal stress change, and implications of the effect of large erosional events on the seismic cycle

### 5.3.1 Introduction

Over geological time scales, mountain belts classically grow through the thrusting and thickening of the Earth's crust under tectonic forces (e.g., Dahlen et al., 1984, Davis et al., 1983). This long-term building process is the result of deformation by viscous, ductile and brittle processes and by slip along major faults, leading to rock uplift over a succession of seismic cycles (King et al., 1988, Le Béon et al., 2014). Mass transfers at the Earth's surface due to erosional processes imply stress changes at depth. Based on numerical modelling results, these stress changes can influence the size of mountain ranges and their long-term deformation (Willett, 1999, Whipple, 2009) and even enhance fault slip over one to several interseismic periods (Cattin and Avouac, 2000, Calais et al., 2010, Vernant et al., 2013). However, the influence of erosion on seismicity at short time scales (100-1000 years) is poorly understood.

A seasonal modulation of seismic activity is observed in many tectonically active settings such as the Himalayas (Bollinger et al., 2007), Japan (Heki, 2003) or California (Gao et al., 2000). These seasonal changes correlate well with static stress changes due to the annual variations of snowload (Christiansen et al., 2007, Heki, 2003), annual precipitation (Bollinger et al., 2007) or atmospheric pressure changes (Gao et al., 2000). In turn, these surface processes are suggested to modulate seismicity, despite their relative low magnitude (1-5 kPa) compared to earthquake stress drops or to tectonic loading.

Numerical studies suggest that documented erosion rates in active tectonic settings such as Taiwan are high enough to induce static stress changes in the vicinity of shallow faults of 0.25 to 2 bars during the interseismic phase (Steer et al., 2014). Moreover, in mountainous areas, hillslopes experience catastrophic landsliding events due to either large earthquakes or rainfall. Those episodic events mobilize a large volume (up to several $km^3$) of sediments (Keefer, 1994, Marc et al., 2016a, Steer et al., 2018) that are ultimately evacuated by rivers. The time-scale of this evacuation is poorly constrained; however, measurements suggest a time scale of one year to decades for suspended load (Hovius et al., 2011), and recent numerical studies suggest similar time scales for coarse sediments (Croissant et al., 2017). Therefore, such large erosional events are likely to induce sufficiently large static stress changes in the shallow crust to modify the activity of the neighboring crustal faults. For example, Steer et al. (2018) reported a change in earthquake statistics in Taiwan following the 2008 Typhoon Morakot, which triggered 10000 landslides and removed 0.7 $km^3$ of sediments from the hillslopes (Lee et al., 2015, Huang and Montgomery, 2013). They noticed an increase in both earthquake frequency and b-value (i.e., an increase in the proportion of small earthquakes compared to large ones) directly following the typhoon and lasting at least 2.5 years. However, no other direct observation of erosion-induced seismicity change has been made at this time scale.

Understanding the potential effects of large erosional events on earthquake cycle requires understanding of fault response to transient shear stress increase or normal stress decrease (Steer et al., 2014). To address this question, it is necessary to account for the time-dependency of fault friction, simple static stress change calculations offering limited comprehension of the problem (Ader et al., 2014). How fault respond to stress changes have been investigated through numerical modelling studies either for continuous periodic stress perturbations (Perfettini et al., 2001, Ader et al., 2014) or for static stress steps (Dieterich and Kilgore, 1994, Kaneko and Lapusta, 2008), but never for one single but transient event.

Fault response to periodic normal (Perfettini et al., 2001) or shear stress variations (Ader et al., 2014) have been derived. In such studies, the fault is simplified to a spring-slider block with a rate-and-state friction law (Dieterich, 1979, Rice and Ruina, 1983). Those models show a dependency of fault response to the perturbation period. Using a numerical model to study finite fault response to such periodic stress

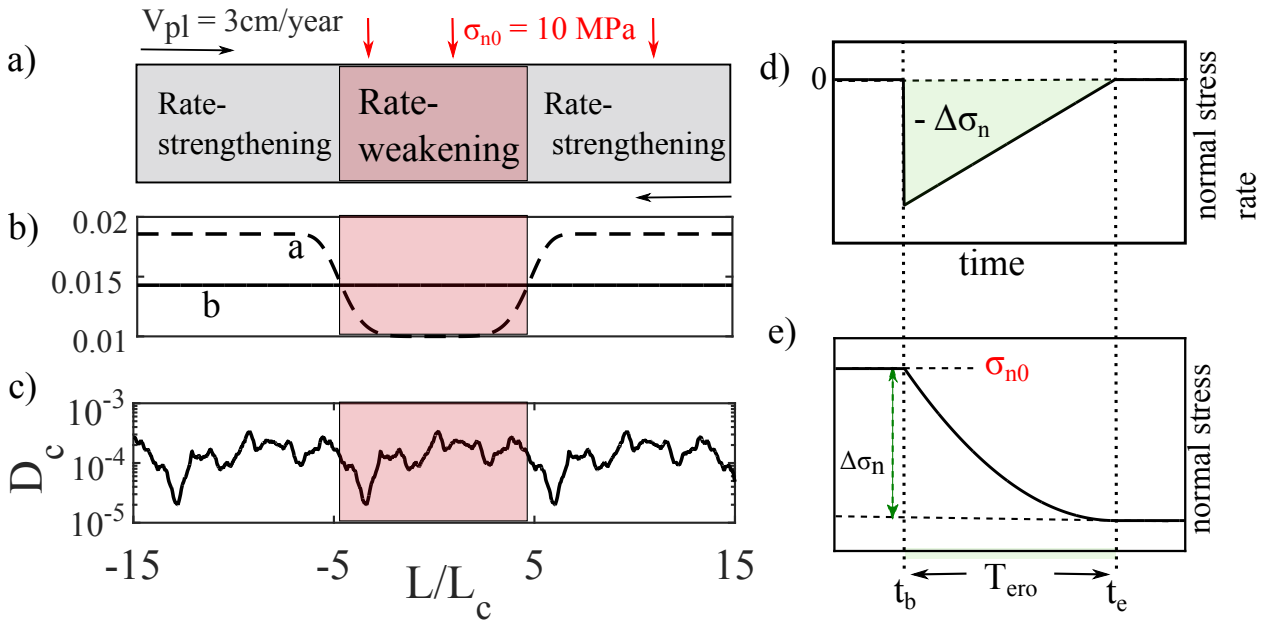


Figure 5.3 – Numerical setup used in this study. a) Schematic of the simulated fault. Slip weakening acts over the central portion of the fault, of length 10 $L_c$. The fault is loaded at velocity $V_{pl}$ = 3 cm/yr and a constant normal stress $\sigma_n$ acts over the whole fault. b-c) Along-strike distribution of friction parameters (b) and critical distance $D_c$ (c). d) Normal stress rate temporal variation implemented in QDYN to model one large erosional event, and the corresponding variation of normal stress (e). Before the landsliding event, the normal stress is constant and has a background value $\sigma_{n0}$. Erosion begins at time $t_b$. A quantity $\Delta\sigma$ is removed over a period $T_{ero}$ until a new background value of normal stress is reached at $t_e$.

variations, Ader et al. (2014) demonstrated that finite faults are highly sensitive compared to rate-and-state spring slider models. Kaneko and Lapusta (2008) and Ader et al. (2014) found similar conclusions studying a finite fault response to static shear stress step.

In this paper, we use a numerical model that considers a single fault embedded in an elastic medium, obeying rate-and-state friction laws (Dieterich, 1979, Rice and Ruina, 1983, Ruina, 1983), to investigate the effects of one large erosional event on seismic cycle. We model the effects of erosion by a decrease in normal stress and study the fault response in term of seismicity rate and earthquake size distribution.

### 5.3.2 Methods

We study the behavior of a one-dimensional fault embedded in an elastic medium, as shown in figure 5.3. For that purpose, we used QDYN (Luo et al., 2017), a boundary element software that simulates fault slip under the quasi-dynamic approximation (i.e., quasi-elasticity with radiation damping). The adaptive time-stepping implemented in QDYN allows simulation of earthquake cycles including seismic and aseismic slip. The friction acting on the fault interface obeys a rate-and-state friction law (Marone, 1998) :

$$\tau = \sigma_n \times \left[\mu_0 + a\ log\left(\frac{V}{V_0}\right) + b\ log\left(\frac{\theta V_0}{D_c}\right)\right] \tag{5.10}$$

where $\tau$ is the shear stress, $\sigma_n$ is the applied normal stress, $\mu_0$ is the value of the friction coefficient corresponding to the reference slip rate $V_0$, $\theta$ is the state variable, and $D_c$ is the characteristic slip for state variable evolution. The parameters a and b describe the rate and state dependencies, respectively. The state variable varies according to an ageing law (Ruina, 1983):

$$\dot{\theta} = 1 - \frac{V\theta}{D_c} \tag{5.11}$$

The modelled fault is infinite in one direction and includes a seismogenic patch with rate-weakening properties (a-b $< 0$) surrounded by rate-strengthening areas (a-b $> 0$) (figure 5.3a and b). The steady-state frictional properties are constant along the fault ($\mu_0 = 0.6$ and $V_0 = 1.10^{-9}$ m.s$^{-}$1). The value of b is 0.014 and a varies from 0.02 in the rate-strengthening domain to 0.01 in the seismogenic zone, where a/b = 0.7 corresponding to rate-weakening properties. The fault is loaded at velocity $V_pl$ = 3 cm/yr, the applied normal stress is 10 MPa, corresponding to a depth around 1-5 km (Suppe, 2014), and the medium has a shear modulus of G = 30 GPa. In such quasi-dynamic simulations, seismogenic patches with constant frictional properties produce one characteristic, repeating event (Rice, 1993). Spatio-temporal complexity can be obtained by varying in space the critical distance $D_c$ by several orders of magnitude (Hillers et al., 2006, 2007, Ide and Aochi, 2005). To generate earthquakes with various magnitudes, we thus vary $D_c$ along the strike of fault following a self-similar pattern in the rate-weakening zone (figure 5.3c) that we repeat in the rate-strengthening zone. The size of the cohesive zone $L_b$ (Rice, 1993, Lapusta and Liu, 2009) is defined as:

$$L_b = \frac{GD_c}{b\sigma_n} \tag{5.12}$$

and the characteristic length for nucleation (Rubin and Ampuero, 2005) is :

$$L_c = 2 * \frac{L_b}{\pi(1 - a/b)^2} \tag{5.13}$$

These need to be chosen in order to correctly capture the model response. We set the length of the seismogenic patch to 10 $L_c$ in order to get dynamic events. Cell size is set by the minimum cohesive zone, which is in turn set by the minimum $D_c$ value. The seismogenic patch length is set by the maximum nucleation size, which depends upon the maximum $D_c$ value. Therefore, the number of cells in the model depends directly on the ratio between maximum and minimum $D_c$. Here we vary $D_c$ between $2.10^{-5}$ and $3.4.10^{-4}$ m in the seismogenic patch, so the minimum $L_b$ value is 4.2 meters, and the maximum $L_c$ = 561 m. This ratio of 17 between minimum and maximum $D_c$ values allows us to model seismic moments covering one order of magnitude within a reasonable computation time (one week for a typical simulation of 30 years). The modelled fault is discretized into 32768 cells, ensuring at least 8 cells per minimum $L_b$ unit.

To model the effects of an erosional event, we here assume that erosion leads mostly to change in the normal stress of a fault. The amplitude, duration and functional relationship of the change in normal stress need to determined. Using an elastic half-space model, Steer et al. (2014) showed that co-seismic erosion in active mountain belts such as Taiwan can raise the Coulomb stress on a fault by 0.01-1 MPa in the first few kilometres of the crust. In our model, this corresponds to 0.1-10% of the imposed background normal stress. The duration of erosion depends on many factors such as the landslide connectivity to the drainage network, which often displays significant variation among catchments (Li et al., 2016). It is also controlled by the river dynamics (Croissant et al., 2017, Yanites et al., 2010), and the grain size distribution of landslide sediments (Sklar and Dietrich, 2006, Cowie et al., 2008, Egholm et al., 2013). The inferred residence times of landslide sediments varies between 1-10 years (Hovius et al., 2011, Croissant et al., 2017), several decades (Howarth et al., 2012) to several centuries (Yanites et al., 2010, Stolle et al., 2018). Compared to the duration of a 100 to 1000 years seismic cycle, about (Sieh et al., 1989, Shimazaki and Nakata, 1980, Chen et al., 2007), it leads to a ratio between erosion duration and seismic cycle ranging between $10^{-3}$ and 10. For the functional relationship describing erosion or normal stress through time, we vary the normal stress in time following the observation of Hovius et al. (2011), who showed a sharp increase in erosion rate just after the earthquake, followed by a linear decrease down to its background value. Following this pattern, we implement a sudden change in normal stress rate (figure 5.3d) followed by a linear increase that lasts a certain period $T_{ero}$. The total removed normal stress integrated over $T_{ero}$ is $\Delta\sigma_n$ (figure 5.3). We test different scenarios, with $\Delta\sigma_n$ varying between 0.01 and 1 MPa and $T_{ero}$ between $10^{-3}$ and 10 times the duration of one modelled seismic cycle. This corresponds to mean normal stress rate of 6.34 Pa/s ($\Delta\sigma$ = 1 MPa, $T_{ero}$ = 0.01 years) to $1.5.10^{-5}$ Pa/s ($\Delta\sigma$ = 0.01 MPa, $T_{ero}$ = 20.48 years), corresponding to 5000 to 0.01 times the background loading rate

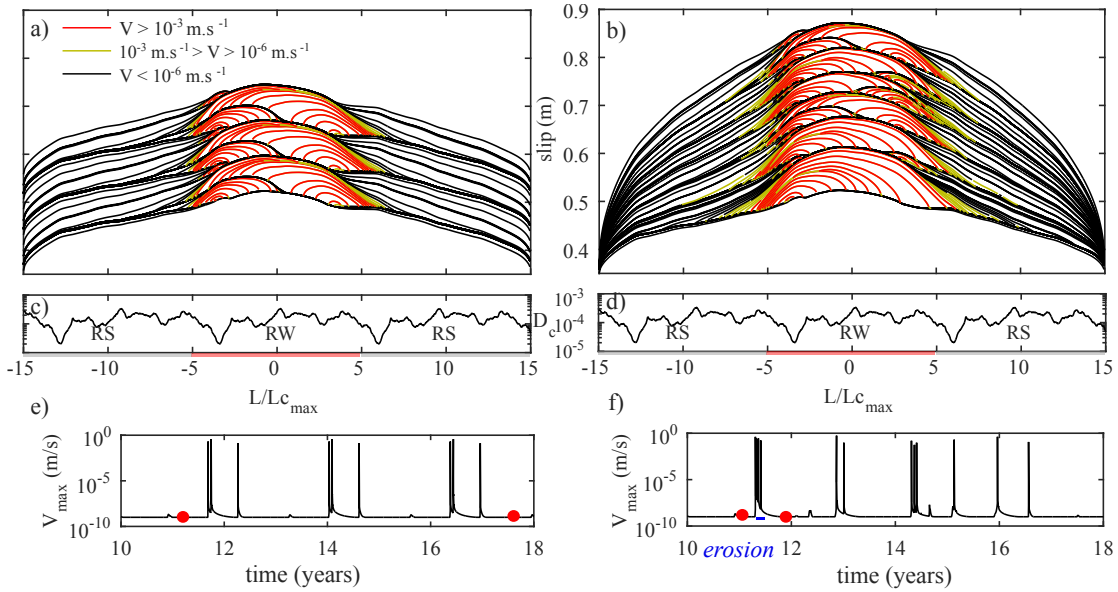


Figure 5.4 – Cumulative slip along strike for a) the undisturbed fault and b) the fault under $\Delta\sigma_n$= 1 MPa and $T_{ero}$ = 0.08 years. Aseismic slip (V < $10^{-6}$ m/s) is plotted in black, slow slip ($10^{-3}$ m/s > V > $10^{-6}$ m/s) in green, and seismic slip (V > $10^{-3}$ m/s) in red. The along-strike value of $D_c$ is plotted in inset c and d, and the rate-strengthening (RS) and rate-weakening (RW) areas are shown in red and green, respectively. e – f) Maximum velocity on undisturbed (e) and disturbed (f) fault between 10 and 18 years. The red dots show the temporal interval used to plot cumulated slip in a) and b), respectively. The erosion is applied a t = 11.3 years; its duration is shown by the blue line.

imposed by the plate velocity (∼1.2.$10^{-3}$ Pa/s). We implement the onset of the normal stress perturbation during the interseismic period once the cycle is stabilized (i.e., produces regular events). In the following, the term 'erosion' refers to normal stress decrease.

To construct the earthquake catalogue, we compute a linear moment rate (equation 5.15) by integrating the velocities over the seismogenic patch :

$$\dot{M}_0(t) = GZ \int V(x,t)dx \tag{5.14}$$

where V(x,t) is the velocity at the location x on the fault at time t, G is Young's modulus and Z is the fault width that we set to Z = 10 km. We then isolate seismic events using a threshold of $M_{0,lim}$ = $10^8$ dyn.cm$^{-2}$.s$^{-1}$, corresponding to the onset of seismic slip in a typical simulation. Changing the moment rate threshold, for example to $10^9$ dyn.cm$^{-2}$.s$^{-1}$, will slightly change individual earthquake magnitudes but does not change the main results of this study. We integrate the moment rate over earthquake duration to compute the moment magnitude:

$$M_w = \frac{2}{3}\, log(M_0) - 6.07 \tag{5.15}$$

## Results

Figure 5.4 a) shows a typical seismic cycle without any normal stress perturbation. A sequence of three characteristic earthquakes repeats with a period of ∼ 2.2 years. The sequence is composed of one first earthquake of intermediate size, which initiates in the lowest $D_c$ value area and expands over half of the seismogenic zone. It is followed by another earthquake that ruptures the entire rate-weakening patch, and then by a small earthquake initiating again on the area of low $D_c$. The magnitudes of those three typical events are 4.85, 5.20 and 4.18, respectively (figure 5.8). Figure 5.4b) shows fault slip in the case of a normal

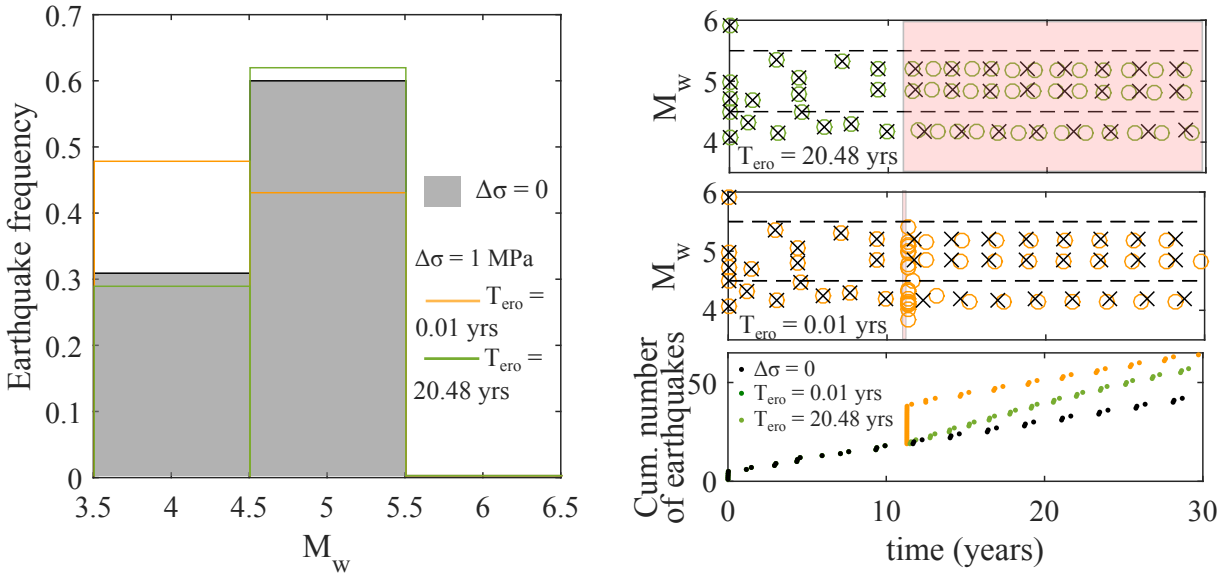


Figure 5.5 – a) Frequency of earthquakes during the erosion period, with $\Delta\sigma = 1$ MPa. The grey bars show the earthquake distribution for the undisturbed fault. Coloured edges show the distribution for two cases with different $T_{ero}$ values. Panels b) and c) show time evolution of earthquake magnitudes (circles) for these two cases ($T_{ero} = 0.01$ year and 20.48 years), compared to the undisturbed fault (black crosses). The period of erosion is shown by the red box. The horizontal dotted lines show the edges of the bins used in a). d) Cumulative number of earthquakes shown for $T_{ero} = 0.01$ year and 20.48 years, and for undisturbed fault (black dots).

stress perturbation with $T_{ero} = 0.08$ years and $\Delta\sigma_n = 1$ MPa. The seismicity rate increases during the erosion period. The first earthquake is a large one, $M_w = 5.34$, that ruptures the entire patch and is followed by a succession of earthquakes with various magnitudes between 4.01 and 5.22 that are not always characteristic of the sequence shown in figure 5.4a). Particularly, nucleation of small events occurs on the right-hand portion of the fault, which is not characterized by small $D_c$ values.

To characterize the size distribution of earthquakes, we bin the earthquake inventory into two categories: $M_w > 4.5$ and $M_w < 4.5$, corresponding to our arbitrary definitions of large and small ruptures. We compute the relative frequency of large and small earthquakes during $T_{ero}$. Figure 5.5 shows two typical examples of simulations displaying different response in term of earthquake size. For $T_{ero} = 20.48$ years, earthquake frequency increases by a factor close to two during around ten years, and then progressively goes back to its background value (figure 5.5b). The characteristic sequence is advanced in time without changing the magnitude of events. For $T_{ero} = 0.01$ years, earthquake size variability increases (figure 5.5c), with a proportion of small events increased by 60% (figure 5.5a).

These observations illustrated in figure 5.4 and 5.5 are summed up in figure 5.6. For each model, we compute the number N of earthquakes during erosion, and earthquake frequency over erosion (i.e., $N/T_{ero}$). We plot earthquake statistics during the erosional event, as a function of $T_{ero}$ normalized by the duration of the seismic cycle of the undisturbed fault ($T_{cycle}$) or by the nucleation time of a typical earthquake ($T_{nuc}$). For all values of $\Delta\sigma_n$, we show an increase in earthquake frequency (figure 5.4a) that depends at first order on the total removed normal stress. It increases by a factor of 1-2 for $\Delta\sigma_n = 0.01$ MPa, 1-100 for $\Delta\sigma_n$=0.1 MPa and 1-10000 for $\Delta\sigma_n = 1$ MPa.

Earthquake frequency also increases with decreasing $T_{ero}$. For $T_{ero} > 2\ T_{cycle}$, earthquake frequency is almost constant, and consequently the number of earthquakes decreases with decreasing erosion period (figure 5.6a). When erosion acts over a time that is shorter than the duration of a seismic cycle, earthquake

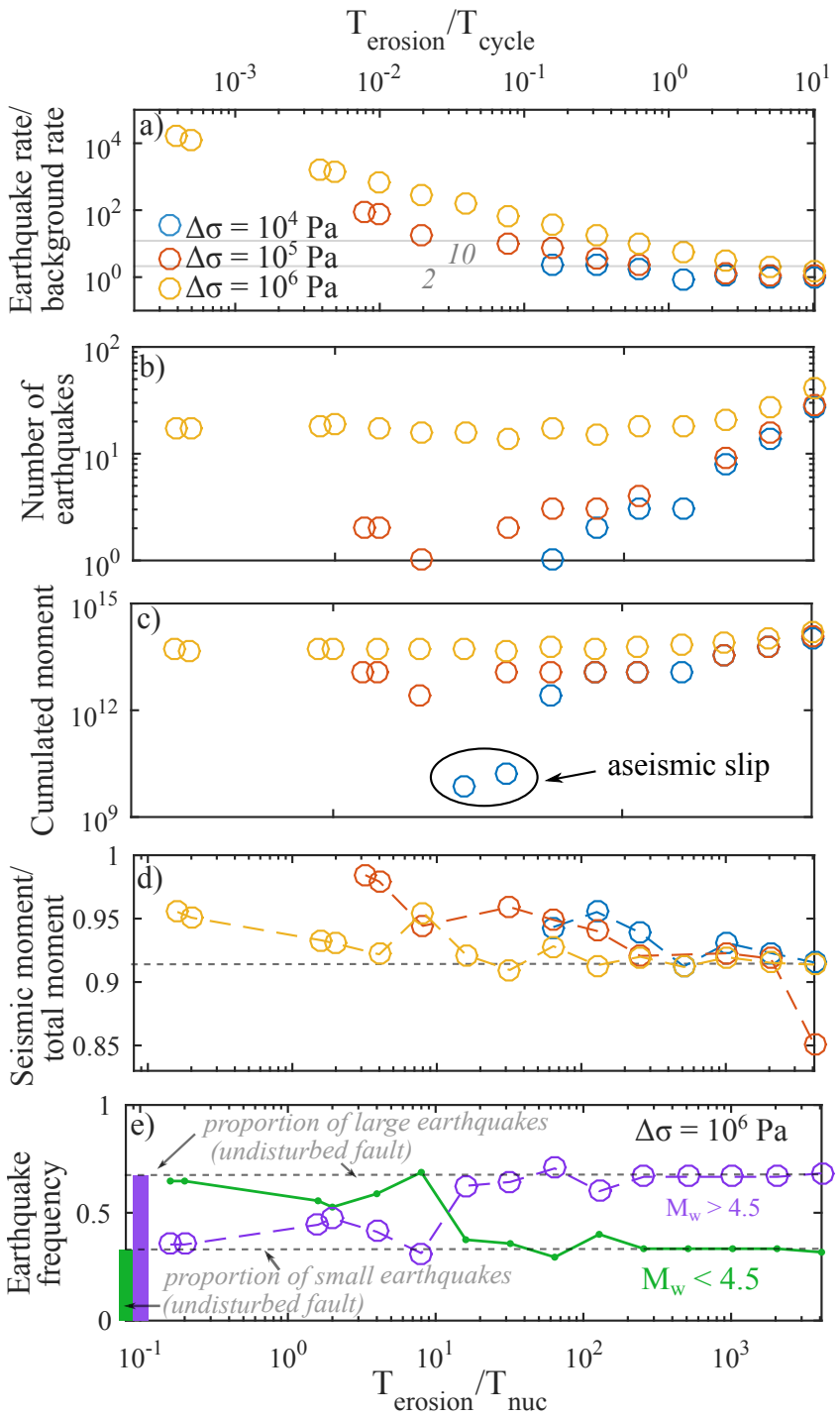


Figure 5.6 – a) Earthquake rate during erosion, normalised by the rate of the undisturbed fault. The dots represent the models for which at least one earthquake occurs during erosion. b) Number of earthquakes during erosion. C) Cumulated moment during erosion. The two points quoted "aseismic slip" correspond to two models in which no earthquake occurs. d) Cumulated moment during seismic slip normalised by the total cumulated moment, during erosion. e) Proportion of large ($M_w > 4.5$, purple rounds) and small ($M_w < 4.5$, green dots) earthquakes during erosion for each model with $\Delta\sigma = 106$ MPa. The dotted grey lines extending the bars on the left side of the figure show the proportion of small and large earthquakes in the case of the undisturbed fault.

frequency increases significantly. It increases at least by a factor of 2 for $T_{ero}$ lower than 2 $T_{cycle}$ with $\Delta\sigma_n$ = 1 MPa, and 0.3 or 0.5 $T_{cycle}$ with $\Delta\sigma_n$ = 0.01 or 0.1 MPa, respectively. In the case of $\Delta\sigma_n$ = 0.01 to 0.1 MPa, this increase in earthquake frequency with decreasing $T_{ero}$ stops at $T_{ero}$ = 0.1 $T_{cycle}$ and $T_{ero}$ = $8.10^{-3}$ $T_{cycle}$, respectively. In the case of faster erosion, the normal stress decrease happens over a too short time scale to trigger seismic rupture, and no earthquake happens during that time (figure 5.6b). In the case with $\Delta\sigma_n$ = 1 MPa, earthquake frequency increases with decreasing $T_{ero}$ for all the values tested. Figure 5.6c) shows the cumulative moment over $T_{ero}$ for all the simulations for which at least one earthquake occurs during erosion. At first order, it depends on $\Delta\sigma_n$ and is two orders of magnitude higher for $\Delta\sigma_n = 10^6$ MPa than for $\Delta\sigma_n = 10^4$ MPa. In the models noted 'aseismic slip' in figure 5.6c), the decrease in normal stress triggers an acceleration which aborts when erosion stops, before reaching seismic velocity. We show in figure 5.7 the time evolution of maximum slip velocity for two of these cases. In the case $\Delta\sigma_n$ = 0.1 MPa, $T_{ero}$ = 0.014 years, the normal stress decrease triggers an acceleration that reaches seismic velocity after the erosion stops (figure 5.7 b). The following seismicity rate is not changed significantly after this triggering (figure 5.7a), but the seismic cycle is advanced in time, and erratic during at least 5 years. In the case $\Delta\sigma_n$ = 0.01 MPa, $T_{ero}$ = 0.04 years, the normal stress decrease triggers an acceleration that ceases shortly after the end of the erosion period (figure 5.7d). The small moment release causes a delay in the next earthquake compared to the case with no perturbation (figure 5.7c), with no major changes in the following earthquake cycle.

Figure 5.6d) shows cumulative moment over seismic slip normalized by the cumulative moment over all erosion. It is higher than background value for all models, and tends to be higher for smallest $\Delta\sigma_n$, showing that aseismic slip represents a higher part of overall slip in the case of largest $\Delta\sigma_n$. Figure 5.6e shows the proportion of large ($M_w > 4.5$) and small ($M_w < 4.5$) earthquakes during erosion ($\Delta\sigma_n$ = 1 MPa). For all models, the proportion of large and small earthquakes is lower and greater, respectively, than in the undisturbed case. This is not the case for $\Delta\sigma_n$ = 0.1 and 0.01 MPa (figure 5.11). In these cases, the distribution of event sizes does not change significantly. For $\Delta\sigma_n$ = 1 MPa and $T_{ero} > T_{nuc}$, the size distribution of earthquakes does not vary with $T_{ero}$. However, for $T_{ero}$ < 5-10 $T_{nuc}$ the proportion of small events increases and become larger than the proportion of large ones (see figures 5.9 and 5.10).

### 5.3.3 Discussion and concluding remarks

We have implemented a transient normal stress variation in a quasi-dynamic model of the earthquake cycle to mimic the effect of a large, erosional event of amplitude $\Delta\sigma_n$ during a certain time $T_{ero}$. The large erosional event results in an increase in earthquake frequency. Indeed, earthquake frequency raises with decreasing $T_{ero}$ and with increasing $\Delta\sigma_n$. Earthquake frequency increases by at least a factor 2 for $\Delta\sigma_n$ between 0.01 and 1 MPa, (0.1 to 10% of the background normal stress), when $T_{ero}$ is smaller than the typical duration of the earthquake cycle. For $\Delta\sigma_n$ = 0.01 to 0.1 MPa, this effect holds for $T_{ero}$ greater than a critical period for which the erosion applies at too short of a time scale to increase seismicity rate. This critical period corresponds to 0.5 ($\Delta\sigma_n$ = 0.1 MPa) to 5 ($\Delta\sigma_n$ = 0.01 MPa) times the nucleation time.

Such an amplitude and period-dependency of fault response to environmental stress changes has already been documented. For example, static stress changes below 0.01 MPa were observed to be insufficient to trigger seismicity (Reasenberg and Simpson, 1992, Hardebeck et al., 1998). Seismicity does not systematically display variations at tidal periods (Vidale et al., 1998, Cochran et al., 2004), despite the similar magnitude of static stress change induced by Earth's tides and the hydrological cycle. Period-dependency and amplitude-dependency of fault response to periodic stress variations have also been inferred from laboratory experiments (Lockner and Beeler, 1999, Beeler and Lockner, 2003, Savage and Marone, 2008) and numerical studies (Ader et al., 2014). In laboratory experiments, (Savage and Marone, 2007) showed that at high period, the fault response is amplitude-dependent and at short period, it also increases with increasing frequency; the transition corresponds to the time necessary to displace the critical distance $D_c$. Such a frequency-dependence was also suggested by Ader et al. (2014), who demonstrates the existence of a resonance in fault response to harmonic stress perturbation.

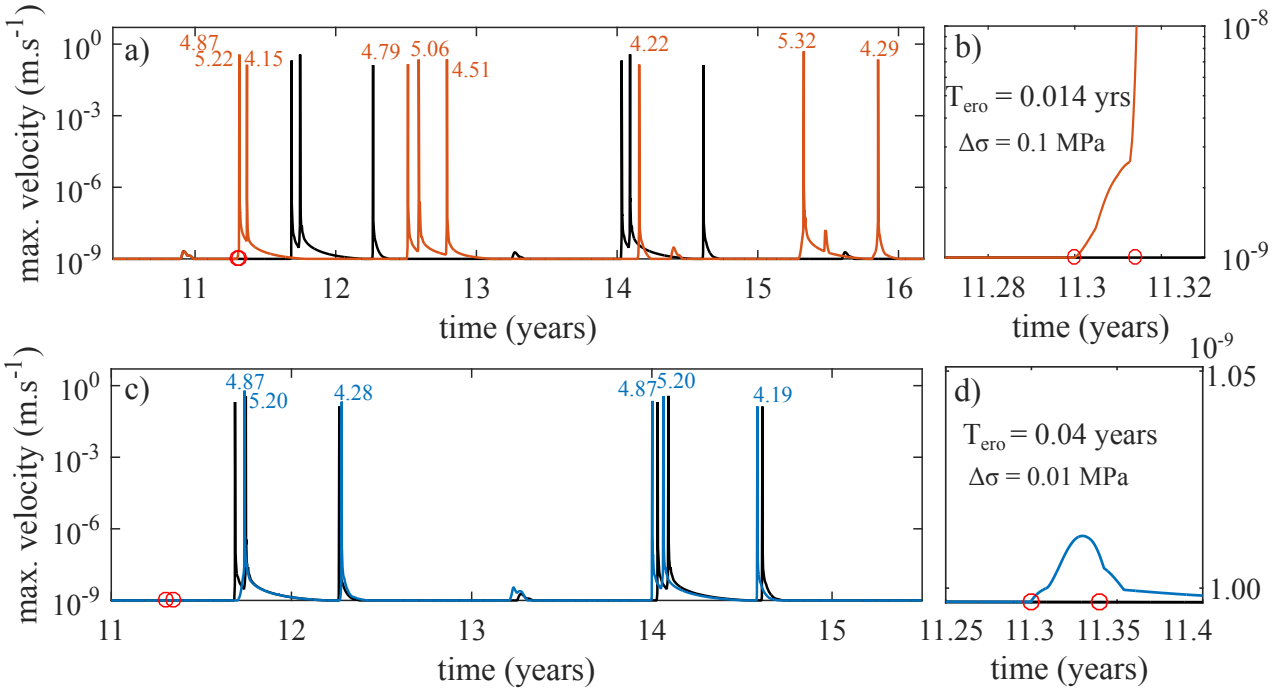


Figure 5.7 – Time evolution of the fault maximum velocity for $\Delta\sigma_n = 0.1$ MPa, $T_{ero} = 0.014$ years (a-b) and $\Delta\sigma_n = 0.01$ MPa, $T_{ero} = 0.04$ years (c-d), labelled with the magnitude of each earthquake. The red dots show the beginning and the end of the erosion period. The insets on the right panels show this time window. The black line shows the time-evolution of velocity on the undisturbed fault.

Here we show that such a period-dependency is also implied in fault response to one transient stress change. There is a range of erosion periods for which normal stress variations of 0.1 to 1% of the background normal stress can significantly trigger seismicity in our modelled fault. This range is set by the typical time-scales of the seismic cycle and earthquake nucleation. In nature, such time scales are about 100-1000 years for a seismic cycle (Sieh et al., 1989, Shimazaki and Nakata, 1980, Chen et al., 2007). Even if it could be as long as centuries (Yanites et al., 2010, Stolle et al., 2018), landscape response to large erosional events is likely to occur at much smaller time scales, from 1-10 years (Hovius et al., 2011, Croissant et al., 2017) to several decades (Howarth et al., 2012). Moreover, it is over the first years that sediment export is expected to be the most intense and significantly exceed background rates of erosion or sediment export (e.g., Hovius et al., 2011, Croissant et al., 2017). The nucleation time of earthquakes is less constrained. Extrapolation of laboratory experiments to the Earth's crust suggests that nucleation of natural earthquakes could last several months (Savage and Marone, 2007) to one year (Beeler and Lockner, 2003), which is shorter than the time needed to evacuate a large amount of sediments in most of the geomorphological settings. Therefore, extrapolated to natural seismic cycle and erosional process time-scales, our results suggest that one large erosional event is likely to increase seismicity at least by a factor of two, if it produces a normal stress decrease of at least 0.1% of the background normal stress. However, these results are likely to depend on the loading rate (Ader et al., 2014) and therefore should change quantitatively depending on the far-field relative velocity.

We also show that under high and rapid normal stress variations, the size distribution of events produced by one fault is likely to change toward more numerous small ruptures, relative to large ones. In our model, this observation can be explained by the fact that earthquakes always nucleate at the boundaries of the seismogenic patch (figure 5.4a), which includes the lowest $D_c$ values (figure 5.3 b-c). However, such observations have also been made with homogeneous faults. For example, (Ader et al., 2014) noted a change in the distribution of events following a step-like increase in shear stress, with a significant number of earthquakes smaller than the smallest earthquake than the fault can produce. In the case of $\Delta\sigma = 1$ MPa, the fault response is quite

simple: earthquake frequency increases with decreasing perturbation duration. For smaller $\Delta\sigma$, our results illustrate the complexity of fault response to transient stress changes. For example, stress variation with low magnitudes ($\Delta\sigma = 0.01$ MPa) occurring within too short a period can trigger transient aseismic slip (figure 5.7c-d), which relieves stress in the nucleation zone and postpones the subsequent earthquake, consistent with the results of (Kaneko and Lapusta, 2008). If the same total normal stress is removed over a longer period, an earthquake is triggered during erosion. Erosion can also trigger aseismic slip that accelerates and results in a seismic event, even if the erosion is finished (figure 5.7 a-b). In those models, the small number of triggered earthquakes does not allow us to make any robust statistical inference. However, it suggests that within a population of faults close to their critical state, even small normal stress variations such as those illustrated in figure 5.7 could trigger numerous earthquakes within or in the years following a large erosional event.

The normal stress variation due to erosion is different from a sudden static shear stress induced by other earthquakes, because it is likely to be transient. However, contrary to hydrological, tidal or atmospheric forcing, surface processes such as erosion and sedimentation are not periodic. Therefore, the induced stress changes are likely to accumulate over time. Our results confirm previous calculations based on static stress changes (Steer et al., 2014), showing that erosion can significantly trigger seismicity at a seismic cycle time-scale, and suggest that such cumulative processes, including large erosional events, but also glacial melting, or human-induced water extraction, may have the potential to significantly contribute to the long-term deformation of the shallow crust.

## 5.4 Supplementary material

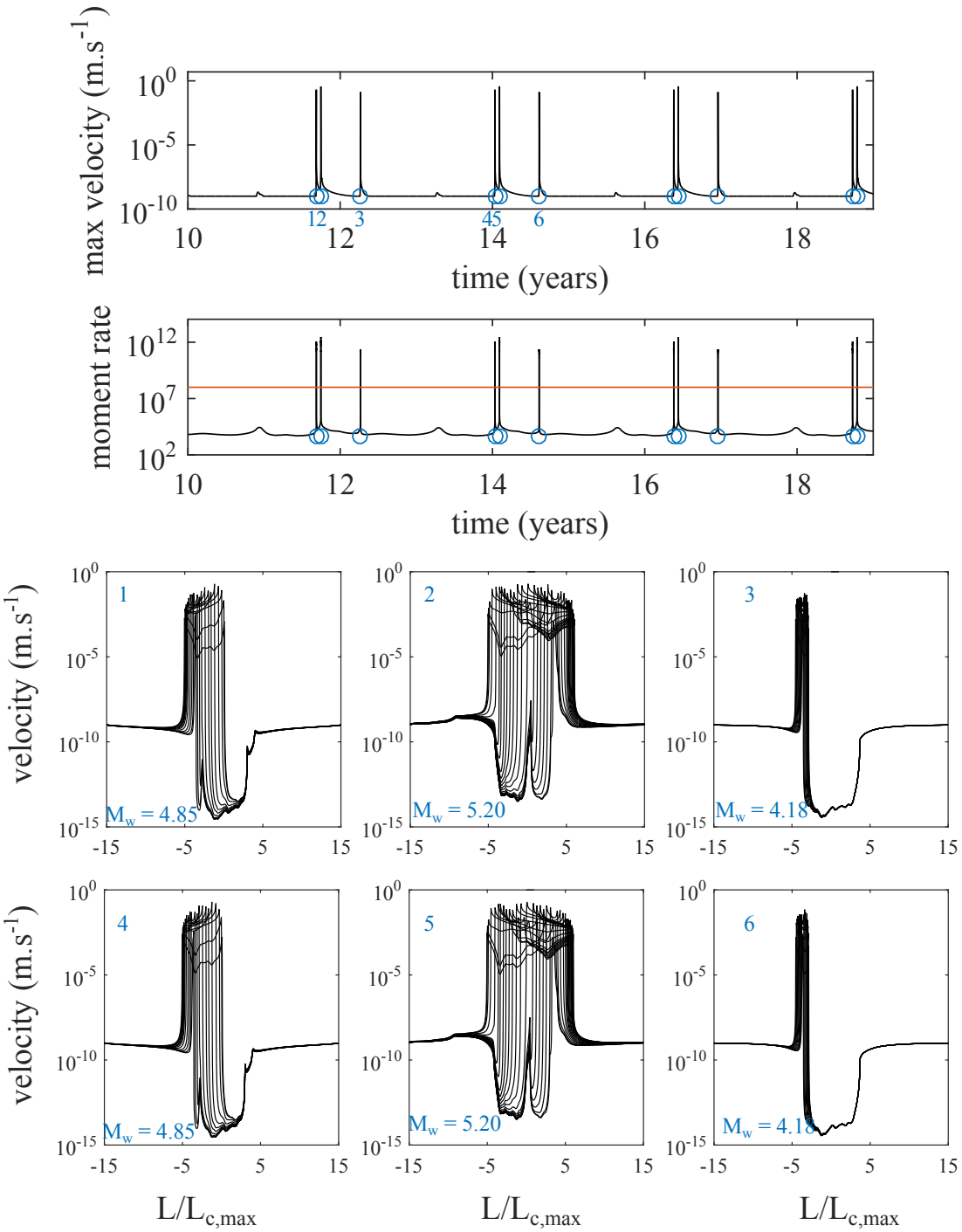


Figure 5.8 – Time evolution of fault maximum velocity (a) and moment rate (b), for the undisturbed fault. The red line shows the threshold moment rate ($10^8$ dyn.cm$^{-2}$.s$^{-1}$) used to define earthquakes. The labelled earthquakes are plotted in the lower panels, showing the along-strike velocity. Each line corresponds to a model time-step.

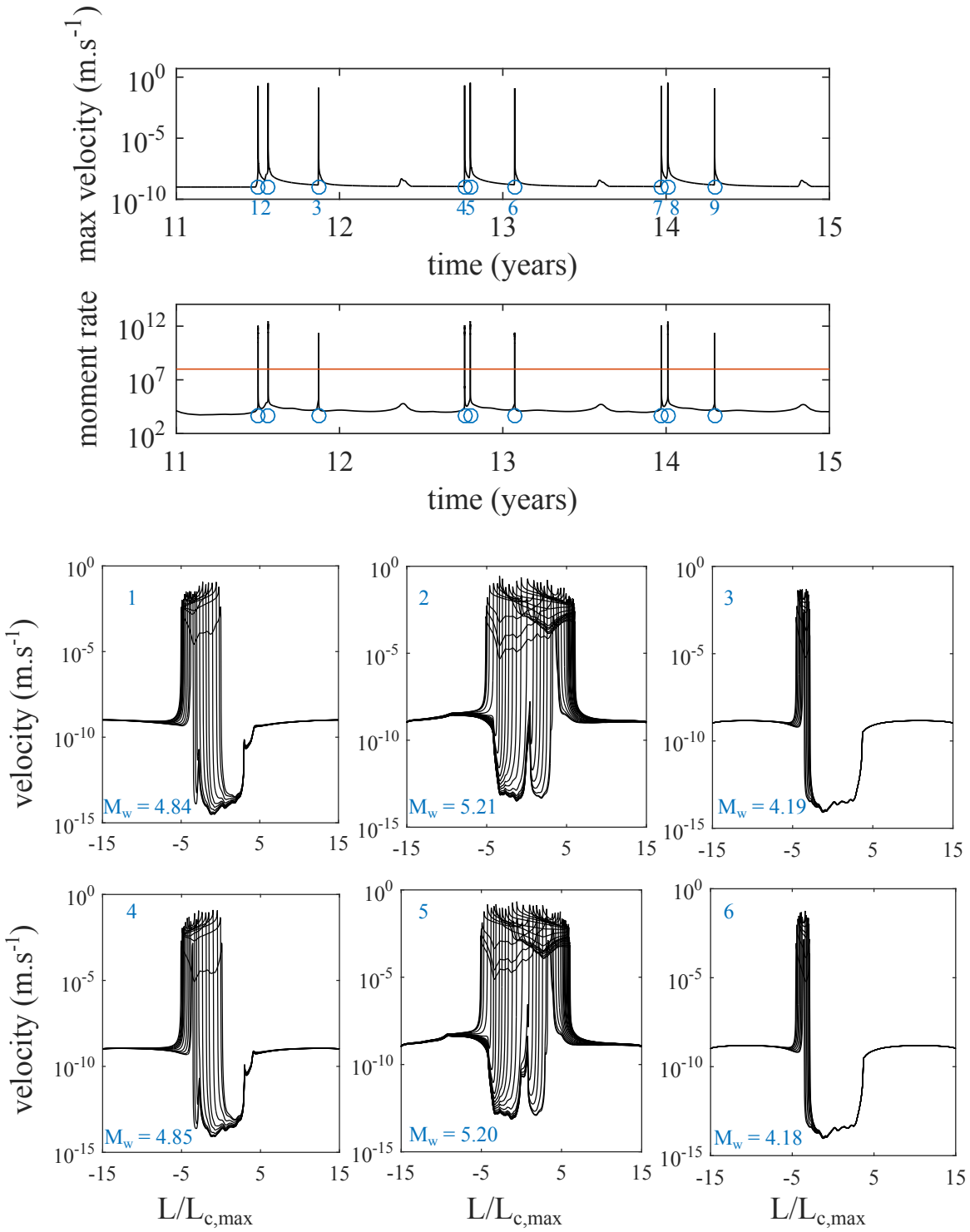


Figure 5.9 – Same as figure 5.8 with $\Delta\sigma$ = 1MPa, $T_{ero}$ = 20.48 years.

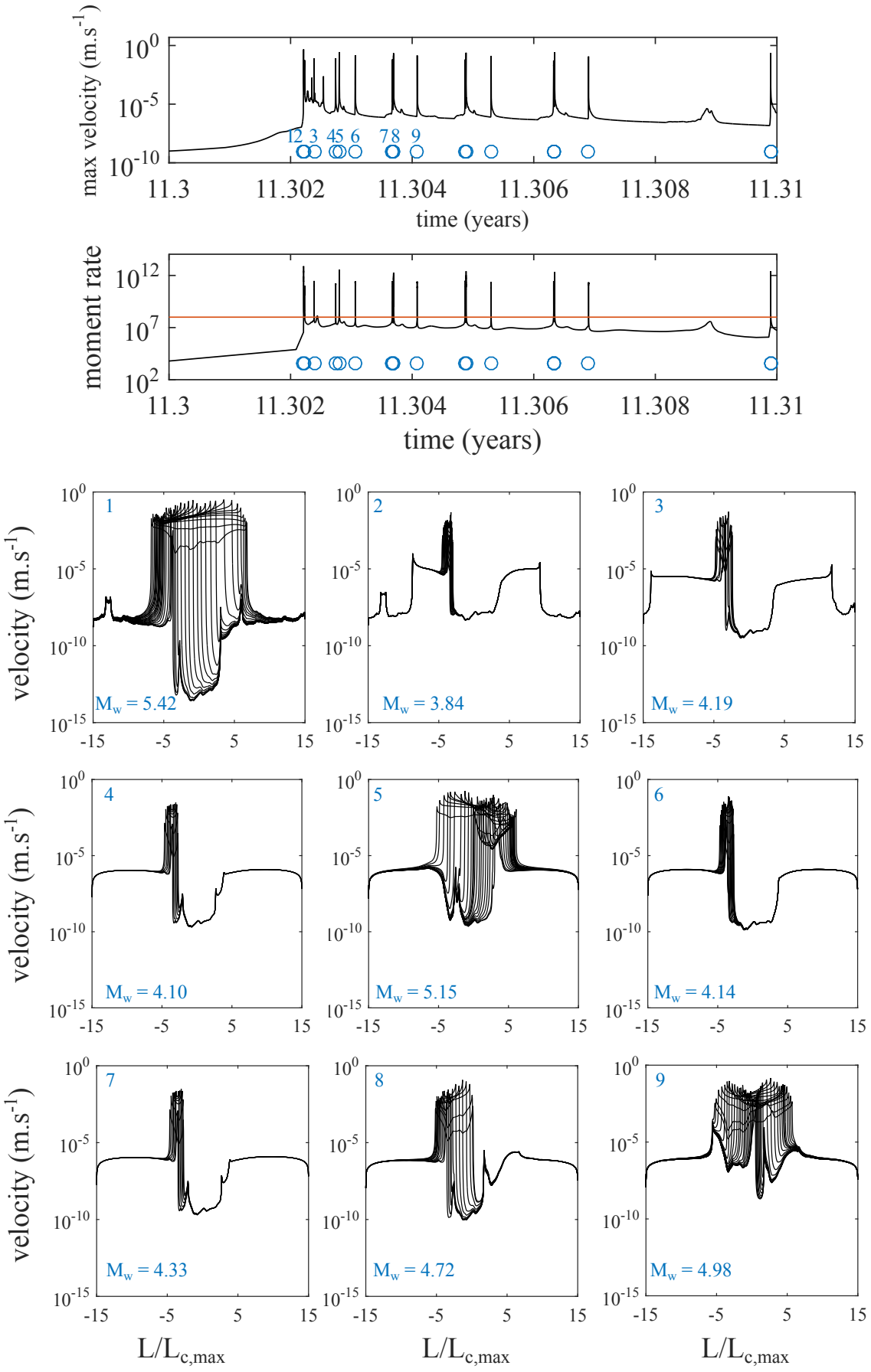


Figure 5.10 – Same as figure 5.8 with $\Delta\sigma$ = 1MPa, $T_{ero}$ = 0.01 years.

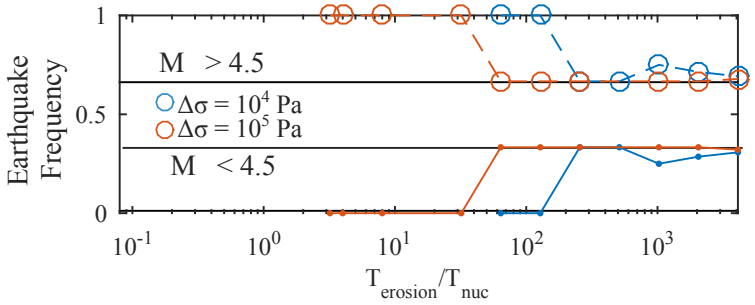


Figure 5.11 – Same as figure 5.7e) for the case $\Delta\sigma_n = 0.01$ (in blue) and 0.1 MPa (in red).

## 5.5 Comparison of homogeneous and heterogeneous fault response

The early observations that natural faults are heterogeneous at a wide range of scales (Brown and Scholz, 1985, Power et al., 1987, 1988) have been reinforced during the last decade together with the recent development of terrestrial LIDAR (Candela et al., 2009, Bistacchi et al., 2011, Thom et al., 2017). Fault plane roughness is thought to control many aspects of fault mechanics and seismic rupture, such as frictional strength and critical slip distance (Scholz, 2002), nucleation process (Tal et al., 2018), and static stress drop (Candela et al., 2011). In the previous section, I have run QDYN on a single fault with heterogeneous frictional properties. This choice was motivated by the purpose of modelling different earthquake magnitudes, to study how earthquake size varies under a normal stress change. However, comparing those results with the behaviour of a homogeneous fault can provide an insight into the role of fault heterogeneities in fault response to transient stress changes.

Here I compare the main results of this study with the same model applied to a fault with the same parameters, within the same medium and under the same loading, but with homogeneous frictional properties ($D_c = 10^{-4}$ meter along all the fault). The ratio between asperity length and nucleation size is also 10. The nucleation size of this fault is 160 meters (equation 5.13), and so the length of this fault is 1.6 km. Because of its constant $D_c$ value, the fault does not need to be as finely discretized as the one modelled in section 5.3 and includes N = 2048 points. In this section, we compute only a linear magnitude $M_{w,lin}$, (or '1D magnitude'). It corresponds to the magnitude computed in section 5.3 but without introducing a fault depth equal to 10 km, which would not make sense for such a tiny fault. This does not change the results qualitatively, the introduction of a depth in the $M_w$ calculation only being useful to expand the range of magnitudes.

This simple fault produces, as expected, a regular earthquake cycle with events of magnitude 2 repeating every $\sim$ 2 years (figure 5.12a). We introduce the normal stress variations at t = 10.4 years (during an interseismic period). For example, a variation of $\Delta\sigma = 1$ MPa, $T_{ero} = 0.01$ years (figure 5.12b) produces three earthquakes during $T_{ero}$, with magnitudes slightly below that of the characteristic event.

Similarly to what was done in section 5.3, we bin the earthquake catalogue, separating the events larger and smaller than $M_{w,lin} = 1.9$. Figure 5.13a) shows the results as a function of $T_{ero}$ for $\Delta\sigma = 1$ MPa (for smaller $\Delta\sigma$, no change in earthquake magnitude with respect to our binning is observed). For $T_{ero}$ larger than twice the nucleation time, no change occurs in earthquake magnitude, and the fault always produces events larger than $M_{w,lin} = 1.9$. For $T_{ero}$ smaller than twice $T_{nuc}$, the catalogue includes a significant proportion ($\sim$ 25-75%) of small earthquakes. This observation is similar to the one made with the heterogeneous fault in the previous section. It confirms that in such models, faults under rapid and large enough normal stress decrease produce smaller earthquakes, even if their mechanical properties a priori do not allow them to produce ruptures of different sizes. This shows that, in the case of the heterogeneous fault, the location of small $D_c$ areas with respect to the tips of the rate-weakening zone is not the only cause of small earthquake triggering.

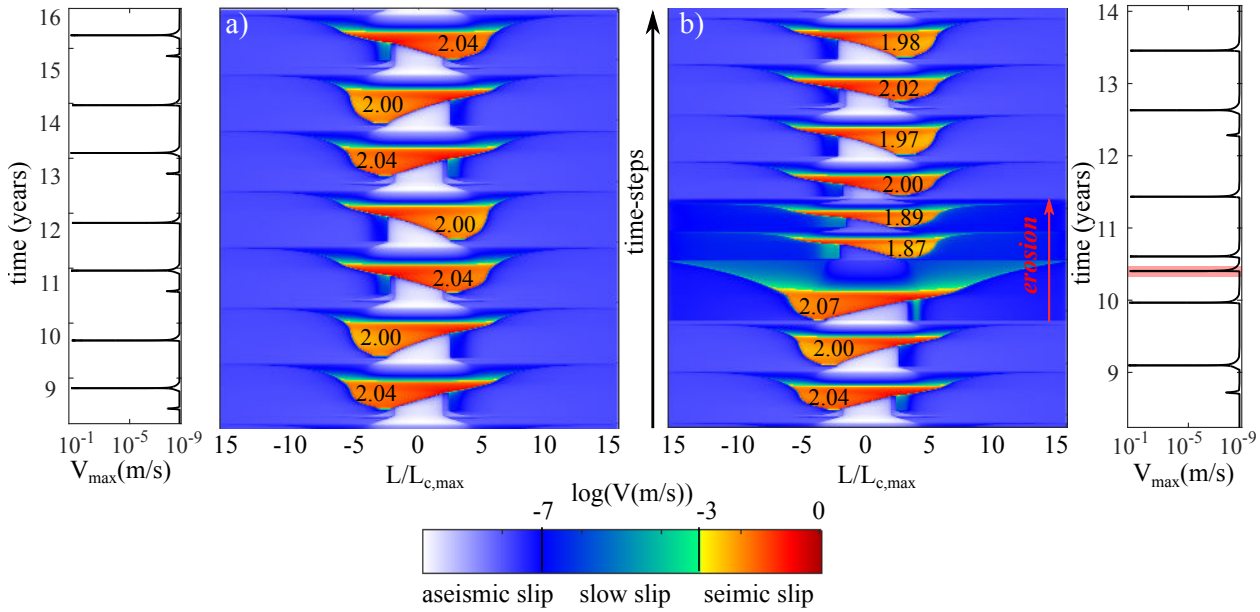


Figure 5.12 – Seismic cycle modelled with QDYN on one single fault with homogeneous frictional properties. a) Undisturbed fault; b) fault with an applied normal stress variation ($\Delta\sigma$ = 1MPa, $T_{ero}$ = 0.01 years). The horizontal axis shows the along-strike distance normalized by the nucleation size; the vertical axis is the number of time-steps. The red arrow and rectangle in b) indicate the duration of erosion.

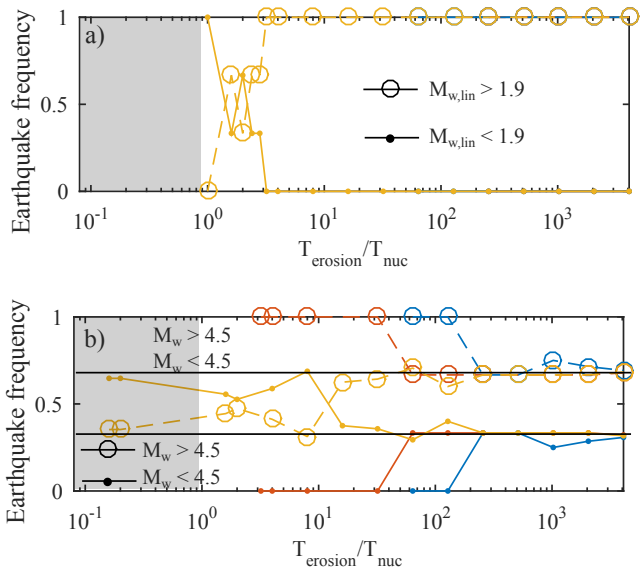


Figure 5.13 – Frequency of large and small earthquakes, separated by an arbitrary magnitude threshold, in a) the case of the simple fault and b) the case of the heterogeneous fault in figure 5.3. See figure 5.14 for color legend. $M_{w,lin}$ in a) is the linear (1D) magnitude computed for the simple fault. $M_w$ is the magnitude computed for the heterogeneous fault, supposing a rupture width of 10 km. The grey box shows the range of $T_{ero}$ for which no simulation was done in the case of the simple fault.

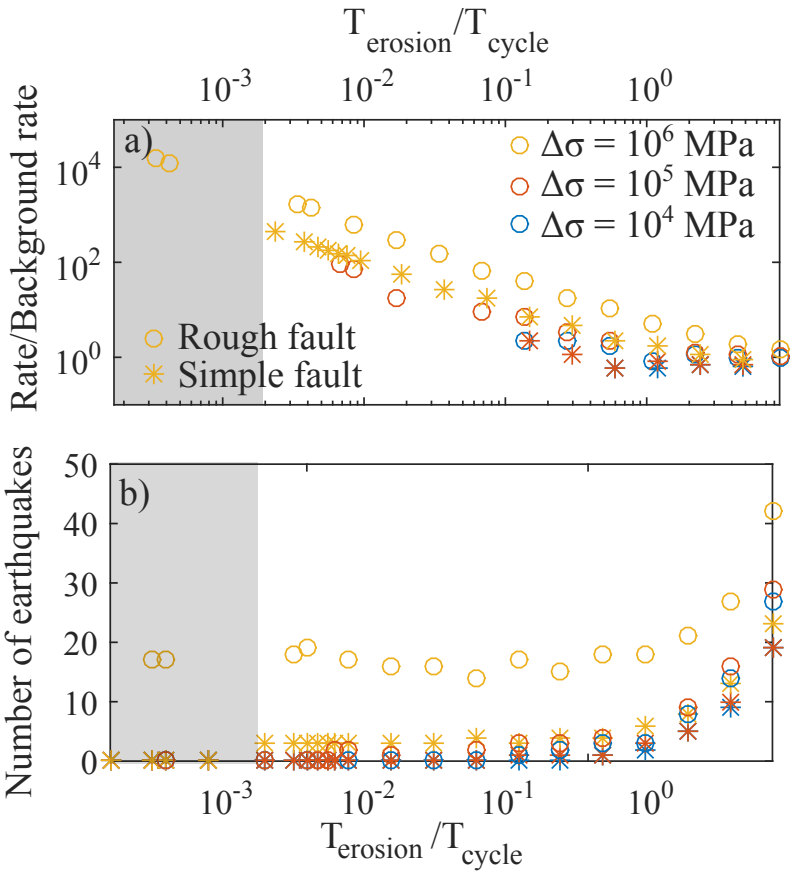


Figure 5.14 – Earthquake rate (a) and number of earthquakes (b) during erosion period, for the case of the simple fault (stars) and the fault with heterogeneous $D_c$ (circles). The grey box shows the range of $T_{ero}$ for which no simulation was done in the case of the simple fault.

The simple fault qualitatively displays the same response in term of earthquake rate as the heterogeneous one (figure 5.14). However, the background seismicity is increased by a higher factor in the case of the heterogeneous fault. For $\Delta\sigma = 1$ MPa, the ratio between seismicity rate during erosion and background rate is $\sim 5$ times larger in the case of the heterogeneous fault. Those results suggest that faults with heterogeneous properties are more sensitive to normal stress changes than homogeneous, idealized faults.

## 5.6 Perspective - modelling a fault network under normal stress change

The release of FastCycle (Romanet, 2017) provided the opportunity to model several faults leading to earthquakes with different magnitudes without increasing dramatically the computation time, which is a great step forward in earthquake cycle modelling. The work of Romanet et al. (2018) has shown that interactions between simple, homogeneous faults lead to complex spatio-temporal slip. A simple example is shown in figure 5.1. Figure 5.1c) shows a fault similar to the one in figure 5.1a) but modelled with FastCycle. As expected, the fault ruptures periodically, producing the same characteristic earthquake. If we add a second fault identical to the first one, separated by a distance small enough compared to their nucleation size (figure 5.1b and d), we can see a rich complexity merging from the interactions between the two faults, with seismic and aseismic slip, and ruptures of different sizes. The next step in this part of my work is to use FastCycle to model a fault network spanning several orders of fault size, leading to several orders of earthquake magnitudes.

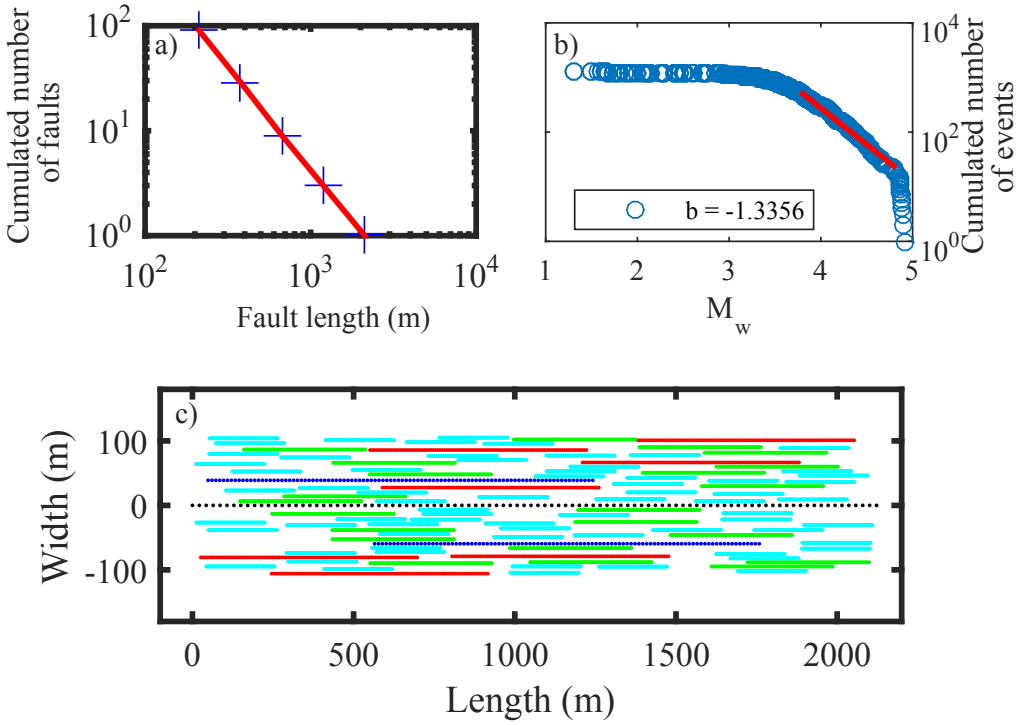


Figure 5.15 – a) Cumulative number of faults as a function of fault length in the modelled network. b) Cumulative number of earthquakes as a function of their moment magnitude, the red line represents a power-law fit, with a b-value of -1.14. c) Geometry of the modelled fault network. The box is 2 km long and 400 m wide. Each color represents a fault size category. The black, dotted line represents the largest fault, located at y = 0. Other faults are randomly distributed around the large one.

Figure 5.15 shows the result of a first attempt to design a fault network capable of producing different earthquake magnitudes, following the procedure developed by Mercury (2018). The modelled network includes 90 faults of five different sizes. Their cumulative distribution follows a power-law with an exponent of -2 (figure 5.15 a), and the ratio between the largest and the smallest fault size is 10. They are distributed randomly around a large, central fault (figure 5.15 c). Because the number of cells in each fault depends on $D_c$, the fault $D_c$ is adapted to the fault length. The proportion $L_{fault}/D_c$ is linearly distributed and increases with fault length. For the largest fault, it is twice the value of the ratio $L_{fault}/D_c$ for the smallest fault. This allows to reduce the number of points in the network, and to significantly save computation time (Mercury, 2018).

Running FastCycle on this setup during 300000 iterations ($\sim$ 4 days), I obtained a catalogue of about 2000 slow and fast ruptures, including 1251 dynamic events. The magnitude distribution of those earthquakes is shown in figure 5.15 b). It follows a power-law over at least one order of magnitude, with a b-value of -1.34.

The next step is to implement a time-dependant normal stress variation on such a fault network to study the b-value changes induced by this perturbation. This step is still ongoing, because of the need to solve numerical issues related to the implementation of the normal stress rate.

# Chapter 6

# Discussion

## 6.1 Main results

This work has allowed improvement of our current knowledge on the processes contributing to shape the Earth's surface at short time scales (10-1000 years). My approach, based on numerical studies, has led to the following results :

1) A very simple mechanical model of landslides, taking into account hillslope geometry, is able to reproduce landslide size distribution. This model has emphasized the importance of cohesion for small landslide distribution, the contribution of 2D rupture propagation for the power-law scaling, and the influence of landscape shape for large landslide size distribution.

2) Hillslope geometry has a fundamental importance in setting the landslide size distribution. A simple criterion measuring the height of unstable hillslopes, $h_C$, is reflected in landslide inventories. This metric is exponentially distributed in many regions of the world and appears to control the large landslide probability.

3) Large erosional events have the potential to significantly trigger seismicity and change the size distribution of earthquakes during sediment export. Constraining the magnitude and duration of the erosion event is fundamental to evaluate the fault response. Our study, modelled on one single fault, must be extended to a population of faults in order to quantify the potential b-value change due to large erosional events.

## 6.2 Rupture processes during the seismic cycle

I have discussed the results of my PhD, presented in the format of scientific papers, in each chapter of my thesis. These results were focused on explaining the role of hillslope mechanical and geometrical properties in controlling landslide size distribution (chapter 3), on the distribution of the unstable height of hillslopes and its influence on landslide maximum size (chapter 4) and on modeling the impact of surface unloading by erosion on the seismicity of faults (chapter 5). I therefore here only examine some common features of landslides and earthquakes, such as their size distributions, and discuss their differences based on my experience acquired during this thesis.

### 6.2.1 Size of rupture events

#### 6.2.1.1 Small events

At small magnitudes, the magnitude-frequency distribution inferred from earthquake catalogues departs from power-law scaling, which is classically characterized by a constant b-value close to 1. This break in the power-law scaling occurs below a threshold in magnitude. This threshold magnitude, referred to as the completeness

magnitude ($M_c$), is traditionally attributed to the detection threshold of the seismic network. Alternatively, some studies suggest there are actually fewer earthquakes of small magnitude than self-similarity predicts (Aki, 1987). However, several earthquake catalogues follow a power-law scaling for very small (Brune and Allen, 1967), and even negative magnitudes (Reyes et al., 1975). The fact that the b-value characterizing microseismicity is in agreement with the b-value characterizing larger earthquakes supports the idea of a scale-invariant rupture process even for small earthquakes (Abercrombie and Brune, 1994). Since instrumental detection threshold is improving, it is now well established that below $M_c$, a fraction of events is missed only due the limit of sensitivity of the seismic network (Wiemer and Wyss, 2000, Woessner and Wiemer, 2005), and that, in turn, $M_c$ does not reflect deviation from self-similar scaling.

On the contrary, for landslide inventories, the fact that the rollover at small areas is not a detection artifact (as it was for instance proposed by Stark and Hovius (2001)), but a robust feature, has become the dominant view. This is supported by the observation of a rollover for recent landslide inventories obtained from satellite imagery with a resolution lower than the characteristic scale of the rollover (Malamud et al., 2004a).

There is therefore a now well established difference between the frequency-magnitude distribution of earthquakes and landslides. At a first order, landslides and earthquakes roughly consist of dynamic ruptures along a possibly existing surface that is favored when the resisting forces (friction and cohesion) are exceeded by the driving forces (elastic force in the tangential direction). In my work, I have demonstrated the major role of cohesion for shallow plane stability and in controlling the existence of a rollover, as also proposed by Stark and Guzzetti (2009). Therefore, one might argue that earthquakes should also follow a rollover at low magnitudes, as they roughly respond to similar physical processes. The differences between landslide and earthquake size or magnitude distribution for small events could result from the role of cohesion in both processes. Indeed, cohesion values, despite their large variability ranging at least from a few kPa to a few MPa, probably become more and more negligible compared to frictional strength, that depends on normal stress, when reaching large stresses at depth. Because landslide rupture occurs at shallow depths, from a few millimeters to hundred meters, compared to earthquakes, I suggest that this might explain the lack of a rollover for earthquake distributions. This is also supported by the general thinking that earthquakes occur along pre-existing faults that can grow during the rupture, with probably very low cohesion (depending on interseismic strengthening processes such as fault healing, (e.g., Muhuri et al., 2003), while landslides are thought to occur on weakened but not fully ruptured surfaces (e.g., Stark and Guzzetti, 2009) that may still be characterized by significant cohesion.

#### 6.2.1.2 Large events

The role of the size distribution of faults on earthquake size have been proposed for decades. For example, Scholz (1997) demonstrated that taking into account the size distribution of faults in nature could explain simply the frequency-magnitude variation of large earthquakes. Interestingly, it has also been noticed that small and large earthquakes (i.e., that do or do not rupture the full depth of the seismogenic zone) exhibit different power-law frequency-magnitude distributions (Pacheco et al., 1992, Triep and Sykes, 1997), with a break in self-similarity at earthquake size corresponding to the depth of seismogenic zone. Earthquakes larger than this size follow a power-law with an exponent higher than for smaller earthquakes. It has also been noticed that this is the case when considering a population of faults, but not when considering a single fault or plate boundary (Wesnousky et al., 1983, Schwartz and Coppersmith, 1984, e.g.,).

Even if this break in self-similarity has been suspected to result from statistical artifacts (Main, 2000), those ideas deserve to be compared to the problem of understanding landslide size distributions. It was proposed that small earthquakes, that are not limited in space, growth according to self-similar scaling; on the contrary, large earthquake, that grows along the fault length, have a frequency-magnitude scaling that depends on the size distribution of natural faults (Scholz, 1997). Our first simulations conducted with FastCycle (chapter 5) also show that the size distribution of natural faults could control the b-value exponent.

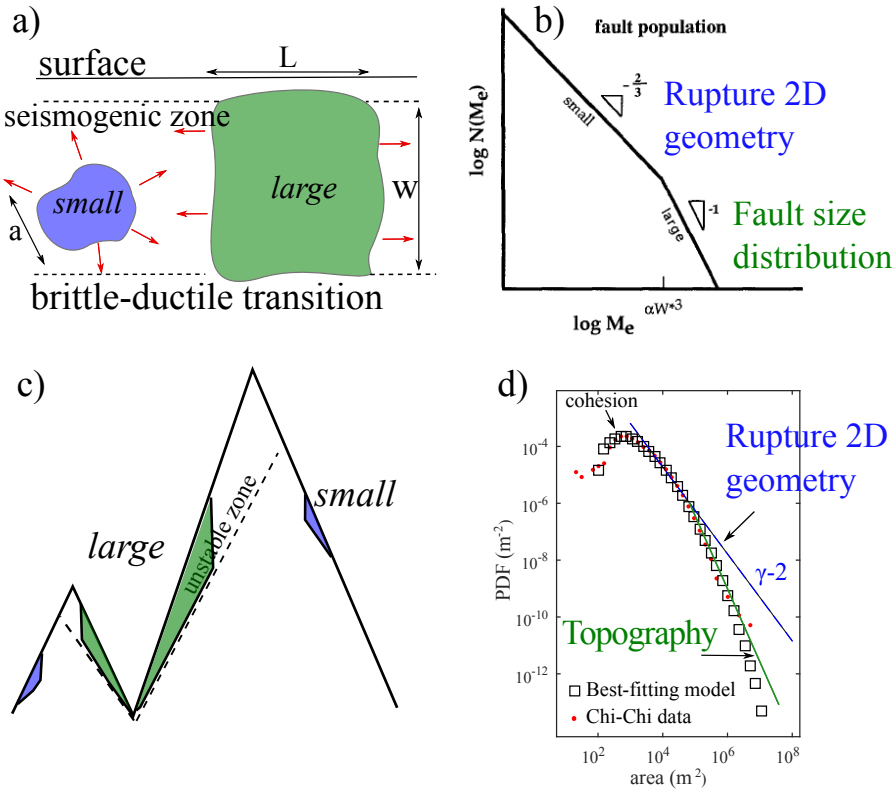


Figure 6.1 – a) Schematic representation of the seismogenic zone, with a small earthquake of diameter $a$ and a large earthquake of width w and length L, that can expand only in one direction. After Pacheco et al. (1992). b) Magnitude-frequency relationship observed for a population of faults. A break in self-similarity is observed for a size corresponding to the width of the seismogenic zone. After Scholz (1997). c) Schematic representation of two hillslopes with a given frictional angle that sets the size of the unstable zone. Small landslides can growth in all directions. On the contrary, when landslides are large enough, they start to be limited by the length of the hillslopes. d) Observed and modelled PDF of landslide areas for Chi-Chi earthquakes (chapter 3). The medium landslide distribution is controlled by the 2D rupture geometry, and the scaling for large landslides is controlled by the landscape shape.

In the light of this earthquake literature and the results of my work, we can think of landslide size distribution as the result of the size distribution of hillslopes (figure 6.1). We have shown that the maximum height of unstable hillslopes strongly influences the size distribution of large landslide sizes. We have also demonstrated (chapter 3) that the PDF of landslide sizes was controlled by the 2D aspects of rupture propagation for medium landslides, and mostly controlled by the landscape shape for large landslides. This suggests that small landslides, that are not limited in space, can grow only according to rupture processes. On the contrary, large landslide size distribution seems the be controlled by the availability of unstable hillslope height. The idea that the distribution of unstable slopes (i.e. high slope) patches in the landscape sets the power-law scaling for landslide size distribution has been proposed by Frattini and Crosta (2013). Similarly to studies that have linked fault surface heterogeneity to the earthquake size distribution (Mogi, 1967, Goebel et al., 2017), they proposed that landslide scaling arises from the heterogeneity of low strength (or high stress) zones. But the role of finite size of hillslopes have not been investigated in landslide size distribution. I have demonstrated that this finite size (quantified by $h_C$) is exponentially distributed, and varies spatially. The results of my work shows that this finite size should be taken into account for a better understanding of large landslide probability.

My modelling approach reveals that the scaling of 2D rupture is also important for the size distribution of landslides at least for a certain range of sizes. However, we cannot investigate this aspect further only

with a 1D approach. We could think, however, that the geometry of the hillslopes may set a limit to the landslide width, and not only to the landslide height. Those aspects would need to be investigated through 3D modelling.

### 6.2.2 Implications for interaction between landslides and earthquakes at short time-scales

I have shown that the distribution of the unstable height of hillslopes is likely to constrain the large landslide probability. However, large landslide occurrence depends also on the frequency of triggering events (Geist and Parsons, 2014) such as earthquakes or rainfall. I have illustrated in chapter 4 that the areas with high values of $h_C$ correlate at first order with tectonically active areas, where seismic hazard is likely to be high. This has many implications for co and post-seismic landscape evolution.

First, because the small number of large landslides often dominates the total area and volume of sediment that is produced (e.g., Hovius et al., 2000), the hillslope size is likely to constrain the total volume of eroded material. I have shown that despite its exponential distribution which seems universal, the mean $h_C$ value displays a lot of variation among landscapes. This could partially explain why so much variability is found in landslide volumes induced by earthquakes of same magnitude (Keefer, 1994, Marc et al., 2016b). A high total volume of sediment is likely to induce greater stress variations near the shallow faults, and therefore to induce stress variations high enough to trigger shallow seismicity.

However, I have also demonstrated in chapter 5 that the time scale of erosion is fundamental in controlling fault response to stress changes, and that landslides need to be evacuated rapidly to trigger seismicity. The idea that large landslides remain for a long time in the landscape has been widely supported. This was based on the idea that the time needed by the rivers to export landslide sediment was simply depending on the ratio between landslide volume and river transport capacity. Therefore, large landslides were thought to remain for centuries (Yanites et al., 2010) or even millennia (Berryman et al., 2012) in the landscape. Recently, Croissant et al. (2017) founded that for landslides with high enough volume, a dynamic narrowing of the alluvial channel occurs and increases river transport capacity. This allows to speed up coarse sediment export, leading to export time for large landslides of about ten years.

Moreover, large landslides have long runout (Lucas et al., 2014), and tend to be more connected to the river network (Li et al. (2016), Roback et al. (2017), and figure 6.2a). If the evacuation of one landslide by the river network depends mainly on river geometry and discharge, and on sediment grain size (Croissant et al.,

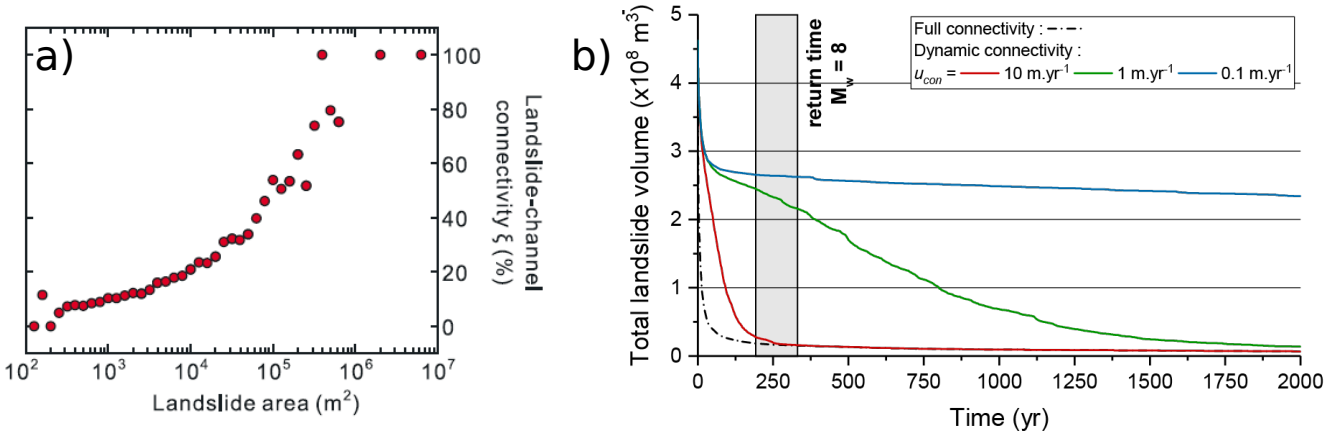


Figure 6.2 – a) Landslide-channel connectivity (in %) as a function of landslide area. From Li et al. (2016). b) Temporal evolution of the landslide volume for different connection velocities, for $M_w$ 8 earthquake simulations. After Croissant et al. (2018) (see Appendix B for complete article in preparation). The case where all landslides are connected to the river is shown by the dotted line.

2017), the evacuation of a population of landslides depends on the proportion of landslides connected to the drainage network (i.e., landslide connectivity), and on the rate at which landslides migrate and connect to the drainage network (Li et al., 2016, Roback et al., 2017). The temporal evolution of landslide connectivity remains an open question (Zhang et al., 2016). In an article in preparation (Croissant et al., 2018), we explore the evacuation of a population of landslides. The approach combines an empirical description of co-seismic landslide clusters with the physical processes involved in landslide removal during the post-seismic phase. Our results show that landslide connectivity impacts the amplitude and duration of sediment remobilization rates. For example, the volume of sediments in the rivers decreases slowly, linearly, during thousands or years if landslide material slowly migrates from hillslopes to rivers (figure 6.2b). However, if the landslides are initially connected to the river, the total landslide volume decreases dramatically in a very short time (Croissant et al., 2018).

Therefore, because it can constrain the probability of large landslides, the height of unstable hillslopes is able to control the co-seismic and post-seismic landscape evolution by 1) increasing the total amount of produced sediments; 2) inducing changes in rivers dynamics that can boost the transport of large landslide sediments, and 3) increasing landslide connectivity, and therefore reducing the timing for sediment evacuation.

The potential different modes of landslide evacuation illustrated in figure 6.2b) imply different modes for normal stress decrease induced by erosion following large landsliding event. In chapter 5, I have assumed a linearly decreasing erosion rate with time, following the few natural observations that we have (Hovius et al., 2011). However, because it has been monitored only for a few specific cases of post-seismic landslide evacuation, the functional relationship between time and landslide volume is still poorly known.

To illustrate this, I implemented a constant normal stress rate, instead of the linearly increasing normal stress rate used in section 5.3. For comparison, the removed total normal stress $\Delta\sigma_n$ is the same, over the same erosional period $T_{ero}$. Figure 6.3 shows the temporal evolution of maximum fault velocity, and illustrates that when the sediment is evacuated at a constant rate, the seismicity increases and maintains a constant rate during the erosion period. On the contrary, when the erosion rate is greater at the beginning

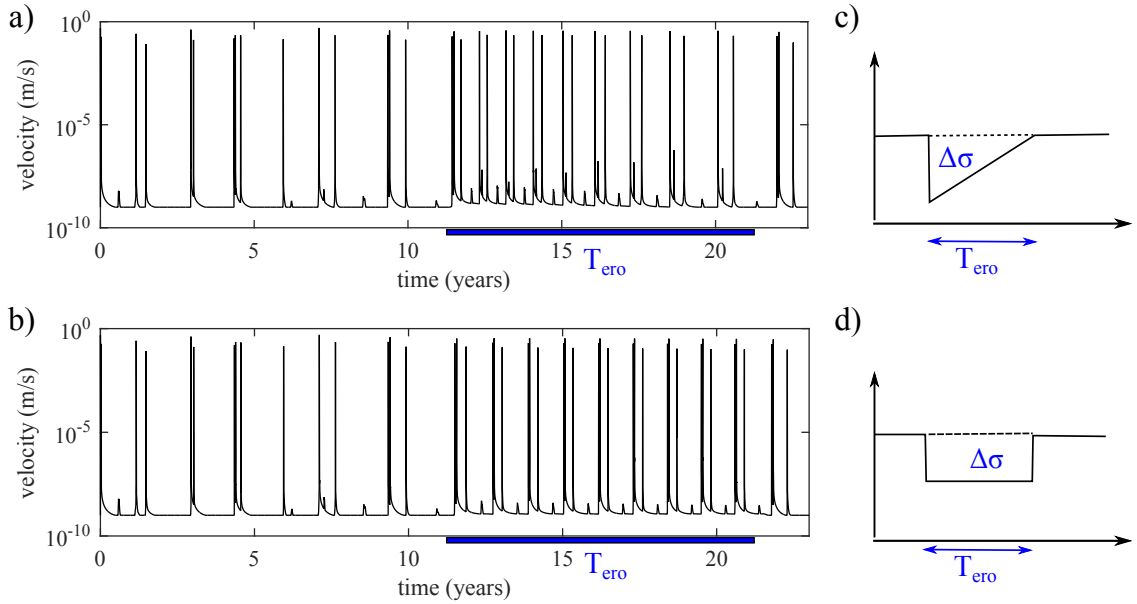


Figure 6.3 – a) Maximum fault velocity as a function of time in the case of undisturbed fault. b) Same as a) but with a normal stress decrease of amplitude $\Delta\sigma_n = 1$ MPa and $T_{ero} = 10.24$ years, with an erosion rate decreasing linearly in time as modelled in section 5.3. c) Same as b) but with an erosion rate constant in time, with same duration of erosion $T_{ero} = 10.24$ years and total normal stress removed $\Delta\sigma_n = 1$ MPa.

and then decreases linearly, the seismicity rate is also greater during the beginning of erosion.

This illustrates the need for a better understanding of the mode and timing of export of a population of landslides, in order to constrain the potential effects of large erosional events on seismicity rate. Nevertheless, it appears that such large erosional events have the potential to boost the regional seismicity, especially in areas characterized by high topography. This can explain why, in areas with high relief such as Taiwan, we could observe an increase in earthquake frequency after a large erosional event (Steer et al. (2014), Appendix A). Relief grows, in turn, by the succession of shallow earthquakes (Avouac, 2007). Because the effects of such erosive events are likely to accumulate over time, we can expect some feedbacks between erosion and tectonic at short time scales that may be fundamental to take into account in the evolution of landscapes over geological time.

# Bibliography


Abercrombie, R. E. and Brune, J. N. (1994). Evidence for a constant b-value above magnitude 0 in the southern san andreas, san jacinto and san miguel fault zones, and at the long valley caldera, california. *Geophysical research letters*, 21(15):1647–1650.

Adams, J. (1980). Contemporary uplift and erosion of the southern alps, new zealand. *Geological Society of America Bulletin*, 91(1_Part_II):1–114.

Ader, T. J. and Avouac, J.-P. (2013). Detecting periodicities and declustering in earthquake catalogs using the schuster spectrum, application to himalayan seismicity. *Earth and Planetary Science Letters*, 377:97–105.

Ader, T. J., Lapusta, N., Avouac, J.-P., and Ampuero, J.-P. (2014). Response of rate-and-state seismogenic faults to harmonic shear-stress perturbations. *Geophysical Journal International*, 198(1):385–413.

Aki, K. (1967). Scaling law of seismic spectrum. *Journal of Geophysical Research*, 72(4):1217–1231.

Aki, K. (1972). Earthquake mechanism. *Tectonophysics*, 13(1-4):423–446.

Aki, K. (1987). Magnitude-frequency relation for small earthquakes: A clue to the origin of f max of large earthquakes. *Journal of Geophysical Research: Solid Earth*, 92(B2):1349–1355.

Alvioli, M., Guzzetti, F., and Rossi, M. (2014). Scaling properties of rainfall induced landslides predicted by a physically based model. *Geomorphology*, 213:38–47.

Amitrano, D. (2003). Brittle-ductile transition and associated seismicity: Experimental and numerical studies and relationship with the b value. *Journal of Geophysical Research: Solid Earth*, 108(B1).

Amitrano, D. (2012). Variability in the power-law distributions of rupture events. *The European Physical Journal Special Topics*, 205(1):199–215.

Amonton, G. (1699). De la resistance causee dans les machines. *Histoire de l'Academie Royale des Science avec les Memories de Mathematiques et de Physique Paris*, 12:206.

Anderson, M., Richards, K., and Kneale, P. (1980). The role of stability analysis in the interpretation of the evolution of threshold slopes. *Transactions of the Institute of British Geographers*, pages 100–112.

Anderson, R. S. and Anderson, S. P. (2010). Geomorphology: the mechanics and chemistry of landscapes.

Aochi, H. and Ide, S. (2004). Numerical study on multi-scaling earthquake rupture. *Geophysical Research Letters*, 31(2).

Avouac, J.-P. (2007). Mountain building: From earthquakes to geological deformation. *Dynamic processes in extensional and compressional settings: Treatise on Geophysics*, 6:377–439.

Bak, P., Tang, C., and Wiesenfeld, K. (1988). Self-organized criticality. *Physical review A*, 38(1):364.

Baker, R. and Garber, M. (1978). Theoretical analysis of the stability of slopes. *Geotechnique*, 28(4):395–411.

Beaumont, C., Kamp, P. J., Hamilton, J., and Fullsack, P. (1996). The continental collision zone, south island, new zealand: Comparison of geodynamical models and observations. *Journal of Geophysical Research: Solid Earth*, 101(B2):3333–3359.

Beeler, N. and Lockner, D. (2003). Why earthquakes correlate weakly with the solid earth tides: Effects of periodic stress on the rate and probability of earthquake occurrence. *Journal of Geophysical Research: Solid Earth*, 108(B8).

Berryman, K. R., Cochran, U. A., Clark, K. J., Biasi, G. P., Langridge, R. M., and Villamor, P. (2012). Major earthquakes occur regularly on an isolated plate boundary fault. *Science*, 336(6089):1690–1693.

Bettinelli, P., Avouac, J.-P., Flouzat, M., Bollinger, L., Ramillien, G., Rajaure, S., and Sapkota, S. (2008). Seasonal variations of seismicity and geodetic strain in the himalaya induced by surface hydrology. *Earth and Planetary Science Letters*, 266(3-4):332–344.

Bieniawski, Z. (1968). The effect of specimen size on compressive strength of coal. In *International Journal of Rock Mechanics and Mining Sciences & Geomechanics Abstracts*, volume 5, pages 325–335. Elsevier.

Bilham, R., Larson, K., and Freymueller, J. (1997). Gps measurements of present-day convergence across the nepal himalaya. *Nature*, 386(6620):61.

Birchfield, G. E. and Wertman, J. (1983). Topography, albedo-temperature feedback, and climate sensitivity. *Science*, 219(4582):284–285.

Bird, J. F. and Bommer, J. J. (2004). Earthquake losses due to ground failure. *Engineering geology*, 75(2):147–179.

Bistacchi, A., Griffith, W. A., Smith, S. A., Di Toro, G., Jones, R., and Nielsen, S. (2011). Fault roughness at seismogenic depths from lidar and photogrammetric analysis. *Pure and Applied Geophysics*, 168(12):2345–2363.

Blanpied, M., Lockner, D., and Byerlee, J. (1991). Fault stability inferred from granite sliding experiments at hydrothermal conditions. *Geophysical Research Letters*, 18(4):609–612.

Blöthe, J. H., Korup, O., and Schwanghart, W. (2015). Large landslides lie low: Excess topography in the himalaya-karakoram ranges. *Geology*, 43(6):523–526.

Bollinger, L., Perrier, F., Avouac, J.-P., Sapkota, S., Gautam, U., and Tiwari, D. (2007). Seasonal modulation of seismicity in the himalaya of nepal. *Geophysical Research Letters*, 34(8).

Bonnet, E., Bour, O., Odling, N. E., Davy, P., Main, I., Cowie, P., and Berkowitz, B. (2001). Scaling of fracture systems in geological media. *Reviews of geophysics*, 39(3):347–383.

Bowden, F. P. and Tabor, D. (1964). *The friction and lubrication of solids. Vol. 2.* OUP.

Bowdon, F. and Tabor, D. (1950). The friction and lubrication of solids. *Oxford Univ. Press, Oxford, 1950.*

Brace, W. and Byerlee, J. (1966). Stick-slip as a mechanism for earthquakes. *Science*, 153(3739):990–992.

Brenguier, F., Campillo, M., Hadziioannou, C., Shapiro, N., Nadeau, R. M., and Larose, E. (2008). Postseismic relaxation along the san andreas fault at parkfield from continuous seismological observations. *science*, 321(5895):1478–1481.

Brideau, M.-A., Stead, D., and Couture, R. (2006). Structural and engineering geology of the east gate landslide, purcell mountains, british columbia, canada. *Engineering geology*, 84(3):183–206.

Brown, S. R. and Scholz, C. H. (1985). Broad bandwidth study of the topography of natural rock surfaces. *Journal of Geophysical Research: Solid Earth*, 90(B14):12575–12582.

Brune, J. N. (1970). Tectonic stress and the spectra of seismic shear waves from earthquakes. *Journal of geophysical research*, 75(26):4997–5009.

Brune, J. N. and Allen, C. R. (1967). A micro-earthquake survey of the san andreas fault system in southern california. *Bulletin of the Seismological Society of America*, 57(2):277–296.

Bulirsch, R. and Stoer, J. (1966). Numerical treatment of ordinary differential equations by extrapolation methods. *Numerische Mathematik*, 8(1):1–13.

Burbank, D. (2002). Rates of erosion and their implications for exhumation. *Mineralogical Magazine*, 66(1):25–52.

Burbank, D. W., Leland, J., Fielding, E., Anderson, R. S., Brozovic, N., Reid, M. R., and Duncan, C. (1996). Bedrock incision, rock uplift and threshold hillslopes in the northwestern Himalayas. *Nature*, 379(6565):505–510.

Burridge, R. and Knopoff, L. (1967). Model and theoretical seismicity. *Bulletin of the seismological society of america*, 57(3):341–371.

Byerlee, J. (1970). The mechanics of stick-slip. *Tectonophysics*, 9(5):475–486.

Byerlee, J. (1978). Friction of rocks. *Pure and applied geophysics*, 116(4-5):615–626.

Calais, E., Freed, A., Van Arsdale, R., and Stein, S. (2010). Triggering of new madrid seismicity by late-pleistocene erosion. *Nature*, 466(7306):608.

Candela, T., Renard, F., Bouchon, M., Brouste, A., Marsan, D., Schmittbuhl, J., and Voisin, C. (2009). Characterization of fault roughness at various scales: Implications of three-dimensional high resolution topography measurements. In *Mechanics, Structure and Evolution of Fault Zones*, pages 1817–1851. Springer.

Candela, T., Renard, F., Bouchon, M., Schmittbuhl, J., and Brodsky, E. E. (2011). Stress drop during earthquakes: effect of fault roughness scaling. *Bulletin of the Seismological Society of America*, 101(5):2369–2387.

Cao, A. and Gao, S. S. (2002). Temporal variation of seismic b-values beneath northeastern japan island arc. *Geophysical research letters*, 29(9):48–1.

Cardinali, M., Ardizzone, F., Galli, M., Guzzetti, F., and Reichenbach, P. (2000). Landslides triggered by rapid snow melting: the december 1996–january 1997 event in central italy. In *Proceedings 1st Plinius Conference on Mediterranean Storms*, pages 439–448. Citeseer.

Carpinteri, A. (1994). Fractal nature of material microstructure and size effects on apparent mechanical properties. *Mechanics of materials*, 18(2):89–101.

Catlos, E. J., Friedrich, A. M., Lay, T., Elliott, J., Carena, S., Upreti, B., DeCelles, P., Tucker, B., and Bendick, B. (2016). Nepal at risk: Interdisciplinary lessons learned from the april 2015 nepal (gorkha) earthquake and future concerns. *GSA Today*, 26(6):42–43.

Cattin, R. and Avouac, J. (2000). Modeling mountain building and the seismic cycle in the himalaya of nepal. *Journal of Geophysical Research: Solid Earth*, 105(B6):13389–13407.

Chang, K.-t., Chiang, S.-h., Chen, Y.-c., and Mondini, A. C. (2014). Modeling the spatial occurrence of shallow landslides triggered by typhoons. *Geomorphology*, 208:137–148.

Charpentier, J. d. (1841). Essai sur les glaciers. *Ducloux, Lausanne*.

Chen, L. and Talwani, P. (2001). Mechanism of initial seismicity following impoundment of the monticello reservoir, south carolina. *Bulletin of the Seismological Society of America*, 91(6):1582–1594.

Chen, W.-S., Yang, C.-C., Yen, I.-C., Lee, L.-S., Lee, K.-J., Yang, H.-C., Chang, H.-C., Ota, Y., Lin, C.-W., Lin, W.-H., et al. (2007). Late holocene paleoseismicity of the southern part of the chelungpu fault in central taiwan: Evidence from the chushan excavation site. *Bulletin of the Seismological Society of America*, 97(1B):1–13.

Chinnery, M. (1964). The strength of the earth's crust under horizontal shear stress. *Journal of Geophysical Research*, 69(10):2085–2089.

Chinnery, M. A. (1969). Earthquake magnitude and source parameters. *Bulletin of the Seismological Society of America*, 59(5):1969–1982.

Christiansen, L. B., Hurwitz, S., and Ingebritsen, S. E. (2007). Annual modulation of seismicity along the san andreas fault near parkfield, ca. *Geophysical Research Letters*, 34(4).

Christiansen, L. B., Hurwitz, S., Saar, M. O., Ingebritsen, S. E., and Hsieh, P. A. (2005). Seasonal seismicity at western united states volcanic centers. *Earth and Planetary Science Letters*, 240(2):307–321.

Clauset, A., Shalizi, C. R., and Newman, M. E. (2009). Power-law distributions in empirical data. *SIAM review*, 51(4):661–703.

Cocco, M. and Rice, J. R. (2002). Pore pressure and poroelasticity effects in coulomb stress analysis of earthquake interactions. *Journal of Geophysical Research: Solid Earth*, 107(B2):ESE–2.

Cochran, E. S., Vidale, J. E., and Tanaka, S. (2004). Earth tides can trigger shallow thrust fault earthquakes. *Science*, 306(5699):1164–1166.

Collins, B. D. and Jibson, R. W. (2015). Assessment of existing and potential landslide hazards resulting from the april 25, 2015 gorkha, nepal earthquake sequence. Technical report, US Geological Survey.

Commend, S., Geiser, F., and Tacher, L. (2004). 3d numerical modeling of a landslide in switzerland. In *Proceedings of the International Symposium on Numerical Models in Geomechanics NUMOG IX, Ottawa*, pages 595–601.

Cowie, P. A., Whittaker, A. C., Attal, M., Roberts, G., Tucker, G. E., and Ganas, A. (2008). New constraints on sediment-flux–dependent river incision: Implications for extracting tectonic signals from river profiles. *Geology*, 36(7):535–538.

Croissant, T., Lague, D., Steer, P., and Davy, P. (2017). Rapid post-seismic landslide evacuation boosted by dynamic river width. *Nature Geoscience*, 10(9):680.

Croissant, T., Steer, P., Lague, D., Davy, P., Jeandet, L., and Hilton, R. (2018). Modulation of post-seismic sediment evacuation by landslide dynamic connectivity. in prep.

Culmann, K. (1875). *Die graphische statik*, volume 2. Meyer & Zeller (A. Reimann).

Dahlen, F., Suppe, J., and Davis, D. (1984). Mechanics of fold-and-thrust belts and accretionary wedges: Cohesive coulomb theory. *Journal of Geophysical Research: Solid Earth*, 89(B12):10087–10101.

Dai, F., Xu, C., Yao, X., Xu, L., Tu, X., and Gong, Q. (2011). Spatial distribution of landslides triggered by the 2008 ms 8.0 wenchuan earthquake, china. *Journal of Asian Earth Sciences*, 40(4):883–895.

Dana, J. (1856). *The American Journal of Science and Arts*.

Davis, D., Suppe, J., and Dahlen, F. (1983). Mechanics of fold-and-thrust belts and accretionary wedges. *Journal of Geophysical Research: Solid Earth*, 88(B2):1153–1172.

Densmore, A. L., Anderson, R. S., McAdoo, B. G., and Ellis, M. A. (1997). Hillslope evolution by bedrock landslides. *Science*, 275(5298):369–372.

Densmore, A. L., Ellis, M. A., and Anderson, R. S. (1998). Landsliding and the evolution of normal-fault-bounded mountains. *Journal of Geophysical Research: Solid Earth (1978–2012)*, 103(B7):15203–15219.

Dieterich, J. (1994). A constitutive law for rate of earthquake production and its application to earthquake clustering. *Journal of Geophysical Research: Solid Earth*, 99(B2):2601–2618.

Dieterich, J. H. (1979). Modeling of rock friction: 1. experimental results and constitutive equations. *Journal of Geophysical Research: Solid Earth*, 84(B5):2161–2168.

Dieterich, J. H. and Kilgore, B. D. (1994). Direct observation of frictional contacts: New insights for state-dependent properties. *Pure and Applied Geophysics*, 143(1-3):283–302.

Dodge, D. A., Beroza, G. C., and Ellsworth, W. (1996). Detailed observations of california foreshock sequences: Implications for the earthquake initiation process. *Journal of Geophysical Research: Solid Earth*, 101(B10):22371–22392.

Duncan, C. W. and Christopher, W. M. (2004). Rock slope engineering: civil and mining. *Spon Press, New York*.

Duncan, J. M. (2000). Factors of safety and reliability in geotechnical engineering. *Journal of geotechnical and geoenvironmental engineering*, 126(4):307–316.

Dunham, E. M. (2007). Conditions governing the occurrence of supershear ruptures under slip-weakening friction. *Journal of Geophysical Research: Solid Earth*, 112(B7).

Dussauge, C., Grasso, J.-R., and Helmstetter, A. (2003). Statistical analysis of rockfall volume distributions: Implications for rockfall dynamics. *Journal of Geophysical Research: Solid Earth*, 108(B6).

Egholm, D. L., Knudsen, M. F., and Sandiford, M. (2013). Lifespan of mountain ranges scaled by feedbacks between landsliding and erosion by rivers. *Nature*, 498(7455):475–478.

Ellsworth, W. L. (2013). Injection-induced earthquakes. *Science*, 341(6142):1225942.

Ellsworth, W. L. and Bulut, F. (2018). Nucleation of the 1999 izmit earthquake by a triggered cascade of foreshocks.

Fan, X., Domènech, G., Scaringi, G., Huang, R., Xu, Q., Hales, T. C., Dai, L., Yang, Q., and Francis, O. (2018). Spatio-temporal evolution of mass wasting after the 2008 m w 7.9 wenchuan earthquake revealed by a detailed multi-temporal inventory. *Landslides*, 15(12):2325–2341.

Feng, W., Lindsey, E., Barbot, S., Samsonov, S., Dai, K., Li, P., Li, Z., Almeida, R., Chen, J., and Xu, X. (2017). Source characteristics of the 2015 mw 7.8 gorkha (nepal) earthquake and its mw 7.2 aftershock from space geodesy. *Tectonophysics*, 712:747–758.

Frattini, P. and Crosta, G. B. (2013). The role of material properties and landscape morphology on landslide size distributions. *Earth and Planetary Science Letters*, 361:310–319.

Gallen, S. F., Clark, M. K., and Godt, J. W. (2015). Coseismic landslides reveal near-surface rock strength in a high-relief, tectonically active setting. *Geology*, 43(1):11–14.

Gao, S. S., Silver, P. G., Linde, A. T., and Sacks, I. S. (2000). Annual modulation of triggered seismicity following the 1992 landers earthquake in california. *Nature*, 406(6795):500.

Gardner, J. and Knopoff, L. (1974). Is the sequence of earthquakes in southern california, with aftershocks removed, poissonian? *Bulletin of the Seismological Society of America*, 64(5):1363–1367.

Geist, E. L. and Parsons, T. (2014). Undersampling power-law size distributions: effect on the assessment of extreme natural hazards. *Natural hazards*, 72(2):565–595.

Giardini, D., Grünthal, G., Shedlock, K. M., and Zhang, P. (1999). The gshap global seismic hazard map. *Annals of Geophysics*, 42(6).

Gilbert, G. K. (1884). A theory of the earthquakes of the great basin, with a practical application. *American Journal of Science (1880-1910)*, 27(157-162):49.

Girard, L., Amitrano, D., and Weiss, J. (2010). Failure as a critical phenomenon in a progressive damage model. *Journal of Statistical Mechanics: Theory and Experiment*, 2010(01):P01013.

Goebel, T. H., Kwiatek, G., Becker, T. W., Brodsky, E. E., and Dresen, G. (2017). What allows seismic events to grow big?: Insights from b-value and fault roughness analysis in laboratory stick-slip experiments. *Geology*, 45(9):815–818.

Gorum, T., Korup, O., van Westen, C. J., van der Meijde, M., Xu, C., and van der Meer, F. D. (2014). Why so few? landslides triggered by the 2002 denali earthquake, alaska. *Quaternary Science Reviews*, 95:80–94.

Grieve, S. W., Mudd, S. M., and Hurst, M. D. (2016). How long is a hillslope? *Earth Surface Processes and Landforms*, 41(8):1039–1054.

Griffith, A. (1924). The theory of rupture. In *First Int. Cong. Appl. Mech*, pages 55–63.

Griffith, A. A. and Eng, M. (1921). Vi. the phenomena of rupture and flow in solids. *Phil. Trans. R. Soc. Lond. A*, 221(582-593):163–198.

Gross, S. and Kisslinger, C. (1997). Estimating tectonic stress rate and state with landers aftershocks. *Journal of Geophysical Research: Solid Earth*, 102(B4):7603–7612.

GSI (2005). 1:25,000 damage map of the mid niigata prefecture earthquale in 2004: 3sheets, edited. Technical report, Geospatial Information Authority of Japan.

Gu, J.-C., Rice, J. R., Ruina, A. L., and Simon, T. T. (1984). Slip motion and stability of a single degree of freedom elastic system with rate and state dependent friction. *Journal of the Mechanics and Physics of Solids*, 32(3):167–196.

Gutenberg, B. and Richter, C. (1955). Magnitude and energy of earthquakes. *Nature*, 176(4486):795.

Gutenberg, B. and Richter, C. F. (1944). Frequency of earthquakes in california. *Bulletin of the Seismological Society of America*, 34(4):185–188.

Guzzetti, F., Ardizzone, F., Cardinali, M., Rossi, M., and Valigi, D. (2009). Landslide volumes and landslide mobilization rates in umbria, central italy. *Earth and Planetary Science Letters*, 279(3):222–229.

Guzzetti, F., Malamud, B. D., Turcotte, D. L., and Reichenbach, P. (2002). Power-law correlations of landslide areas in central italy. *Earth and Planetary Science Letters*, 195(3-4):169–183.

Hanks, T. C. and Kanamori, H. (1979). A moment magnitude scale. *Journal of Geophysical Research: Solid Earth*, 84(B5):2348–2350.

Hardebeck, J. L., Nazareth, J. J., and Hauksson, E. (1998). The static stress change triggering model: Constraints from two southern california aftershock sequences. *Journal of Geophysical Research: Solid Earth*, 103(B10):24427–24437.

Harp, E. L. and Jibson, R. W. (1995). Inventory of landslides triggered by the 1994 northridge, california earthquake.

Harp, E. L. and Jibson, R. W. (1996). Landslides triggered by the 1994 northridge, california, earthquake. *Bulletin of the Seismological Society of America*, 86(1B):S319–S332.

Harp, E. L., Wilson, R. C., and Wieczorek, G. F. (1981). Landslides from the february 4, 1976, guatemala earthquake. Technical report, US Government Printing Office Washington, DC.

Heki, K. (2001). Seasonal modulation of interseismic strain buildup in northeastern japan driven by snow loads. *Science*, 293(5527):89–92.

Heki, K. (2003). Snow load and seasonal variation of earthquake occurrence in japan. *Earth and Planetary Science Letters*, 207(1-4):159–164.

Hergarten, S. (2003). Landslides, sandpiles, and self-organized criticality. *Natural Hazards and Earth System Science*, 3(6):505–514.

Hergarten, S. (2012). Topography-based modeling of large rockfalls and application to hazard assessment. *Geophysical Research Letters*, 39(13).

Hewitt, K. (2009). Catastrophic rock slope failures and late quaternary developments in the nanga parbat–haramosh massif, upper indus basin, northern pakistan. *Quaternary Science Reviews*, 28(11-12):1055–1069.

Heyman, J. (1972). *Coulomb's memoir on statics: an essay in the history of civil engineering*. CUP Archive.

Hillers, G., Ben-Zion, Y., and Mai, P. (2006). Seismicity on a fault controlled by rate-and state-dependent friction with spatial variations of the critical slip distance. *Journal of Geophysical Research: Solid Earth*, 111(B1).

Hillers, G., Mai, P., Ben-Zion, Y., and Ampuero, J.-P. (2007). Statistical properties of seismicity of fault zones at different evolutionary stages. *Geophysical Journal International*, 169(2):515–533.

Hoek, E. and Bray, J. D. (1981). *Rock slope engineering*. CRC Press.

Hoek, E. and Brown, E. T. (1980a). Empirical strength criterion for rock masses. *Journal of Geotechnical and Geoenvironmental Engineering*, 106(ASCE 15715).

Hoek, E. and Brown, E. T. (1980b). *Underground excavations in rock*. CRC Press.

Hoek, E. and Brown, E. T. (1997). Practical estimates of rock mass strength. *International Journal of Rock Mechanics and Mining Sciences*, 34(8):1165–1186.

Hovius, N., Meunier, P., Lin, C.-W., Chen, H., Chen, Y.-G., Dadson, S., Horng, M.-J., and Lines, M. (2011). Prolonged seismically induced erosion and the mass balance of a large earthquake. *Earth and Planetary Science Letters*, 304(3):347–355.

Hovius, N., Stark, C. P., and Allen, P. A. (1997). Sediment flux from a mountain belt derived by landslide mapping. *Geology*, 25(3):231–234.

Hovius, N., Stark, C. P., Hao-Tsu, C., and Jiun-Chuan, L. (2000). Supply and removal of sediment in a landslide-dominated mountain belt: Central range, taiwan. *The Journal of Geology*, 108(1):73–89.

Howarth, J. D., Fitzsimons, S. J., Norris, R. J., and Jacobsen, G. E. (2012). Lake sediments record cycles of sediment flux driven by large earthquakes on the alpine fault, new zealand. *Geology*, 40(12):1091–1094.

Huang, A. Y.-L. and Montgomery, D. R. (2014). Topographic locations and size of earthquake-and typhoon-generated landslides, tachia river, taiwan. *Earth Surface Processes and Landforms*, 39(3):414–418.

Huang, M. Y.-F. and Montgomery, D. R. (2013). Altered regional sediment transport regime after a large typhoon, southern taiwan. *Geology*, 41(12):1223–1226.

Huang, R. and Fan, X. (2013). The landslide story. *Nature Geoscience*, 6(5):325.

Hurst, M. D., Mudd, S. M., Walcott, R., Attal, M., and Yoo, K. (2012). Using hilltop curvature to derive the spatial distribution of erosion rates. *Journal of Geophysical Research: Earth Surface*, 117(F2).

Ide, S. and Aochi, H. (2005). Earthquakes as multiscale dynamic ruptures with heterogeneous fracture surface energy. *Journal of Geophysical Research: Solid Earth*, 110(B11).

Imoto, M. (1991). Changes in the magnitude - frequency b-value prior to large (mw 6.0) earthquakes in japan. *Tectonophysics*, 193(4):311–325.

Jaeger, J. C., Cook, N. G., and Zimmerman, R. (2009). *Fundamentals of rock mechanics*. John Wiley & Sons.

Jahns, H. et al. (1966). Measuring the strength of rock in situ at an increasing scale. In *1st ISRM Congress*. International Society for Rock Mechanics.

Jansson, M. B. (1982). *Land erosion by water in different climates*. Uppsala Univ.

Jeandet, L., Lague, D., Steer, P., Davy, P., and Quigley, M. (2016). Calibration of the landsliding numerical model slipos and prediction of the seismically induced erosion for several large earthquakes scenarios in new-zealand. In *AGU Fall Meeting Abstracts*.

Jeandet, L., Steer, P., Lague, D., and Davy, P. (2019). Coulomb mechanics and relief constraints explains landslide size distribution. *Geophysical Research Letters*.

Jibson, R. W., Harp, E. L., and Michael, J. A. (2000). A method for producing digital probabilistic seismic landslide hazard maps. *Engineering Geology*, 58(3):271–289.

Johnson, P., Ferdowsi, B., Kaproth, B., Scuderi, M., Griffa, M., Carmeliet, J., Guyer, R., Le Bas, P.-Y., Trugman, D., and Marone, C. (2013). Acoustic emission and microslip precursors to stick-slip failure in sheared granular material. *Geophysical Research Letters*, 40(21):5627–5631.

Jones, L. M. and Molnar, P. (1979). Some characteristics of foreshocks and their possible relationship to earthquake prediction and premonitory slip on faults. *Journal of Geophysical Research: Solid Earth*, 84(B7):3596–3608.

Jouanne, F., Mugnier, J., Pandey, M., Gamond, J., Le Fort, P., Serrurier, L., Vigny, C., and Avouac, J. (1999). Oblique convergence in the himalayas of western nepal deduced from preliminary results of gps measurements. *Geophysical Research Letters*, 26(13):1933–1936.

Kanamori, H. (1977). The energy release in great earthquakes. *Journal of geophysical research*, 82(20):2981–2987.

Kanamori, H. and Anderson, D. L. (1975). Theoretical basis of some empirical relations in seismology. *Bulletin of the Seismological Society of America*, 65(5):1073–1095.

Kaneko, Y. and Lapusta, N. (2008). Variability of earthquake nucleation in continuum models of rate-and-state faults and implications for aftershock rates. *Journal of Geophysical Research: Solid Earth*, 113(B12).

Kargel, J., Leonard, G., Shugar, D. H., Haritashya, U., Bevington, A., Fielding, E., Fujita, K., Geertsema, M., Miles, E., Steiner, J., et al. (2016). Geomorphic and geologic controls of geohazards induced by nepal 2015 gorkha earthquake. *Science*, 351(6269):aac8353.

Katz, O. and Aharonov, E. (2006). Landslides in vibrating sand box: What controls types of slope failure and frequency magnitude relations? *Earth and Planetary Science Letters*, 247(3):280–294.

Keefer, D. K. (1994). The importance of earthquake-induced landslides to long-term slope erosion and slope-failure hazards in seismically active regions. *Geomorphology*, 10(1):265–284.

King, G. and Cocco, M. (2001). Fault interaction by elastic stress changes: New clues from earthquake sequences. In *Advances in Geophysics*, volume 44, pages 1–VIII. Elsevier.

King, G. C., Stein, R. S., and Lin, J. (1994). Static stress changes and the triggering of earthquakes. *Bulletin of the Seismological Society of America*, 84(3):935–953.

King, G. C., Stein, R. S., and Rundle, J. B. (1988). The growth of geological structures by repeated earthquakes 1. conceptual framework. *Journal of Geophysical research: solid Earth*, 93(B11):13307–13318.

Klein, F. W., Einarsson, P., and Wyss, M. (1977). The reykjanes peninsula, iceland, earthquake swarm of september 1972 and its tectonic significance. *Journal of Geophysical Research*, 82(5):865–888.

Koons, P. (1990). Two-sided orogen: Collision and erosion from the sandbox to the southern alps, new zealand. *Geology*, 18(8):679–682.

Korup, O. (2005a). Distribution of landslides in southwest new zealand. *Landslides*, 2(1):43–51.

Korup, O. (2005b). Large landslides and their effect on sediment flux in south westland, new zealand. *Earth Surface Processes and Landforms: The Journal of the British Geomorphological Research Group*, 30(3):305–323.

Korup, O. (2008). Rock type leaves topographic signature in landslide-dominated mountain ranges. *Geophysical Research Letters*, 35(11).

Korup, O., Clague, J. J., Hermanns, R. L., Hewitt, K., Strom, A. L., and Weidinger, J. T. (2007). Giant landslides, topography, and erosion. *Earth and Planetary Science Letters*, 261(3):578–589.

Korup, O., Densmore, A. L., and Schlunegger, F. (2010). The role of landslides in mountain range evolution. *Geomorphology*, 120(1):77–90.

Kotô, B. (1893). On the cause of the great earthquake in central japan, 1891. *J. Sci. Coll. Imp. Univ.*, 5:295–353.

Kranz, R. L. (1983). Microcracks in rocks: a review. *Tectonophysics*, 100(1-3):449–480.

Kutzbach, J., Guetter, P., Ruddiman, W., and Prell, W. (1989). Sensitivity of climate to late cenozoic uplift in southern asia and the american west: Numerical experiments. *Journal of Geophysical Research: Atmospheres*, 94(D15):18393–18407.

Labuz, J. F. and Zang, A. (2012). Mohr–coulomb failure criterion. *Rock mechanics and rock engineering*, 45(6):975–979.

Lapusta, N. and Liu, Y. (2009). Three-dimensional boundary integral modeling of spontaneous earthquake sequences and aseismic slip. *Journal of Geophysical Research: Solid Earth (1978–2012)*, 114(B9).

Lapusta, N., Rice, J. R., Ben-Zion, Y., and Zheng, G. (2000). Elastodynamic analysis for slow tectonic loading with spontaneous rupture episodes on faults with rate-and state-dependent friction. *Journal of Geophysical Research: Solid Earth*, 105(B10):23765–23789.

Larsen, I. J. and Montgomery, D. R. (2012). Landslide erosion coupled to tectonics and river incision. *Nature Geoscience*, 5(7):468–473.

Larsen, I. J., Montgomery, D. R., and Korup, O. (2010). Landslide erosion controlled by hillslope material. *Nature Geoscience*, 3(4):247–251.

Larson, K. M., Bürgmann, R., Bilham, R., and Freymueller, J. T. (1999). Kinematics of the india-eurasia collision zone from gps measurements. *Journal of Geophysical Research: Solid Earth*, 104(B1):1077–1093.

Le Béon, M., Suppe, J., Jaiswal, M. K., Chen, Y.-G., and Ustaszewski, M. E. (2014). Deciphering cumulative fault slip vectors from fold scarps: Relationships between long-term and coseismic deformations in central western taiwan. *Journal of Geophysical Research: Solid Earth*, 119(7):5943–5978.

Lee, S., Chwae, U., and Min, K. (2002). Landslide susceptibility mapping by correlation between topography and geological structure: the janghung area, korea. *Geomorphology*, 46(3-4):149–162.

Lee, T.-Y., Huang, J.-C., Lee, J.-Y., Jien, S.-H., Zehetner, F., and Kao, S.-J. (2015). Magnified sediment export of small mountainous rivers in taiwan: chain reactions from increased rainfall intensity under global warming. *PloS one*, 10(9):e0138283.

Li, G., West, A. J., Densmore, A. L., Hammond, D. E., Jin, Z., Zhang, F., Wang, J., and Hilton, R. G. (2016). Connectivity of earthquake-triggered landslides with the fluvial network: Implications for landslide sediment transport after the 2008 wenchuan earthquake. *Journal of Geophysical Research: Earth Surface*, 121(4):703–724.

Li, G., West, A. J., Densmore, A. L., Jin, Z., Parker, R. N., and Hilton, R. G. (2014). Seismic mountain building: Landslides associated with the 2008 wenchuan earthquake in the context of a generalized model for earthquake volume balance. *Geochemistry, Geophysics, Geosystems*, 15(4):833–844.

Liao, H.-W. and Lee, C.-T. (2000). Landslides triggered by the chi-chi earthquake. In *Proceedings of the 21st asian conference on remote sensing, Taipei*, volume 1, page 2.

Lin, C.-W., Shieh, C.-L., Yuan, B.-D., Shieh, Y.-C., Liu, S.-H., and Lee, S.-Y. (2004). Impact of chi-chi earthquake on the occurrence of landslides and debris flows: example from the chenyulan river watershed, nantou, taiwan. *Engineering geology*, 71(1-2):49–61.

Liucci, L., Melelli, L., Suteanu, C., and Ponziani, F. (2017). The role of topography in the scaling distribution of landslide areas: A cellular automata modeling approach. *Geomorphology*, 290:236–249.

Lockner, D. A. and Beeler, N. M. (1999). Premonitory slip and tidal triggering of earthquakes. *Journal of Geophysical Research: Solid Earth*, 104(B9):20133–20151.

Locknet, D. and Byerlee, J. D. (1995). Precursory ae patterns leading to rock fracture. *Series on rock and soil mechanics*, 19:45–58.

Lucas, A., Mangeney, A., and Ampuero, J. P. (2014). Frictional velocity-weakening in landslides on Earth and on other planetary bodies. *Nature communications*, 5.

Luo, Y., Ampuero, J., Galvez, P., Van den Ende, M., and Idini, B. (2017). Qdyn: A quasi-dynamic earthquake simulator (v1. 1). *URL: https://github. com/ydluo/qdyn*.

Lyell, C. (1875). *Principles of geology*. Murray, London.

Main, I. (2000). Apparent breaks in scaling in the earthquake cumulative frequency-magnitude distribution: fact or artifact? *Bulletin of the Seismological Society of America*, 90(1):86–97.

Malamud, B. D. and Turcotte, D. L. (1999). Self-organized criticality applied to natural hazards. *Natural Hazards*, 20(2):93–116.

Malamud, B. D., Turcotte, D. L., Guzzetti, F., and Reichenbach, P. (2004a). Landslide inventories and their statistical properties. *Earth Surface Processes and Landforms*, 29(6):687–711.

Malamud, B. D., Turcotte, D. L., Guzzetti, F., and Reichenbach, P. (2004b). Landslides, earthquakes, and erosion. *Earth and Planetary Science Letters*, 229(1):45–59.

Marano, K. D., Wald, D. J., and Allen, T. I. (2010). Global earthquake casualties due to secondary effects: a quantitative analysis for improving rapid loss analyses. *Natural hazards*, 52(2):319–328.

Marc, O. and Hovius, N. (2014). Amalgamation in landslide maps: effects and automatic detection. *Natural Hazards and Earth System Sciences Discussions*, 2:7651–7678.

Marc, O., Hovius, N., and Meunier, P. (2016a). The mass balance of earthquakes and earthquake sequences. *Geophysical Research Letters*, 43(8):3708–3716.

Marc, O., Hovius, N., Meunier, P., Gorum, T., and Uchida, T. (2016b). A seismologically consistent expression for the total area and volume of earthquake-triggered landsliding. *Journal of Geophysical Research: Earth Surface*, 121(4):640–663.

Marc, O., Hovius, N., Meunier, P., Uchida, T., and Hayashi, S. (2015). Transient changes of landslide rates after earthquakes. *Geology*, 43(10):883–886.

Marc, O., Stumpf, A., Malet, J.-P., Gosset, M., Uchida, T., and Chiang, S.-H. (2018). Towards a global database of rainfall-induced landslide inventories: first insights from past and new events.

Marone, C. (1998). Laboratory-derived friction laws and their application to seismic faulting. *Annual Review of Earth and Planetary Sciences*, 26(1):643–696.

Marone, C., Raleigh, C. B., and Scholz, C. (1990). Frictional behavior and constitutive modeling of simulated fault gouge. *Journal of Geophysical Research: Solid Earth*, 95(B5):7007–7025.

Marone, C. and Scholz, C. (1988). The depth of seismic faulting and the upper transition from stable to unstable slip regimes. *Geophysical Research Letters*, 15(6):621–624.

Martin, Y., Rood, K., Schwab, J. W., and Church, M. (2002). Sediment transfer by shallow landsliding in the queen charlotte islands, british columbia. *Canadian Journal of Earth Sciences*, 39(2):189–205.

Massey, C., Townsend, D., Rathje, E., Allstadt, K. E., Lukovic, B., Kaneko, Y., Bradley, B., Wartman, J., Jibson, R. W., Petley, D., et al. (2018). Landslides triggered by the 14 november 2016 m w 7.8 kaikōura earthquake, new zealand. *Bulletin of the Seismological Society of America*.

Mendoza, C. and Hartzell, S. H. (1988). Aftershock patterns and main shock faulting. *Bulletin of the Seismological Society of America*, 78(4):1438–1449.

Mercier, J. P., Zambelli, G., and Kurz, W. (1999). *Introduction à la science des matériaux*, volume 1. PPUR presses polytechniques.

Mercury, N. (2018). Modélisation physique de réseaux complexes de failles afin de déterminer l'origine de la loi de gutenberg-richter. Master's thesis, ENS Ulm, Paris.

Meunier, P., Hovius, N., and Haines, A. J. (2007). Regional patterns of earthquake-triggered landslides and their relation to ground motion. *Geophysical Research Letters*, 34(20).

Meunier, P., Hovius, N., and Haines, J. A. (2008). Topographic site effects and the location of earthquake induced landslides. *Earth and Planetary Science Letters*, 275(3):221–232.

Milledge, D. G., Bellugi, D., McKean, J. A., Densmore, A. L., and Dietrich, W. E. (2014). A multidimensional stability model for predicting shallow landslide size and shape across landscapes. *Journal of Geophysical Research: Earth Surface*, 119(11):2481–2504.

Mitchell, S. G. and Montgomery, D. R. (2006). Influence of a glacial buzzsaw on the height and morphology of the cascade range in central washington state, usa. *Quaternary Research*, 65(1):96–107.

Mogi, K. (1967). Earthquakes and fractures. *Tectonophysics*, 5(1):35–55.

Montgomery, D. R. and Brandon, M. T. (2002). Topographic controls on erosion rates in tectonically active mountain ranges. *Earth and Planetary Science Letters*, 201(3-4):481–489.

Moon, S., Perron, J., Martel, S., Holbrook, W., and St. Clair, J. (2017). A model of three-dimensional topographic stresses with implications for bedrock fractures, surface processes, and landscape evolution. *Journal of Geophysical Research: Earth Surface*, 122(4):823–846.

Mori, N., Takahashi, T., Yasuda, T., and Yanagisawa, H. (2011). Survey of 2011 tohoku earthquake tsunami inundation and run-up. *Geophysical research letters*, 38(7).

Morimoto, R. (1951). Geology of imaichi district with special reference to the earthquakes of dec. 26th., 1949 (ii). *Bulletin of the Earthquake Research Institute*, 29:349–358.

Muhuri, S. K., Dewers, T. A., Scott Jr, T. E., and Reches, Z. (2003). Interseismic fault strengthening and earthquake-slip instability: Friction or cohesion? *Geology*, 31(10):881–884.

Newmark, N. M. (1976). Effects of earthquakes on dams and embankments.

Noever, D. A. (1993). Himalayan sandpiles. *Physical Review E*, 47(1):724.

Nuannin, P., Kulhanek, O., and Persson, L. (2005). Spatial and temporal b value anomalies preceding the devastating off coast of nw sumatra earthquake of december 26, 2004. *Geophysical research letters*, 32(11).

Olami, Z., Feder, H. J. S., and Christensen, K. (1992). Self-organized criticality in a continuous, nonconservative cellular automaton modeling earthquakes. *Physical Review Letters*, 68(8):1244.

Orowan, E. (1949). Fracture and strength of solids. *Reports on progress in physics*, 12(1):185.

Pacheco, J. F., Scholz, C. H., and Sykes, L. R. (1992). Changes in frequency–size relationship from small to large earthquakes. *Nature*, 355(6355):71.

Palmer, A. C. and Rice, J. R. (1973). The growth of slip surfaces in the progressive failure of over-consolidated clay. *Proc. R. Soc. Lond. A*, 332(1591):527–548.

Pandey, M., Tandukar, R., Avouac, J., Vergne, J., and Heritier, T. (1999). Seismotectonics of the nepal himalaya from a local seismic network. *Journal of Asian Earth Sciences*, 17(5-6):703–712.

Parise, M. and Jibson, R. W. (2000). A seismic landslide susceptibility rating of geologic units based on analysis of characteristics of landslides triggered by the 17 january, 1994 northridge, california earthquake. *Engineering geology*, 58(3):251–270.

Parker, R. N., Densmore, A. L., Rosser, N. J., De Michele, M., Li, Y., Huang, R., Whadcoat, S., and Petley, D. N. (2011). Mass wasting triggered by the 2008 Wenchuan earthquake is greater than orogenic growth. *Nature Geoscience*, 4(7):449–452.

Pelletier, J. D., Malamud, B. D., Blodgett, T., and Turcotte, D. L. (1997). Scale-invariance of soil moisture variability and its implications for the frequency-size distribution of landslides. *Engineering Geology*, 48(3):255–268.

Peltzer, G., Rosen, P., Rogez, F., and Hudnut, K. (1998). Poroelastic rebound along the landers 1992 earthquake surface rupture. *Journal of Geophysical Research: Solid Earth*, 103(B12):30131–30145.

Perfettini, H., Schmittbuhl, J., Rice, J. R., and Cocco, M. (2001). Frictional response induced by time-dependent fluctuations of the normal loading. *Journal of Geophysical Research: Solid Earth*, 106(B7):13455–13472.

Perrin, G., Rice, J. R., and Zheng, G. (1995). Self-healing slip pulse on a frictional surface. *Journal of the Mechanics and Physics of Solids*, 43(9):1461–1495.

Petley, D. (2012). Global patterns of loss of life from landslides. *Geology*, 40(10):927–930.

Plafker, G., Ericksen, G. E., and Fernandez Concha, J. (1971). Geological aspects of the may 31, 1970, peru earthquake. *Bulletin of the Seismological Society of America*, 61(3):543–578.

Power, W., Tullis, T., Brown, S., Boitnott, G., and Scholz, C. (1987). Roughness of natural fault surfaces. *Geophysical Research Letters*, 14(1):29–32.

Power, W. L., Tullis, T. E., and Weeks, J. D. (1988). Roughness and wear during brittle faulting. *Journal of Geophysical Research: Solid Earth*, 93(B12):15268–15278.

Pratt, H., Black, A., Brown, W., and Brace, W. (1972). The effect of speciment size on the mechanical properties of unjointed diorite. In *International Journal of Rock Mechanics and Mining Sciences & Geomechanics Abstracts*, volume 9, pages 513–516. Elsevier.

Rabinowicz, E. (1951). The nature of the static and kinetic coefficients of friction. *Journal of applied physics*, 22(11):1373–1379.

Rabinowicz, E. (1958). The intrinsic variables affecting the stick-slip process. *Proceedings of the Physical Society*, 71(4):668.

Ramsay, W. (1924). The probable solution of the climate problem in geology. *Geological Magazine*, 61(4):152–163.

Raymo, M. E., Ruddiman, W. F., and Froelich, P. N. (1988). Influence of late cenozoic mountain building on ocean geochemical cycles. *Geology*, 16(7):649–653.

Reasenberg, P. A. and Simpson, R. W. (1992). Response of regional seismicity to the static stress change produced by the loma prieta earthquake. *Science*, 255(5052):1687–1690.

Reid, H. F. (1910). The mechanics of the earthquake. *The California Earthquake of April 18, 1906, Report of the State Earthquake Investigation Commission*.

Reyes, A., Brune, J., Barker, T., Canales, L., Madrid, J., Rebollar, J., and Munguia, L. (1975). A microearthquake survey of the san miguel fault zone, baja california, mexico. *Geophysical Research Letters*, 2(2):56–59.

Rice, J. and Ruina, A. L. (1983). Stability of steady frictional slipping. *Journal of applied mechanics*, 50(2):343–349.

Rice, J. R. (1993). Spatio-temporal complexity of slip on a fault. *Journal of Geophysical Research: Solid Earth*, 98(B6):9885–9907.

Rice, R. M., Crobett, E., and Bailey, R. (1969). Soil slips related to vegetation, topography, and soil in southern california. *Water Resources Research*, 5(3):647–659.

Rivière, J., Lv, Z., Johnson, P., and Marone, C. (2018). Evolution of b-value during the seismic cycle: Insights from laboratory experiments on simulated faults. *Earth and Planetary Science Letters*, 482:407–413.

Roback, K., Clark, M. K., West, A. J., Zekkos, D., Li, G., Gallen, S. F., Chamlagain, D., and Godt, J. W. (2017). The size, distribution, and mobility of landslides caused by the 2015 m w 7.8 gorkha earthquake, nepal. *Geomorphology*.

Rogers, G. and Dragert, H. (2003). Episodic tremor and slip on the cascadia subduction zone: The chatter of silent slip. *Science*, 300(5627):1942–1943.

Romanet, P. (2017). *Fast algorithms to model quasi-dynamic earthquake cycles in complex faults networks*. PhD thesis, Institut de physique du globe de Paris.

Romanet, P., Bhat, H. S., Jolivet, R., and Madariaga, R. (2018). Fast and slow slip events emerge due to fault geometrical complexity. *Geophysical Research Letters*.

Rubin, A. and Ampuero, J.-P. (2005). Earthquake nucleation on (aging) rate and state faults. *Journal of Geophysical Research: Solid Earth*, 110(B11).

Ruina, A. (1983). Slip instability and state variable friction laws. *Journal of Geophysical Research: Solid Earth*, 88(B12):10359–10370.

Rydelek, P. A. and Sacks, I. S. (1989). Testing the completeness of earthquake catalogues and the hypothesis of self-similarity. *Nature*, 337(6204):251–253.

Savage, H. M. and Marone, C. (2007). Effects of shear velocity oscillations on stick-slip behavior in laboratory experiments. *Journal of Geophysical Research: Solid Earth*, 112(B2).

Savage, H. M. and Marone, C. (2008). Potential for earthquake triggering from transient deformations. *Journal of Geophysical Research: Solid Earth*, 113(B5).

Savin, S. M. (1977). The history of the earth's surface temperature during the past 100 million years. *Annual review of earth and planetary sciences*, 5(1):319–355.

Schmidt, K. M. (1994). Moutain Scale Strength Properties, Deep-Seated Landsliding, and Relief Limits.

Schmidt, K. M. and Montgomery, D. R. (1995). Limits to relief. *Science*, 270(5236):617.

Scholz, C. (1968). The frequency-magnitude relation of microfracturing in rock and its relation to earthquakes. *Bulletin of the seismological society of America*, 58(1):399–415.

Scholz, C. (1988). The brittle-plastic transition and the depth of seismic faulting. *Geologische Rundschau*, 77(1):319–328.

Scholz, C. H. (1997). Size distributions for large and small earthquakes. *Bulletin of the Seismological Society of America*, 87(4):1074–1077.

Scholz, C. H. (2002). *The mechanics of earthquakes and faulting*. Cambridge university press.

Scholz, C. H. (2015). On the stress dependence of the earthquake b value. *Geophysical Research Letters*, 42(5):1399–1402.

Schorlemmer, D., Wiemer, S., and Wyss, M. (2005). Variations in earthquake-size distribution across different stress regimes. *Nature*, 437(7058):539.

Schwanghart, W., Ryan, M., and Korup, O. (2018). Topographic and seismic constraints on the vulnerability of himalayan hydropower. *Geophysical Research Letters*.

Schwanghart, W. and Scherler, D. (2014). Topotoolbox 2–matlab-based software for topographic analysis and modeling in earth surface sciences. *Earth Surface Dynamics*, 2(1):1–7.

Schwartz, D. P. and Coppersmith, K. J. (1984). Fault behavior and characteristic earthquakes: Examples from the wasatch and san andreas fault zones. *Journal of Geophysical Research: Solid Earth*, 89(B7):5681–5698.

Seeber, L., Armbruster, J. G., Kim, W.-Y., Barstow, N., and Scharnberger, C. (1998). The 1994 cacoosing valley earthquakes near reading, pennsylvania: A shallow rupture triggered by quarry unloading. *Journal of Geophysical Research: Solid Earth*, 103(B10):24505–24521.

Senent, S., Jimenez, R., and Reyes, A. (2013). Numerical simulation of the influence of small-scale defects on the true-triaxial strength of rock samples. *Computers and Geotechnics*, 53:142–156.

Shaw, B. E. (2013). Earthquake surface slip-length data is fit by constant stress drop and is useful for seismic hazard analysis. *Bulletin of the Seismological Society of America*, 103(2A):876–893.

Shimazaki, K. and Nakata, T. (1980). Time-predictable recurrence model for large earthquakes. *Geophysical Research Letters*, 7(4):279–282.

SI, F., Kostoglodov, V., KM, L., Manea, M., and JA, S. (2005). Propagation of the 2001-2002 silent earthquake and interplate coupling in the oaxaca subduction zone, mexico. *Earth, planets and space*, 57(10):973–985.

Sidle, R. C. and Ochiai, H. (2006). *Landslides: processes, prediction, and land use*, volume 18. American Geophysical Union.

Sidle, R. C., Pearce, A. J., and O'Loughlin, C. L. (1985). *Hillslope stability and land use*. American Geophysical Union.

Sieh, K., Stuiver, M., and Brillinger, D. (1989). A more precise chronology of earthquakes produced by the san andreas fault in southern california. *Journal of Geophysical Research: Solid Earth*, 94(B1):603–623.

Simpson, G. (2015). Accumulation of permanent deformation during earthquake cycles on reverse faults. *Journal of Geophysical Research: Solid Earth*, 120(3):1958–1974.

Sitar, N., MacLaughlin, M. M., and Doolin, D. M. (2005). Influence of kinematics on landslide mobility and failure mode. *Journal of geotechnical and geoenvironmental engineering*, 131(6):716–728.

Sklar, L. S. and Dietrich, W. E. (2006). The role of sediment in controlling steady-state bedrock channel slope: Implications of the saltation–abrasion incision model. *Geomorphology*, 82(1-2):58–83.

Smith, W. D. (1981). The b-value as an earthquake precursor. *Nature*, 289(5794):136.

Sornette, D. (2006). *Critical phenomena in natural sciences: chaos, fractals, selforganization and disorder: concepts and tools*. Springer Science & Business Media.

Stark, C. and Guzzetti, F. (2009). Landslide rupture and the probability distribution of mobilized debris volumes. *Journal of Geophysical Research: Earth Surface (2003–2012)*, 114(F2).

Stark, C. P. and Hovius, N. (2001). The characterization of landslide size distributions. *Geophysical Research Letters*, 28(6):1091–1094.

Steer, P., Jeandet, L., Cubas, N., Marc, O., Meunier, P., Hovius, N., Simoes, M., Cattin, R., Shyu, J. B. H., Mouyen, M., Liang, W.-T., Theunissen, T., and Chiang, S.-h. (2018). Earthquake statistics changed by typhoon-driven erosion. *Nature Geoscience*.

Steer, P., Simoes, M., Cattin, R., and Shyu, J. B. H. (2014). Erosion influences the seismicity of active thrust faults. *Nature communications*, 5.

Stolle, A., Schwanghart, W., Andermann, C., Bernhardt, A., Fort, M., Jansen, J. D., Wittmann, H., Merchel, S., Rugel, G., Adhikari, B. R., et al. (2018). Protracted river response to medieval earthquakes. *Earth Surface Processes and Landforms*.

Strauss, D., Bednar, L., and Mees, R. (1989). Do one percent of the forest fires cause ninety-nine percent of the damage? *Forest Science*, 35(2):319–328.

Suppe, J. (1981). Mechanics of mountain building and metamorphism in taiwan. *Mem. Geol. Soc. China*, 4(6):67–89.

Suppe, J. (2014). Fluid overpressures and strength of the sedimentary upper crust. *Journal of Structural Geology*, 69:481–492.

Sutcliffe, D., Yu, H., and Sloan, S. (2004). Lower bound solutions for bearing capacity of jointed rock. *Computers and Geotechnics*, 31(1):23–36.

Tada, T. (1996). Boundary integral equations for the time-domain and time-independent analyses of 2d non-planar cracks. *PhD Thesis, The University of Tokyo*.

Tada, T. and Madariaga, R. (2001). Dynamic modelling of the flat 2-d crack by a semi-analytic biem scheme. *International Journal for Numerical Methods in Engineering*, 50(1):227–251.

TAI, Y.-C. (2009). Aerial photogrammetry investigation and numerical simulation of tsaoling landslide triggered by the 1999 chi-chi earthquake, taiwan.

Tal, Y., Hager, B. H., and Ampuero, J. P. (2018). The effects of fault roughness on the earthquake nucleation process. *Journal of Geophysical Research: Solid Earth*, 123(1):437–456.

Tanaka, S., Ohtake, M., and Sato, H. (2004). Tidal triggering of earthquakes in japan related to the regional tectonic stress. *Earth, planets and space*, 56(5):511–515.

Tanyaş, H., Van Westen, C. J., Allstadt, K. E., Jessee, M. A. N., Görüm, T., Jibson, R. W., Godt, J. W., Sato, H. P., Schmitt, R. G., Marc, O., et al. (2017). Presentation and analysis of a worldwide database of earthquake-induced landslide inventories. *Journal of Geophysical Research: Earth Surface*, 122(10):1991–2015.

Terzaghi, K. (1962). Stability of steep slopes on hard unweathered rock. *Geotechnique*, 12(4):251–270.

Thom, C., Brodsky, E., Carpick, R., Pharr, G., Oliver, W., and Goldsby, D. (2017). Nanoscale roughness of natural fault surfaces controlled by scale-dependent yield strength. *Geophysical Research Letters*, 44(18):9299–9307.

Thomas, M. Y., Lapusta, N., Noda, H., and Avouac, J.-P. (2014). Quasi-dynamic versus fully dynamic simulations of earthquakes and aseismic slip with and without enhanced coseismic weakening. *Journal of Geophysical Research: Solid Earth*, 119(3):1986–2004.

Toda, S., Stein, R. S., Beroza, G. C., and Marsan, D. (2012). Aftershocks halted by static stress shadows. *Nature Geoscience*, 5(6):410.

Toda, S., Stein, R. S., and Sagiya, T. (2002). Evidence from the ad 2000 izu islands earthquake swarm that stressing rate governs seismicity. *Nature*, 419(6902):58.

Townend, J. and Zoback, M. D. (2000). How faulting keeps the crust strong. *Geology*, 28(5):399–402.

Triep, E. G. and Sykes, L. R. (1997). Frequency of occurrence of moderate to great earthquakes in intracontinental regions: Implications for changes in stress, earthquake prediction, and hazards assessments. *Journal of Geophysical Research: Solid Earth*, 102(B5):9923–9948.

Uchida, T., Niwa, S., Horie, K., Hida, Y., Okamura, S., Hayashi, S., and Kanbara, J. (2014). Prolonged effects of large sediment yield events on sediment dynamics in mountainous catchments. *Proceeding of the INTERPRAEVENT*, pages 43–51.

Utsu, T. (1971). Aftershocks and earthquake statistics (2): further investigation of aftershocks and other earthquake sequences based on a new classification of earthquake sequences. *Journal of the Faculty of Science, Hokkaido University. Series 7, Geophysics*, 3(4):197–266.

Utsu, T. (2002). Statistical features of seismicity. *International Geophysics Series*, 81(A):719–732.

Van Den Eeckhaut, M., Poesen, J., Govers, G., Verstraeten, G., and Demoulin, A. (2007). Characteristics of the size distribution of recent and historical landslides in a populated hilly region. *Earth and Planetary Science Letters*, 256(3):588–603.

Vernant, P., Hivert, F., Chery, J., Steer, P., Cattin, R., and Rigo, A. (2013). Erosion-induced isostatic rebound triggers extension in low convergent mountain ranges. *Geology*, 41(4):467–470.

Vidale, J. E., Agnew, D. C., Johnston, M. J., and Oppenheimer, D. H. (1998). Absence of earthquake correlation with earth tides: An indication of high preseismic fault stress rate. *Journal of Geophysical Research: Solid Earth*, 103(B10):24567–24572.

Viesca, R. C. and Rice, J. R. (2012). Nucleation of slip-weakening rupture instability in landslides by localized increase of pore pressure. *Journal of Geophysical Research: Solid Earth*, 117(B3).

Wang, J., Jin, Z., Hilton, R. G., Zhang, F., Densmore, A. L., Li, G., and West, A. J. (2015). Controls on fluvial evacuation of sediment from earthquake-triggered landslides. *Geology*, 43(2):115–118.

Wesnousky, S., Scholz, C., Shimazaki, K., and Matsuda, T. (1983). Earthquake frequency distribution and the mechanics of faulting. *Journal of Geophysical Research: Solid Earth*, 88(B11):9331–9340.

West, A., Lin, C.-W., Lin, T.-C., Hilton, R., Liu, S.-H., Chang, C.-T., Lin, K.-C., Galy, A., Sparkes, R., and Hovius, N. (2011). Mobilization and transport of coarse woody debris to the oceans triggered by an extreme tropical storm. *Limnology and oceanography*, 56(1):77–85.

Whipple, K. X. (2009). The influence of climate on the tectonic evolution of mountain belts. *Nature geoscience*, 2(2):97.

Whipple, K. X. and Tucker, G. E. (1999). Dynamics of the stream-power river incision model: Implications for height limits of mountain ranges, landscape response timescales, and research needs. *Journal of Geophysical Research: Solid Earth*, 104(B8):17661–17674.

Whitehouse, I. (1983). Distribution of large rock avalanche deposits in the central southern alps, new zealand. *New Zealand journal of geology and geophysics*, 26(3):271–279.

Wiemer, S. and Wyss, M. (2000). Minimum magnitude of completeness in earthquake catalogs: Examples from alaska, the western united states, and japan. *Bulletin of the Seismological Society of America*, 90(4):859–869.

Wilcock, W. S. (2001). Tidal triggering of microearthquakes on the juan de fuca ridge. *Geophysical Research Letters*, 28(20):3999–4002.

Willett, S., Beaumont, C., and Fullsack, P. (1993). Mechanical model for the tectonics of doubly vergent compressional orogens. *Geology*, 21(4):371–374.

Willett, S. D. (1999). Orogeny and orography: The effects of erosion on the structure of mountain belts. *Journal of Geophysical Research: Solid Earth*, 104(B12):28957–28981.

Wilson, L. (1973). Variations in mean annual sediment yield as a function of mean annual precipitation. *American Journal of Science*, 273(4):335–349.

Woessner, J. and Wiemer, S. (2005). Assessing the quality of earthquake catalogues: Estimating the magnitude of completeness and its uncertainty. *Bulletin of the Seismological Society of America*, 95(2):684–698.

Wolfe, J. A. (1978). A paleobotanical interpretation of tertiary climates in the northern hemisphere: Data from fossil plants make it possible to reconstruct tertiary climatic changes, which may be correlated with changes in the inclination of the earth's rotational axis. *American Scientist*, 66(6):694–703.

Xia, K., Rosakis, A. J., and Kanamori, H. (2004). Laboratory earthquakes: The sub-rayleigh-to-supershear rupture transition. *Science*, 303(5665):1859–1861.

Xie, J., Wang, M., Liu, K., and Coulthard, T. J. (2018). Modeling sediment movement and channel response to rainfall variability after a major earthquake. *Geomorphology*, 320:18–32.

Xu, C., Xu, X., Yao, X., and Dai, F. (2014). Three (nearly) complete inventories of landslides triggered by the may 12, 2008 wenchuan mw 7.9 earthquake of china and their spatial distribution statistical analysis. *Landslides*, 11(3):441–461.

Yanites, B. J., Tucker, G. E., Mueller, K. J., and Chen, Y.-G. (2010). How rivers react to large earthquakes: Evidence from central taiwan. *Geology*, 38(7):639–642.

Zhang, S., Zhang, L., Lacasse, S., and Nadim, F. (2016). Evolution of mass movements near epicentre of wenchuan earthquake, the first eight years. *Scientific Reports*, 6:36154.

Ziv, A. and Cochard, A. (2006). Quasi-dynamic modeling of seismicity on a fault with depth-variable rate-and state-dependent friction. *Journal of Geophysical Research: Solid Earth*, 111(B8).

**APPENDIX A**

EARTHQUAKE STATISTICS CHANGED BY TYPHOON-DRIVEN EROSION

**AUTHORS:**
Philippe Steer[1], Louise Jeandet[1], Nadaya Cubas[2], Odin Marc[3,4], Patrick Meunier[3,5], Martine Simoes[6], Rodolphe Cattin[7], J. Bruce H. Shyu[8], Maxime Mouyen[1], Wen-Tzong Liang[9], Thomas Theunissen[10], Shou-Hao Chiang[11] and Niels Hovius[3,4].

[1]Géosciences Rennes, Univ Rennes and CNRS, UMR 6118, F-35000 Rennes, France
[2]Institut des Sciences de la Terre, Université Pierre et Marie Curie and CNRS UMR7193, 75005 Paris, France
[3]Helmholtz Centre Potsdam, German Research Center for Geosciences (GFZ), 14473 Potsdam, Germany
[4]Institute of Earth and Environmental Sciences, University of Potsdam, 14476 Potsdam-Golm, Germany
[5]Laboratoire de Géologie, École Normale Supérieure de Paris, 75231 Paris CEDEX 5, France
[6]Institut de Physique du Globe de Paris, Sorbonne Paris Cité, Univ. Paris Diderot, UMR 7154 CNRS, F-75005 Paris, France
[7]Géosciences Montpellier, Université Montpellier and CNRS UMR5243, 34090 Montpellier, France
[8]Department of Geosciences, National Taiwan University, Taipei, Taiwan
[9]Institute of Earth Sciences, Academia Sinica, Taipei, Taiwan
[10]Department of Earth Science, University of Bergen, N-5007 Bergen, Norway
[11]Center for Space and Remote Sensing Research, National Central University, Taoyuan City 32001, Taiwan

**SUMMARY PARAGRAPH:**

**Tectonics and climate-driven surface processes govern the evolution of Earth's surface topography[1,2]. Topographic change in turn influences lithospheric deformation[3-5], but the elementary scale at which this feedback can be effective is unclear. Here we show that it operates in a single weather-driven erosion event. In 2009, typhoon Morakot delivered ~3 m of precipitation in southern Taiwan, causing exceptional landsliding and erosion[6,7]. This event was followed by a step increase in the shallow (< 15 km depth) earthquake frequency lasting at least 2.5 years. Also, the scaling of earthquake magnitude and frequency underwent a sudden increase in the area where mass wasting was most intense. These observations suggest that the progressive removal of landslide debris by rivers from southern Taiwan has acted to increase the crustal stress rate to the extent that earthquake activity was demonstrably affected. Our study offers the first quasi-real-time observation of the impact of a single weather-driven erosion event on tectonics.**

**TEXT:**

Theoretical predictions and numerical models suggest that changes of surface topography due to erosion and sedimentation can promote tectonic deformation over geological times[3,4] (1–10 Myr), enhance fault slip over intermediate time scales[8-11] (1 kyr–1 Myr), and induce sufficient static stress changes over a seismic cycle (1-1000 yr) to trigger earthquakes[12]. However, the influence of ongoing surface processes on tectonics has not been directly observed. Here we ask if a single erosional event can have a discernable effect on seismogenic processes, which dominate deformation of the Earth's upper crust. Extreme rainfall events can trigger instantaneous and widespread landsliding, driving the export of millions of tons of sediment from mountain areas over periods of months to years[2,13]. At these time-scales, geophysical methods allow monitoring of changes in earthquake activity associated with erosional perturbations.

For an example of an erosional perturbation, we consider typhoon Morakot, which made landfall in Taiwan from 7 to 9 August 2009. It delivered up to 3 m of precipitation in 3 days (Fig. 1), the largest recorded rainfall event in Taiwan in the past 50 years[14]. The typhoon triggered more than 10.000 landslides (see Methods) in mountainous southwest Taiwan, where cumulative rainfall exceeded ~1 m (Fig. 1 and Extended Data Fig. 1). In this area of ~7000 $km^2$ (hereafter the landsliding zone), that accounts for ~99% of the 0.7 $km^3$ of total landslide volume, the landslide spatial density ranges between 4 and 22 $km^{-2}$ (see Methods and Extended Data Fig. 2). The equivalent average erosion induced by these landslides is ~10 cm, which corresponds to 10-100 years of erosion at the decadal average rate[2]. Most triggered landslides were connected to the river network[15], which has led to a sharp increase of suspended sediment export after Morakot[6,7]. Consistent with geomorphological observations after the 1999 Mw 7.6 Chi-Chi earthquake[16], enhanced sediment removal persisted for >2 years[6,7], although export of the coarse fraction of landslide debris may take about a decade[17]. The exact volume of sediment export is difficult to estimate, but the landsliding zone must have undergone a progressive surface mass unloading after one of the largest weather-driven erosion events on record.

The landsliding zone belongs to a tectonically active region and is bounded in the east and west by several identified active thrust faults[18]. Thrust faults located in the western foothills have a

dip angle between 10 and 30° and merge at depth, probably around ~10-15 km, into a basal decollement beneath the range[18,19]. In the east, the Longitudinal Valley fault has a dip angle ~45-60°. Together, these faults accommodate ~40 mm.yr$^{-1}$ of slip rate, that is about half of the total convergence rate across the Taiwan plate boundary[20]. In addition, less well constrained faults are located beneath the range, as testified by the frequent and potentially shallow seismicity observed in Central Taiwan.

To determine how the erosional unloading due to typhoon Morakot has impacted fault dynamics, we analyze the evolution of shallow (<15 km) seismicity in Taiwan after it made landfall. Because the expected stress change is small compared to tectonic loading at seismogenic depth[12], we focus on detecting changes in the statistics of recorded seismicity, such as the earthquake frequency, seismic moment rate and the b-value of the Gutenberg-Richter earthquake size distribution (see Methods), rather than on individual events. We use the seismicity catalogue of the Central Weather Bureau of Taiwan, which includes >340,000 earthquakes during the period 1995-2015 over Taiwan island.

First, we assess the time evolution of earthquake statistics using a temporal sliding window of 1001 earthquakes (see Methods). Results show a step-wise increase of the frequency of shallow (<15 km) earthquakes in the landsliding zone after Morakot (Fig. 2 and Extended Data Fig. 3). Although this frequency increase is orders of magnitude lower than after the Chi-Chi earthquake, it is observed both for earthquakes with magnitude above the completeness magnitude (from ~0.8 to ~2 earthquakes per day) and for all recorded earthquakes (from ~5 to ~10 earthquakes per day). The increase of earthquake frequency during the 2.5 yr after Morakot has a probability of 1 (see Methods and Extended Data Fig. 4). The probability is still significant, in the 90% confidence interval, when considering a frequency increase by a factor ~1.2-1.5. Except for Chichi earthquake, this is the only significant and probable increase in earthquake frequency, over a period of 2.5 yr, observed over the investigated period (1994-2013).

Moreover, the increase in earthquake frequency after Morakot is associated with an increase in the b-value from 1.18±0.1 to 1.28±0.1 (Fig. 3 a). Both increases have a step-like shape, which lasts

for at least 2.5 years (Extended Data Fig. 5 and 6) and does not correspond to an Omori-type inverse law, which describes the temporal evolution of aftershock sequences. Because the seismometer network used to detect earthquakes remained similar in the time period January 2007 to December 2011 (see Methods and Extended Data Fig. 7), we restrict our comparison to the time period from 2.5 years before to 2.5 years after Morakot. More instruments were added, mainly in North Taiwan, at the beginning of 2012, which could explain why the frequency of earthquakes remains high in the landsliding zone after 2012, despite a decrease of the b-value towards its pre-Morakot value. The increase of the b-value in the landsliding zone after Morakot is found for different fitting methods of the Gutenberg-Richter law and sampling methods associated with the sliding time window (see Methods and Extended Data Fig. 5 and 6) and therefore deemed robust.

In addition, considering all earthquakes during the 2.5 years before and after Morakot gives b-value estimates of 1.17±0.03 and 1.31±0.04 (Fig. 2c), respectively, similar to the values obtained by averaging the temporal b-value signal (Fig. 3a). We observe that the increase in earthquake frequency and b-value in the landsliding zone after Morakot coincides with an increase (~30% for peak-to-peak change) in the number of shallow earthquakes at depths <10 km (Fig. 3 b). However, the rate of seismic moment release remains low after typhoon Morakot, and potentially lower than before (Extended Data Fig. 3). Crucially, earthquakes outside the landsliding zone do not show a significant temporal evolution of their frequency and b-value after Morakot.

These temporal changes in earthquake statistics after Morakot are determined from an undeclustered earthquake catalog. However, using a declustered catalog (see Methods) also lead to similar changes in earthquake frequency and in its associated probability, b-value and depth-distribution after Morakot (Extended Data Fig. 9). This demonstrates that these seismicity changes are not associated to triggering processes by large mainshocks. In addition, based on comparisons between the observed earthquake catalog and synthetic catalogs that share the same average properties, we demonstrate that the observed changes in earthquake frequency and b-value after Morakot depart statistically from random temporal changes in seismicity in the landsliding zone

(Extended Data Fig. 11).

Previous intense erosional events associated with Chi-Chi earthquake (1999), and typhoons Herb (1996) and Toraji (2001) did not induce any detectable change of seismicity. This may be because these events had less erosion, the total volume of ~0.45 $km^3$ of landslides triggered by Chi-Chi earthquake[21] being by far the largest, and because most landslides triggered by these events deposited debris distant from rivers[13]. Besides, the high rate of aftershocks after Chi-Chi prevents detection of a change in earthquake frequency or b-value associated with erosion due to Chi-Chi or Toraji, if there was any.

To assess how the chosen delimited area affects our results, we compute the change in the spatial pattern of the frequency and b-value of shallow (<15 km) earthquakes from before to after Morakot. For this, we use a sliding window in space with a radius of 30 km, which allows us to detect large-scale features not affected by small sub-samples of events (see Methods). It is applied separately to earthquakes in the 2.5 years before and after Morakot, respectively. Consistent with the temporal evolution of earthquake frequency, results show an increase in the number $N$ of earthquakes after the typhoon over the landsliding zone (Fig. 4 and Extended Data Fig. 8). This increase is observed for earthquakes with magnitudes above the completeness magnitude and also for all recorded earthquakes. It is not limited to the vicinity of the landsliding zone, but it also occurred in northeast Taiwan. However, outside the landsliding zone, changes in the b-value appear not to be associated to changes in the number of earthquakes. We note that the spatial correlation between earthquake statistics change and the landsliding zone is less resolved and less robust (see Methods) than the temporal correlation.

Non-erosional causes of the observed changes in earthquake statistics in SW Taiwan are possible but appear unlikely. Earthquakes can be triggered by stresses induced by tectonics, in general, but also by other earthquakes[22]. In March 2010, the Mw 6.3 Jiashian earthquake occurred within the landsliding zone, close to its western limit, and was followed by many aftershocks. However, this earthquake and most aftershocks are located at 15-25 km depth, as shown by

seismological records[23] and further confirmed by the declustering process, which mostly removes events below 15 km depth, (Extended Data Fig. 10). Therefore, the Jiashian earthquake does not affect shallow earthquake statistics and cannot be responsible for the increase of the b-value after Morakot (Extended Data Fig. 10). Hydrological triggering of seismicity after the heavy rainfall during typhoon Morakot, either by surface loading or by pore pressure diffusion[24], could be an alternative mechanism. Indeed, on the east coast of Taiwan, where landslide erosion was limited, borehole water levels rose by 4 m after typhoon Morakot, and a volumetric contractional strain was observed[25,26]. However, both signals decayed in ~6 months and their amplitudes and temporal evolutions do not depart from the mean seasonal trends observed from 2006 to 2011. Moreover, pore pressure diffusion along permeable faults after large rainfall events generally leads to episodic increases of seismicity[27] and not to prolonged changes as observed in our case.

The temporal and spatial collocation of intense landsliding triggered by typhoon Morakot and the observed increase of shallow earthquake frequency and b-value suggest a potential mechanistic link. Direct physical modeling of the impact of erosion during and after Morakot on seismicity is beyond our reach because the location and rate of sediment export from the landsliding zone are not reliably constrained. Despite this, simple elastic models show that large erosional events with rapid sediment export can induce static stresses at depth, sufficient to overcome tectonic stresses on the shallower (<5-10 km) parts of faults[12]. Removing 10 to 100% of the landslide volume in 2.5 years, equivalent to about 1 to 10 cm of erosion over the landsliding zone, would lead to a Coulomb stress increment on a nearby thrust fault of about 0.5 $10^{-2}$ to 0.5 $10^{-1}$ bar at 5 km depth[12], using a thrust dip angle of 30° and a friction of 0.6. These stress increments are roughly similar to the ones induced by seasonal hydrologic loading in the Himalaya, ~0.2-0.4 $10^{-1}$ bar, which are suggested to lead to a seasonal modulation of earthquake frequency[28].

In addition, spring-slider models[29] and 2D elasto-dynamic models of seismogenic faults[30] with rate-and-state friction laws[31,32] show that the rate of seismicity can increase linearly or more than linearly due to a positive, step-like stress perturbation. It is also observed that shallow earthquakes

143 generally have smaller magnitudes and larger b-values than deeper earthquakes[33] possibly because
144 they nucleate at lower differential stresses[34].Our observations suggest that the intense and prolonged
145 sediment export and surface unloading after typhoon Morakot could have acted as a succession of
146 step-wise increase of stresses on the shallow parts of underlying thrust faults[12], giving rise to a similar
147 increase of shallow earthquake frequency and b-value in Southwest Taiwan.

148 This result offers new perspectives on the links between climate, erosion and tectonics[4,5] at
149 the time scale of elementary processes. While numerous studies have shown that earthquakes and
150 storms can trigger landslides[2,13,16,21], this is to our knowledge the first direct evidence of the ongoing
151 influence of erosion on seismicity. Because the mechanical link between erosion and stresses is
152 promoted by crustal elasticity[12], crustal deformation is sensitive not only to extreme weather-driven
153 erosion but also to the cumulative effects of smaller but numerous erosion events. More frequent
154 extreme rainfall under a warmer climate[35] could result in accelerated sediment transport[7] and in turn
155 in more frequent shallow earthquakes. The shallow but small-magnitude seismicity induced by
156 erosion is not likely to trigger new landslides, and the seismic moment rate would not be affected.
157 Hence, we do not expect a significant feedback of this additional deformation on erosion. However,
158 our results do call for a new generation of process-based models coupling landscape dynamics[17] and
159 fault dynamics[30] at scales relevant to natural hazards and societal issues. In these models, storms,
160 floods, mass wasting, river sediment transport, elastic stress transfer, seismicity and seismic wave
161 propagation should all be represented to account for the complexity of the links between climate,
162 erosion and tectonics.

**REFERENCES:**


1. Molnar, P., & England, P. Late Cenozoic uplift of mountain ranges and global climate change: chicken or egg?. Nature 346, 29-34 (1990).
2. Dadson, S. J. et al. Links between erosion, runoff variability and seismicity in the Taiwan orogen. Nature 426, 648-651 (2003).
3. Dahlen, F. A., & Suppe, J. Mechanics, growth, and erosion of mountain belts. Geological Society of America Special Papers 218, 161-178 (1988)
4. Willett, S. D. Orogeny and orography: The effects of erosion on the structure of mountain belts. Journal of Geophysical Research: Solid Earth 104, 28957-28981 (1999).
5. Whipple, K. X. The influence of climate on the tectonic evolution of mountain belts. Nature

Geoscience 2, 97-104 (2009).
6. Huang, M. Y. F., & Montgomery, D. R. Altered regional sediment transport regime after a large typhoon, southern Taiwan. Geology 41, 1223-1226 (2013).
7. Lee, T. Y. et al. Magnified sediment export of small mountainous rivers in Taiwan: chain reactions from increased rainfall intensity under global warming. PloS one 10, e0138283 (2015).
8. Cattin, R., & Avouac, J. P. Modeling mountain building and the seismic cycle in the Himalaya of Nepal. Journal of Geophysical Research: Solid Earth 105, 13389-13407 (2000).
9. Calais, E., Freed, A. M., Van Arsdale, R., & Stein, S. Triggering of New Madrid seismicity by late-Pleistocene erosion. Nature 466, 608-611 (2010).
10. Vernant, P. et al. Erosion-induced isostatic rebound triggers extension in low convergent mountain ranges. Geology 41, 467-470 (2013).
11. Maniatis, G., Kurfeß, D., Hampel, A., & Heidbach, O. Slip acceleration on normal faults due to erosion and sedimentation—Results from a new three-dimensional numerical model coupling tectonics and landscape evolution. Earth and Planetary Science Letters, 284(3), 570-582 (2009).
12. Steer, P., Simoes, M., Cattin, R., & Shyu, J. B. H. Erosion influences the seismicity of active thrust faults. Nature communications 5 (2014).
13. Dadson, S. J. et al. Earthquake-triggered increase in sediment delivery from an active mountain belt. Geology 32, 733-736 (2004).
14. Chien, F. C., & Kuo, H. C. On the extreme rainfall of Typhoon Morakot (2009). Journal of Geophysical Research: Atmospheres 116 (2011).
15. West, A. J. et al. Mobilization and transport of coarse woody debris to the oceans triggered by an extreme tropical storm. Limnology and oceanography 56, 77-85 (2011).
16. Hovius, N. et al. Prolonged seismically induced erosion and the mass balance of a large earthquake. Earth and Planetary Science Letters 304, 347-355 (2011).
17. Croissant, T., Lague, D., Steer, P. & Davy, P. Rapid post-seismic landslide evacuation boosted by dynamic river width. Nature Geosciences, in press. (2017).
18. Shyu, J. B. H., Sieh, K., Chen, Y. G., & Liu, C. S. Neotectonic architecture of Taiwan and its implications for future large earthquakes. Journal of Geophysical Research: Solid Earth 110 (2005).
19. Brown, D., Alvarez□Marron, J., Schimmel, M., Wu, Y. M., & Camanni, G. The structure and kinematics of the central Taiwan mountain belt derived from geological and seismicity data. Tectonics, 31(5) (2012).
20. Simoes, M., & Avouac, J. P. Investigating the kinematics of mountain building in Taiwan from the spatiotemporal evolution of the foreland basin and western foothills. Journal of Geophysical Research: Solid Earth, 111(B10) (2006).
21. Marc, O., Hovius, N., Meunier, P., Gorum, T., & Uchida, T. A seismologically consistent expression for the total area and volume of earthquake□triggered landsliding. Journal of Geophysical Research: Earth Surface 121, 640-663 (2016).
22. Stein, R. S. The role of stress transfer in earthquake occurrence. Nature 402, 605-609 (1999).
23. Hsu, Y. J., Yu, S. B., Kuo, L. C., Tsai, Y. C., & Chen, H. Y. Coseismic deformation of the 2010 Jiashian, Taiwan earthquake and implications for fault activities in southwestern Taiwan. Tectonophysics 502, 328-335 (2011).
24. Roeloffs, E. A. Fault stability changes induced beneath a reservoir with cyclic variations in water level. Journal of Geophysical Research: Solid Earth 93, 2107-2124 (1988).
25. Hsu, Y. J. et al. Revisiting borehole strain, typhoons, and slow earthquakes using quantitative estimates of precipitation□induced strain changes. Journal of Geophysical Research: Solid Earth 120, 4556-4571 (2015).
26. Mouyen, M., Canitano, A., Chao, B. F., Hsu, Y. J., Steer, P., Longuevergne, L., & Boy, J. P. Typhoon□Induced Ground Deformation. Geophysical Research Letters, 44(21) (2017).
27. Hainzl, S., Kraft, T., Wassermann, J., Igel, H., & Schmedes, E. Evidence for rainfall□triggered earthquake activity. Geophysical Research Letters 33 (2006).
28. Bettinelli, P. et al. Seasonal variations of seismicity and geodetic strain in the Himalaya induced

by surface hydrology. Earth and Planetary Science Letters, 266(3), 332-344 (2008).
29. Dieterich, J. A constitutive law for rate of earthquake production and its application to earthquake clustering. Journal of Geophysical Research: Solid Earth 99, 2601-2618 (1994).
30. Ader, T. J., Lapusta, N., Avouac, J. P., & Ampuero, J. P. Response of rate-and-state seismogenic faults to harmonic shear-stress perturbations. Geophysical Journal International 144 (2014).
31. Dieterich, J. H. Modeling of rock friction: 1. Experimental results and constitutive equations. Journal of Geophysical Research: Solid Earth 84, 2161-2168 (1979).
32. Ruina, A. Slip instability and state variable friction laws. Journal of Geophysical Research: Solid Earth 88, 10359-10370 (1983).
33. Mori, J., & Abercrombie, R. E. Depth dependence of earthquake frequency□magnitude distributions in California: Implications for rupture initiation. Journal of Geophysical Research: Solid Earth 102, 15081-15090 (1997).
34. Scholz, C. H. On the stress dependence of the earthquake b value. Geophysical Research Letters 42, 1399-1402 (2015).
35. Liu, S. C., Fu, C., Shiu, C. J., Chen, J. P., & Wu, F. Temperature dependence of global precipitation extremes. Geophysical Research Letters 36 (2009).

**Acknowledgements** P.S. and L.J. acknowledge funding by Université Rennes 1 and by Agence Nationale pour la Recherche (ANR) through the EROQUAKE project. We are grateful for support by the France-Taiwan International Associate Laboratory "From Deep Earth to Extreme Events", and thank the Central Weather Bureau of Taiwan and the Taiwan Typhoon and Floods Research Institute for access to their data. We thank Edwin Baynes, Dimitri Lague and Harsha Bhat for discussions, as well as two anonymous reviewers for their constructive comments. This is IPGP contribution # XXX.

**Author Contributions** P.S initiated this project, analyzed the data and led the writing of the paper. L.J and N.C. helped with the mechanical and statistical interpretation of the earthquake catalog that was partly analyzed and provided by W.-T.L. and T.T.. O.M., P.M. and N.H. checked and completed the landslide catalog that was provided by S.-H.C.. N.H. suggested investigation of the impact of typhoon Morakot. M.S., R.C., J.B.H.S. and M.M. contributed to the design of this study. All authors contributed to the writing of the paper.

**Author Information** Reprints and permissions information is available at www.nature.com/reprints. The authors declare no competing financial interest. Correspondence and requests for materials should be addressed to P.S. (philippe.steer@univ-rennes1.fr).

## METHODS:

### Morakot rainfall data:

The map of cumulated rainfall during Morakot was obtained by natural-neighbor interpolation of cumulated hourly rain gauge measurements over the period 7 to 9$^{th}$ of August 2009. Data from 377

stations across Taiwan were used from the Data Bank for Atmospheric Research at the Taiwan Typhoon and Floods Research Institute.

**Morakot landslide catalogue:**

Mapped landslides were delineated manually by comparing surface reflectivity and morphology on pre- and post-event FORMOSAT-2 satellite images[36] (2 m panchromatic and 8 m multi-spectral). To cover most of the islands we mosaicked multiple cloud-free pre-event (01/14, 05/08, 05/09, 05/10, 06/06) and post-event (08/17, 08/19, 08/21, 08/28, 08/30, 09/06) images taken in 2009. For parts of the inventory, especially east of the main divide, landslides were first mapped automatically and then edited manually. For both approaches, the scar, runout and deposit areas are not differentiated. We did not consider debris flow transport areas and excluded gentle slopes (<20°) from mapping to avoid confusion with human activity. Special attention was given to the separation of individual landslides, which had common transport or deposit areas but independent initiation points[37]. The robust and conservative estimation of landslide surface area is especially important for the estimation of landslide volume[38].

**Estimation of landslide volume:**

The landslide volume was estimated based on landslide area, following the method of ref. 37. Briefly, we assumed constant size ratios between scar and deposit areas of 1.1 and 1.9 for mixed and bedrock landslides, respectively[38]. Then, we converted the scar area into volume using a power law with different prefactor ($\alpha$) and exponent ($\gamma$) for mixed and bedrock landslides, with $\alpha = 0.146$ and $\gamma = 1.332$ for $A_{scar} < 1e5$ m$^2$ and $\alpha = 0.234$ and $\gamma = 1.41$ for $A_{scar} > 1e5$ m$^2$, respectively[37]. Recent studies have proposed a regional scaling relationship for the south of Taiwan, based on measurement of large landslides caused by typhoon Morakot[39]. With these parameters ($\alpha = 0.202$, $\gamma = 1.268$), and without scar correction, we obtain volumes ~3 times larger for intermediate size (mixed) landslides and twice smaller volume for very large (bedrock) landslides. Overall this would not change the order of magnitude of erosion nor the results discussed in this study.

**Earthquake catalogue of Taiwan:**

We extracted earthquakes at shallow depths (<15 km) from the earthquake catalogue of the Taiwan Central Weather Bureau[40] for the period 1995-2015 over the emergent part of Taiwan. This catalogue is accessible through the Taiwan Central Weather Bureau (http://gdms.cwb.gov.tw). The monitoring network includes short-period and broadband seismographic systems stations. The location and number of seismic stations changed during the period 1995-2015. The configuration of the seismic network in the south of Taiwan and in the landsliding zone remained relatively similar over the period January 2007 to December 2012 (see Extended Figure 8), but after 2012, 2.5 years after Morakot, the number of stations was increased mostly in North Taiwan. This has caused a decrease of the measured completeness magnitude over all of Taiwan, including in the landsliding zone (see Extended Figure 2). We therefore do not interpret changes in the frequency of earthquakes occurring after 2.5 years after Morakot (beginning of 2012).

**Characterization of earthquake size distribution:**

The Gutenberg-Richter distribution is classically used to characterize the relation of the number of earthquakes above a given magnitude, $n(\geq M) = 10^{a-bM}$, to the magnitude $M$, where a and b are parameters related to the number of earthquakes and to the slope of the relationship, respectively. This relationship is verified only for magnitudes above the completeness magnitude, $M_c$, of the catalogue. $M_c$ is determined by a modified version of the simple but robust maximum curvature method[41], where $M_c$ is equal to the maximum of the first derivative of the frequency-magnitude curve, plus 0.5. We compute a maximum likelihood estimate[42] of the b-value, $b = log_{10}e/(\overline{M} - M_c)$ and of its uncertainty, $\sigma = b/\sqrt{n(\geq M_c)}$, where $\overline{M}$ is the mean magnitude of the considered earthquakes with $M \geq M_c$. Note that the number of earthquakes considered has a strong control on the b-value estimate and its uncertainty[43], and that only relative spatial or temporal changes of the b-value should be interpreted.

**Time evolution of earthquake statistical properties:**

We use a temporal sliding window to subsample the earthquake catalogue and to assess time variations of earthquake statistical properties. Because uncertainty on the b-value strongly depends

on the number of considered events, and because larger samples give better estimates, we use a sliding window of $N = 1001$ events to prevent undue statistical bias. The window is centred on a given earthquake and the corresponding b-value and earthquake frequency are determined for the 500 earthquakes that occurred immediately before and immediately after this event. Earthquake frequency is computed by dividing $N$ by the temporal length of the sliding window. Among the 1001 earthquakes, only those with magnitude above $M_c$ are used to estimate the b-value. We assess the effect of changing the sampling method of the temporal window, by considering an *a priori* value of $M_c = 2.25$, and considering a fixed number of earthquakes with a magnitude $> M_c$ ranging from $N = 101$ to $N = 1001$ (Extended Data Fig. 5 and 6). We find a consistent increase of b-value in the 2.5 years after Morakot for $N$ ranging from 101 to 501, as all these earthquakes occurred within a time window duration lower than 2.5 years. For $N = 751$ or $N = 1001$ the window duration is equal to or greater than 2.5 years (about 3 years for $N = 1001$), which leads to over-smoothing of the signal, and prevents detection of changes occurring on shorter time-scales. It is also notable that changing the fitting method from maximum likelihood to least-square, which is generally considered less reliable, does not significantly change the relative variation of the b-value in time (Extended Data Fig. 5). This includes the changes occurring after Morakot.

**Probability of earthquake frequency change with time:**

Following ref. 44, we compute the probability *P* that the earthquake frequency increases by a factor greater than *r* between a period 1 and 2,

$$P\left(\frac{\lambda_2}{\lambda_1} > r\right) = 1 - \frac{1}{N_2!\,N_1!}\int_0^{\infty} e^{-x}\,\Gamma\left(N_2 + 1, rx\frac{\Delta t_2}{\Delta t_1}\right)x^{N_1}\,dx$$

where $\Gamma(n, x) = \int_0^{\infty} e^{-t}\,t^{n-1}\,dt$ is the incomplete Gamma function, $N$ is the number of earthquake over a certain period $\Delta t$ and $\lambda = N/\Delta t$ is the earthquake frequency. The subscripts 1 and 2 refer to the time periods 1 and 2. We first apply this approach to determine the probability of earthquake frequency change between the 2.5 yr before and after Morakot, in the landsliding zone (Extended Data Fig. 4 a). We find a probability 1 for an increase of earthquake frequency (i.e. with $r = 1$), when

considering all the earthquakes or only earthquakes above the completeness magnitude. The 90% confidence interval, $0.05 < P < 0.95$, of an earthquake frequency change is found for $1.23 < r < 1.40$, when considering only the earthquakes above the completeness magnitude, and $1.45 < r < 1.52$ for all magnitudes. This demonstrates that the change of earthquake frequency after Morakot is significant with a ratio of 1.23, at least. We then apply the same analysis to the entire catalog by using a double sliding window of period 2.5 yr after and before the center time (Extended Data Fig.4 b). Except for Chichi, Morakot represents the only event associated with a significant and positive change of earthquake frequency over a period of 2.5 yr since 1994.

**Spatial variations of earthquake statistical properties:**

We use a common spatial sliding window to subsample the earthquake catalogue and to assess variations of earthquake statistical properties in space[45] between the 2.5 years before and after typhoon Morakot. We use a radius of 30 km for the sliding window, which enables sampling of a sufficiently large number of earthquakes at a length scale that is smaller than that of the landslide zone of 7000 km$^2$. The sampling window effectively corresponds to a disk shape extending to a depth of 15 km. The b-value is determined for the recorded earthquakes in each disk volume by maximum likelihood estimation. This method has an inherent statistical bias as the number of sampled earthquakes changes significantly depending on the local rate of seismicity. The minimum number of events for the determination of the b-value is set arbitrarily at 50. Our method can give rise to small-scale shapes in the maps of b-value, such as disk and rod shapes, that are not the focus of this study. We use a disk shape kernel with a radius of 15 km, convolved with the initial b-value map to blur the mapped patterns and to isolate features with longer wavelengths. More sophisticated methods exist to compute spatial variations of b-value, including a penalized likelihood-based method[46] and a distance-dependent sampling algorithm[47].

**Declustering and seismicity changes after Morakot:**

Several studies investigating potential earthquake frequency changes use declustered earthquake catalogs. However, declustering is an ill-posed problem that does not have a unique solution[48] and

that will lead to method-dependent results. Yet, to test the impact of potential earthquake clustering on our results, we have applied the traditional Reasenberg declustering algorithm[49], obtained from the ZMAP toolbox[50], to the CWB earthquake catalog. This deterministic algorithm aims to remove earthquake sequences, defined as chains of connected earthquakes in space and time, leaving only the initial earthquake in a given sequence. We use standards parameters[48] adapted for Taiwan with $\tau_{min} = 1$ and $\tau_{max} = 10$, the minimum look-ahead time for not clustered events , $\tau_{max} = 10$, the maximum look-ahead time for clustered events, $p_{clust} = 0.95$, a confidence probability, $x_{meff} = 2.0$, the effective lower cutoff magnitude chosen here to be consistent with the CWB catalog, $x_k = 0.5$, the increase in lower cutoff magnitude during clusters, and $r_{fact} = 10$, the number of crack radii surrounding each earthquake within new events considered to be part of the cluster. We emphasize here that declustering has been performed over the entire catalog, without any regional selection of the seismicity (i.e. not only in the landsliding zone and not only above 15 km of depth), to prevent potential declustering biases associated to earthquake censoring.

Extended Data Fig. 9 shows the influence of declustering on earthquake frequency, b-value, depth distribution and the probability of earthquake frequency change after Morakot in the landsliding zone (< 15 km depth). We observe that declustering mainly leads to a decrease of earthquake frequency over the 2.5 years before typhoon Morakot, and to very minor changes after. It results that declustering even slightly enhances the probability of an increase in earthquake frequency after Morakot. In addition, declustering does not significantly changes the time variation in b-value nor the depth-distribution of seismicity. We note that Reasenberg declustering approach is well-suited to remove earthquake sequences that lead to significant changes (e.g. an aftershock sequence after a large mainshock) and less-adapted to remove earthquake sequences over relatively quiet period[48]. Under this potential limitation, this analysis demonstrates that earthquake clustering is not the reason for the observed changes after typhoon Morakot.

Yet, we are confident that large and deep mainshocks occurring in the landsliding zone, below 15 km, such as Mw 6.3 Jiashian earthquake in 2010, are not the cause for the observed seismicity changes.

Indeed, declustering is efficient to remove most of the aftershocks caused by the Jiashian earthquake, which appear to be concentrated at depth between 15 and 30 km (Extended Data Fig. 10).

**Seismicity temporal variation: random hypothesis versus significant regional seismicity change versus local earthquake interactions**

Having a declustered catalog implies that all the earthquakes are seismically independent from each other. In turn, earthquakes should be randomly distributed in time, unless a non-seismic process triggers them. Here we test this hypothesis by comparing the observed changes, in earthquake frequency and b-value after Morakot, obtained from the "true" declustered catalog with those from 200 "synthetic" earthquake catalogs over the period 2006-2015. Each synthetic catalog is generated using the exact same earthquakes than the true declustered catalog, including their magnitudes, but the time of occurrence of each earthquake is randomly sampled over the period of interest (2006-2015) using a time step of 1 s. It results that each synthetic catalog has the exact same magnitude distribution and average earthquake frequency than the true one, but the temporal distribution of earthquakes is randomly distributed. For each catalog (true or synthetic), the probability of frequency change and the change in b-value after Morakot are computed by comparing the earthquakes occurring in the 2.5 years after and before Morakot (see Extended Data Fig. 11). The probability of a frequency change after Morakot for all the synthetic catalogs drops around a ratio 0.8-1.2, centered around 1, meaning there is no significant frequency change. This clearly departs from the frequency change observed using the true catalog that drops around a ratio of 1.3-1.6. In addition, the change in b-value of the true catalog is significantly greater than the changes of all the synthetic catalogs. Overall, these results mean that both the frequency change and the b-value increase after Morakot are robust features, that depart from random changes. In addition, because we performed these tests using the declustered catalog, that should only include independent earthquakes, this means that these robust and non-random changes should not be associated to the occurrence of large mainshocks. We also note that potential earthquake interactions in a local subset of the landsliding zone[51] can not explain the increase in earthquake frequency after Morakot (Extended Data Fig.12)

36. Chang, K., Chiang, S., Chen, Y., & Mondini, A. C. Modeling the spatial occurrence of shallow landslides triggered by typhoons, Geomorphology 208, 137–148, (2014).
37. Marc, O., & Hovius, N. Amalgamation in landslide maps: effects and automatic detection. Natural Hazards and Earth System Sciences 15, 723-733 (2015).
38. Larsen, I. J., Montgomery, D. R., & Korup, O. Landslide erosion controlled by hillslope material. Nature Geoscience 3, 247-251 (2010).
39. Chen, Y.-C., Chang, K., Chiu, Y.-J., Lau, S.-M. & Lee, H.-Y. Quantifying rainfall controls on catchment-scale landslide erosion in Taiwan, Earth Surf. Process. Landforms 38, 372–382 (2013).
40. Shin, T. C., Chang, C. H., Pu, H. C., Lin, H. W., & Leu, P. L. The Geophysical Database Management System in Taiwan. Terrestrial, Atmospheric & Oceanic Sciences 24 (2013).
41. Wiemer, S., & Wyss, M. Minimum magnitude of completeness in earthquake catalogs: Examples from Alaska, the western United States, and Japan. Bulletin of the Seismological Society of America 90, 859-869 (2000).
42. Aki, K. Maximum likelihood estimate of b in the formula logN= a-bM and its confidence limits. Bull. Earthquake Res. Inst., Tokyo Univ. 43, 237-239 (1965).
43. Nava, F. A., Márquez-Ramírez, V. H., Zúñiga, F. R., Ávila-Barrientos, L., & Quinteros, C. B. Gutenberg-Richter b-value maximum likelihood estimation and sample size. Journal of Seismology 1-9 (2016).
44. Marsan, D., & M. Wyss. Seismicity rate changes. Community Online Resource for Statistical Seismicity Analysis, doi:10.5078/corssa-25837590 (2011).
45. Wiemer, S., & Wyss, M. Spatial and temporal variability of the b-value in seismogenic volumes: an overview. Advances in Geophysics 45, 259-302 (2002).
46. Kamer, Y., & Hiemer, S. Data□driven spatial b value estimation with applications to California seismicity: To b or not to b. Journal of Geophysical Research: Solid Earth 120, 5191-5214 (2015).
47. Tormann, T., Wiemer, S., & Mignan, A. Systematic survey of high□resolution b value imaging along Californian faults: Inference on asperities. Journal of Geophysical Research: Solid Earth 119, 2029-2054 (2014).
48. van Stiphout, T., Zhuang, J., & Marsan, D. Seismicity declustering. Community Online Resource for Statistical Seismicity Analysis, 10, 1 (2012).
49. Reasenberg, P. Second□order moment of central California seismicity, 1969–1982. Journal of Geophysical Research: Solid Earth, 90(B7), 5479-5495 (1985).
50. Wiemer, S. A software package to analyze seismicity: ZMAP. Seismological Research Letters, 72(3), 373-382 (2001).
51. Chan, C. H., & Wu, Y. M. A seismicity burst following the 2010 M 6.4 Jiashian earthquake–implications for short-term seismic hazards in southern Taiwan. Journal of Asian Earth Sciences, 59, 231-239 (2012).

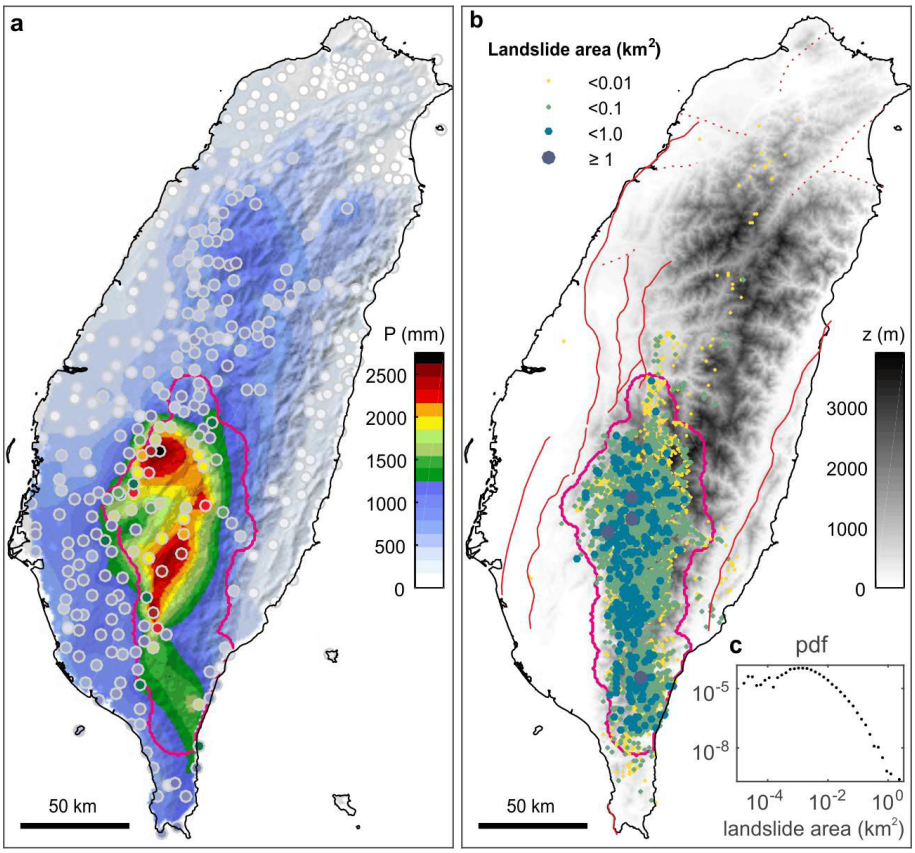


**Figure 1 | Morakot-driven rainfall and landslides in Taiwan. a)** Hillshaded map of cumulative rainfall during typhoon Morakot (7-9 August 2009), obtained by interpolation of data from local weather stations (colored dots). **b)** Digital elevation model of Taiwan with location of mapped landslides triggered by typhoon Morakot. Circle size and color indicate the surface area of a landslide, while the magenta line delimits the area with highest spatial density of landslides (see Methods and Extended Data Figure 2). Solid and dashed red lines indicate active thrust and strike-slip or normal faults, respectively[18]. Other less well identified faults exist inside the range[23]. **c)** Probability density distribution of the surface area of landslides triggered by typhoon Morakot for areas greater than 10 $m^2$.

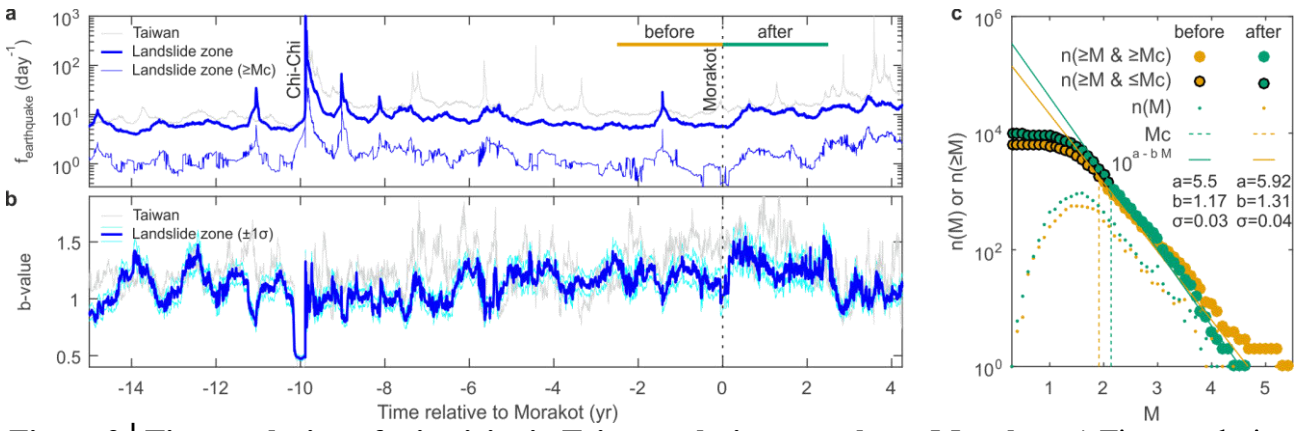


**Figure 2 | Time evolution of seismicity in Taiwan relative to typhoon Morakot. a)** Time evolution of frequency of shallow (<15km) earthquakes. The light blue line indicates the frequency of earthquakes greater than the completeness magnitude. **b)** Time evolution of the b-value of the Gutenberg-Richter law inside (heavy blue line) and outside (light grey line) the landsliding zone (see Methods and Extended Figure 1). **c)** Gutenberg-Richter law fits over the distributions of cumulative earthquake numbers in the landsliding zone as a function of earthquake magnitude during the 2.5 years before (yellow) and after (green) typhoon Morakot (see Methods).

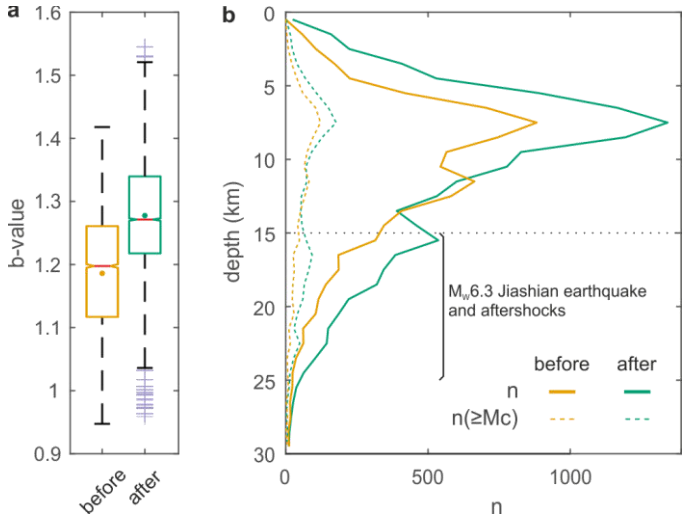


**Figure 3 | Change in b-value and depth of earthquakes after typhoon Morakot. a)** Notched whisker plots of b-value estimates for 2.5 years before (yellow) and after (green) typhoon Morakot inside the landsliding zone show the median (red line), mean (dot), 25th and 75th percentiles (box limits), whisker lengths (dashed lines) and outliers (purple crosses) of the b-value. Notches display the variability of the median between samples. **b)** Histograms of earthquake depth during the 2.5 years before (yellow) and after (green) typhoon Morakot in the landsliding zone. Solid and dashed lines indicate depth-distribution for earthquakes of all magnitudes and magnitudes greater than the completeness magnitude, respectively.

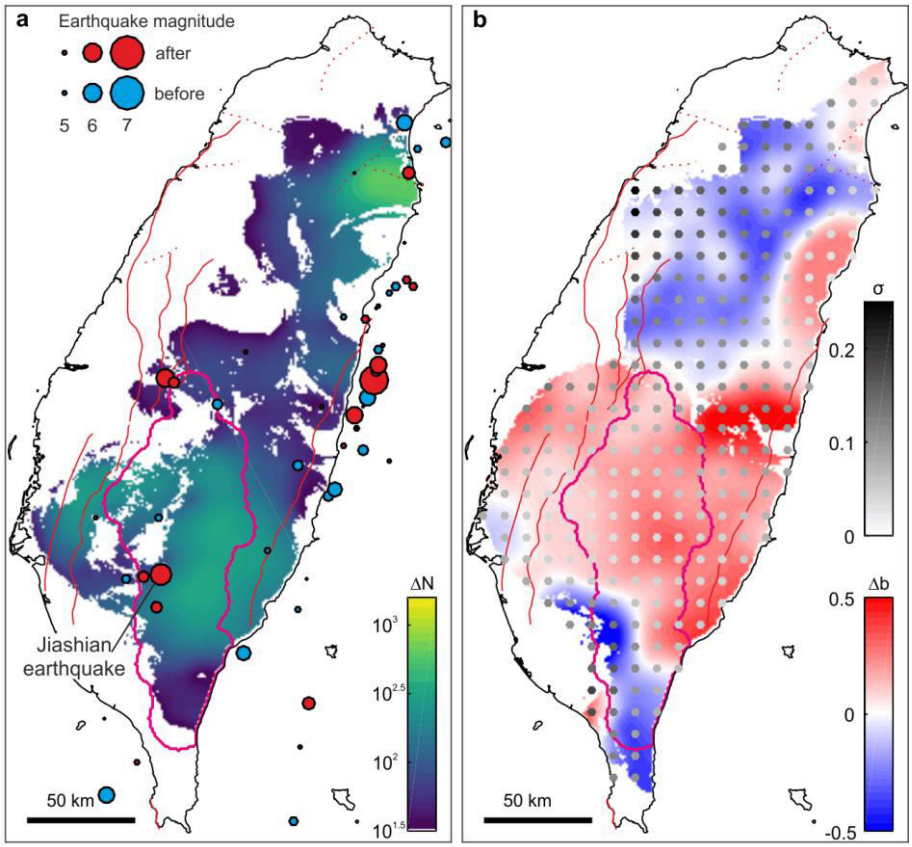


**Figure 4 | Changes in seismicity after typhoon Morakot. a**) Map of difference of shallow (<15 km) earthquake numbers, $\Delta N$ , during the 2.5 years after and before typhoon Morakot. Only earthquakes greater than the completeness magnitude were considered. For readability, $\Delta N$ values lower than $10^{1.5}$ are shown in white. Red and blue circles locate earthquakes greater than magnitude 5 after and before typhoon Morakot, respectively. **b)** Change in b-value, $\Delta b$ (red-blue colormap), and uncertainty, $\sigma$ (gray circles) of b-value estimates (see Methods and Extended Figure 3).

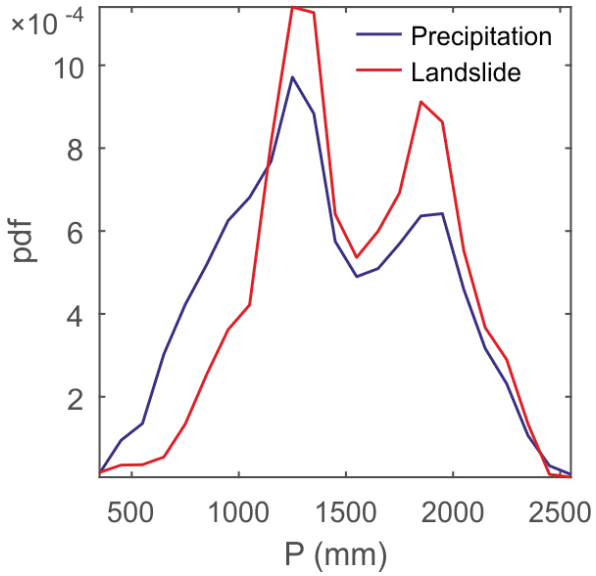


**Extended Figure 1 | Influence of rainfall on landsliding during Morakot.** Probability density functions (pdf) of cumulated rainfall *P* (blue line) in the landsliding zone and of cumulated rainfall at the location of the landslides (red line) during Morakot typhoon (7th to 9th of August 2009). Rainfall at the location of each landslide was obtained by natural-neighbor interpolation from local weather stations (see Methods).

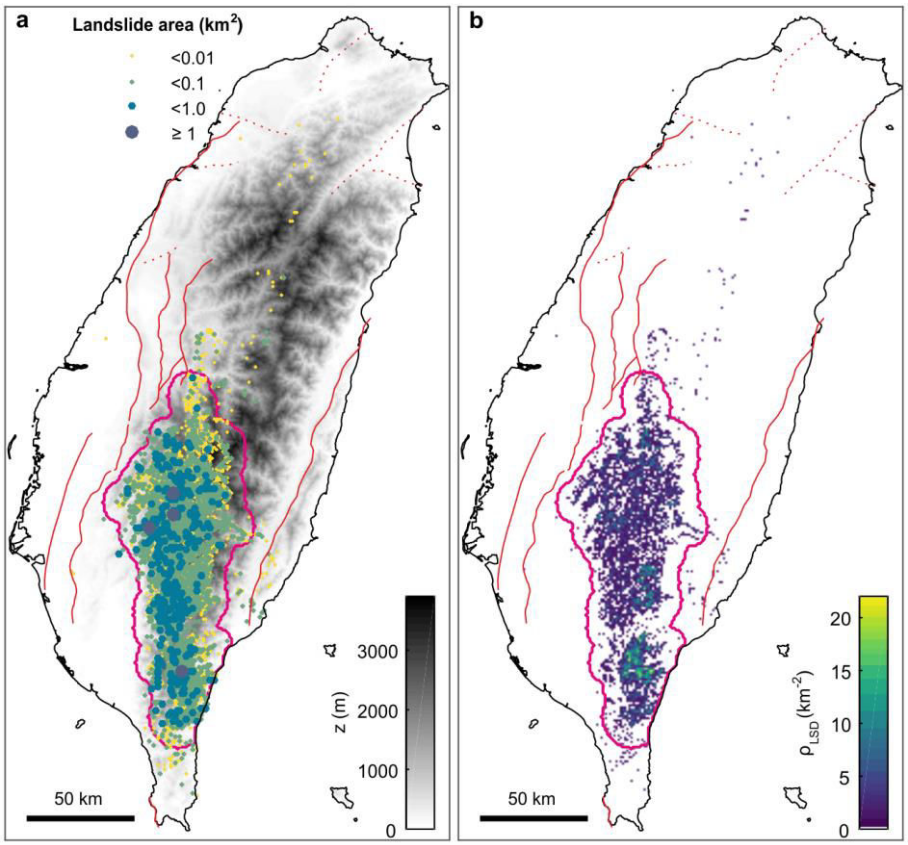


**Extended Figure 2 | Morakot-driven landslides. a**) Digital elevation model of Taiwan with location of the detected landslides triggered during Morakot typhoon. Circle size and color indicate the surface area of the landslides, while the magenta line bounds the area with a high spatial density of landslides (see Methods). **b**) Landslide spatial density estimated by dividing the number of landslides by the surface area of 1 km$^2$ pixels. The landsliding zone is bounded by the magenta contour line.

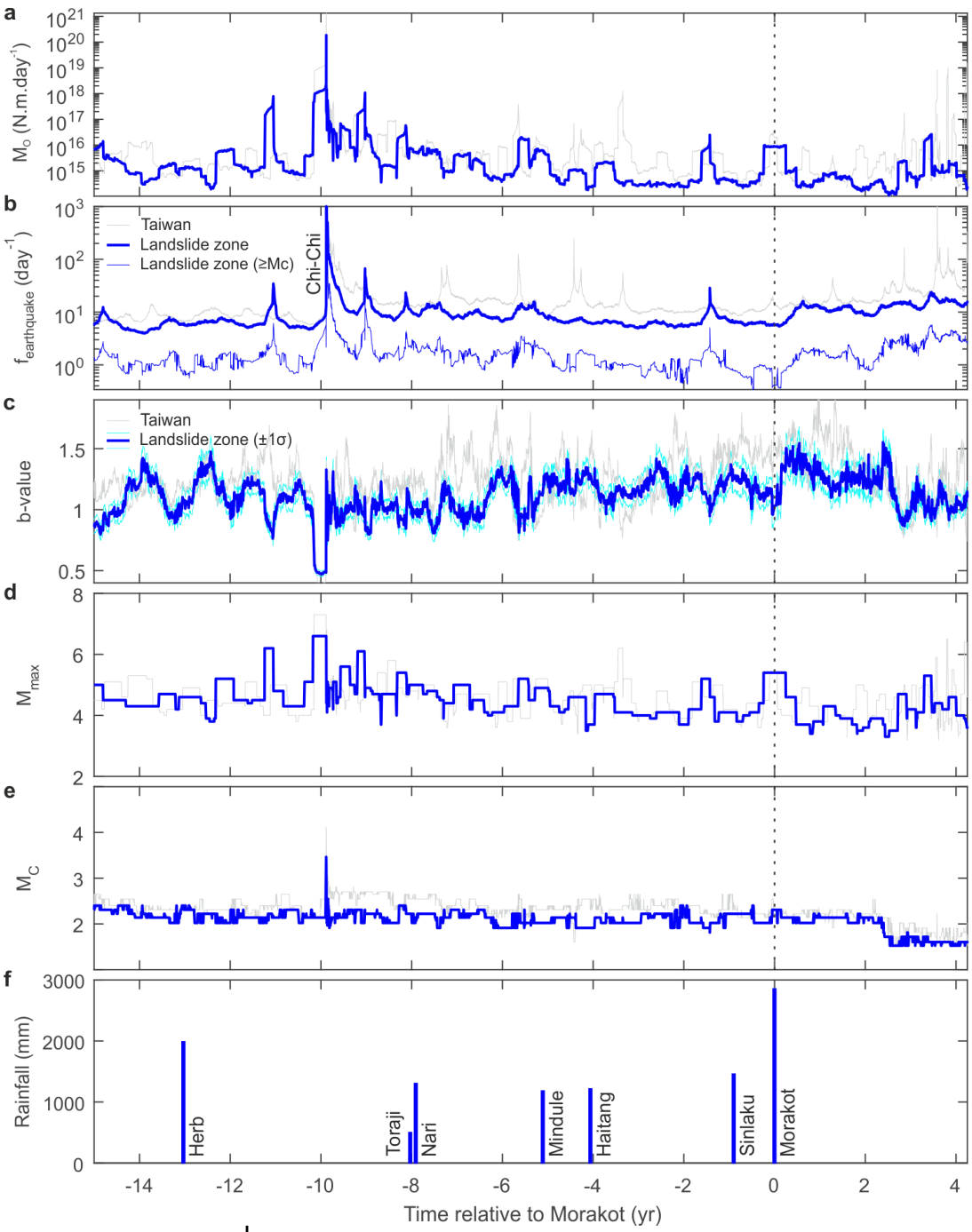


**Extended Figure 3 | Time evolution of seismicity in Taiwan relative to Morakot.** Temporal evolution of shallow (<15 km) earthquake **a)** seimic moment rate, **b)** frequency, **c)** b-value of the Gutenberg-Richter law, **d**) maximum magnitude and **e**) completeness magnitude inside (heavy blue line) and outside (light grey line) the landsliding zone in time relative to Morakot. The light blue line on panel a and b indicates the moment seismic rate or frequency of earthquakes greater than the completeness magnitude. **e)** Rainfall associated to large typhoons over the same time period.

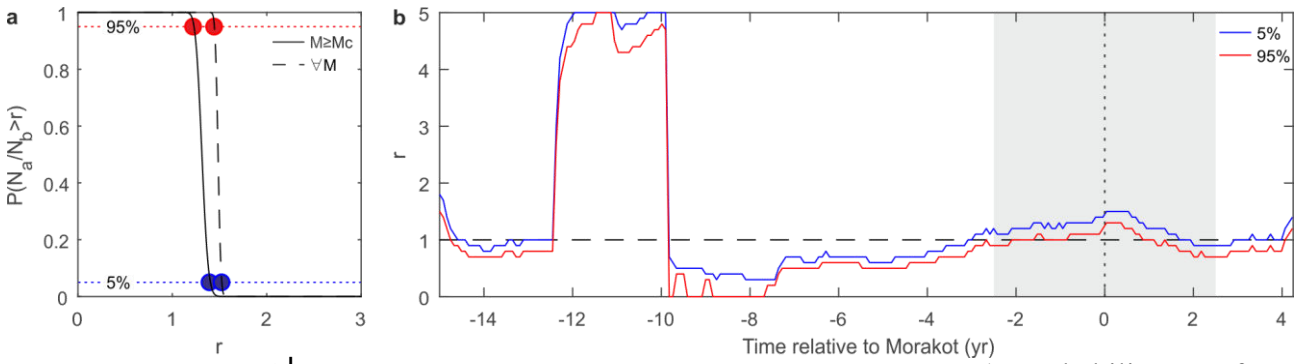


**Extended Figure 4 | Probability of earthquake frequency change. a)** Probability $P$ of an earthquake frequency change of a ratio greater than $r$ in the 2.5 yr after Morakot considering earthquakes of all magnitudes ($\forall M$, dashed black line) or only earthquakes above completeness magnitude ($\geq M_c$, solid black line). Red and blue dots indicate the bounds of the 90% confidence interval ($0.05 < P < 0.95$). **b)** Time variation of the 90% confidence interval on $r$. Except for Chichi, Morakot (dashed vertical line) the only event associated with a significant and positive change of earthquake frequency over a period of 2.5 yr since 1994. The grey zone indicates the time when the analysis integrates events occurring simultaneously with Morakot.

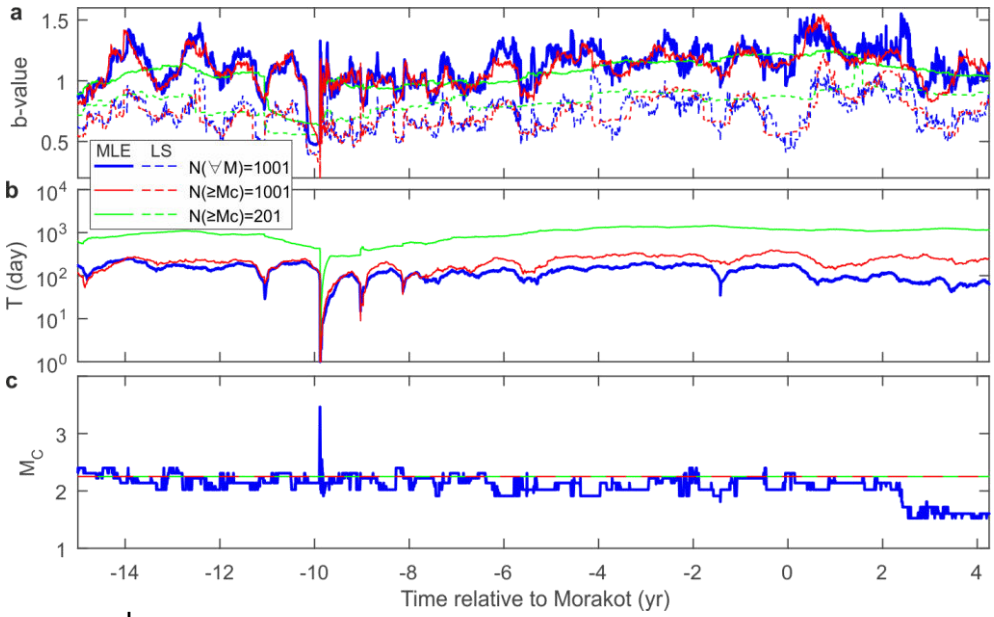


**Extended Figure 5 | Sensitivity of b-value estimates to sampling and fitting methods. a)** The temporal sliding window sample either a fixed number of earthquakes considering earthquakes of all magnitudes ($N(\forall M) = 1001$ events, blue line, same than the one on Fig. 1) or only earthquakes above completeness magnitude ($N(\geq M_c) = 1001$ or 201 events, red and green lines, respectively). **b)** Increasing the number of samples events increases the time duration $T$ of the sliding window and smooths out temporal variations at high frequencies. **c)** In one method, the completeness magnitude $M_c$ is determined from the sampled events (blue line) and varies with time, while in the other one the completeness magnitude is chosen *a priori*, here to 2.25 (red and green lines). On panel a) solid and dashed lines represent b-values obtained by maximum likelihood MLE or least-square LS fitting, respectively.

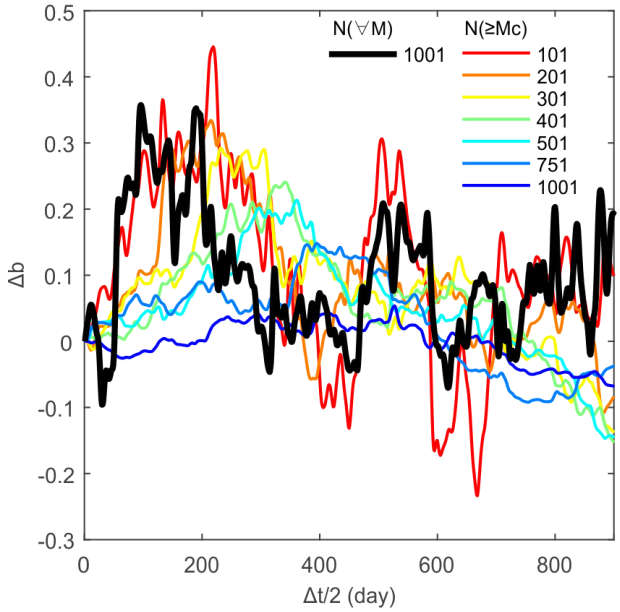


**Extended Figure 6 | Sensitivity of b-value change after Morakot to sampling methods.** Change in b-value estimate ($\Delta b = b(t_{Morakot} + \Delta t/2\,) - (t_{Morakot} - \Delta t/2\,)$) when comparing b-value at the date of Morakot $t_{Morakot}$ plus $\Delta t/2$ and minus $\Delta t/2$. The temporal sliding window samples either a fixed number of earthquakes considering earthquakes of all magnitudes ($N(\forall M) = 100$ events, black bold line, same than the bold blue line on Fig. 1) or only earthquakes above completeness magnitude ($N(\geq M_c) = 101$ to $1001$ events, red to blue lines, respectively). For the latter, $M_c$ is chosen at 2.25.

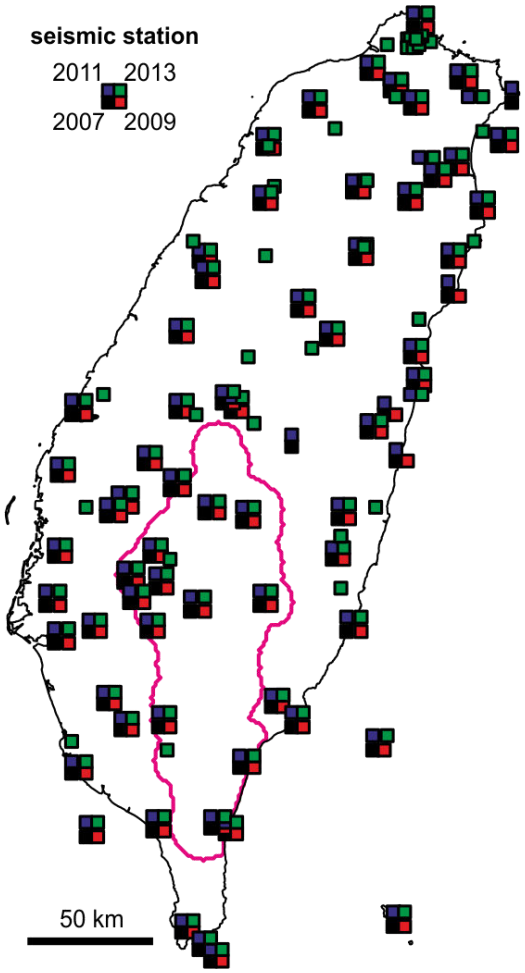


**Extended Figure 7 | Seismic network configuration and evolution.** The location of seismic stations is shown by colored squares for 2007 (black), 2009 (red), 2011 (blue) and 2013 (green).

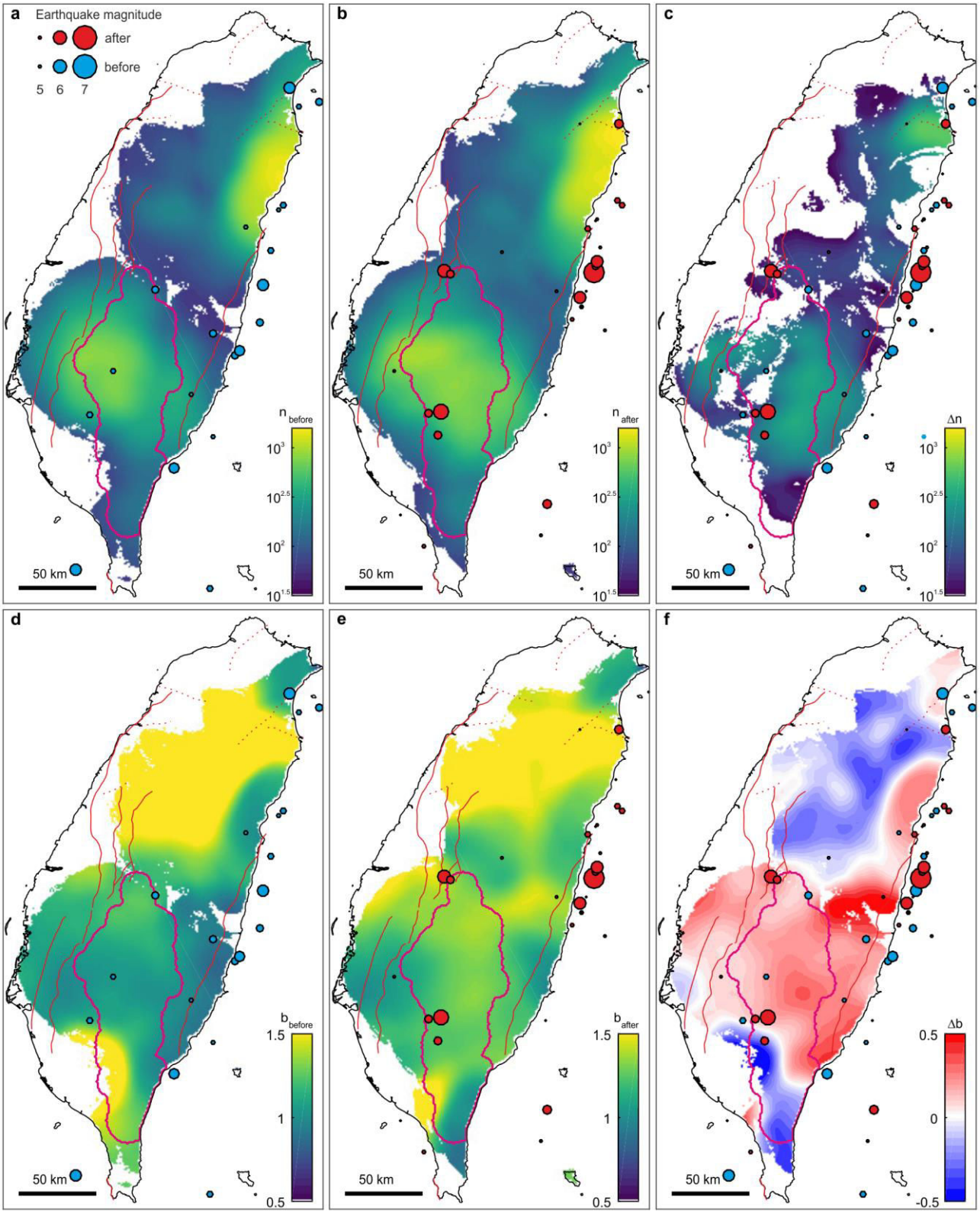


**Extended Figure 8 | Changes in seismicity after Morakot.** Maps of the of shallow (<15 km) earthquake number that have occurred during the 2.5 years **a**) before Morakot ($n_{before}$), **b**) after Morakot ($n_{after}$) and **c**) of the difference $(\Delta n = n_{after} - n_{before})$. Only earthquakes greater than the completeness magnitude were considered. **d-f**) Same than **a-c**) but for the b-value **d**) before Morakot ($b_{before}$), **e**) after Morakot ($b_{after}$) and **f**) the difference $(\Delta n = n_{after} - n_{before})$.

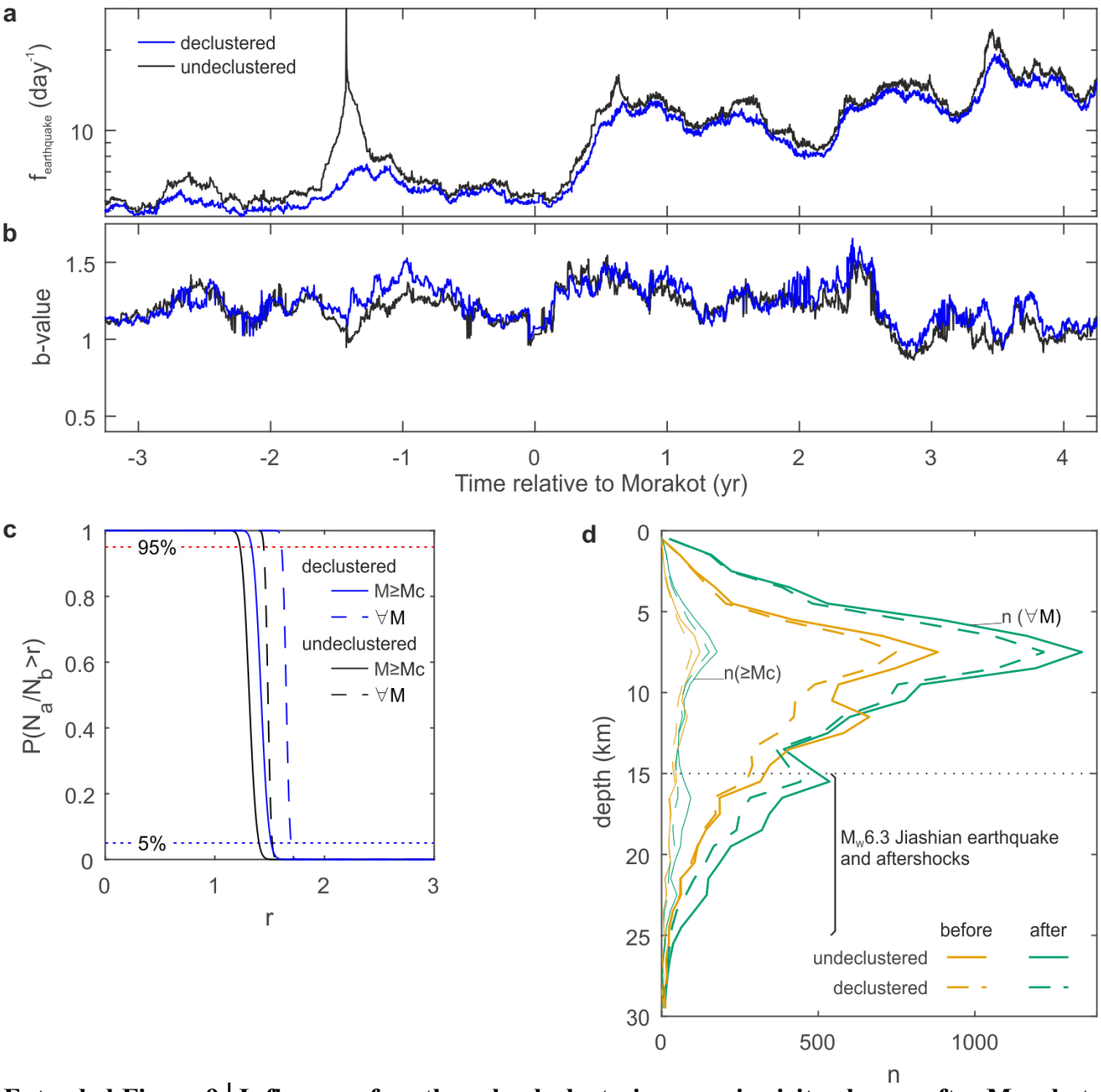


**Extended Figure 9 | Influence of earthquake declustering on seismicity change after Morakot.** Temporal evolution of shallow (<15 km) earthquake **a**) frequency and **b**) b-value of the Gutenberg-Richter law for the declustered (blue line) and undeclustered (black line) catalogs in the landsliding zone. **c**) Probability $P$ of an earthquake frequency change of a ratio greater than $r$ in the 2.5 yr after Morakot considering earthquakes of all magnitudes ($\forall M$, dashed black line) or only earthquakes above completeness magnitude ($\geq M_c$, solid black line). Same color convention for the declustered (blue line) and undeclustered (black line) catalogs. **d**) Histograms of earthquake depth during the 2.5 years before (yellow) and after (green) typhoon Morakot in the landsliding zone. Solid and dashed lines indicate undeclustered and declustered catalog, respectively, while the bold or light lines indicate the use of all magnitudes or only magnitudes greater than the completeness magnitude, respectively.

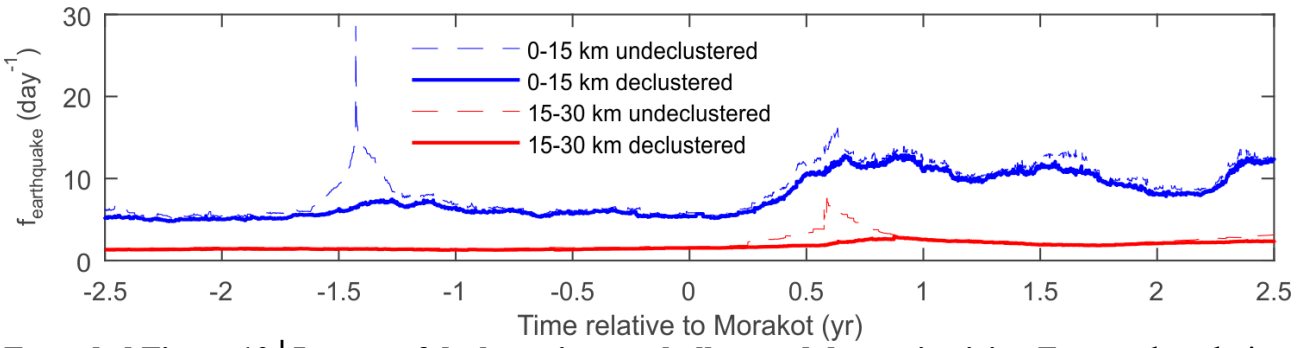


**Extended Figure 10 | Impact of declustering on shallow and deep seismicity.** Temporal evolution of shallow (<15 km; in blue) and deep (15-30 km; in red) earthquake frequency using declustered (solid lines) or undeclustered (dashed lines) catalogs in the 2.5 years after and before Morakot.

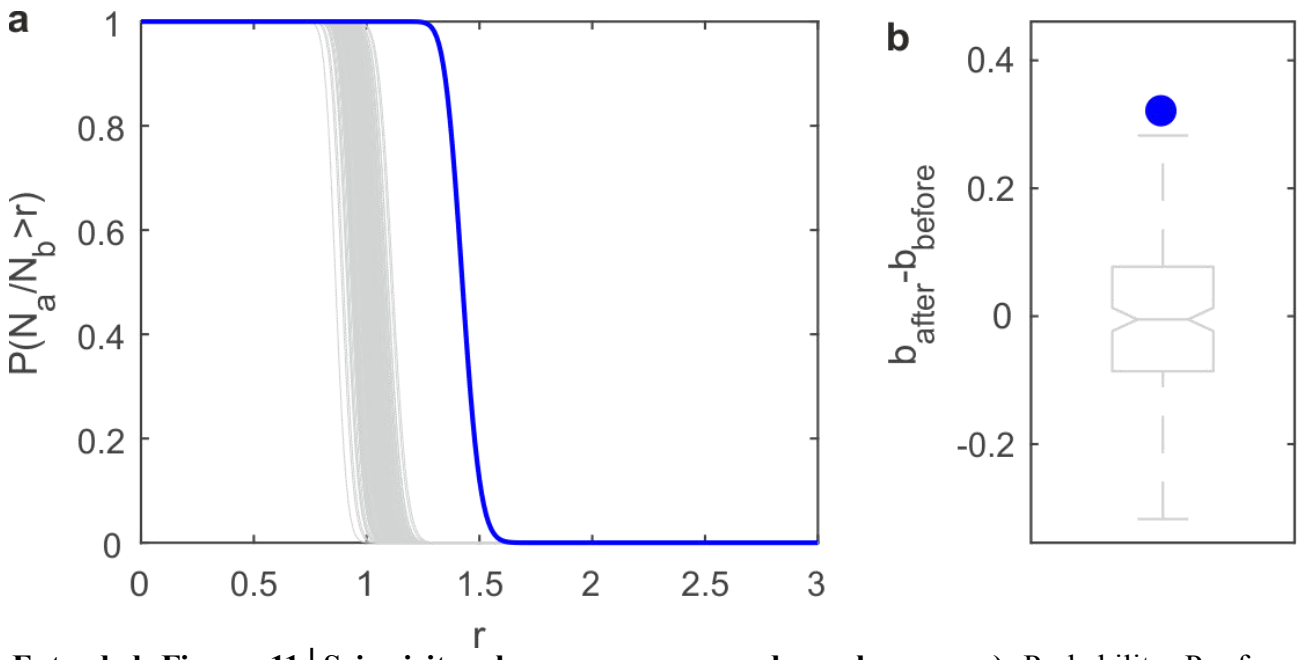


**Extended Figure 11 | Seismicity changes versus random changes. a)** Probability P of an earthquake frequency change of a ratio greater than r in the 2.5 yr after Morakot (compared to the 2.5 years before) using the true declustered catalog (blue line) or 200 synthetic ones (grey lines) that share the same average statistical properties. B) b-value change in the 2.5 yr after Morakot using the true declustered catalog (blue dot) or the synthetic ones, shown by a whisker plot.

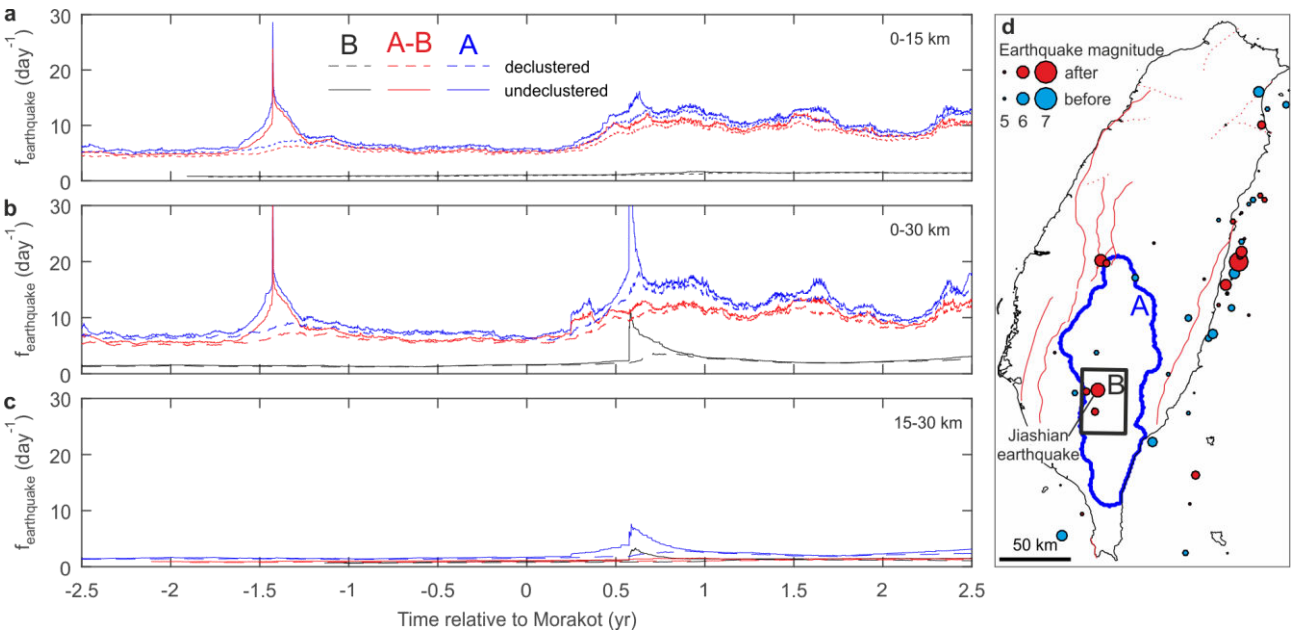


**Extended Figure 12 | Earthquake interactions versus regional seismicity change.** Temporal evolution of b) all, a) shallow and c) deep earthquake frequency in the landsliding zone (A), in Chan & Wu (2012) zone[51] (B) and in A minus B zone (A-B). Declustered (dashed lines) or undeclustered (solid lines) catalogs are indicated. d) Locations of the A and B zones. "After" and "before" relate to Morakot typhoon. Chan & Wu (2012) studied earthquakes statistics bounded to zone B and suggested that the temporal variability of the seismicity in this area was due to the interaction of three M≥5.5 earthquakes: Jiashian (2010), Taoyuan (2010) and Wutai (2012). They claim that this interaction is the consequence of local stress increase. However, when excluding zone B from our statistics (bounded to zone A), our results remain unchanged. Therefore, the increase of seismicity and b-value changes that we evidenced in this study cannot be explained by local earthquake interactions, which are restricted to zone B.

# APPENDIX B - Modulation of post-seismic sediment evacuation by landslide dynamic connectivity

Thomas Croissant[1,2*], Philippe Steer[1], Dimitri Lague[1], Philippe Davy[1], Louise Jeandet[1] and Robert G. Hilton[2]

[1] *Géosciences Rennes, OSUR, CNRS, Université de Rennes 1, Campus de Beaulieu, Rennes*

[2] *Department of Geography, Durham University, Durham, DH1 3LE, UK*

[*]Corresponding author: T. Croissant; thomas.croissant@durham.ac.uk

## Abstract

**In active mountain ranges, landslides triggered by large earthquakes mobilise large volumes of sediment that affect river dynamics. This sediment delivery can cause downstream changes in river geometry and transport capacity that affect the river efficiency to export this sediment out of the epicentre area. The subsequent propagation of landslide deposits in the fluvial network has implications for downstream hazards management and for landscape dynamics at the timescale of the seismic cycle. However, a full understanding of the processes and time scales associated to landslide sediment removal by bedload transport is still lacking in a post-seismic context. Here, we propose an upscaling approach in which results for reach scale are used to inform a larger scale modelling. First, we explore the river morphodynamic response to a landslide occurrence at the reach-scale using a 2D modelling approach. We use a simplified bedrock channel to systematically study the influence of the landslide volume ($V_{ls}$) and channel transport capacity ($Q_T$) on the export time of landslides. Two regimes are identified: (i) the export time is linearly related to $Vs/Q_T$ when the sediment pulse does not significantly affect river hydrodynamics for low $Vs/Q_T$ and (ii) the export time is a non-linear function of $Vs/Q_T$ when the pulse undergoes significant morphodynamic modifications during its evacuation for high $Vs/Q_T$. In the latter, the active narrowing of the river within the landslide deposit is responsible to the significant increase of the transport capacity, resulting in faster evacuation times than predicted by theory. Secondly, we propose a nested numerical approach to quantify evacuation times of earthquake-triggered landslide clusters at the scale of a mountain range in the context of a Mw 7.9 earthquake occurring on the Alpine Fault, New Zealand. Our approach combines an empirical description of co-seismic landslides clusters with the physical processes involved during the post-seismic phase. In particular, the role of landslide connectivity on the modulation of post-seismic sediment fluxes is explored. We also show the capacity of this approach to estimate sediment fluxes at longer timescales (i.e. several seismic cycles) and its potential to be coupled to a 2D landscape evolution model.**

**Key words: landslide, earthquake, river morphodynamics, landscape evolution, extreme events.**

# 1. Introduction

Large earthquakes impact the landscapes of active mountain by mobilizing massive volumes of sediment through widespread landsliding (Malamud et al., 2004b; Ouimet, 2011) (Fig. 1). These clusters of landslides deliver large volumes of sediment to the fluvial network and affect its dynamics on estimated periods lasting from decades to centuries (Croissant et al., 2017; Hovius et al., 2011; Wang et al., 2015; Wang et al., 2017; Yanites et al., 2010). If numerous studies have focused on the co-seismic response of hillslopes to large earthquakes (e.g. Gallen et al., 2015; Keefer, 1984, 1999; Malamud et al., 2004a; Marc et al., 2016; Meunier et al., 2007, 2008), very few have investigated the post-seismic evolution of landscapes and sediment transport (e.g. Yanites et al., 2010; Hovius et al., 2011; Croissant et al., 2017). This probably results, on one hand from the extensive datasets constraining co-seismic landsliding and sediment production (Keefer, 1999; Larsen et al., 2010; Li et al., 2014; Malamud et al., 2004a; Odin Marc et al., 2016; Tanyaş et al., 2017, 2018), and on the other hand from the difficulty to monitor post-seismic sediment fluxes and topographic changes on the field over tens of years. Most of the observations relate to suspended sediment concentration data (Dadson et al., 2004; Hovius et al., 2011; Wang et al., 2015; Wang et al., 2017) completed with analytical and numerical models of bedload evacuation (Croissant et al., 2017; Yanites et al., 2010).

Investigating how the fluvial system digest these abrupt and large sediment pulses is critical to understand intra-catchment sediment transfers (Benda & Dunne, 1997), bedrock incision patterns in landslide-dominated mountain ranges (Lague, 2010; Yanites et al., 2011), anticipate hydro-sedimentary hazards in alluvial fans (Croissant et al., 2017; Robinson & Davies, 2013) and even quantify the feedbacks of surface processes on fault stress loading (Steer et al., 2014). On short-times scales (i.e. < 1000 years), the downstream propagation of sediment pulses has been studied principally at the reach scale using flume experiments and 1D numerical modelling (Cui et al., 2003; Cui & Parker, 2005; Lisle et al., 2001; Sklar et al., 2009; Sutherland et al., 2002). However, these studies have focused primarily on the end-member case of a low amplitude sediment supply compared to the transport capacity of the river. Croissant et al, [2017] proposed a 2D morphodynamic approach that extends these approaches to high-amplitude sediment supplies compared to the river transport capacity. In this latter case, the critical role of dynamic river narrowing in accelerating the removal of landslide-driven sediments has been identified. Despite these recent efforts, a full understanding of post-seismic sediment fluxes at a mountain range scale is still lacking.

Locally, post-seismic sediment export is controlled by the sediment supply and by the transport capacity of the river stream receiving the landslide. As such, the quantity of sediment transported by the river is strongly dependent on the degree of connectivity of sources (landslides) to the fluvial network at the initial stage and through time. Several studies provide a quantification of the initial percentage of landslide connected to the drainage network (Dadson et al., 2004; Li et al., 2016). However, work on the temporal evolution of connectivity along time remains an open question

(Zhang et al., 2016). On the first hand, landslides connecting directly to the river network inject an almost instantaneous sediment load into the river. This departs from landslides resting on the hillslope that will deliver the same sediment volume but in a more progressive manner, depending also on post-seismic meteorological and hydrological conditions (inducing surface runoff) (Fan et al., 2018). Once a landslide reaches the river channel, its export time depends mostly on the river geometry and discharge and on sediment grain size (Croissant et al., 2017). If the evacuation of one landslide has already received attention, no work has been dedicated to the evacuation of seismically-triggered clusters of landslides.

Landslides are not only individual morphological features, and their distribution can statistically inform on the dynamics of connectivity and subsequent export by river transport. For instance, old landslides, older than several seismic cycles and persisting in the landscapes have been argued to indicate a low efficiency of sediment export (ref). However, such inference cannot be made solely based on individual and old landslides, which represent, by definition, outliers of the whole cluster of landslides triggered by earthquakes or rainfall events. Understanding the triggering and export of landslide clusters over several seismic cycles is required to assess the topographic budget of large earthquakes (R. N. Parker et al., 2011), the role of aftershocks relatively to mainshocks, sediment fluxes at the range scale (ref), the geochemical signature of these extreme events (Frith et al., 2018; Wang et al., 2016), or the impact and risks associated to these natural hazards (Croissant et al., 2017; Keefer, 1999).

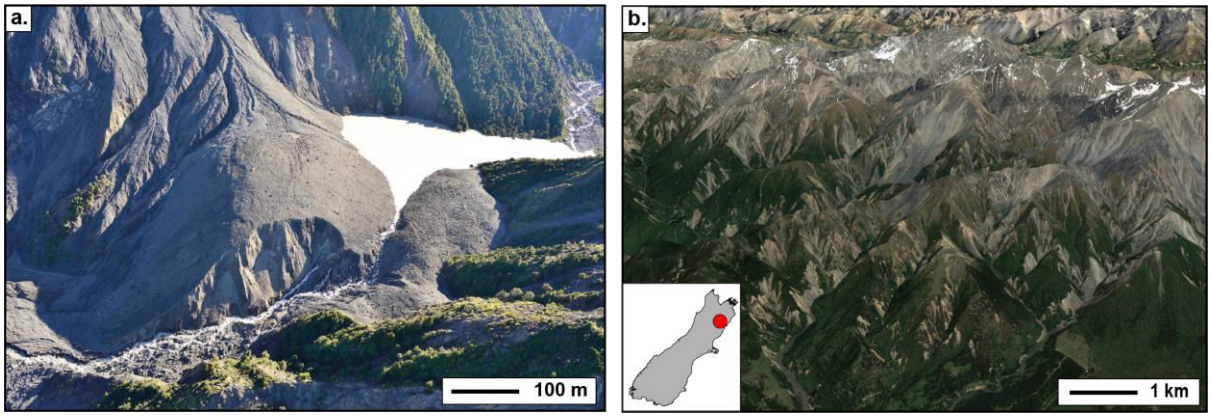


**Figure 1 | Illustration of the geomorphic impact of landslides at different spatial scales a.** Aerial image of the Hapuku river landslide dam (taken the 5th Dec. 2016) triggered by the 2016 Kaikoura earthquake, New Zealand (photo credit: Townsend, GNS) **b.** Satellite image of the area affected by the Kaikoura earthquake that triggered thousands of landslides (source: Google Earth).

In this study, we develop a nested numerical approach to simulate the temporal and spatial distributions of earthquakes over several seismic cycle, the triggering of landslides, their dynamic connectivity to the fluvial network and the subsequent sediment transport. The nested model integrates sediment export times defined at the reach scale, using the Eros river morphodynamic model (e.g. Davy et al., 2017; Croissant et al., 2017), in a statistical model generating earthquakes and

landslides at the mountain range scale, refered to as Quakos. The paper is divided in three sections. First, at the reach-scale, we investigate the impact of one or a series of landslides on the morphodynamic response of a river, the efficiency of sediment export and the persistence of downstream deposits. Second, we focus on embedding the fine-scale model outcomes into the large-scale model. We define a reduced-complexity model that accounts for the different processes driving the sediment export of landslide debris that can be applied to clusters of landslides triggered by earthquakes. We apply this model to the case of a hypothetical $M_w$ 8 earthquake occurring in the Southern Alps of New Zealand. Third, at the mountain range scale, we investigate the morphological impact of series of earthquakes on landscape dynamics. We focus specifically on the role of landslide dynamic connectivity and of runoff that modulate river transport capacity. Our results illustrate how the model parametrization impacts the number and volume of triggered landslides, their time persistence, the sediment fluxes leaving the range and the evolution of landslide-size distributions. Our approach is deliberatively simplified to put forward the challenges that emerge when trying to answer the post-seismic sediment evacuation problematic. We also propose new elements of reflection about this problem without necessarily answering it definitively as it remains highly complex.

## 2. Morphodynamic modeling of landslide sediment export

In this section, we explore the fine-scale dynamics of sediment export of a river that is impacted by a cascade of landslides. We first describe the 2D morphodynamic model Eros that we use to quantify the evacuation of individual landslides at the reach scale in a bedrock channel setting (Croissant et al., 2017; Davy et al., 2017). Following Croissant et al. (2017), we start by presenting the mechanisms controlling the downstream propagation of a single landslide deposited in a bedrock river reach. We then explore the impact of a cascade of landslides on sediment export by introducing several landslides along the same river channel. On top of evidencing the morphodynamic evolution of the landslides, the results from this section will be used in the Quakos study to tackle the problematic of landslide clusters evacuation.

### 2.1 Model description

This study is placed in the context of a bedrock river experiencing a high amplitude sediment forcing that causes perturbations of the river geometry including its width and slope. Therefore, an accurate quantification of landslides removal at the reach scale requires a model containing the physical processes allowing for the feedbacks between river erosion, transport capacity, flow, geometry and sediment supply. Here, we use Eros (Davy et al., 2017), a particle-based model that is well-suited to simulate the evolution of river submitted to large sediment supplies (Croissant et al, 2017a, b). The particles referred as precipitons are elementary volumes of water that moves on the top

of the topography and interact with it along their downstream path by entraining, transporting or depositing sediment. This model is composed of:

- A hydrodynamic model that predicts water depth and flow velocity patterns on high resolution topographies (Davy et al, 2017). This model resolves a reduced form of the shallow-water equations under the stationary assumption.

- A vertical and horizontal sediment transport and deposition model that is coupled with the hydrodynamic model. In the following, we only briefly describe the constitutive equations of sediment entrainment, transport and deposition, as a more detailed description can be found Davy et al., [2017]. The sediment entrainment rate is defined by the bedload transport law of Meyer-Peter and Muller [1948]:

$$\dot{e} = E(\tau - \tau_c)^{1.5} \quad (1)$$

with $E$ a constant, $\tau$, the shear stress and $\tau_c$ the critical shear stress. The sediment deposition rate $\dot{d}$ is a function of the sediment specific discharge $q_s$ and transport length, $\xi$ (Davy & Lague, 2009):

$$\dot{d} = \frac{q_s}{\xi} \quad (2)$$

In the morphodynamic simulations, $\xi$ is set to 2 m to insure a bedload transport regime where the flow is close to at-capacity conditions in non-supply-limited cases. The model also includes horizontal sediment dynamics. The lateral erosion of the neighbor cells is described by:

$$\dot{e}_{lat} = k_e S_y \dot{e} \quad (3)$$

with $k_e$ a dimensionless coefficient (here set at 0.05) and $S_y$ the slope in the transverse direction. The lateral sediment deposition $q_{sl}$ is defined as:

$$q_{sl} = k_d q_s S_y \quad (4)$$

with $k_d$ a constant (here set to 0.5).

The model allows for marginal instabilities to emerge and to be sustained (i.e. the river flow to converge in a self-formed width) when the local sediment flux is non-linearly correlated with the river discharge. Using a bedload transport equation, this condition is met only when the local shear stress is close from the threshold of sediment motion (Davy et al, 2017). Far from this threshold, this condition is not reach as the sediment flux is a function of $Q^{0.9}$. On simulations presenting a simple tilted bed as initial topography and no sediment input, Eros shows that the river width that emerges scales with discharge at a power 0.5 which is similar than the one measured on natural cases and flume experiments (Métivier et al., 2017).

### 2.2 Initial topography and boundary conditions

The model setup is similar to the one used in Croissant et al., [2017]. The initial topography is a 3 km long bedrock channel. Its transport capacity is set by its width and slope (Fig. 2a). The water enters through the upstream boundary condition at a constant effective discharge. The landslide deposit is introduced near the upstream end of the bedrock channel. It has a Gaussian shape in the

longitudinal direction and is described by its volume, length and median grain size. Bedrock incision is neglected as we assume that the morphological changes induced by the landslide export at short times scale (i.e. a seismic cycle) do not significantly affect the river transport capacity. In the following, we also investigate the evacuation of several landslides introduced along the same channel. In these cases, the bedrock channel is stretched to accommodate each landslide based on the inter-landslide distance that ranges from 0 to 1 km (Fig. 2b).

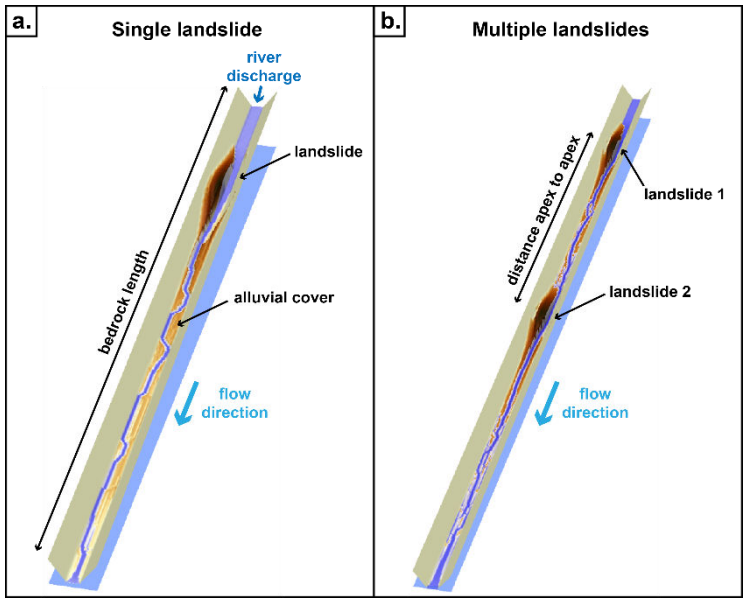


**Figure 2 | Eros model set up. a.** The case of a single landslide (in brown) evacuated in a bedrock channel (in beige). This snapshot illustrates an advances staged of one simulation where the river incise the deposit with a reduced width. **b.** The case of landslide cascade deposited in the same channel.

### 2.3 Sediment evacuation of a cascade of landslides

Here, we investigate the export dynamics of a landslide deposits in a bedrock river. To fully understand the mechanisms controlling landslide export, we run 80 simulations exploring the parameter space governing the bedrock transport capacity (i.e. width slope, river discharge) and landslides properties (i.e. median grain size, volume) (Fig. 2a). In a previous work, Croissant et al [2017] identified two end-members in terms of landslide evacuation which depends on the ratio between the landslide volume $V_{ls}$ and the river initial transport capacity $Q_T$.

- For low $V_{ls}/Q_T$, the width of the alluvial cover remains equal to the width of the bedrock river and the morphodynamic adaptation of the alluvial cover occurs mainly in slope. The landslide is removed by the river at the rate set by the initial bedrock river transport capacity.
- For high $V_{ls}/Q_T$, the model predicts an acceleration of the evacuation of a large part of the landslide (50 to 70%) compared to the case where the landslide would be exported at a

constant rate. This acceleration is induced by the dynamic narrowing of the alluvial river inside the landslide deposit. The remaining volume of sediment (30-50%) is removed during a latter phase of lateral erosion. This phase is less efficient than vertical incision to mobilize sediments as the lateral entrainment rate is only a fraction of the vertical one (eq. 3).

However, after large earthquakes, rivers are likely to receive sediments incoming from multiple co-seismic landslides. Here, we investigate the impact of several landslides, referred to as a cascade of landslides affecting the same channel on the sediment transport and evacuation. Two scenarios are explored. In the first one, the total volume of sediment introduced in the river remains constant (i.e. $2.10^6$ m$^3$) but is distributed along stream in a cascade of 1 to 4 landslides separated by the same apex to apex distance. In the second one, we investigate the effect of the distance separating two individual landslides on the sediment evacuation dynamics. In both cases, sediment export is evaluated at the outlet of the most downstream landslide.

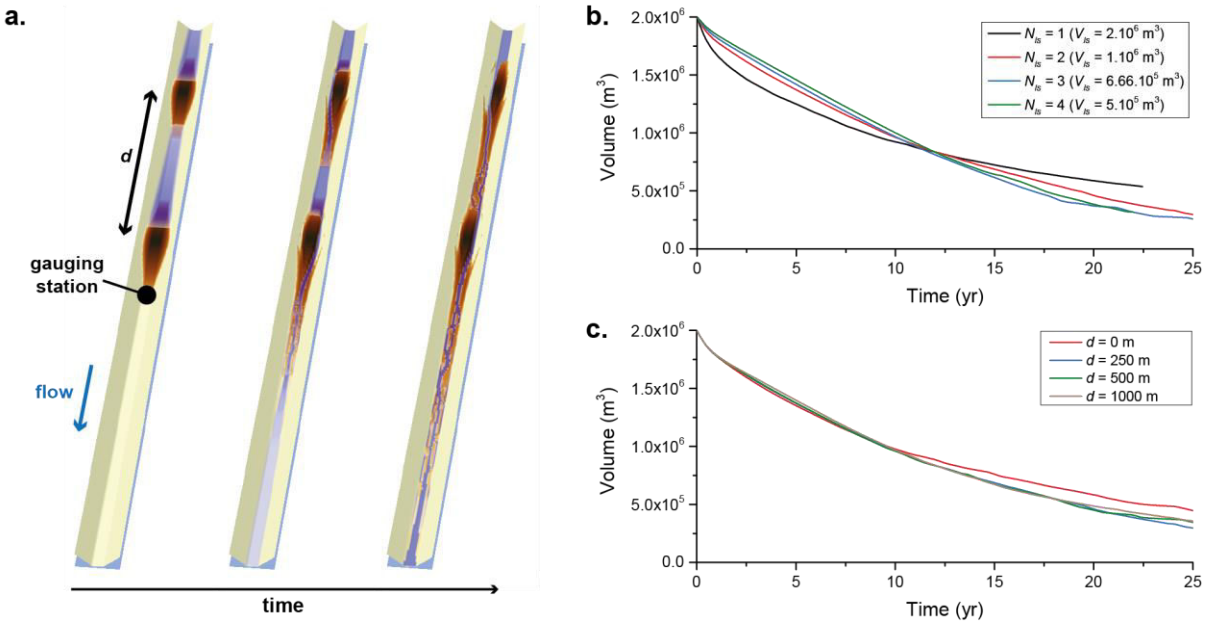


**Figure 3 | Morphodynamic evolution of a reach evacuating several landslides. a.** Snapshots of different stages of the Eros simulation. This is the case of 2 landslides of $V_s$ = $1.10^6$ m$^3$ separated by a distance of $d$ = 500 m. **b.** Evolution of the remaining sediment volume upstream of the 'gauging station' at constant total volume but for different number of landslides. $N_{ls}$ is the number of landslides **c.** Evolution of the remaining sediment volume upstream of the 'gauging station' for different distance ($d$) between the landslides.

In terms of morphodynamic evolution, the simulations with a cascade of landslides (Fig. 2b and 3a) share similarities with the ones with single landslides. During the first stages, the landslides are large enough to create partial or total landslide dams. The lakes forming in between two deposits have zero transport capacity. Regressive erosion lead to the progressive and simultaneous incision of each landslide deposits with a river narrower than the bedrock channel width. While sediments eroded from the downstream landslide are rapidly evacuated downstream, similarly to the simulation with

one landslide, sediments from the upstream landslide enter the lake and form a prograding delta that lasts until the lake is drained. The river eventually incises vertically both deposits until it reaches the bedrock surface and then removes the remaining volume of sediment by lateral erosion.

Figure 3b shows the evolution of the sediment volume stored upstream of the last landslide (see gauging station in Fig. 3a) for the same total volume of sediment distributed equally in one to four landslides. The cases where the number of landslides $N_{ls} \geq 2$ display similar export rates. The principal differences arise when these cases are compared with the evacuation of a single large landslide. In the latter, the landslide evacuation is more efficient until ~70% of the deposit is evacuated. The period of river increased efficiency (i.e. when the alluvial river width is less than 40% the one of the bedrock width) is also longer (Croissant et al, 2017). We then vary the inter-landslide distance $d$ to 0, 250, 500 and 1000 m. The results show that the distance between successive landslides play only a minor role in the efficiency of sediment evacuation.

An important result from this section is that our modelling results show that downstream landslides are not impacted by upstream sediment delivery emerging from other landslides. This observation allows us to treat landslides independently from each other, which is a critical step in building an upscaling approach where thousands of landslides can be triggered simultaneously in the river stream.

## 3. A reduced-complexity model for landslide sediment export

Earthquakes generally trigger numerous landslides that will eventually reach the fluvial network at locations that present varying local transport capacity. As such, a cluster of landslides can be described as a distribution of the ratio $V_{ls}/Q_T$ (Croissant et al., 2017) spanning the studied end-members in the previous section. While morphodynamic modelling provides useful information on the mechanisms of landslide removal at the reach scale, it is still too computationally demanding to apply it a whole mountain range over hundreds to thousands of years and accounting for thousands or more landslides. Therefore, we aim here at defining a reduced-complexity model to describe the post-seismic evolution of landslide volume for any value of $V_{ls}/Q_T$ using the results obtained with the already wide range of 80 simulations performed in the previous section for the single landslide scenario.

Using these simulations, we compute the time $T_{exp}$ needed to export 20 to 90% of the initial $V_{ls}$ as a function of $V_{ls}/Q_T$ at a 10% percent interval (Fig. 4a). As described in Croissant et al, 2017, the export time computed for each interval follows a trend with $V_{ls}/Q_T$ that can be fitted with a function of the form:

$$T_{exp,i} = \delta_i \left(\mu_i \frac{V_{ls}}{Q_T}\right) \left[1 + \left(\frac{V_{ls}}{Q_T}\right)^{\varphi_i}\right]^{\frac{(\beta-1)}{\varphi_i}} \quad (5)$$

with $\delta$ and $\mu$ two constants, $\varphi$ a curvature parameter, $\beta$ an exponent (here fixed at 0.1) and $i$ corresponds to the studied percent interval. The values of these parameters are found by a least-square fitting using equation 5 on each percent interval (Fig. 4a, Table 1).

We obtain a discrete description of the evolution of a landslide volume for any value of $V_{ls}/Q_T$ (Fig. 5b,c). The continuous description is obtained by interpolating linearly between the points.

Figure 4b and c shows the reconstruction of the temporal evolution of landslide evacuation using the results from the previous step for two values of $V_{ls}/Q_T$ encompassing the two end-members behaviours. Comparing with outputs from Eros shows the reduced-complexity method performs well to reconstruct the export of landslide volume for any given $V_{ls}/Q_T$ value. Simulations presenting a high $V_{ls}/Q_T$ ratio never succeed to evacuate 100% of the initial volume of sediment as a small fraction of sediment remains captured in lateral terraces. Therefore, to reconstruct fully the landslide export we assume that the last 10% of sediment volume is exported at the same rate than the one estimated for the last 20% to 10%. However, this might lead a slight over-estimation of the sediment transport efficiency during the lateral erosion phase.

This reduced-complexity method provides an efficient way to appraise the post-seismic sediment evolution of landslide clusters. It also presents the advantage of implicitly accounting for the evolution of the width and slope of the river. This reduced-complexity description of sediment export can therefore be applied at a larger spatial scale (i.e. a mountain range) provided that the distribution of $V_{ls}/Q_T$ is known. In the next section, we combined this method with our newly developed large-scale model, Quakos, which determines clusters of earthquake-triggered landslides, including their volume and the transport capacity of the river they are connected to.

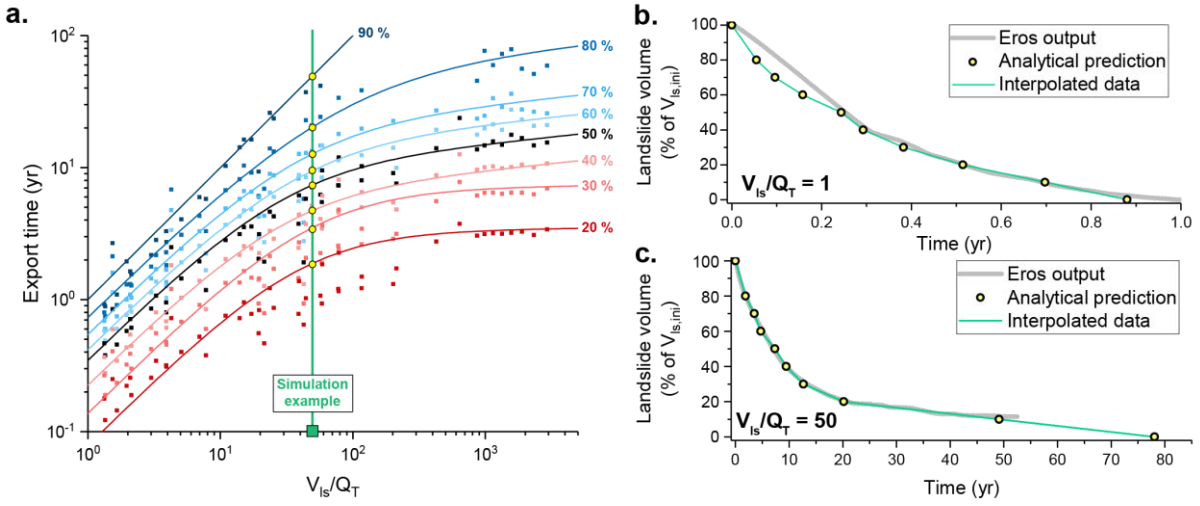


**Figure 4 | Predicting the dynamic evacuation of landslides using Eros results. a.** Series of fitting functions applied to predict the landslide export when x% of it has been evacuated. **b.** and **c.** Comparison between our predictions (yellow dots, green line) and Eros output (grey line) for 2 values of $V_{ls}/Q_T$.

# 4. Upscaling to sediment fluxes at the mountain range scale during several seismic cycles

Here, we propose a statistical approach to quantify post-seismic sediment fluxes at the mountain ranges scales. Quakos is composed of three main components that can be used independently (Fig. 5a): i. a statistical earthquake generator; ii. a landslide generator that predicts the 2D distribution of co-seismic landslides using empirical laws; iii. a sediment evacuation model based on the reduced-complexity method described in previous section. The values of the parameters used in this section can be found in Table 2.

## 4.1. Model description

### 4.1.1. Study area

In the following, we consider a hypothetical failure of the Alpine Fault in the Southern Alps, New Zealand as a case study (Fig. 5). Indeed, the Southern Alps formation and recent morphologic evolution has occurred under extreme tectonic and climatic forcing. The high tectonic activity is expressed by frequent large magnitude earthquakes ($M_w$ > 7.5) with a recurrence time of 263 ± 68 years occurring along the Alpine Fault (Berryman et al., 2012; Cochran et al., 2017; Howarth et al., 2012). The range of the Southern Alps extends on ~450 km from southwest to northeast and rises up to 3724 m at Mount Cook. It forms a natural barrier to western winds that leads to high precipitation rates up to 13 $m.yr^{-1}$ along the west coast (Tait & Zheng, 2007). Landscapes in the Southern Alps are characterized by steep hillslopes with modal values averaging at 35° (Korup et al., 2010) and are prone to landsliding even during aseismic period (Hovius et al., 1997). Thousands of landslides are expected to be triggered in the next large seismic event, potentially mobilizing ~1 $km^3$ of sediment (Odin Marc et al., 2016; Robinson et al., 2016).

### 4.1.2 Fault, earthquakes and peak ground acceleration

Here, we design a thrust fault of length $F_L$ = 400 km and width $F_W$ = 19 km with a dipping angle of 60° that approximatively mimics the geometry of the Alpine Fault (Robinson et al., 2016). Earthquakes, including mainshocks and aftershocks, are generated on this fault. When mainshocks are generated their ruptures cover the entire fault width, which leads to earthquakes of magnitude $M_w$ = 7.9. The position of each mainshock is randomly sampled along the fault plane. Each mainshock triggers a series of aftershocks, which location, date and magnitude are determined using the BASS model (Turcotte et al., 2007). The aftershocks series needs to be described along with three criterion:

- The difference between the mainshock magnitude and its largest associated aftershock ($\Delta M_w$ = 1.25) using a modified version of the Båth's law (Shcherbakov et al., 2004).

- The rate of aftershocks is submitted to a temporal decay described by a generalized form of Omori's law (Shcherbakov et al., 2004). Parameters from this law are the exponent $p$ = 1.25 and offset $c$ = 0.1 days.
- The spatial distribution of aftershocks is given by a spatial form of the Omori's law (Helmstetter & Sornette, 2003) with the exponent $q$ = 1.35 and offset $d$ = 4 meters.

All the parameter values defined are taken from Turcotte et al., [2007] and are constant for all the simulations performed in this paper.

The range of simulated magnitudes is bounded by fault dimensions, for the largest magnitude, and by the spatial discretization of the fault, for the smallest magnitude. Simulated earthquakes have magnitudes ranging from 2.5 to 7.9. For each earthquake (mainshocks and aftershocks), the associated rupture length ($R_L$) and width ($R_W$) are estimated as a function of seismic moment, $M_O$ following a consistent set of scaling laws based on empirical observations determined for strike-slip faults (Leonard, 2010):

$$R_L = \left( \frac{M_O}{\mu {C_1}^{3/2} C_2} \right)^{\beta} \quad (6)$$

$$R_W = C_1 R_L^{\delta} \quad (7)$$

where $\mu = 33$ GPa is the shear modulus and $C_2$ = 3.6.10$^{-5}$, $C_1$, $\beta$ and $\delta$ are constants which value depends on the rupture length:

- $R_L$ < 5 km: $C_1$ = 1, $\beta$ = 1/3 and $\delta$ = 1.
- 5 km < $R_L$ < 45 km: $C_1$ = 15, $\beta$ = 2/5 and $\delta$ = 2/3.
- $R_L$ > 45 km: $C_1 = F_W$, $\beta$ = 2/3 and $\delta$ = 1.

To determine the appropriate set of parameters for each seismic event, the range can be found a priori rewriting eq. 6 and replacing $R_L$ by the values of the range limits.

For a given earthquake, a synthetic peak ground acceleration (PGA) map is computed as a function of earthquake magnitude, ruptured fault geometry (rake, dip, dimension), fault mechanism, lithological controls and site effects (Fig. 5b) (Campbell & Bozorgnia, 2008). The theoretical framework that derive from this work is quite extensive, we then refer the reader to equations 1 to 12 in Campbell & Bozorgnia, [2008]. Here, we consider the sediment depth $Z_{2.5}$ = 0 m, a S-wave velocity in the first 30 m of the crust $V_{s,30}$ = 180 m.s$^{-1}$ and a reference PGA at $V_s$ = 1100 m.s$^{-1}$, $A_{1100}$ = 0.10 g (Robinson et al., 2016). For other parameter values, we refer to Table 2 in Campbell & Bozorgnia, [2008].

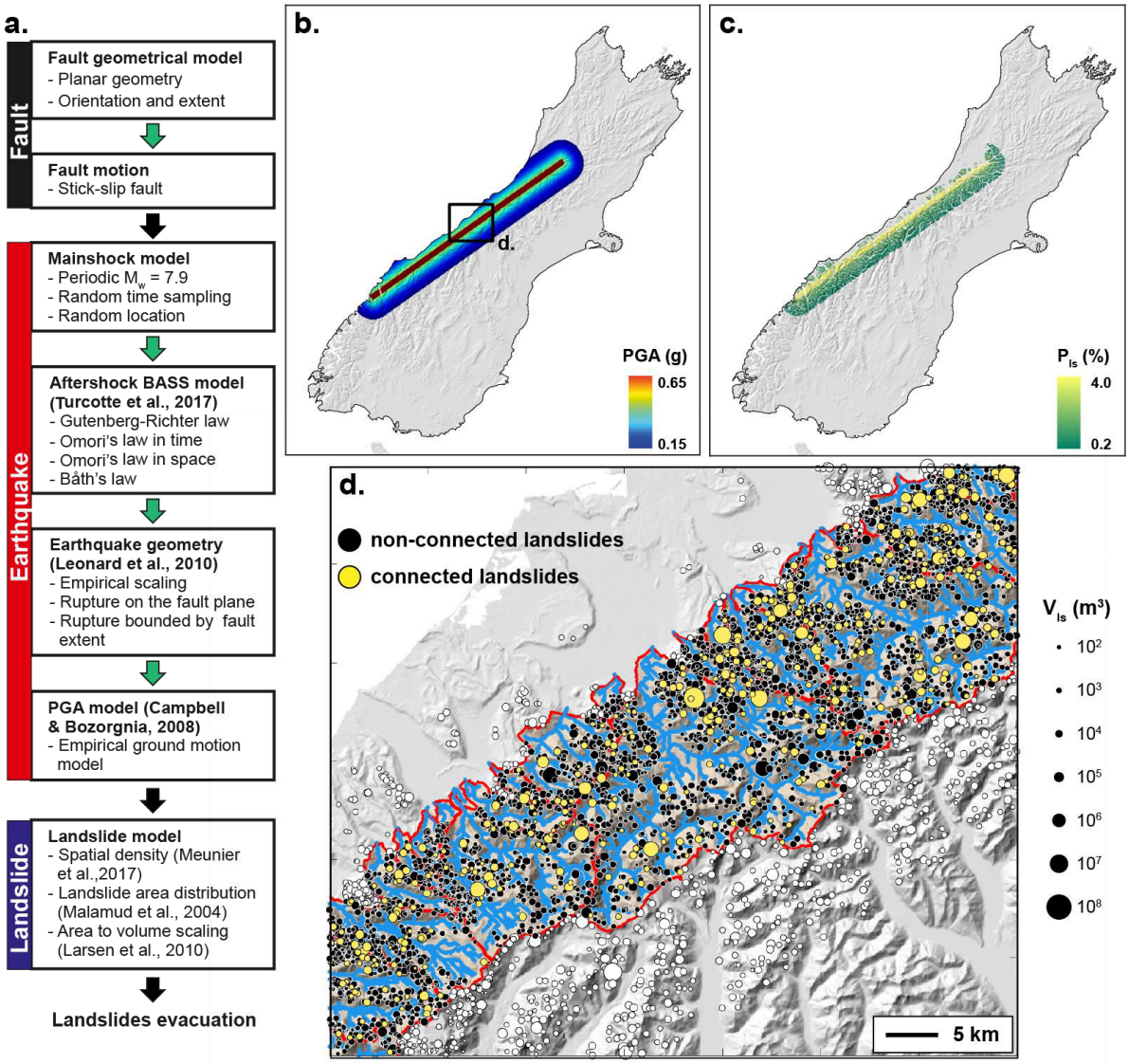


**Figure 5 | Quakos workflow used to predict landsliding pattern at the mountain range scale. a.** Quakos workflow. **b.** PGA pattern predicted by the model for a $M_w$ 8 scenario on the Alpine Fault, New Zealand. **c.** Map of the landslide density. **d.** Landslide pattern predicted by Quakos. The view is focused on catchments located on the Central Southern Alps. Yellow dots indicate landslides, their sizes are a function of landslide area. White dots outside of the considered catchments only represent landslides location. Notation: $V_{ls}$, landslide volume.

### 4.1.3 Landslide triggering by earthquakes

Modelled PGA maps are then used to infer the spatial density of triggered landslides, i.e. the number of landslides by unit area. Some studies have demonstrated that the density of earthquake-triggered landslides is linearly dependent on the PGA (Meunier et al., 2007; Yuan et al., 2013):

$$P_{ls} = \alpha_p PGA - \beta_p \quad (8)$$

with $\alpha_p$ and $\beta_p$, two empirical parameters that controls respectively the maximum landslide density and its spatial repartition. The parameter $\beta_p$ is a critical PGA value under which no or very few landslides are triggered. The values of these parameters are highly dependent on the studied case and the choice of their value is explained in the result section. Following the work of Meunier et al., [2007], locations where the local slope is inferior to 20% are not affected by landsliding. In our case study, this prevents landslides from being triggered on alluvial fans and large river valleys (Fig. 5c, d).

The distribution of earthquake-triggered landslides areas is commonly given by an inverse gamma probability density function:

$$pdf(A_{ls}) = \frac{1}{a\Gamma(a)}\left[\frac{a}{A_{ls}-s}\right]^{\rho+1} exp\left[-\frac{a}{A_{ls}-s}\right] \quad (9)$$

with $a$ a parameter controlling the position of the *pdf* maximum, $s$ a parameter controlling the roll-over for small landslides and $\rho$ is a positive exponent controlling the tail of the *pdf* (Malamud et al., 2004a). The area of each landslide belonging to a landslide cluster is determined by randomly sampling $pdf(A_{ls})$. The locations of landslides are then determined according to the landslide density map (Fig. 5d). Individual landslides areas are converted to volume $V_{ls}$ by using an empirical scaling law:

$$V_{ls} = \alpha A_{ls}^{\gamma} \quad (10)$$

with $\alpha$ and $\gamma$ are set to 0.05 and 1.5 (Hovius et al., 1997; Larsen et al., 2010), values that are well-suited for estimating the volume of deep-seated bedrock landslides that dominate the volume budget of a population of triggered-landslides.

### 4.1.4 Post-seismic landslide sediment evacuation

After the triggering of a cluster of landslides by an earthquake, the prediction of post-seismic landslide evacuation depends mostly on: i. the sediment supply rate to the channel network, i.e. the transfer of material from hillslopes to channels and ii. the rate of sediment transport by the river.

Several studies have pointed out the importance of the initial and dynamic connectivity of landslides to the channel network on post-seismic sediment fluxes (Li et al., 2016; Roback et al., 2018). While this process only has a limited impact on suspended load fluxes, it is suggested to control the transfer of coarser sediments (Li et al., 2016). Several studies provide an estimation of initial connectivity ranging from 8% to 43 % (Dadson et al., 2004; Li et al., 2016). Based on the data of Li et al [2016] and Roback et al., [2018], the initial landslide-channel connectivity $C$ of each landslide is determined as a function of its area $A_{ls}$:

$$C = mA_{ls,bin}^{\omega} \quad (11)$$

where $m$ is an empirical constant and $\omega$ an empirical exponent (see Supplementary Figure S3). Equation (11) applies for landslides presenting an area lower than $1.10^6$ m$^2$. Above this threshold, we

assume that landslides are always initially connected to the drainage network. This assumption is supported by empirical data and by the fact that larger landslides usually present a longer run out (Lucas et al., 2014). Here, $C$ gives the percentage of connected landslide in the considered bin of landslide area ($A_{ls,bin}$) on a logarithmic scale.

The loose material composing the cluster of non-initially-connected landslides is destined to reach the fluvial network with a velocity that likely depends on the climatic and meteorological context, the frequency of earthquakes and local topography. However, studies aiming at quantifying the post-seismic mass transfer from hillslopes to channel are scarce due to the difficulties to measure it on the field or using remote sensing (Fan et al., 2018; Zhang et al., 2016).

We therefore develop a simplified approach to account for the dynamic connectivity of landslides to rivers. This approach finds the distance ($d$) between the landslide and the closest river connection point using a steepest descent algorithm. The timing of connection is obtained by setting a constant and arbitrary connectivity velocity ($u_{con}$) to each landslide. The connection time is then computed as $t_{con} = d/u_{con}$ . Once the landslide is connected to the river network we assume that the whole volume is connected, i.e. completely available to be removed by the river.

Once a landslide reaches the closest stream, its subsequent evacuation depends on the ratio between its volume $V_{ls}$ and the river local transport capacity $Q_T$ and follows Equation 5. If the landslide volume is determined for each landslide using Quakos, the transport capacity needs to be computed. The along-stream transport capacity of bedrock rivers is set by its geometry (width and slope), local river discharge and sediment grain size. The bedrock river width ($W$), slope ($S$) and mean discharge ($\bar{Q}$) are expressed as a function of the local drainage area ($A$) as:

$$\begin{cases} W = k_{wn}A^{0.5} \\ S = k_{sn}A^{-0.45} \\ \bar{Q} = \bar{r}A \end{cases} \quad (12)$$

with $k_{wn}$ the normalized width index, $k_{sn}$ the normalized steepness index and $\bar{r}$ mean annual runoff (Lague, 2014). Here, the critical drainage area used to extract the drainage network is equal to 0.5 km$^2$.

To be in the same context than Eros simulations, the river transport capacity is described using an effective daily discharge ($Q_{eff}$) presenting a return time of one year which is a good compromise between frequency of occurrence and the amount of geomorphic work of such events. The bedload transport capacity (Meyer-Peter & Müller, 1948) is then computed as:

$$Q_T = WK\left(\rho_w g\left(\frac{nQ_{eff}}{W}\right)^{0.6} S^{0.7} - (\rho_s - \rho_w)g\tau_c^* D_{50}\right)^{1.5} \quad (13)$$

with $\tau_c^*$ the critical Shields stress, $\rho_w$ the water density, $\rho_s$ the sediment density, $n$ the Manning friction coefficient and $g$ the gravitational constant. For simplicity, the grain size distribution of landslide is reduced to the median grain size descriptor ($D_{50}$) and will be uniform for all landslides.

To compute the value of $Q_{eff}$, we assume that the range of daily discharges experienced at any point along the river follows an inverse-gamma probability density function:

$$pdf(Q) = \frac{k^{k+1}}{\Gamma(k+1)} exp\left(-\frac{k}{Q/\bar{Q}}\right)(Q/\bar{Q})^{-(2+k)} \quad (14)$$

with $\Gamma$ the gamma function and $k$ a parameter linked to the variability of the hydrological forcing, here, fixed at $k$ = 1, based on empirical data (Croissant et al., 2017; Lague et al., 2005). This assumption is supported by empirical data, that demonstrate that the runoff of rivers located along the West Coast of New Zealand present a high variability ($k$ = 1) (Croissant et al, 2017b). From this distribution, the return time ($t_r$) of a particular daily discharge can be assessed using:

$$t_r(Q_{eff}) = \Gamma(k/Q_{eff}, k+1)^{-1} \quad (15)$$

Using this equation, the value of $Q_{eff}$ can be computed.

Computations involving operations on digital elevation models have been performed using TopoToolbox (Schwanghart & Scherler, 2014).

## 4.2 Landslide triggering and sediment export over a seismic cycle

### 4.2.1 The volume of triggered landslides by earthquakes on the Alpine Fault

To assess Quakos outputs, we compare them to natural observations and existing analytical models (Keefer, 1999; Odin Marc et al., 2016). We plot the total volume of landslide clusters as a function of earthquake magnitude (Fig. 7). Consistent with Marc et al, [2016], Quakos leads to a threshold magnitude, here ~4.5, under which no landslide is generated. This threshold emerges from the fact the landslides are only generated if a critical PGA is reached (eq. 6; see Supplementary Movie S1). Above this threshold, the total landslide volume triggered by an earthquake increases with magnitude and shows a sensitivity to the depth of earthquake nucleation. The variability of total landslide volume for earthquakes of equal magnitude results from earthquake depth but also from the variability of the topography impacted by landsliding, including the proportion of the topography with local slope greater than 20%. For low magnitudes, total landslide volume becomes strongly sensitive to earthquake depth. Indeed, the width extent of the rupture is small compared to fault width, and earthquake depth becomes the controlling factor to generate PGA above the critical value for landsliding. This mostly explains the spread in the distribution of total landslide volume as a function of magnitude, for earthquakes with magnitude lower than ~6.5. Larger earthquakes are less prone to this spread in total landslide volume as their rupture width becomes closer to fault width. We also note that Quakos outputs asymptotically tend, for large magnitudes, towards the analytical model from Marc et al, [2016] for $R_0$ = 15 km, independently from Quakos earthquake depth. This results from the PGA model in Quakos which depends on rupture extent (Campbell & Bozorgnia, 2008), covering the entire fault width for the largest earthquakes, and not on earthquake depth. Whereas Marc et al. [2016] only considers the depth of the sources of seismic waves, and not the rupture

extent. Total landslide volume is also sensitive to the parameters in equations 8 and 9, which control the number of triggered landslides for a given PGA and their volume distribution (see supplementary Figure S2).

For a $M_w$ 7.9 earthquake occurring on the Alpine Fault, without considering aftershocks, the total number of landslides generated is $N_{ls,tot}$ = 13960 landslides with a total volume of sediment $V_{ls,tot}$ = 0.8 km$^3$ (Fig. 6). There is no empirical constraint allowing for a more accurate estimation of the characteristics of a future earthquake on the Alpine Fault. However, the total number of landslides is of the same order of magnitude than most of the natural cases documented in Tanyaş et al., [2017] and the total volume matches the one estimated from two independent studies (Odin Marc et al., 2016; Robinson et al., 2016).

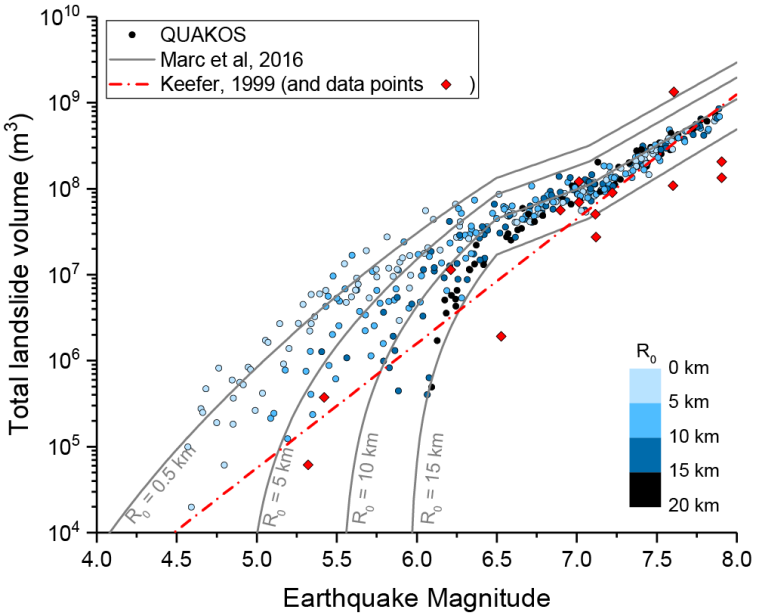


**Figure 6 | Relationship between the total volume of landslides triggered by earthquakes and their magnitude, in the case of a strike-slip fault**. Quakos results (circles) are coloured as a function of the depth of the earthquake compared to the surface ($R_0$). Quakos output are compared to two empirical models from Marc et al, [2016] and Keefer, [1999].

### 4.2.2 Sediment export over a seismic cycle

Here, we explore the dynamic of sediment export over a single seismic cycle that follows a $M_w$ 7.9 earthquake. We focus on the role of landslides initial and dynamic connectivity to the fluvial network, characterized by its velocity $u_{con}$, in controlling post-seismic sediment evacuation. Based on the morphodynamic modelling results, we assume that landslides located in the same river reach are evacuated independently of each other.

At the initial stage, ~41% of the total sediment volume is connected to the drainage network leading to a fast evacuation of the landslide deposits with 43, 50 and 96% of the total volume evacuated over 263 years, the average duration of a seismic cycle, for $u_{con}$ equals to 0.1, 1 and 10

m.yr$^{-1}$, respectively. The 'full connectivity' case leads to the highest sediment transport rates with 70% of the landslide mass evacuated in less than 10 years (Fig. 7a). This value matches the order of magnitude of the predictions of Croissant et al, [2017] for high mean annual runoff and runoff variability and for which the full population of landslides was assumed fully connected. After 2000 years, most of the sediment volume is removed for $u_{con} \geq 1$ m.yr$^{-1}$, while the rivers are starving of sediments due to the absence of new connected landslides for $u_{con} = 0.1$ m.yr$^{-1}$. This illustrates, that landslide connectivity can become the limiting factor of sediment evacuation after the triggering of landslides by a large earthquake. In turn, landslide connectivity is critical to assess the likelihood of evacuating sediments over a duration smaller than a seismic cycle.

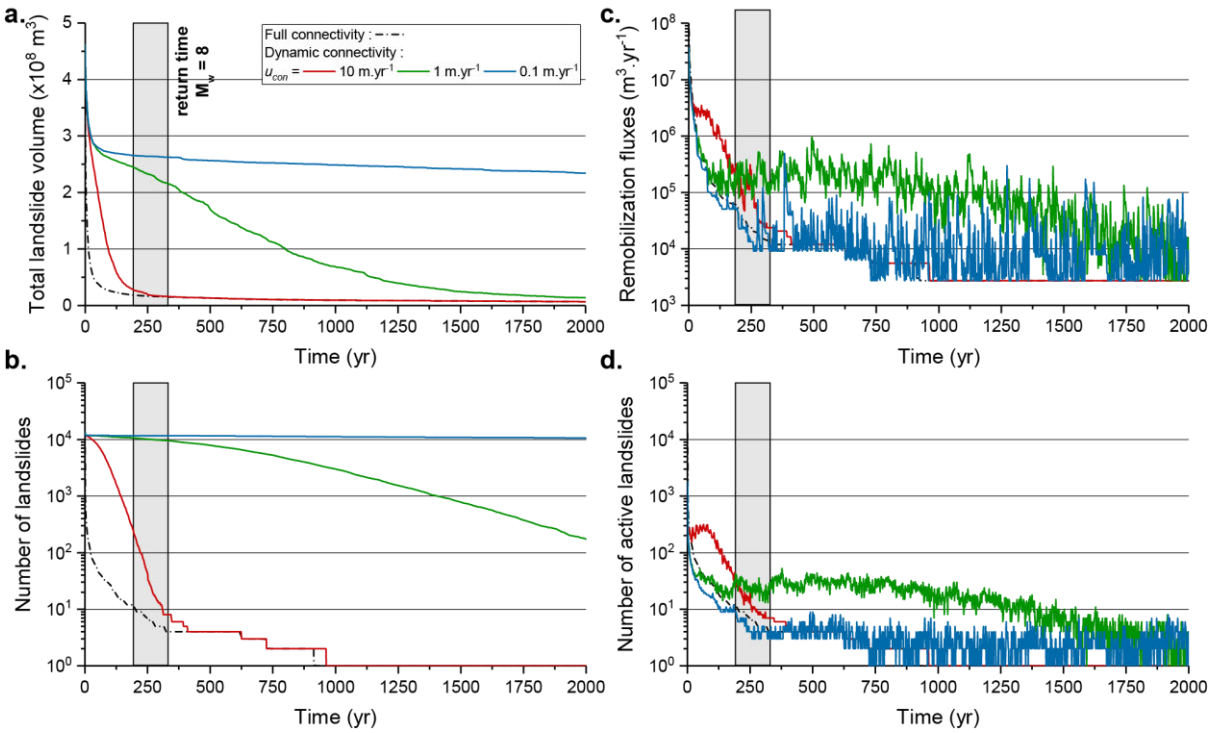


**Figure 7 | Temporal evolution of the $M_w$ 8 earthquake simulations with different connectivity properties. a.** Temporal evolution of the landslide volume for different connection velocities. **b.** Temporal evolution of the number of landslides. **c.** Sediment remobilization fluxes**. d** Temporal evolution of the number of active landslides, i.e. landslide that are being connected to the drainage network and being actively evacuated by the river. Note: The grey area indicates the estimated return time of a $M_w$ 8 earthquake on the Alpine Fault.

Interestingly, the number of active landslides, i.e. connected landslides with remaining sediments, do not exactly follow the volume evolution. This occurs because the volume of landslide is controlled by the largest landslides. For low values of $u_{con}$, model predictions show that a large proportion of the initial landslide population can be preserved within the mountain range while having evacuated a moderate to large proportion of the volume of earthquake-produced sediment (Fig. 8b).

Connectivity also impacts the amplitude and duration of sediment remobilization rates (Fig. 8c). The full connectivity case present rates at least one order of magnitude greater than any other

model during the first years after the earthquake. However, this rate drops abruptly by 3 orders of magnitude in less than a century. On the contrary, for $u_{con}$ < 10 m.yr$^{-1}$, the remobilization rate oscillates around a steady average during the first 200 years before decreasing progressively. The different rates are controlled by the sediment supply from hillslope to the channels (Fig. 8d). A low value of $u_{con}$ ensures a progressive and near-constant release of sediment with a steady number of landslides being active during the first 200 years.

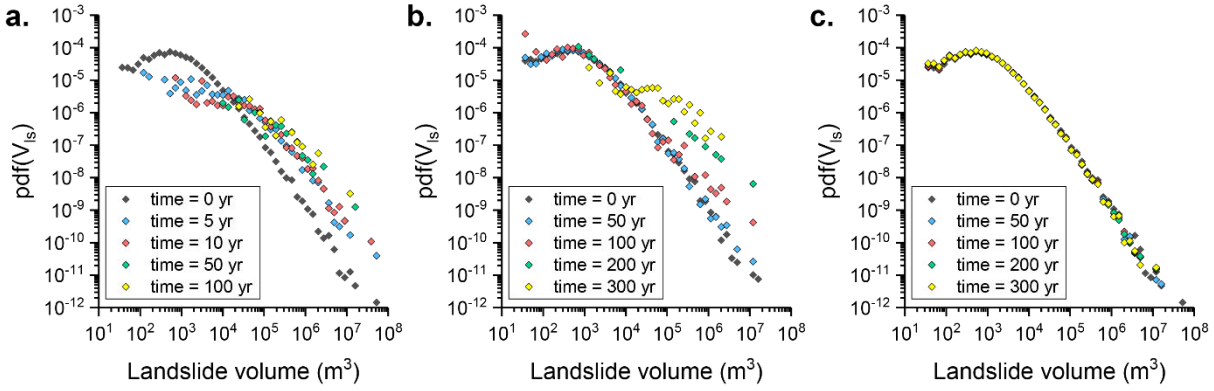


**Figure 8 | Probability density function of landslide volumes at different time steps. a.** For the Full connectivity case. **b.** For the case $u_{con}$ = 10 m.yr$^{-1}$. **c.** For the case $u_{con}$ = 1 m.yr$^{-1}$.

The velocity of connection has also an impact of the evolution of the distribution of landslide volume (Fig. 8). We here account for the volume changes as landslide are being evacuated by river sediment export. The temporal evolution of the probability density function (pdf) of landslide volume, pdf($V_{ls}$), for the full connectivity case shows that landslide presenting an volume inferior to $10^3$ m$^3$ disappear from the distribution after only five years as they preferentially present $V_{ls}/Q_t$ < 1 year. For longer duration, the remaining landslides tend towards the largest areas and the distribution shrinks towards these largest areas. There is however no change in the scaling of the tail of the pdf($V_{ls}$). The $u_{con}$ = 10 m.yr$^{-1}$ case show that the shape of the pdf is preserved during 50 yr until the largest landslides start to dominate the long-term signal. Moreover, the slope of the tail of the pdf changes with time and get less steep. This occurs due to the parametrization of the initial connectivity in Equation (11) that favors the connection of large landslides and tend to preserve small landslides. The cases with $u_{con}$ ≤ 1 m.yr$^{-1}$ show a different dynamic. The shape of the pdf is always preserved with time. As the connection velocity is uniform between landslides they are preserved within the mountain range.

## 4.3 Upscaling to several seismic cycles

In this section, we extend model duration to several seismic cycles. The scenario is chosen to mimic the behaviour observed on the Alpine fault, i.e. a temporal series of 12 $M_w$ = 7.9 mainshocks

separated by recurrence period randomly sampled in the 263 +/- 68 years range (Fig. 9). The co-seismic landslides production is slightly different for each mainshocks, with a total volume ranging from 8.6 to 8.9.$10^8$ $m^3$ and an average total number of landslides of 14500.

Each mainshock is followed by a series of aftershocks which magnitude vary between 2.5 and 7.5, some of which mobilise an additional volume of sediment. In most cases, the contribution of aftershocks is generally lower than that of mainshocks for two reasons: 1. they mobilize sediment volumes inferior by 1 to 5 orders of magnitude (Fig. 9a) and 2. most of landslide-triggering aftershocks events are quasi-synchronous of their associated mainshocks and therefore the total sediment delivery is dominated by the one of the mainshock. However, aftershocks occurring between two mainshocks can have a visible impact on the sediment delivery as highlighted by the $M_w$ 7.5 earthquake at ~2000 years it mobilises sediment volumes comparable to the mainshocks.

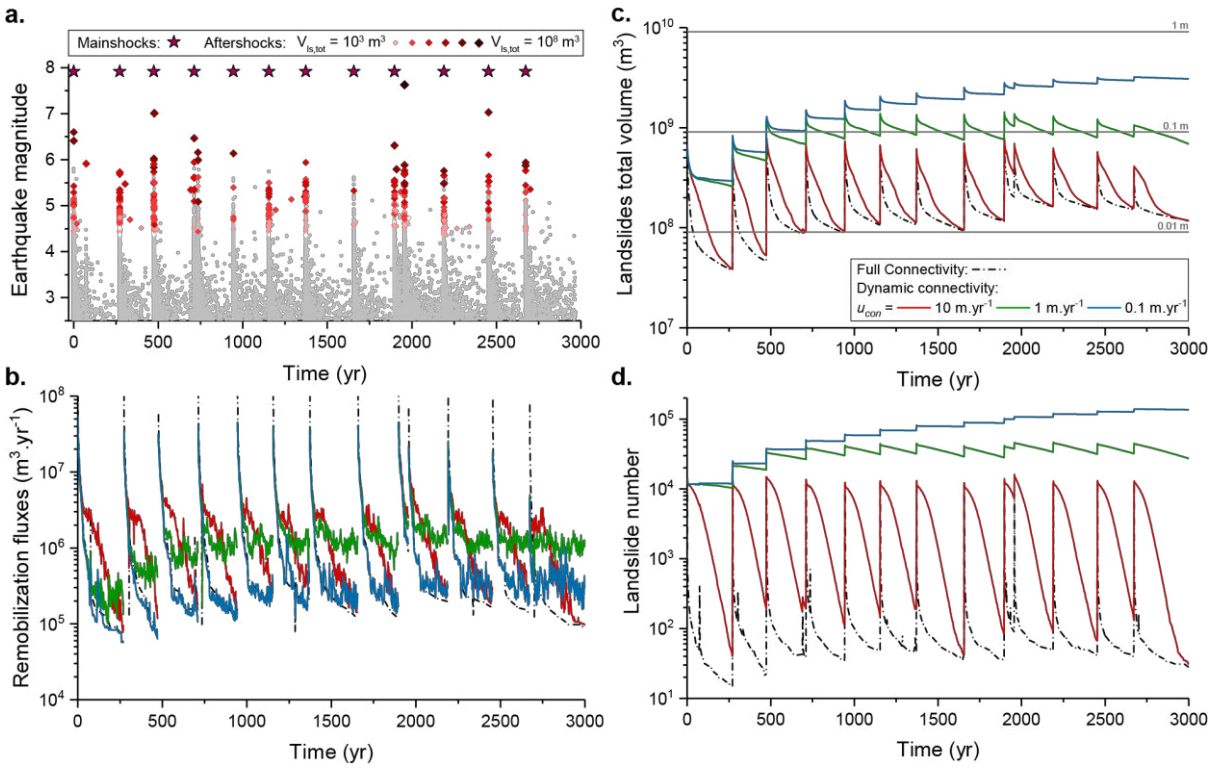


**Figure 9 | Temporal upscaling over several seismic cycles. a.** Times series of earthquakes generated on the faults. It is characterised by a series of mainshocks of $M_w$ = 7.9 followed by their aftershocks sequences. The dot size and color are a function of the total volume of the landslide population ($V_{ls,tot}$). The grey dots indicates the earthquakes that have not triggered any landslides. **b.** Evolution of the remobilization fluxes. **c.** Evolution of the total volume of sediment mobilized by the successive earthquakes. The grey lines represent the mean sediment thickness that would be deposited on the total area affected by landsliding. **d.** Evolution of the number of landslides in the mountain range.

Over the 12 seismic cycles, the rivers are never able to export the totality of the sediment (Fig. 9c). This results in the persistence of sediment storage within the mountain range reaching a minimum of 10-20% of one $M_w$ 7.9 earthquake worth of sediment for $u_{con}$ > 10 $m.yr^{-1}$. However, for these

cases, most of the landslides are evacuated within the seismic cycles reaching a minimum of 20-50 landslides remaining in the catchments (Fig. 9d). Scenarii with $u_{con} \leq 1$ m.yr$^{-1}$ show a different evolution of the total landslide volume. Over several seismic cycles, the earthquake-produced sediment piles-up inside the mountain range until an equilibrium situation is reached in which a certain percentage of the newly triggered population is removed. In these cases, the sediment volume that is stored within the mountain range at the end of each seismic cycle is equivalent to 120% ($u_{con}$ = 1 m.yr$^{-1}$) to 600% ($u_{con}$ = 0.1 m.yr$^{-1}$) of the average value of earthquake-triggered initial landslide volume. These cases are also characterized by the persistence of several thousands of landslides in the mountain range.

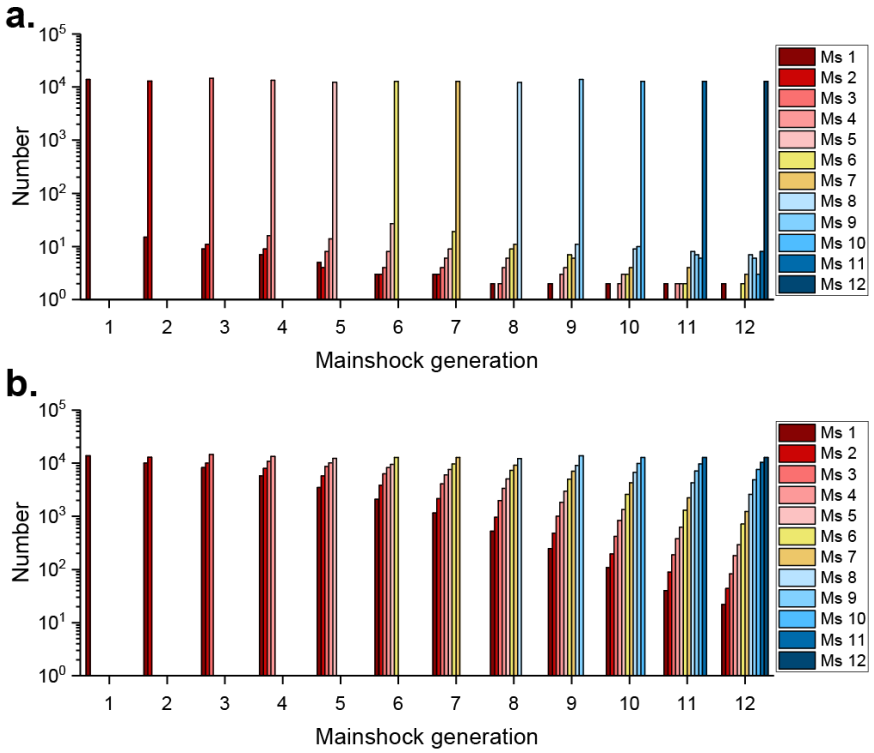


**Figure 10 | Landslide generations. a.** For the Full connectivity case. **b.** For the case $v_{con}$ = 1 m.yr$^{-1}$. Notation: Ms: mainshocks.

Figure 10 shows the repartition of landslides generation at each mainshocks occurrence. For any case, the number of landslides generated by the mainshocks dominates are its time of occurrence. The full connectivity case shows that even if the majority of the first 11 mainshocks-triggered landslides are removed when the twelfth earthquake occurs, there is still a small amount of landslide remaining in the mountain range belonging to the previous generations. In this case, the connection velocity is not involved in the post-seismic sediment evolution meaning that landslides presenting a very low $V_{ls}/Q_t$ can persist for a long time. On the contrary, the low velocity of connection tends to preserve a large amount of landslides as mainshocks occurs as shown by the wide diversity of all generations of landlsides when the last mainshocks occurs.

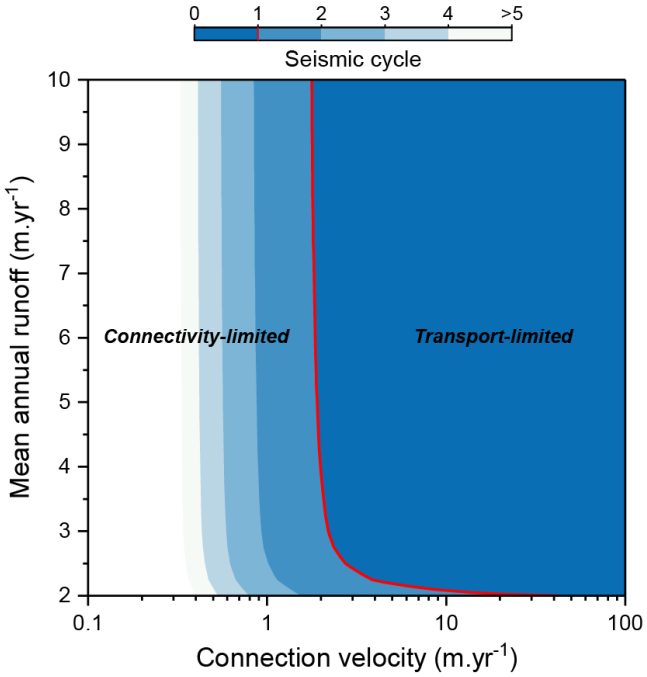


**Figure 11 | Time necessary to evacuate a landslide cluster as a function of mean annual runoff and connection velocity.** The time here is normalized by the average value of a seismic cyle (i.e. 263 year)

Based on the results of Figure 9, we aim at defining an index that could described a priori the mountain range response to a large earthquake. This index is based on the two intrinsic timescales that are in involved in these simulations. One is the time necessary to transport the landslides sediment by the river network and the other the transfer time of landslide material from hillslopes to channels. The former is computed as the time necessary to remove of 90% of the total landslide volume for different mean annual runoff intensity under the assumption that all the landslide are connected. The latter is computer as the mean connection time ($\overline{t_{con}}$) of the whole landslide cluster:

$$\overline{t_{con}} = \frac{\sum_{i=1}^{N_{ls}} V_{ls,i} t_{con,i}}{\sum_{i=1}^{N_{ls}} V_{ls,i}} \quad (16)$$

Figure 11 shows that for a mean annual runoff superior to 3 m.yr$^{-1}$, results shows a higher sensitivity to the connection velocity. When the mean annual runoff decreases under 3 m.yr$^{-1}$, the predicted shear stress of the effective discharge is closer to threshold of sediment motion and the export time display more sensitivity to its value. This figure highlight the presence of critical connection velocity ~ 2 m.yr$^{-1}$ above which the mountain range is a connectivity-limited regime, i.e. the landslide evacuation is controlled by the transfer rates of material from hillslopes to channels. In this regime, the landslide population is never entirely evacuated over one seismic cycle. Below this critical value, the mountain range is in a transport-limited regime where the evacuation time is dependent on the transport capacity of the rivers.

# 5. Discussion

## 5.1 Limitations of the approach

### 5.1.1 The reach scale

The morphodynamic simulations performed with Eros contain the necessary processes description to account for the feedbacks between rivers flow, river geometry and transport capacity. More importantly in this context, how the sudden introduction of large volume of sediment affects these feedbacks. However, as any numerical model, Eros contains some simplifications. For instance, the description of the landslide deposit evolution could be augmented with additional processes description that could lead to a boost of the lateral erosion efficiency during the landslide evacuation:

1. As the river cuts through the landslide deposit, gravitational effects could lead to a more efficient lateral delivery.
2. The water seepage through the landslide deposit could potentially play a role to structurally weaken the deposit and lead to a higher efficiency of the lateral erosion during the last phase of the landslide removal.

The case of the landslide cascade is interesting as it allows to estimate the impact of several discrete sediment supply distributed alongstream of the dynamic of system. This case is still idealize as the bedrock reach present the same characteristic alongstream but on distances inferior to 5 km this assumptions can hold. To fully appreciate the sediment cascade problematic, the problem should be tackled using a real catchment geometry coupled with a realistic landslide population. This is described in the next section.

### 5.1.2 The mountain range scale

The upscaling to the mountain range makes the application of a 2D morphodynamic model remains to date highly computationally expensive. For this reason, we have proposed a reduced-complexity approach with the simplifications that it entails. As such, QUAKOS does not provide 'real' sediment fluxes as the assumption implied in the treatment of sediment evacuation is similar than the detachment-limited one, i.e. once the sediment is entrained it is systematically exported out of the catchment. This has the effect to neglect the entrain/transport/deposition of coarse sediments that occur within the catchment but that is still too computationally heavy to consider at the mountain range scale. A higher accuracy in the quantification of the sediment transfers intra-catchment and from catchments to the alluvial fans would necessitate the application of a 2D morphodynamic model to a high resolution DEM (cell size inferior to 5 m) that still seems out of reach for now.

As shown by our results, the quantification of post-seismic fluxes highly depend on the description of the sediment supply rates from hillslopes to river channels. However, empirical studies aiming at investigate which processes control the evolution of loose sediment masses resting on hillslopes are still rare. In addition, the post-seismic sediment masses evolution cannot be estimated at

more than a decade as technologies allowing scientist to do it have been only developed recently. The diversity of factor that could influence the dynamic is discussed in the next section.

QUAKOS depends on two aspects: a statistical framework informed by empirical laws and the topography of the studied domain. The latter exerts a control on different parts of the workflow and cannot be bypassed: i. the computed slopes gives

However, the use of DEM could be pushed forward to improve for instance the location of landslides instead of using a random allocation. i.e. the impact of hillslope size, upslope area, …

and ii. the lack of empirical data to describe physically the processes in play on post-seismic landslide evacuation.

Other extreme events such as dam breaks, debris flows and glacial lake outbursts are frequently happening in mountain ranges affected by intense landsliding. These events are extremely efficient to entrain and transport large quantity of sediment downstream. However, the numerical reproduction of these events is to date a very complicated task to achieve, especially at long spatial and time scales.

### 5.2 The role of dynamic connectivity

At the landscape scale, our results highlight the predominant role of dynamic connectivity on modulating the sediment mobilization fluxes. As such, all the conditions that control this process are to take into account. For instance, our case of study, the West Coast of the Southern Alps of New Zealand contains several properties that would promote a high degree of initial connectivity and a rather high connection velocity. These properties are high intensity and frequent runoff events, a slope distribution displaying a high modal value (~ 35°) and most of the rivers are incised in a narrow bed promoting a high availability for the river to access and transport this landslide-derived material. This could be corroborated by the fact that traces of the last large magnitude earthquake are not observable in the landscape, i.e. there is not large thicknesses of sediment on low order stream riverbeds and the hillslopes seem to have recover from their last disturbance. However, large sediment deposits can be observed in high order river valley that have not completely recovered from the last glacial maximum (i.e. presenting large valley, implying a low transport capacity). The behaviour of the western side of the Southern Alps can be contrasted by the one expected from the Eastern side as runoff events have a lower intensity and large glacial valleys. The latter implies that even if a landslide deposit would reach the rivers is would be still be difficult for the river to reach it. Its subsequent export would depend on the lateral mobility of the river and of the frequency of river lateral erosion. These observations could also be applied on other mountain ranges presenting a wide range of climatic, tectonic and topographic properties. For instance the Andes (dry climate in the Central part), Taiwan (typhoons) and Himalaya (monsoons + subject to GLOFs).

Constraining the connection velocity on empirical datasets remains a difficult. This calls for a better understanding of the processes in play in the material transfers between hillslopes and the rivers. This task is not straightforward as most of mountain ranges experiences heavy co-seismic landsliding are also the site of intense and frequent high magnitude precipitations events (monsoon, typhoon, and storm) that can make transfer rates hard to decipher. These events frequently trigger new landslides populations and have the potential to re-activate existent ones (Zhang et al, 2016). As demonstrated in the recent work of Fan et al, [2018], the vegetation growth on deposit plays a role in stabilizing landslide deposit reducing their activity during the first years following an earthquake. However, the inclusion of this processes could be complex as the model would have to account of the frequency of the deposit mobilisation that could prevent the vegetation from developing. As shown by Fan et al, [2018], a more accurate way of describing hillslope to channel transfer rate will be dependent on upslope drainage (+ surface runoff) area and local slope

# 6. Future directions

During the last decades, the research effort has been mainly focused of co-seismic slope processes and the post-seismic evolution of fine sediment. We are now confronted to a gap of knowledge concerning the post-seismic evacuation of coarse sediment that has paradoxically the most influence on long-term landscape evolution and geomorphic hazards. In this section, we propose different ideas on where the research effort could be focused to significantly increase our understanding of the short to medium-scale landscape dynamic over one to several seismic cycles and hydro-sedimentary hazards management.

## 6.1 Empirical data collection to quantify post-seismic landslide evacuation

The study of post-seismic sediment fluxes is confronted to a lack of empirical data documenting the evolution of coarse material fluxes during the inter-seismic period. Until now, the data collected to improve our understanding of the geomorphic impact of large earthquakes have been focused on the co-seismic landslide production via manual and/or semi-automatic mapping on satellite images (Odin Marc et al., 2017) and the evolution of the post-seismic sediment masses have been investigated mainly in regard with the fine sediment. This problem would have also to be tackled at different scales to understand how local processes control the overall evacuation of the whole landslide population triggered in a given catchment.

To fully characterize the problem, empirical data gathering would have to be focus on:

i. The processes controlling the transfer of material from hillslopes to river channels, i.e. local slope, surface runoff, vegetation growth, water infiltration.

ii. The partitioning between the production of fine and coarse sediment and its implication on the subsequent sediment evacuation.

iii. The tracking of the sediment mass evolution at different spatial scales i.e. from the reach to the catchment.

Given the spatial scale of the problem (i.e. several hundreds of kilometres) and the difficulties to measure coarse material fluxes, remote sensing is probably one of the central tools for future work to track the macro-evolution of the sediment masses. With increasing technological power and a more systematic acquisition of high resolution datasets with a variety of techniques (photogrammetry, laser scanning and tri-stereo satellite imagery) we can tend toward a finer quantification of the system evolution (Fan et al., 2018). Notably concerning the local processes controlling material transfer rates from hillslope to channel and thus the evolution of connectivity between different parts of the catchment. While remote sensing is a sensible tool to track sedimentary masses evolution, a full understanding of the processes involved would also require field-based data such a precipitation patterns, river discharge and grain size distributions. Additionally, in the same spirit as numerical and flume studies developed to understand which processes dictates the evolution of sediment pulses in rivers, similar experiments could be applied to loose deposits resting on hillslopes. The study of the influence of GSD, runoff and slope could be a good starting point.

The partitioning between fine and coarse particles within a landslide remains an open question as well as the grain size organisation within the deposit (at the surface but also in the deeper layers). This question is a critical importance as we can expect different timescales of sediment export associated with bedload or suspended load. This factor will also be important to quantify precisely transport rates as fine particles can either hide in the subsurface layers or facilitate the entrainment of coarser grains on the surface of the layer. However, measurements of GSD could be a complex and extensive endeavour on the field. Using complex GSD In numerical approaches would lead to the use of more detailed sediment transport laws that accounts for i. the feedback between subsurface sand composition and entrainment rate, ii. the hiding effects and iii. the assignment of transport rates for each classes of grain size (Parker, 1990; Wilcock & Crowe, 2003). However, the use of such description of sediment transport would have the advantage to trigger the emergence of natural processes such as armoring. Accounting for the impact of a complete GSD produced by landslides on sediment transport requires coupling the model with a stochastic hydrologic description to generate a cyclicity between armoring and armor breaching. This would obviously lead to a substantial higher level of complexity. This would need to be addressed in the future to fully appreciate the whole processes in play in landslide evacuation.

Given the return time of large earthquakes (classically several hundred years) our observation timescale would be one seismic cycle. However, it would inform a lot on the processes in play to upscale them on several seismic cycles using numerical modelling. In the meantime, numerical and/or analogical approaches are still a useful tool to understand the mechanisms and processes controlling the transient dynamic of landslide export and at the same time give information on where the empirical data collection could be focused.

### 6.2 Mountain ranges dynamics on several seismic cycles ($10^3$-$10^4$ year)

Landscape evolution is controlled by the actions and feedbacks between tectonic, surface processes and climate (Dadson et al., 2003; Whipple & Meade, 2006). While mountain ranges building and decay have been studied over long timescales (i.e. > $10^5$ years) (Whipple & Tucker, 1999) it still remains complex to investigate their dynamics at shorter time scales. As such, only a few studies have accounted for the effect of stochastic large sediment supplies at the mountain range scale (Benda & Dunne, 1997; Egholm et al., 2013). However, a successful application of such modelling approach would give clues on how to answer to several fundamental questions concerning the inter-seismic behaviour of mountain ranges.

- For larger timescales, bedrock incision could be accounted for to identify how erosion patterns are affected by the antagonist effect of large sediment supplies, i.e. the shield effect and the tools abundance to identify key periods of bedrock incision effectiveness. In that sense, the sediment supply rates from hillslope to channel plays a critical part as for instance low velocity can slowly release the material with time thus enhancing the tool effect. On the contrary, a high increase of sediment supply could lead to massive aggradation rates inhibit the vertical erosion of the bedrock but could however, increase the lateral erosion. The effect of the sediment supply intensity on knickpoint retreat could be studied.
- Moreover, the comparison of the landslide population export time and the recurrence interval of large earthquakes would give valuable information on the timescale of incision inhibition phase triggered by an intense and widespread alluviation of the fluvial network.
- Several authors have hypothesised a potential destructive role of earthquakes, i.e. the erosive action of a seismic event could be superior to the material influx brought by surface uplift. However, this effect can only be fully accounted for if the post-seismic timescale of sediment evacuation is known. As of now, because of the scarcity of studies on the matter, the evacuation time of landslide is generally set to immediate to compute the lithospheric flexural response to massive landsliding (Densmore et al., 2012; O. Marc et al., 2016).
- How rare high amplitude events participate in alluvial fans dynamics to decipher recent sedimentary archives and help understand the dynamics of mountains ranges.

The last decades have seen the development of a wide diversity of morphodynamic models that can model landscape evolution spanning large spatial and time scales (Tucker & Hancock, 2010). The scale of the problem generally determines the complexity of the processes that need to be accounted for in the model. To answer the problematic of post-seismic mountain range evolution, numerical approaches would have to face several challenges.

1. The fluvial processes description, morphodynamic model accounting for width and slope modification. However, only a handful of models contain the necessary elements that allow for a dynamic width to emerge as a function of the different forcing that the river experiences (discharge and sediment supply).
2. The former putting a constraint on the grid cell size that should be used in the model, i.e. it has to be small enough to describe the river cross section accurately with several pixels. This would increase the computational power and time.
3. Dislocations at the fault trace location disrupting the river profile to create knickpoints (Steer et al, in prep).
4. A bedrock incision model must account for the complex pattern of spatialized sediment delivery.

In addition, a successful application of numerical model would depend on the quality of the description of the processes governing the, and importantly here the transport laws. As of now, the processes are poorly constrained and the previously described empirical data collection would greatly help to constrain and '*feed'* numerical approached therefore leading to more accurate landscape evolution predictions.

### 6.3 Hydro-sedimentary hazards in alluvial fans

The downstream propagation of coarse material derived from the numerous landslides can inject large volumes of sediment in alluvial fans, inducing a series of potential hydro-sedimentary hazards. Several studies have documented cases of riverbed aggradation, river avulsion, increased frequency of inundation and bank erosion (Robinson & Davies, 2013). Most of the hydro-sedimentary hazards emerge from the sediment deposition patterns on the active river bed that gives the river freedom to explore laterally the fan surface. Alluvial fans response to large sediment supply is sensitive to the intensity of sediment flux and total volume of sediment feeding the fan (Croissant et al, 2017b). Therefore, an accurate quantification of coarse material mass movement is critical to anticipate intra-catchment and alluvial plain hazard.

Our results shows that the connectivity would play a role in modulating the amplitude of sediment masses that would be available to be transported out from the catchments to the alluvial plains. However, the first-order response of the alluvial in the post-seismic period would be to the proportions of landslides initially connected to the rivers. These landslides are generally the largest ones of the total co-seismic distribution and present risks from two main reasons: i. in confined river sections they have the ability to block efficiently the channel forming natural dams (Costa & Schuster, 1988). These dams are highly hazardous as their failures are generally causing tremendous damages and geomorphic changes in their downstream pathway including alluvial fans (Hancox et al., 2005). ii. large landslide usually present a high $V_{ls}/Q_t$ which evacuation of the first half of their volumes is

greatly accelerated by dynamic river width reduction (Croissant et al., 2017). Whereas the initial proportion of connected landslide could impact the short term sediment supply rate to alluvial fans the connection velocity of the remaining part of the landslide cluster would control the fan dynamic over longer timescale. For instance, a high velocity of connection would promote high sediment fluxes over short-timescales. In this scenario, the river transport capacity at the transition between the catchment and the alluvial fans is generally not large enough to transport the landslide-derived sediment leading to large aggradation rates. A lower connection velocity would promote a slower sediment delivery to the alluvial fans potentially preventing the emergence of hydro-sedimentary hazards.

Another aspect to account for when assessing the impact of large sediment deliveries on hydro-sedimentary hazards is the transport distance between the source of the sediment supplies and the at-risk areas. As demonstrated by Dingle et al [2017], abrasion is an efficient process to limit the extent of hazardous region in large catchments. For transport distances reaching several hundreds of kilometers, the population of gravel decreases its size until only sand reaches the outlet. In these cases, abrasion is an efficient process to limit the risks of channel aggradation in alluvial fans. However in other settings such as Taiwan and New Zealand, catchments have the particularity to be shorts, i.e. 80% of the streams measure less than 40 km long (see supplementary). On these distances, most of the coarse sediment can be transported downstream without losing a significant mass (Dingle et al., 2017). An accurate prediction of sediment remobilization within the catchment is therefore mandatory to full assess potential hazards in alluvial plains.

# Conclusion

In this paper, we study the post-seismic dynamics of rivers and mountain range during the aftermath of large sediment volume injection. More particularly, we build on reach scale 2D modelling results to develop a regional scale model of landslide clusters evacuation. This reduced-complexity approach is justified by the high computational cost of numerical simulation on large time and spatial scale.

Our 2D morphodynamic modeling results shows simulations of cascades of landslides shows that the evacuation of downstream deposits are not affected by the upstream sediment feed resulting from the evacuation of an upstream deposit. We then use Eros modeling results to develop a generic way to predict landslide evacuation for any $V_{ls}/Q_t$ value. This result is critical to account for sthe morphodynamic adaptation of river to the injection of landslide without having to describe analytically their width and slope evolution.

At the mountain range scale, our statistical model Quakos, shows that the landslide dynamic connectivity to the drainage network is a critical element in the modulation of post-seismic sediment transfers. Indeed, two regimes are identified based on the simulations results:

- a transport-limited regime in which the connectivity velocity only affects the transient sediment evacuation but where the state of the mountain range in the same than the full connectivity case at the end of a seismic cycle. In this regime, the timing of landslide evacuation only relies on the capacity of rivers to transport the sediment.
- a connectivity-limited regime in which and the connection velocity is large enough to delay the sediment delivery to the rivers that in turn can reach several seismic cycles.

Overall, one of the main result of the paper point towards the lack of information and robust description of the processes in play during the post-seismic phase of a landscape notably concerning the transfer of sediment from hillslope to the channels. We then propose a series of arguments on where future research could focus in order to push forward how understating of the role of large earthquakes on mountain ranges evolution.

***Acknowledgments***

T.C., P.S. and L.J. acknowledge supports by the EROQUAKE project funded by the Agence Nationale de la Recherche (ANR). D.L. acknowledge support by CNRS/INSU/ALEAS project SEDIQUAKE.

***Code availability***

The code, Eros, used to generate the morphodynamic simulations can be accessed at https://osur.univ-rennes1.fr/eros/. The source code can be obtained by making an inquiry to P.D. (philippe.davy@univ-rennes1.fr). The code, QUAKOS, can be obtained by making an inquiry to T.C. or P.S.

# References

Benda, L., & Dunne, T. (1997). Stochastic forcing of sediment supply to channel networks from landsliding and debris flow. *Water Resources Research*, *33*(12), 2849–2863. https://doi.org/10.1029/97WR02388

Berryman, K. R., Cochran, U. A., Clark, K. J., Biasi, G. P., Langridge, R. M., & Villamor, P. (2012). Major Earthquakes Occur Regularly on an Isolated Plate Boundary Fault. *Science*, *336*(6089), 1690–1693. https://doi.org/10.1126/science.1218959

Campbell, K. W., & Bozorgnia, Y. (2008). NGA ground motion model for the geometric mean horizontal component of PGA, PGV, PGD and 5% damped linear elastic response spectra for periods ranging from 0.01 to 10 s. *Earthquake Spectra*, *24*(1), 139–171. https://doi.org/10.1193/1.2857546

Cochran, U. A., Clark, K. J., Howarth, J. D., Biasi, G. P., Langridge, R. M., Villamor, P., … Vandergoes, M. J. (2017). A plate boundary earthquake record from a wetland adjacent to the Alpine fault in New Zealand refines hazard estimates. *Earth and Planetary Science Letters*, *464*, 175–188. https://doi.org/10.1016/j.epsl.2017.02.026

Costa, J. E., & Schuster, R. L. (1988). Formation and Failure of Natural Dams. *Bulletin of the Geological Society of America*. https://doi.org/10.1130/0016-7606(1988)100<1054:TFAFON>2.3.CO

Croissant, T., Lague, D., Steer, P., & Davy, P. (2017). Rapid post-seismic landslide evacuation boosted by dynamic river width. *Nature Geoscience*, *10*(9), 680–684.

https://doi.org/10.1038/ngeo3005

Croissant, T., Lague, D., Davy, P., Davies, T., & Steer, P. (2017). A precipiton-based approach to model hydro-sedimentary hazards induced by large sediment supplies in alluvial fans. *Earth Surface Processes and Landforms*. https://doi.org/10.1002/esp.4171

Cui, Y., Parker, G., Pizzuto, J., & Lisle, T. E. (2003). Sediment pulses in mountain rivers: 2. Comparison between experiments and numerical predictions. *Water Resources Research*, *39*(9), 1–11. https://doi.org/10.1029/2002WR001805

Cui, Y., & Parker, G. (2005). Numerical Model of Sediment Pulses and Sediment-Supply Disturbances in Mountain Rivers. *Journal of Hydraulic Engineering*, *131*(8), 646–656. https://doi.org/10.1061/(ASCE)0733-9429(2005)131:8(646)

Dadson, S. J., Hovius, N., Chen, H., Dade, W. B., Hsieh, M.-L., Willett, S. D., … Lin, J.-C. (2003). Links between erosion, runoff variability and seismicity in the Taiwan orogen. *Nature*, *426*(6967), 648–651. https://doi.org/10.1038/nature02150

Dadson, S. J., Hovius, N., Chen, H., Dade, W. B., Lin, J. C., Hsu, M. L., … Stark, C. P. (2004). Earthquake-triggered increase in sediment delivery from an active mountain belt. *Geology*, *32*(8), 733–736. https://doi.org/10.1130/G20639.1

Davy, P., & Lague, D. (2009). Fluvial erosion/transport equation of landscape evolution models revisited. *Journal of Geophysical Research: Solid Earth*, *114*(3), 1–16. https://doi.org/10.1029/2008JF001146

Davy, P., Croissant, T., & Lague, D. (2017). A precipiton method to calculate river hydrodynamics, with applications to flood prediction, landscape evolution models, and braiding instabilities. *Journal of Geophysical Research: Earth Surface*, *122*(8), 1491–1512. https://doi.org/10.1002/2016JF004156

Densmore, A. L., Parker, R. N., Rosser, N. J., de Michele, M., Yong, L., Runqiu, H., … Petley, D. N. (2012). Reply to "Isostasy can"t be ignored'. *Nature Geoscience*, *5*(2), 83–84. https://doi.org/10.1038/ngeo1385

Dingle, E. H., Attal, M., & Sinclair, H. D. (2017). Abrasion-set limits on Himalayan gravel flux. *Nature*, *544*(7651), 471–474. https://doi.org/10.1038/nature22039

Egholm, D. L., Knudsen, M. F., & Sandiford, M. (2013). Lifespan of mountain ranges scaled by feedbacks between landsliding and erosion by rivers. *Nature*, *498*(7455), 475–478. https://doi.org/10.1038/nature12218

Fan, X., Domènech, G., Scaringi, G., Huang, R., Xu, Q., Hales, T. C., … Francis, O. (2018). Spatio-temporal evolution of mass wasting after the 2008 Mw 7.9 Wenchuan earthquake revealed by a detailed multi-temporal inventory. *Landslides*, (August). https://doi.org/10.1007/s10346-018-1054-5

Frith, N. V., Hilton, R. G., Howarth, J. D., Gröcke, D. R., Fitzsimons, S. J., Croissant, T., … Densmore, A. L. (2018). Carbon export from mountain forests enhanced by earthquake-triggered landslides over millennia. *Nature Geoscience*, *11*(10), 772–776. https://doi.org/10.1038/s41561-018-0216-3

Gallen, S. F., Clark, M. K., & Godt, J. W. (2015). Coseismic landslides reveal near-surface rock strength in a highrelief, tectonically active setting. *Geology*, *43*(1), 11–14. https://doi.org/10.1130/G36080.1

Hancox, G. T., McSaveney, M. J., Manville, V. R., & Davies, T. R. (2005). The october 1999 mt adams rock avalanche and subsequent landslide dam-break flood and effects in poerua river, Westland, New Zealand. *New Zealand Journal of Geology and Geophysics*. https://doi.org/10.1080/00288306.2005.9515141

Helmstetter, A., & Sornette, D. (2003). Predictability in the Epidemic-Type Aftershock Sequence model of interacting triggered seismicity. *Journal of Geophysical Research: Solid Earth*, *108*(B10). https://doi.org/10.1029/2003JB002485

Hovius, N., Stark, C. P., & Allen, P. A. (1997). Sediment flux from a mountain belt derived by landslide mapping. *Geology*, *25*(3), 231–234. https://doi.org/10.1130/0091-7613(1997)025<0231:SFFAMB>2.3.CO;2

951 Hovius, N., Meunier, P., Lin, C. W., Chen, H., Chen, Y. G., Dadson, S., … Lines, M. (2011).
952 Prolonged seismically induced erosion and the mass balance of a large earthquake. *Earth and*
953 *Planetary Science Letters*, *304*(3–4), 347–355. https://doi.org/10.1016/j.epsl.2011.02.005
954 Howarth, J. D., Fitzsimons, S. J., Norris, R. J., & Jacobsen, G. E. (2012). Lake sediments record
955 cycles of sediment flux driven by large earthquakes on the Alpine fault, New Zealand. *Geology*,
956 *40*(12), 1091–1094. https://doi.org/10.1130/G33486.1
957 Keefer, D. K. (1984). Landslide causeb by earthquakes. *GSA Bulletin*.
958 Keefer, D. K. (1999). Earthquake-induced landslides and their effects on alluvial fans. *Journal of*
959 *Sedimentary Research*, *69*(1), 84–104. https://doi.org/10.2110/jsr.69.84
960 Korup, O., Densmore, A. L., & Schlunegger, F. (2010). The role of landslides in mountain range
961 evolution. *Geomorphology*, *120*(1–2), 77–90. https://doi.org/10.1016/j.geomorph.2009.09.017
962 Lague, D. (2010). Reduction of long-term bedrock incision efficiency by short-term alluvial cover
963 intermittency. *Journal of Geophysical Research*, *115*(2), 1–23.
964 https://doi.org/10.1029/2008JF001210
965 Lague, D. (2014). The stream power river incision model: Evidence, theory and beyond. *Earth*
966 *Surface Processes and Landforms*, *39*(1), 38–61. https://doi.org/10.1002/esp.3462
967 Lague, D., Hovius, N., & Davy, P. (2005). Discharge, discharge variability, and the bedrock channel
968 profile. *Journal of Geophysical Research*, *110*(F04006). https://doi.org/10.1029/2004JF000259
969 Larsen, I. J., Montgomery, D. R., & Korup, O. (2010). Landslide erosion controlled by hillslope
970 material. *Nature Geoscience*, *3*(4), 247–251. https://doi.org/10.1038/ngeo776
971 Leonard, M. (2010). Earthquake fault scaling: Self-consistent relating of rupture length, width,
972 average displacement, and moment release. *Bulletin of the Seismological Society of America*,
973 *100*(5 A), 1971–1988. https://doi.org/10.1785/0120090189
974 Li, G., West, A. J., Densmore, A. L., Jin, Z., Parker, R. N., & Hilton, R. G. (2014). Seismic mountain
975 building: Landslides associated with the 2008 Wenchuan earthquake in the context of a
976 generalized model for earthquake volume balance. *Geochemistry, Geophysics, Geosystems*,
977 *15*(4), 833–844. https://doi.org/10.1002/2013GC005067
978 Li, G., West, A. J., Densmore, A. L., Hammond, D. E., Jin, Z., Zhang, F., … Hilton, R. G. (2016).
979 Connectivity of earthquake-triggered landslides with the fluvial network: Implications for
980 landslide sediment transport after the 2008 Wenchuan earthquake. *Journal of Geophysical*
981 *Research: Earth Surface*, *121*(4), 703–724. https://doi.org/10.1002/2015JF003718
982 Lisle, T. E., Cui, Y., Parker, G., Pizzuto, J. E., & Dodd, A. M. (2001). The Dominance of Dispersion
983 in the Evoluation of Bed Material Waves in Gravel -Bed Rivers. *Earth Surface Processes and*
984 *Landforms*, *26*, 1409–1420. https://doi.org/10.1002/esp.300
985 Lucas, A., Mangeney, A., & Ampuero, J. P. (2014). Frictional velocity-weakening in landslides on
986 Earth and on other planetary bodies. *Nature Communications*, *5*, 1–9.
987 https://doi.org/10.1038/ncomms4417
988 Malamud, B. D., Turcotte, D. L., Guzzetti, F., & Reichenbach, P. (2004a). Landslide inventories and
989 their statistical properties. *Earth Surface Processes and Landforms*, *29*(6), 687–711.
990 https://doi.org/10.1002/esp.1064
991 Malamud, B. D., Turcotte, D. L., Guzzetti, F., & Reichenbach, P. (2004b). Landslides, earthquakes,
992 and erosion. *Earth and Planetary Science Letters*, *229*(1–2), 45–59.
993 https://doi.org/10.1016/j.epsl.2004.10.018
994 Marc, O., Meunier, P., & Hovius, N. (2017). Prediction of the area affected by earthquake-induced
995 landsliding based on seismological parameters. *Natural Hazards and Earth System Sciences*,
996 *17*(7), 1159–1175. https://doi.org/10.5194/nhess-17-1159-2017
997 Marc, O., Hovius, N., & Meunier, P. (2016). The mass balance of earthquakes and earthquake
998 sequences. *Geophysical Research Letters*, *43*(8), 3708–3716.
999 https://doi.org/10.1002/2016GL068333
1000 Marc, O., Hovius, N., Meunier, P., Gorum, T., & Uchida, T. (2016). A seismologically consistent
1001 expression for the total area and volume of earthquake-triggered landsliding. *Journal of*
1002 *Geophysical Research: Earth Surface*, *121*(4), 640–663. https://doi.org/10.1002/2015JF003732

1003 Métivier, F., Lajeunesse, E., & Devauchelle, O. (2017). Laboratory rivers: Lacey's law, threshold
1004 theory, and channel stability. *Earth Surface Dynamics*, *5*(1), 187–198.
1005 https://doi.org/10.5194/esurf-5-187-2017
1006 Meunier, P., Hovius, N., & Haines, A. J. (2007). Regional patterns of earthquake-triggered landslides
1007 and their relation to ground motion. *Geophysical Research Letters*, *34*(20), 1–5.
1008 https://doi.org/10.1029/2007GL031337
1009 Meunier, P., Hovius, N., & Haines, J. A. (2008). Topographic site effects and the location of
1010 earthquake induced landslides. *Earth and Planetary Science Letters*, *275*(3–4), 221–232.
1011 https://doi.org/10.1016/j.epsl.2008.07.020
1012 Meyer-Peter, E., & Müller, R. (1948). Formulas for Bed-Load Transport. *Proceedings of the 2nd*
1013 *Meeting of the International Association of Hydraulic Research*, 39–64. https://doi.org/1948-06-
1014 07
1015 Ouimet, W. (2011). The hills came tumbling down. *Nature Geoscience*, *4*(7), 424–425.
1016 Parker, G. (1990). Surface-based bedload transport relation for gravel rivers. *Journal of Hydraulic*
1017 *Research*, *28*(4), 417–436. https://doi.org/10.1080/00221689009499058
1018 Parker, R. N., Densmore, A. L., Rosser, N. J., de Michele, M., Li, Y., Huang, R., … Petley, D. N.
1019 (2011). Mass wasting triggered by the 2008 Wenchuan earthquake is greater than orogenic
1020 growth. *Nature Geoscience*, *4*(7), 449–452. https://doi.org/10.1038/ngeo1154
1021 Roback, K., Clark, M. K., West, A. J., Zekkos, D., Li, G., Gallen, S. F., … Godt, J. W. (2018). The
1022 size, distribution, and mobility of landslides caused by the 2015 M w 7.8 Gorkha earthquake,
1023 Nepal. *Geomorphology*, *301*, 121–138. https://doi.org/10.1016/j.geomorph.2017.01.030
1024 Robinson, T. R., & Davies, T. R. H. (2013). Review Article: Potential geomorphic consequences of a
1025 future great (*M*w Combining double low line 8.0+) Alpine Fault earthquake, South Island, New
1026 Zealand. *Natural Hazards and Earth System Sciences*, *13*(9), 2279–2299.
1027 https://doi.org/10.5194/nhess-13-2279-2013
1028 Robinson, T. R., Davies, T. R. H., Wilson, T. M., & Orchiston, C. (2016). Coseismic landsliding
1029 estimates for an Alpine Fault earthquake and the consequences for erosion of the Southern Alps,
1030 New Zealand. *Geomorphology*, *263*, 71–86. https://doi.org/10.1016/j.geomorph.2016.03.033
1031 Schwanghart, W., & Scherler, D. (2014). Short Communication: TopoToolbox 2 - MATLAB-based
1032 software for topographic analysis and modeling in Earth surface sciences. *Earth Surface*
1033 *Dynamics*, *2*(1), 1–7. https://doi.org/10.5194/esurf-2-1-2014
1034 Shcherbakov, R., Turcotte, D. L., & Rundle, J. B. (2004). A generalized Omori's law for earthquake
1035 aftershock decay. *Geophysical Research Letters*, *31*(11), 1–5.
1036 https://doi.org/10.1029/2004GL019808
1037 Sklar, L. S., Fadde, J., Venditti, J. G., Nelson, P., Aleksandra Wydzga, M., Cui, Y., & Dietrich, W. E.
1038 (2009). Translation and dispersion of sediment pulses in flume experiments simulating gravel
1039 augmentation below dams. *Water Resources Research*, *45*(8), 1–14.
1040 https://doi.org/10.1029/2008WR007346
1041 Sutherland, D. G., Ball, M. H., Hilton, S. J., & Lisle, T. E. (2002). Evolution of a landslide-induced
1042 sediment wave in the Navarro River, California. *Bulletin of the Geological Society of America*,
1043 *114*(8), 1036–1048. https://doi.org/10.1130/0016-7606(2002)114<1036:EOALIS>2.0.CO;2
1044 Tait, A., & Zheng, X. (2007). Analysis of the Spatial Interpolation Error associated with Maps of
1045 Median Annual Climate Variables. *National Institute of Water & Atmospheric Research*, (May).
1046 Tanyaş, H., van Westen, C. J., Allstadt, K. E., Anna Nowicki Jessee, M., Görüm, T., Jibson, R. W., …
1047 Hovius, N. (2017). Presentation and Analysis of a Worldwide Database of Earthquake-Induced
1048 Landslide Inventories. *Journal of Geophysical Research: Earth Surface*, *122*(10), 1991–2015.
1049 https://doi.org/10.1002/2017JF004236
1050 Tanyaş, H., Allstadt, K. E., & van Westen, C. J. (2018). An updated method for estimating landslide-
1051 event magnitude. *Earth Surface Processes and Landforms*. https://doi.org/10.1002/esp.4359
1052 Tucker, G. E., & Hancock, G. R. (2010). Modelling landscape evolution. *Earth Surface Processes and*
1053 *Landforms*, *35*(1), 28–50. https://doi.org/10.1002/esp.1952
1054 Turcotte, D. L., Holliday, J. R., & Rundle, J. B. (2007). BASS, an alternative to ETAS. *Geophysical*

*Research Letters*, *34*(12), 1–5. https://doi.org/10.1029/2007GL029696

Wang, J., Jin, Z., Hilton, R. G., Zhang, F., Densmore, A. L., Li, G., & Joshua West, A. (2015). Controls on fluvial evacuation of sediment from earthquake-triggered landslides. *Geology*, *43*(2), 115–118. https://doi.org/10.1130/G36157.1

Wang, J., Jin, Z., Hilton, R. G., Zhang, F., Li, G., Densmore, A. L., … Joshua West, A. (2016). Earthquake-triggered increase in biospheric carbon export from a mountain belt. *Geology*, *44*(6), 471–474. https://doi.org/10.1130/G37533.1

Wang, W., Godard, V., Liu-Zeng, J., Scherler, D., Xu, C., Zhang, J., … de Sigoyer, J. (2017). Perturbation of fluvial sediment fluxes following the 2008 Wenchuan earthquake. *Earth Surface Processes and Landforms*, *42*(15), 2611–2622. https://doi.org/10.1002/esp.4210

Whipple, K. X., & Meade, B. J. (2006). Orogen response to changes in climatic and tectonic forcing. *Earth and Planetary Science Letters*, *243*(1–2), 218–228. https://doi.org/10.1016/j.epsl.2005.12.022

Whipple, K. X., & Tucker. (1999). Dynamics of the stream-power river incision model: Implications for height limits of mountain ranges, landscape response timescales, and research needs. *Journal of Geophysical Research*, *104*, 661–674. https://doi.org/10.1029/1999JB900120

Wilcock, P. R., & Crowe, J. C. (2003). Surface-based transport model for mixed-size sediment. *Journal of Hydraulic Engineering*, *129*(2), 120–128. https://doi.org/10.1061/(ASCE)0733-9429(2003)129:2(120)

Yanites, B. J., Tucker, G. E., Mueller, K. J., & Chen, Y. G. (2010). How rivers react to large earthquakes: Evidence from central Taiwan. *Geology*, *38*(7), 639–642. https://doi.org/10.1130/G30883.1

Yanites, B. J., Tucker, G. E., Hsu, H. L., Chen, C. C., Chen, Y. G., & Mueller, K. J. (2011). The influence of sediment cover variability on long-term river incision rates: An example from the Peikang River, central Taiwan. *Journal of Geophysical Research: Earth Surface*, *116*(3), 1–13. https://doi.org/10.1029/2010JF001933

Yuan, R. M., Deng, Q. H., Cunningham, D., Xu, C., Xu, X. W., & Chang, C. P. (2013). Density distribution of landslides triggered by the 2008 Wenchuan earthquake and their relationships to peak ground acceleration. *Bulletin of the Seismological Society of America*, *103*(4), 2344–2355. https://doi.org/10.1785/0120110233

Zhang, S., Zhang, L., Lacasse, S., & Nadim, F. (2016). Evolution of Mass Movements near Epicentre of Wenchuan Earthquake, the First Eight Years. *Scientific Reports*, *6*(October), 36154. https://doi.org/10.1038/srep36154

**Table 1 :** Value of the parameters of equation 5.

| $T_{exp}$ | delta | mu | phi | beta |
|---|---|---|---|---|
| 20% | 4 | 0.02 | 1.05 | 0.1 |
| 30% | 7 | 0.02 | 1 | 0.1 |
| 40% | 7 | 0.033 | 1.01 | 0.1 |
| 50% | 10.8 | 0.033 | 1 | 0.1 |
| 60% | 13 | 0.033 | 0.95 | 0.1 |
| 70% | 17 | 0.033 | 0.93 | 0.1 |
| 80% | 23 | 0.033 | 0.79 | 0.1 |

**Table 2 |** Parameters used in QUAKOS

| Parameter | Notation | Values | Units |
|---|---|---|---|
| ***Tectonic*** | | | |
| Fault length | $F_L$ | 400 | km |
| Fault width | $F_W$ | 19 | km |
| Fault dip | $F_D$ | 60 | ° |
| Fault rake | $F_R$ | 172 | ° |
| ***Earthquake rupture – Strike-slip*** | | | |
| Shear modulus | $\mu$ | 33 | GPa |
| Exponent | $\beta$ | 0.66 | / |
| Constant | $C_1$ | 15 | / |
| Constant | $C_{10}$ | $F_W$ | / |
| Constant | $C_{11}$ | 1 | / |
| Constant | $C_2$ | $3.6.10^{-5}$ | / |
| ***Landsliding*** | | | |
| Min. landslide area | $A_{ls,min}$ | 50 | $m^2$ |
| Max. landslide area | $A_{ls,max}$ | $2.10^6$ | $m^2$ |
| pdf($A_{ls}$) roll-over position | $a$ | 2000 | $m^2$ |
| pdf($A_{ls}$) roll-back | $s$ | -200 | $m^2$ |
| pdf($A_{ls}$) tail exponent | $\rho$ | 1.4 | / |
| Volume-Area prefactor | $\alpha$ | 0.05 | / |
| Volume-Area exponent | $\gamma$ | 1.5 | / |
| PGA-$P_{ls}$ coefficient | $\alpha_p$ | 4 | / |
| PGA-$P_{ls}$ coefficient | $\beta_p$ | 0.5 | / |
| Connectivity parameter | $m$ | 0.87 | / |
| Connectivity exponent | $\omega$ | 0.34 | / |
| ***River transport capacity*** | | | |
| Critical drainage area | $A_c$ | 0.5 | $km^2$ |
| Steepness index | $k_{sn}$ | 180 | / |
| Width index | $k_{wn}$ | 0.008 | / |
| Median grain size | $D_{50}$ | 0.3 | m |
| Mean annual runoff | $\bar{r}$ | 7.5 | $m.yr^{-1}$ |
| Discharge variability | $k$ | 1 | / |
| Manning coefficient | $n$ | 0.035 | $s.m^{-1/3}$ |
| Transport capacity parameter | $K$ | $1.5.10^{-5}$ | / |
| Shields number | $\theta_c$ | 0.035 | / |

# Post-seismic sediment evacuation – from single landslide removal to mountain range global fluxes.

Thomas Croissant[1,2*], Philippe Steer[1], Dimitri Lague[1], Philippe Davy[1], Louise Jeandet[1] and Robert G. Hilton[2]

[1] *Géosciences Rennes, OSUR, CNRS, Université de Rennes 1, Campus de Beaulieu, Rennes*

[2] *now at Department of Geography, Durham University, Durham, DH1 3LE, UK*

Corresponding author: T. Croissant; thomas.croissant@durham.ac.uk

## Supplementary methods

1. Initial properties of landslide clusters as a function of the pdf($A_{ls}$) shape

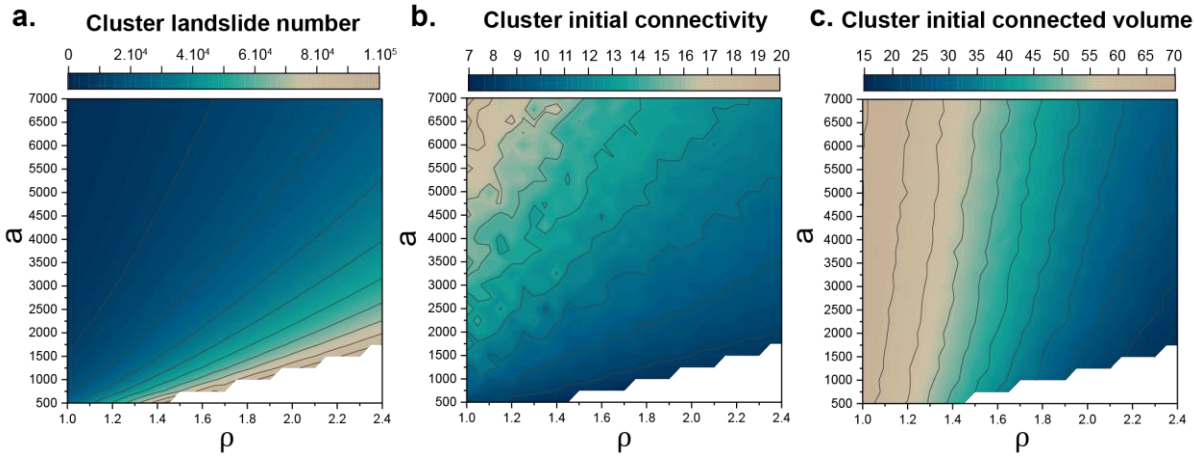


**Figure S1 | Influence of the *pdf*($A_{ls}$) parameters (tail slope (ρ) and roll-over position (a)) on the initial properties of the randomly generated landslide cluster average over 100 simulations. a.** The total number of generated landslides. **b.** The percentage of initially connected landslides within the cluster. **c.** The percentage of sediment volume initially available for fluvial transport.

As *a* increases, *rho* decreases or both, the landslide clusters are characterised by more abundant large landslides that present a higher probability to be initially connected to the drainage network resulting to a more initial efficient sediment delivery.

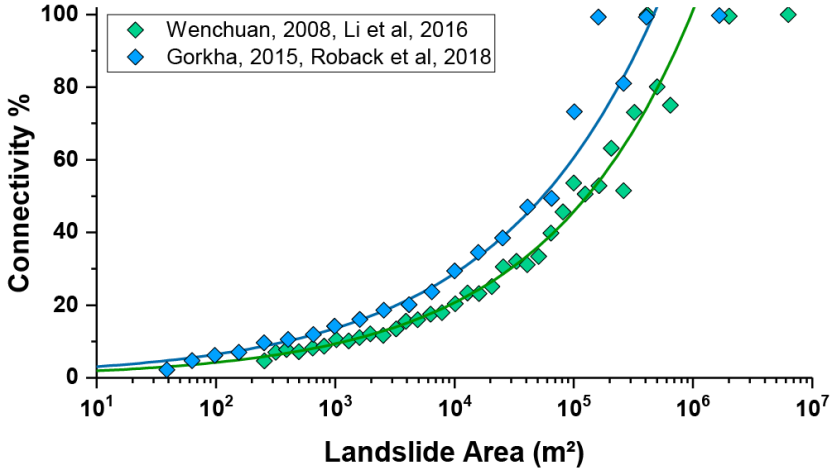


**Figure S2 | Connectivity value as a function of landslide area for 2 empirical datasets, namely the Wenchuan and Gorkha earthquake (Li et al, 2016; Roback et al, 2018).** The value of connectivity is assigned to binned data of landslide areas on a logarithmic scale.

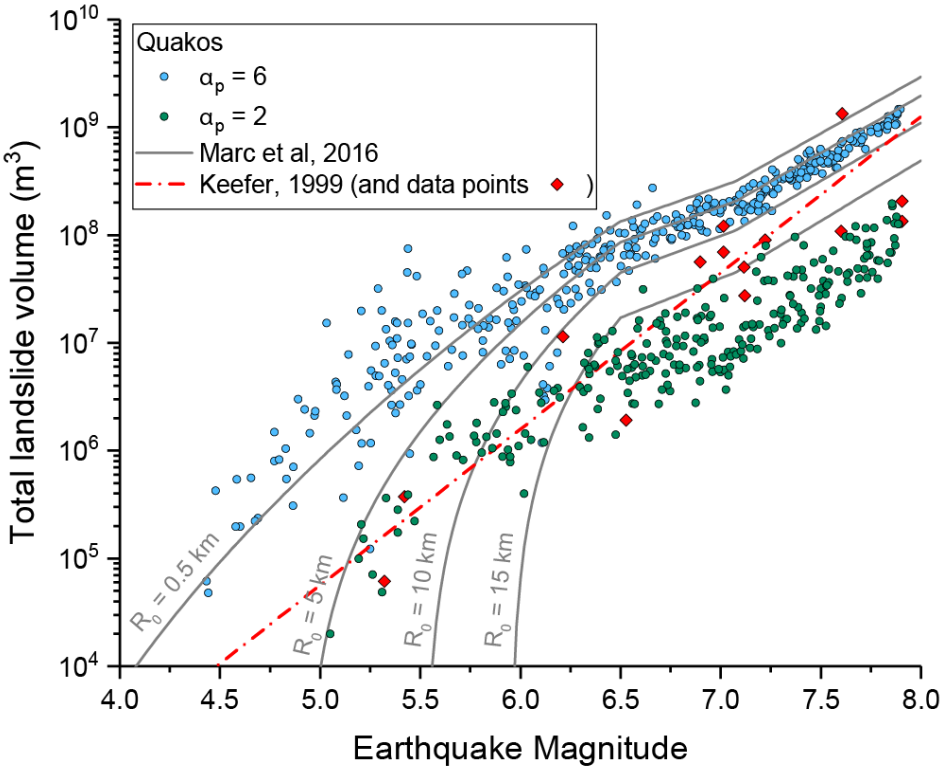


**Figure S3 |** Relationship between the total volume of landslides triggered by earthquakes and their magnitude, in the case of a strike-slip fault for different value of maximum of landslide density. Quakos output are compared to two empirical models from Marc et al, [2016] and Keefer, [1999].

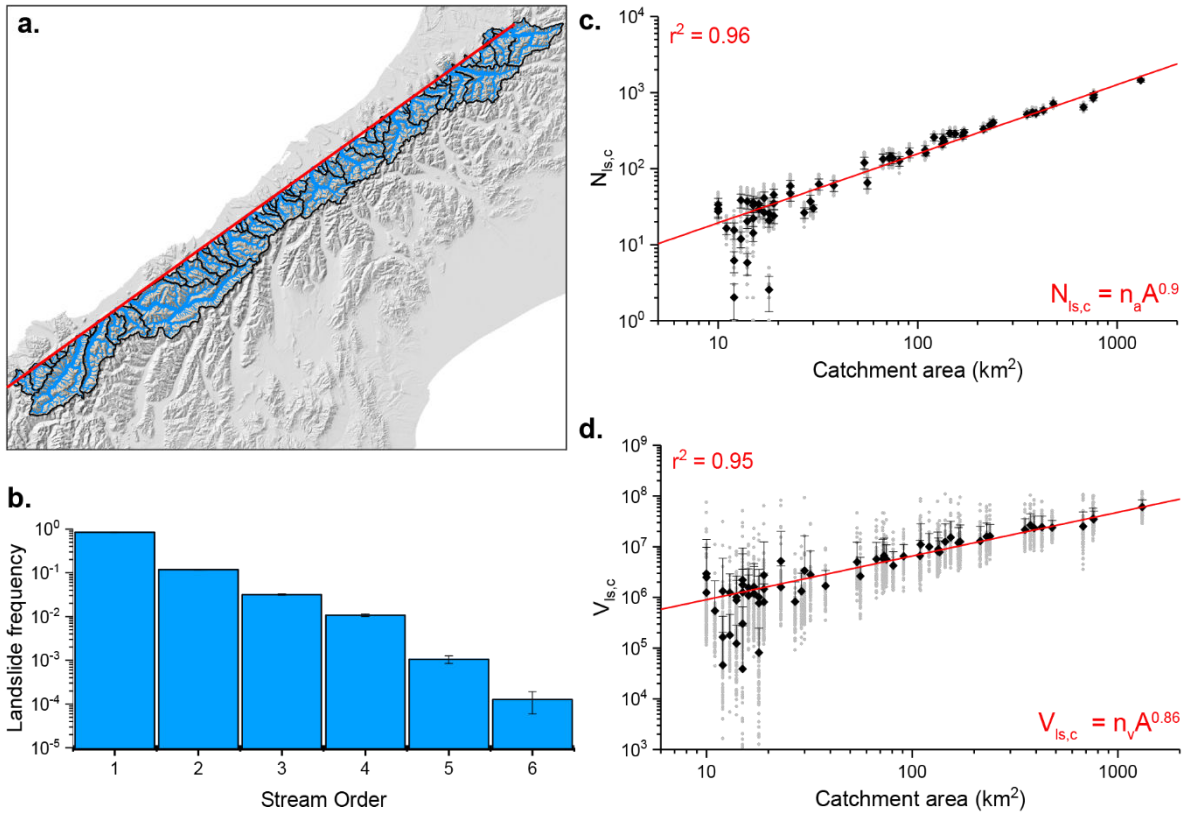


**Figure S4 | a.** Landslide frequency as a function of stream order (Sthraler definition). **b.** Scaling between the total number of landslides triggered in each catchment. **c.** Scaling between the total volume of landslides triggered in each catchment. (in grey: data from the 50 simulations, in black: average and associated standard deviation).

## Supplementary movies

**Movie S1 |** QUAKOS, PGA predictions as a function of earthquake magnitude and depth.

**Movie S2 |** QUAKOS, Post-seismic evolution of a landslide cluster, full-connectivity scenario.

**Movie S3 |** QUAKOS, Post-seismic evolution of a landslide cluster, $v_{con}$ = 10 m.yr$^{-1}$ scenario.

UNIVERSITE ECOLOGIE
BRETAGNE GEOSCIENCES
LOIRE AGRONOMIE ALIMENTATION

UNIVERSITÉ DE RENNES 1

**Titre :** Modélisation numérique des liens entre séismes et glissements de terrain au cours du cycle sismique : processus déclencheurs, distributions de tailles et implications géologiques.

**Mots clés :** glissements de terrain, séismes, cycle sismique, érosion, modélisation numérique

**Résumé :** Les interactions entre les processus tectoniques et l'érosion ont été peu étudiées à des échelles de temps courtes (< 1000 ans). Cependant, les séismes peuvent activement contribuer à l'érosion des chaînes de montagne en déclenchant de nombreux glissements de terrain. Des études récentes ont également montré que ces grands événements érosifs pourraient engendrer des changements de contraintes suffisants à proximité des failles actives pour modifier la sismicité régionale. Dans cette thèse, cette problématique a été abordée via une approche numérique. Dans un premier temps, le développement d'un modèle simple de glissements de terrain prenant en compte la topographie des versants a permis de démontrer le rôle des paramètres mécaniques (cohésion et friction), et de la forme des versants sur la distribution de taille des glissements de terrain. Ce modèle a été validé à l'aide de cas naturels de glissements de terrain co-sismiques Dans un deuxième temps, le rôle de la forme finie des versants sur la probabilité de grands glissements de terrain a été démontrée en se basant sur des données. Enfin, dans un troisième temps, le potentiel effet d'un grand évènement érosif sur la sismicité a été exploré à l'aide d'un modèle numérique de cycle sismique dans lequel ont été implémentées des variations temporelles de la contrainte normale sur la faille. Les résultats mettent en évidence le rôle du volume de sédiments, mais aussi de leur temps d'export. En particulier, les paysages caractérisés par une hauteur unstable des versants importante pourraient, en favorisant de grands glissements de terrain, induire une érosion assez importante et rapide pour modifier de façon significative la sismicité régionale.

**Title:** Numerical modeling of the links between earthquakes and landsliding during the seismic cycle: triggering processes, size distribution, and geological implications.

**Keywords :** landslides, earthquakes, seismic cycle, erosion, numerical modelling

**Abstract:** Interactions between tectonic processes and erosion have been poorly investigated at short time-scales (<1000 years). However, earthquakes can largely contribute to the erosion of mountain belts by triggering widespread landsliding. Moreover, recent studies have shown that such large erosional events could induce stress changes in the fault environment efficient enough to influence regional seismicity. In this thesis, this problematic is tackled through a numerical approach. Firstly, the development of a simple mechanical model accounting for the complexity and variability of natural hillslopes allowed to demonstrate the role of mechanical parameters (cohesion and friction), and of hillslope shape in the probability density function of landslide sizes. This model has been validated using natural cases of co-seismic landsliding. Secondly, the role of unstable hillslope height on large landlside probability has been demonstrated based on natural data, and the exponential distribution of this unstable height has ben shown. Finally, the potential effect of a large erosional event on seismicity has been explored with a numerical model of seismic cycle, in which has been implemented temporal normal stress variations. The results emphasize the role of eroded sediment volume, but also of the export time of sediments away from the mountain belt. In landscape with high unstable hillslopes, large landslides are favored and in turn, coud induce fast an important enough erosion to modify regional seismicity.